

INFORMATION TO USERS

This manuscript has been reproduced from the microfilm master. UMI films the text directly from the original or copy submitted. Thus, some thesis and dissertation copies are in typewriter face, while others may be from any type of computer printer.

The quality of this reproduction is dependent upon the quality of the copy submitted. Broken or indistinct print, colored or poor quality illustrations and photographs, print bleedthrough, substandard margins, and improper alignment can adversely affect reproduction.

In the unlikely event that the author did not send UMI a complete manuscript and there are missing pages, these will be noted. Also, if unauthorized copyright material had to be removed, a note will indicate the deletion.

Oversize materials (e.g., maps, drawings, charts) are reproduced by sectioning the original, beginning at the upper left-hand corner and continuing from left to right in equal sections with small overlaps. Each original is also photographed in one exposure and is included in reduced form at the back of the book.

Photographs included in the original manuscript have been reproduced xerographically in this copy. Higher quality 6" x 9" black and white photographic prints are available for any photographs or illustrations appearing in this copy for an additional charge. Contact UMI directly to order.

UMI

A Bell & Howell Information Company
300 North Zeeb Road, Ann Arbor MI 48106-1346 USA
313/761-4700 800/521-0600

UNIVERSITY OF CALIFORNIA
Santa Barbara

Degradation in
Vertical Cavity Lasers

A Dissertation submitted in partial satisfaction
of the requirements of the degree of

Doctor of Philosophy

in

Electrical Engineering

by

Robert Wallace Herrick

Committee in charge:

Professor Pierre M. Petroff, Chairperson

Professor Larry A. Coldren

Professor Arthur C. Gossard

Professor Mark Rodwell

December 1997

UMI Number: 9819568

**Copyright 1997 by
Herrick, Robert Wallace**

All rights reserved.

**UMI Microform 9819568
Copyright 1998, by UMI Company. All rights reserved.**

**This microform edition is protected against unauthorized
copying under Title 17, United States Code.**

UMI
300 North Zeeb Road
Ann Arbor, MI 48103

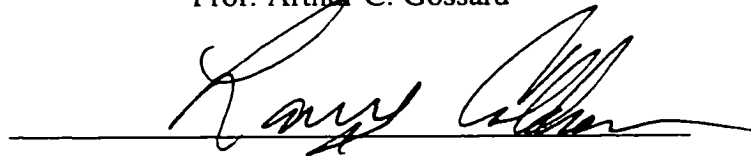
The dissertation of Robert Wallace Herrick is approved:



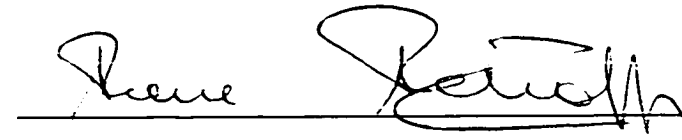
Prof. Mark Rodwell



Prof. Arthur C. Gossard



Prof. Larry A. Coldren



Prof. Pierre M. Petroff
Committee Chairperson

December 1997

Degradation in
Vertical Cavity Lasers

Copyright © by
Robert Wallace Herrick
All rights reserved
September 1997

Department of Electrical and Computer Engineering
University of California, Santa Barbara
Santa Barbara, CA 93106-9560

Acknowledgments:

It has been truly a great experience to work for Pierre Petroff, who is probably the premiere researcher in the field of reliability, having published the first accounts of the causes of laser failure nearly 25 years ago. His years of experience led us into many directions which I would certainly not have pursued on my own. I learned a tremendous amount about Material Science from him, in specialized courses on defects and growth of electronic materials, which are offered almost nowhere else in the world. He has given me a great deal of freedom to follow my own research directions, and has always been there to give assistance and advice. For all these things, I give my most sincere thanks.

I would also like to thank my other committee members: I learned a great deal from Prof. Larry Coldren and his group. I would like to thank him for supporting me in my first few years at UCSB, and for access to his testing labs which I have made extensive use of in my work. Prof. Art Gossard and Prof. Mark Rodwell also gave generously of their time in serving on my committee, and in consulting with me on my dissertation.

Eric Hegblom provided helpful comments on drafts of my thesis, and various presentations. I appreciate the time he took to make comments and make this dissertation a more useful document. Prof. Jim Speck also provided advice and good references for Chapter 2 and Appendix C. I would also like to Thank Drs. Ray Twesten, David Follstaedt, and Mary Crawford for permission to publish the TEM images of InGaP growths shown in Chapter 6.

By and large, the lasers studied were from Honeywell Technology Center. Thanks to Mary Hibbs-Brenner and Bob Morgan for providing excellent samples in large quantities. James Guenter of Honeywell MICRO SWITCH also provided many samples, and many helpful discussions. Hong Hou, Kent Choquette of Sandia National Laboratories provided the 850 nm oxide aperture lasers which are discussed in Chapter 8. Matt Peters, Gerry Robinson, and Brian Thibeault provided packaged UCSB VCSELs for use in aging experiments, and also provided most of my training in laser testing and device fabrication.

Jessie DeAro, Ken Weston, and Prof. Steve Buratto of the UCSB Chemistry department did the NSOM experiments described in Appendix A, which provided important proof that we were on the right track in understanding why the VCSELs degrade. Lucien Ghislain also helped with NSOM experiments and advice on sensitive detectors for the CL system. Ke Luo and Prof. Arun Majumdar of the UCSB Dept. of Mechanical Engineering did the scanning thermal microscopy measurements described in Appendix A — my conversations with Prof. Majumdar (now at UC Berkeley) were always particularly stimulating.

Dan Cohen was always quick to help in finding needed components, and in giving good advice on experimental setups. Many of the experimental CL and TEM results in Chapters 3 and 4 were taken by Michael Cheng. Jeff Schramm built the laser life tester, and helped to provide a path for me to get involved in studying device lifetime. San Liang Lee assisted with the data acquisition software needed for the spectral measurements.

Chris Elsass improved the CL system dramatically, and made possible the results shown in chapter 6, while Irina Maladovich provided assistance with PL measurements shown in chapter 5. Eric Tarsa did the indium-oxide deposition for semitransparent contacts shown in chapter 3, and provided advice on developing a

cleanroom process for depositing ITO. More generally, I wish to thank a number of people for helpful discussions and good ideas, including Frank Peters, Eric Hegblom, Bruce Young, Ryan Naone, James Ibbetson, Jeff Scott, and Geoff Thompson. There were many other students, faculty and staff, to whom I owe a debt of gratitude for what they have contributed to my education here. I would also like to thank my friends for making my five years in Santa Barbara pleasant ones.

I achieved a true respect for the potential of mentorship while working for my boss at McDonnell Douglas, Joseph Levy. He constantly encouraged me to take the extra step, and really expand my potential, even in areas I didn't know I had talent. He also taught me much of what I know about semiconductor lasers. His mentorship has made a major difference in my life, and I will always be grateful for it.

Finally, my parents have always been there for me. For their continual support in many different ways, I dedicate this thesis to them.

Dedicated to my parents,
for their support and encouragement

Vita

August 2, 1963: Born in Santiago, Chile (to American parents)

June, 1984: B.S., Electronics Engineering Technology, with honors,
DeVry Institute of Technology, Atlanta Georgia

January, 1987: M.S., Electrical Engineering, University of Illinois,
Champaign, Illinois

March 1987-
September 1992: Senior Engineer, Electronics, McDonnell Douglas Electronic
Systems Co., St. Louis, Missouri

Sept. 1992 - 1997: Research Assistant, ECE Dept., UC Santa Barbara

Sept 1997: Ph.D., Electrical Engineering, UC Santa Barbara

Publications:

- 28) Robert W. Herrick and Pierre M. Petroff, "Annealing and aging in GaInP-based red VCSELs," accepted for presentation at LEOS '97.
- 27) Robert W. Herrick and Pierre M. Petroff, "Failure Analysis of 850 nm Vertical Cavity Lasers," presented at the IEEE Summer Topicals, Montreal, Canada, August 1997 (pp. 77-78).
- 26) Robert W. Herrick, Y. Michael Cheng, and Pierre M. Petroff, "Degradation in Vertical Cavity Lasers," Presented at the 39th Annual Electronic Materials Conference in Fort Collins, CO. (p. 35)
- 25) K. Luo, R.W. Herrick, A. Majumdar, and P. Petroff, "Scanning thermal microscopy of vertical cavity lasers," accepted by Applied Physics Letters.
- 24) U.S. Patent 5,601,687, "Mask Design," issued to the U.S. Air Force, Feb. 11, 1997. Inventor: Robert W. Herrick.
- 23) K. Luo, R.W. Herrick, A. Majumdar, and P. Petroff, "Internal temperature distribution of a vertical-cavity surface-emitting laser measured by scanning thermal microscopy," ASME International Mechanical Engineering Congress and Exposition, Atlanta, GA, Nov. 1996, published in *ASME Microelectromechanical Systems*, Vol. 59, pp. 25-30.
- 22) Y. Michael Cheng, Robert W. Herrick, Pierre M. Petroff, Mary K. Hibbs-

Brenner, and Robert A. Morgan, "Defect Structures Induced During Degradation of Proton-Implanted GaAs Quantum Well Vertical-Cavity Surface Emitting Lasers," Presented at the 38th Annual Electronic Materials Conference, June 27, 1996.

21) Y. Michael Cheng, Robert W. Herrick, Pierre M. Petroff, Mary K. Hibbs-Brenner, and Robert A. Morgan, "Degradation Mechanisms of Vertical Cavity Surface Emitting Lasers," *Proceedings of the 34th Annual International Reliability Physics Symposium*, pp. 211-213 (May 1, 1996).

20). Robert W. Herrick, Y. Michael Cheng, Pierre M. Petroff, Jeff W. Scott, Matthew G. Peters, Gerald D. Robinson, Larry A. Coldren, Robert A. Morgan, and Mary K. Hibbs-Brenner, "Analysis of VCSEL degradation modes, *Proceedings of the SPIE*, Vol. 2683, ("Fabrication, Testing, and Reliability of Semiconductor Lasers"), pp. 123-133, (1996).

19). Y. Michael Cheng, Robert W. Herrick, Pierre M. Petroff, Mary K. Hibbs-Brenner, and Robert A. Morgan, "Degradation studies of proton-implanted vertical cavity surface emitting lasers," *Applied Physics Letters*, Vol. 67, pp. 1648-1650, (18 Sept. 1995).

18). Robert W. Herrick, Y. Michael Cheng, Pierre M. Petroff, Mary K. Hibbs-Brenner, and Robert A. Morgan, "Spectrally-filtered electroluminescence of vertical cavity surface emitting lasers," *IEEE Photonics Technology Letters*, Vol. 7 #10, pp. 1107-1109, (Oct. 1995).

17). K.H. No, R.W. Herrick, C. Leung, R. Reinhart, and J.L. Levy, "One dimensional scaling of 100 ridge waveguide amplifiers," *IEEE Photonics Technology Letters*, Vol. 6, #9, pp. 1062-1066, (Sept. 1994).

16). M.G. Peters, D.B. Young, F.H. Peters, B.J. Thibeault, J.W. Scott, S.W. Corzine, R.W. Herrick, and L.A. Coldren, "High wall-plug efficiency temperature-insensitive vertical-cavity surface-emitting lasers with low-barrier p-type mirrors," presented at OE-Lase '94 in Los Angeles, Jan. 27, 1994, and published in the *SPIE proceedings*, Vol. 2057, pp. 2-11.

15). K.H. No, R.W. Herrick, C. Leung, R.M. Rhinehart, J.L. Levy, "Two-Dimensional scaling of ridge waveguide amplifiers," presented at OE-Lase '94 in Los Angeles, Jan 25, 1994, and published in the *SPIE proceedings*, Vol 2148, pp 80-90.

14). R.W. Herrick, R.D. Fraser, J.G. Eden, "Fragmentation and emission of POPOP and coumarin dye vapor in an ultraviolet-preionized, transverse discharge," *J. Appl. Phys.*, Vol. 75, #3, pp. 1293-1298, (1 Feb. 1994).

13). U.S. Patent 5,259,925, "Method of Cleaving a Plurality of Semiconductor Devices," issued to the McDonnell Douglas Corporation on Nov. 9, 1993. Inventors: Robert W. Herrick, Joseph L. Levy, and Danny J. Krebs.

12). Kun H. No, Richard J. Blackwell, Robert W. Herrick, and Joseph L. Levy, "Monolithic integration of an amplifier and a phase modulator fabricated in a

GRINSCH-SQW structure by placing the junction below the quantum well," IEEE Photonics Technol. Lett., Vol. 5, #9, pp. 990-993, (Sept. 1993).

11). Chang Shen, Phil Fraundorf, and Robert W. Herrick, "Scanned tip measurement of deep vertical facets on a flat surface - measuring roughness on GaAs laser waveguide mirrors," Proc. 51st Annual Meeting of the Microscopy Society of America, Cincinnati, OH (August 1-6, 1993).

10). R.W. Herrick, J.L. Levy, "Demonstration of a Coherent Scalable Phased Array of Semiconductor Lasers," Invited paper published in the proceedings of the Diode Laser Technology Presentation (DLTP-92). Presented by R.W. Herrick April 21, 1992 at Ft. Walton Beach, Florida.

9). Robert W. Herrick, Lori G. Sabo, and Joseph L. Levy, "Novel technique for the analysis of surface roughness on semiconductor laser etched facets," J. Vacuum Sci. and Technol. B, Vol. 9, #6, pp. 2778-2783, (1991).

8). S. M. Lee, W.C. Chew, M. Moghaddam, M. Nasir, S.L. Chuang, R.W. Herrick, and C.L. Balestra, "Modeling of Rough-Surface Effects in an Optical Turning Mirror Using the Finite-Difference Time-Domain Method," J. Lightwave Technol, Vol. 9, #11, pp. 1471-1480, (1991).

7). R.W. Herrick, Lori G. Sabo, and Joseph L. Levy, "Analysis of Surface Roughness on Semiconductor Laser Etched Facets," Proceedings of LEOS 1991 Summer Topical Meeting on Microfabrication for Photonics and Optoelectronics, July 31-Aug 2, 1991, Newport Beach, California, pp. 43,44.

6). D. Krebs, R. Herrick, K. No, W. Harting, F. Struempf, D. Driemeyer, and J. Levy, "22 W Coherent GaAlAs Amplifier Array with 400 emitters," IEEE Photonics Technol. Lett., Vol. 3, #4, pp. 292-295, (1991).

5.) C.C. Leung, D.J. Krebs, R.W. Herrick, F.L. Struempf, H.R. Appelman, J.L. Levy, "Study of Optical Signal Distribution Networks for Coherent Semiconductor Amplifier Arrays," Paper SCF-4, LEOS summer topical meetings, Aug, 1990.

4). M.S. Zediker, H.R. Appelman, B.G. Clay, J.R. Heidel, R.W. Herrick, J. Haake, J. Martinosky, F. Struempf, and R.A. Williams, "10-Amplifier Coherent Array Based on Active-Integrated Optics." *Proceedings of the SPIE*, Vol. 1219, pp. 197-210 (1990).

3). R.A. Moellering, L.B. Bauer, R.W. Herrick, and C.L. Balestra, "Non-destructive Determination of Proper Etch Depth for AlGaAs/GaAs Rib Laser Diodes Using Fourier Transform Infrared (FTIR) Spectroscopy." *Technical Digest of Advanced Processing and Characterization Technologies*, (Oct. 1989), pp. 35-38.

2) Robert W. Herrick, "Fluorescence Spectra of Electrically-Excited Dye Vapors," a Master's Thesis in Electrical Engineering at the University of Illinois, Champaign-Urbana, published in November 1986.

1). D.P. Greene, R.W. Herrick, and J.G. Eden, "Vapor Dye Lasers," Invited paper published in the proceedings of the Lasers-86 Conference, Orlando, Florida.

Abstract

Degradation in Vertical Cavity Lasers

by

Robert Wallace Herrick

Vertical Cavity Lasers (VCLs) are rapidly being adopted as low-cost sources in data communications links. It is thus important that we understand how VCLs age, if we are to be able to extend their lifetime to meet the desired reliability standards. We focus primarily on the widely-commercialized top-emitting, proton-implanted design, with GaAs quantum wells, and emitting at 850 nm. We also provide extensive characterization of 680 nm GaInP-quantum-well proton-implanted VCLs. A brief discussion is provided regarding the degradation in 980 nm etched pillar VCLs, and 980 and 850 nm oxide-aperture VCLs.

Surprisingly, a number of major differences are noted between the degradation behavior of traditional stripe lasers (which lase in the plane of the active region), and vertical cavity lasers (which lase perpendicular to the active region). The primary degradation mechanism in VCLs appears to be related to passivation of the dopants in the center of the lasers, which forces current out toward the device edges, where it is not useful in the lasing process. In the final stages of device degradation, dislocations appear not only in the active regions, but also surprisingly in the p-mirrors above the active region. The driving mechanism for this degradation process is discussed in detail. Extensive characterization, including

cathodoluminescence (CL), transmission electron microscopy (TEM), photoluminescence (PL), electroluminescence (EL), electron beam induced current (EBIC), and scanning probe techniques are used to shed light on the nature and causes of the aging process. In spite of valid reasons for concern about the potential degradation rates of VCLs, we do not observe dark-line defects in the proton-implanted lasers which are our main research focus, and the lasers appear to be relatively insensitive to damage to the die edges or facets, in contrast to stripe lasers. Further, the proton implant appears not to participate in the aging process as had been expected. Ideas for lengthening the lifetime of VCLs are also discussed.

Table of Contents

1. Introduction

1.1 Applications of Vertical Cavity Lasers	1
1.2 Advantages of Vertical Cavity Lasers	3
1.3 Potential Difficulties with Vertical Cavity Lasers	8
1.4 Background on Present VCL Reliability	10
1.5 Dissertation Overview	13

2. Background Information on Semiconductor Laser Degradation Processes

2.1 Dislocation Climb and $\langle 100 \rangle$ Dark-Line Defects	21
2.2 Dislocation Glide and $\langle 110 \rangle$ Dark-Line Defects	33
2.3 Gradual Degradation in LEDs and Stripe Lasers	37
2.4 Effects of Dark-Line Defects on Devices	39

3. The Early Stages of Degradation

3.1 Background on Traps and Donor Passivation	48
3.2 Description of Structure Studied	49
3.3 Key Assumptions, and Aging Conditions	51
3.4 Cross-Sectional EBIC	54
3.5 Plan-View CL and PL Imaging	55
3.6 Electroluminescence Imaging of Aged VCSELs	63
3.7 C-V and I-V Characterization	67
3.8 Discussion of Early Degradation Mechanisms	68

4. The Late Stages of Degradation

4.1 Degradation in the Active Region	77
4.2 Non-Localized Observations of Degradation by CL	79
4.3 Analysis of TEM Images of Degraded Devices	83
4.4 Examining p-Contact Interdiffusion	87

5. Driving Forces Responsible for Degradation in the DBR Layers

5.1 Identification of Spectral Features	93
5.2 Dependence of Spontaneous Emission on Current	100
5.3 Discussion of Mechanism for p-DBR Degradation.	102
5.4 Results from Wide Bandgap VCSELs	105
5.5 Observations of Deep Levels in VCSEL Spectra	106

6. Degradation in Red InGaP QW Vertical Cavity Lasers

6.1 Introduction to Red InGaP VCSELs	109
6.2 Description of Laser Structure	116
6.3 General Observations in Degraded Red VCSELs	119
6.4 Observations of Bias Annealing Effects	121
6.5 Aging-Induced Changes in Red VCSEL CL Spectra	136
6.6 Discussion and Conclusions	150

7. Degradation in Other Types of Gain Guided VCSELs

7.1 Degradation in Non-Production 850 nm VCSELs	157
7.2 Dielectric Mirror VCSELs	159

8. Degradation in Index-Guided VCSELs

8.1 980 nm UCSB Pillar VCSELs	161
8.2 980 nm UCSB Oxide-Aperture VCSELs	163
8.3 850 nm Sandia Oxide-Aperture VCSELs	167

9. Conclusions and Future Work

9.1 Brief Summary of Findings	173
9.2 Suggested Future Work	174

Appendix A: Scanning Probe Microscopies

A.1 Near-Field Scanning Optical Microscopy (NSOM)	183
A.2 Scanning Thermal Microscopy (SThM)	188

Appendix B: Sample Preparation

B.1 Cross-Sectional Sample Preparation for VCL Arrays	194
B.2 Plan View Sample Preparation	209
B.3 Sample Preparation for Single Die VCSELs	222

Appendix C: Strained-Layer Quantum Wells for Enhanced Lifetime

C.1 Experimental observations of dislocation pinning	237
C.2 Analysis of Dislocation Pinning	238
C.3 Difficulties with InAlGaAs QW Lasers	240

Appendix D: VCSEL Reliability Estimates

D.1 Introduction	243
D.2 The Importance of the Proper Failure Distribution	244
D.3 Extrapolation of Early Degradation	247

Appendix E: Introduction to CL and EBIC

E.1 Description of Experimental Apparatus	249
E.2 Electron Beam Spread in Sample	251
E.3 Limitations and Experimental Artifacts in CL	253

Appendix F: Materials Properties of AlGaAs and AlGaInP

F.1 Materials Properties of AlGaAs	261
F.2 Materials Properties of AlGaInP	263

Appendix G: Spectrally-Filtered Electroluminescence

G.1 Device Degradation	267
G.2 Modal Dynamics	272

Appendix H: L-I-V and C-V Characterization

H.1 Change in L-I Characteristics During Aging	279
H.2 Change in C-V and I-V Characteristics	282

Table of Figures

Fig. 1- 1: Scale drawings of a stripe laser, a gain-guided VCSEL, and an oxide aperture VCSEL.....	4
Fig. 1- 2: VCSELs failure rates, for four ambient temperatures (after ref. [41]).	10
Fig. 1- 3: Failure rates for improved Honeywell VCSELs (after ref. [42]).	11
Fig. 1- 4: Arrhenius plot for VCSEL MTTF vs. Temperature (After ref. [41]).	12
Fig. 1- 5: "Reliability roof" provides an unanticipated reduction in lifetime	13
Fig. 2- 1: Recombination-enhanced defect motion (REDM) process (After Petroff, ref. [12]).	22
Fig. 2- 2: short-lived energy fluctuation (SLEF) (After Khait et al., ref. [13]).	23
Fig. 2- 3: Arrhenius plot with velocity of glide dislocations in GaAs (After Maeda et al., ref [7]).	23
Fig. 2- 4: A plan-view TEM image of a $\langle 100 \rangle$ DLD network (After Petroff et al., Ref.[20].)	24
Fig. 2- 5: Simplified drawing of an interstitial half-loop forming a climb-type dislocation.	24
Fig. 2- 6: Simplified sequence showing vacancy emission.	25
Fig. 2- 7: Schematic view of $\langle 100 \rangle$ DLD originating from a microstep on the cleaved edge.	26
Fig. 2- 8: EBIC images of various types of degraded stripe lasers.	27
Fig. 2- 9: Interstitial clustering.....	28
Fig. 2- 10: Three steps to microloop formation, according to extrinsic theory.....	28
Fig. 2- 11: Dislocation glide process for an undissociated dislocation.	34
Fig. 2- 12: Propagation of $\langle 110 \rangle$ DLD in an oxide-stripe laser.	35
Fig. 2- 13: Microscopic view of the stacking-fault ribbon making up the $\langle 110 \rangle$ DLD.....	35
Fig. 2- 14: EBIC image showing degradation concentrated near facet regions (after ref. [1]).	38
Fig. 2- 15: DLD acts as an optical absorber.	39
Fig. 2- 16: Dislocation acts as a recombination center.....	40
Fig. 3- 1: Structure of the proton-implanted, top-emitting VCSEL structure	50
Fig. 3- 2: SEM of the left side of a stain-etched VCSEL cross section..	51
Fig. 3- 3: Failure mechanisms observed in VCSELs.....	52
Fig. 3- 4: Increase in junction temperature versus drive current.	53
Fig. 3- 5: EBIC Image of aged and cleaved VCSEL shows no evidence of degradation.	54
Fig. 3- 6: Collected current linescans of the VCSEL.....	54
Fig. 3- 7: Unfiltered PL image of VCSEL with p-metal polished off	55
Fig. 3- 8: Top-emitting CL Spectra of normally-degraded. (After ref [23]).	57
Fig. 3- 9: Top-emitting CL spectra of rapidly-degraded VCSELs.....	57
Fig. 3- 10: CL linescans taken from the top of rapidly degraded VCSELs	57
Fig. 3- 11: CL images of p-DBRs in degraded and undegraded VCSELs (after Ref [23]).	58
Fig. 3- 12: CL Spectra from a deeply degraded plan-view sample.....	60
Fig. 3- 13: Monochromatic CL images of deeply degraded plan-view sample.....	61
Fig. 3- 14: Plan-view CL linescans of deeply degraded VCSEL G-60.	62
Fig. 3- 15: Filtered electroluminescence images of three different 850 nm VCSELs.....	64
Fig. 3- 16: Filtered EL of two VCSELs.....	65
Fig. 3- 17: EL images from undegraded VCSELs with semi-transparent In_2O_3 contact.....	66
Fig. 3- 18: EL images from a degraded VCSEL with semi-transparent contact.	66
Fig. 3- 19: Filtered EL from a degraded VCSEL with a semi-transparent contact.	67
Fig. 3- 20: Two competing models to explain declining EL efficiency in device center.....	69
Fig. 3- 21: Low-current L-I curve of a VCSEL before and after degradation.	70
Fig. 3- 22: Ratio of light out before / after degradation, versus current.	70
Fig. 3- 23: Summary of results from the top-emitting CL experiments.....	73

Fig. 3- 24: How aging conditions affect VCSEL degradation.....	73
Fig. 4 - 1: TEM images of totally degraded VCSEL cross-section. (After Cheng et al., ref. [2])... 78	
Fig. 4 - 2: Cross-sectional CL spectra of degraded and undegraded VCSELs (after ref. [6]).	79
Fig. 4 - 3: Monochromatic images from undegraded VCSEL (left, after Cheng et al., ref. [6]) and rapidly degraded VCSEL (right, after Cheng et al., ref. [7]).....	81
Fig. 4 - 4: CL spectra from normally-degraded VCSELs.....	82
Fig. 4 - 5: Monochromatic CL images of a partially-degraded VCSEL.....	82
Fig. 4 - 6: Monochromatic CL images of a totally-degraded VCSEL.....	82
Fig. 4 - 7: TEM Image of dislocation networks localized to the inverted interfaces (After Ref. [7]).84	
Fig. 4 - 8: SIMS profile showing oxygen "spikes" at the inverted interfaces (After ref. [9]).	85
Fig. 4 - 9: Band diagram of VCSEL p-DBR shows charge being trapped at an interface.	85
Fig. 4 - 10: Sub-bandgap PL spectra from AlAs, Al ₁₆ Ga ₈₄ As, and from a p-DBR.....	86
Fig. 4 - 11: TEM image of glide dislocations originating from the p-contact (After ref. [7])	87
Fig. 4 - 12: Microscope photos of sample to test metal interdiffusion.....	88
Fig. 4 - 13: SEM photos of p-metal from aged VCSEL, viewed from underside.....	88
Fig. 4 - 14: Microscope photos are shown of aged VCSELs after removal of most p-metal.	89
Fig. 5- 1: CL spectrum of a VCSEL, taken from the top. (After ref. [1]).....	93
Fig. 5- 2: PL spectra from a bulk p-Al ₁₆ Ga ₈₄ As layer at various pump powers.....	94
Fig. 5- 3: Spectra from p-doped and n-doped samples.	95
Fig. 5- 4: Experimental setup used to measure top-emitting spectra.....	96
Fig. 5- 5: Comparison of spectra from a single-pass and a double-pass spectrometer.	97
Fig. 5- 6: EL spectrum of a laser at 1.4 V, collected in the CL microscope (after ref. [1]).	97
Fig. 5- 7: Sub-threshold spectrum from a multi-filamentary vertical cavity laser.	98
Fig. 5- 8: Sub-threshold spectrum from an InGaAs-QW pillar VCSEL.....	98
Fig. 5- 9: Mirror transmission versus wavelength.....	99
Fig. 5- 10: Spectra from two VCSELs with different resonance wavelengths.....	99
Fig. 5- 11: Spectra taken at 0, 15°, 30°, and 60° from normal.....	100
Fig. 5- 12: Spectra from undegraded proton-implanted VCSEL.....	100
Fig. 5- 13: L-I curve for total output power and spontaneous emission as a function of current..	101
Fig. 5- 14: Schematic of experimental setup for cross-sectional spectra from a cleaved VCSEL..	102
Fig. 5- 15: Cross-sectional spectra from a cleaved VCSEL, taken edge-on.....	103
Fig. 5- 16: High-energy tail from the cross-section of a cleaved VCSEL.....	103
Fig. 5- 17: Reduction in absorbed power expected from increasing bandgap of DBR layer.....	104
Fig. 5- 18: CL spectra from degraded VCSELs with wide-gap (24%) Al mirrors.....	105
Fig. 5- 19: CL images from undegraded (WX) and degraded (other) VCSELs.....	105
Fig. 5- 20: Long-wavelength spectra from top of an undegraded VCSEL.....	106
Fig. 5- 21: Long-wavelength spectra from side of a cleaved VCSEL.....	107
Fig. 6 - 1: Drawing of ideal ordered lattice (after ref. [9]).....	111
Fig. 6 - 2: Schematic views of inhomogeneity in partially-ordered GaInP.....	112
Fig. 6 - 3: A cross-sectional Dark-field TEM images. (after ref. [19]).....	112
Fig. 6 - 4: Band-diagram of spatially-indirect recombination in ordered domains.	113
Fig. 6 - 5: TEM Image of <113>A sample, taken in cross section. (after ref. [19]).....	114
Fig. 6 - 6: TEM image of the active region of an InGaP red VCSEL. (Courtesy Ray Twesten.).	114
Fig. 6 - 7: TEM of layer structure in red VCSEL from Sandia. (Courtesy of Dr. Ray Twesten.).	116
Fig. 6 - 8: Schematic of red VCSEL structure studied.....	117
Fig. 6 - 9: Stained cross-sections from wafer 1001.....	118

Fig. 6 - 10: Stained cross-sections from wafer 999B.	119
Fig. 6 - 11: Spectrally-filtered electroluminescence images of undegraded and degraded VCSELs.	119
Fig. 6 - 12: Cross-sectional EL image and optical image from a degraded red VCSEL.	120
Fig. 6 - 13: Cross-sectional EBIC images of unaged and aged red VCSELs.	121
Fig. 6 - 14: Peak wavelength as a function of drive current and stage temperature.	121
Fig. 6 - 15: Light out plotted against junction temperature.	122
Fig. 6 - 16: L-I curves of VCSEL from wafer 1002 change as a function of annealing stress.	123
Fig. 6 - 17: History of wallplug efficiency from device with annealing stress applied.	123
Fig. 6 - 18: I-V curves show drop in turn on voltage as device is bias-annealed.	124
Fig. 6 - 19: Differential resistance curves increase in differential resistance as device is annealed.	124
Fig. 6 - 20: L-V curves change as a function of bias-annealing stress.	124
Fig. 6 - 21: Peak power versus aging time for two annealed and unannealed red VCSELs.	125
Fig. 6 - 22: Threshold current as a function of temperature.	125
Fig. 6 - 23: Diagram of electron leakage for a simplified flat-band condition. (after ref. [30]).	127
Fig. 6 - 24: Peak output power versus calculated junction temperature at peak power.	127
Fig. 6 - 25: CL data from red VCSEL sample #8 (15°-off wafer 1001).	128
Fig. 6 - 26: CL image of degraded and undegraded VCSELs, taken at 650 nm (direct peak).	129
Fig. 6 - 27: Comparison CL images at 650 nm and 657 nm.	129
Fig. 6 - 28: CL image of an array containing a single bias-annealed red VCSEL.	130
Fig. 6 - 29: Comparison of spectra from center of unaged, and bias-annealed VCSELs.	131
Fig. 6 - 30: EBIC of annealed red VCSELs shows dramatic (>2x) improvement.	132
Fig. 6 - 31: Degradation rate as a function of drive current.	133
Fig. 6 - 32: Improvement in peak power for 673 nm red VCSEL using bias anneal.	134
Fig. 6 - 33: Dead VCSELs restored to life using bias-annealing treatment.	134
Fig. 6 - 34: Spontaneous emission from red VCSEL.	135
Fig. 6 - 35: Low-temperature (10 K) intensity-dependent PL spectra.	139
Fig. 6 - 36: Summary of intensity-dependent PL results, obtained by 3-gaussian best fit.	140
Fig. 6 - 37: Integrated area under peak vs. pump intensity.	140
Fig. 6 - 38: L-I curve of red VCSEL studied, before and after aging.	141
Fig. 6 - 39: Plan-view CL sample preparation.	141
Fig. 6 - 40: Plan-view CL spectra from the center of degraded and undegraded red VCSELs.	142
Fig. 6 - 41: Plan-view CL spectra taken under metal of degraded and undegraded red VCSELs.	144
Fig. 6 - 42: Plan-view CL spectra taken outside from the deep-implanted edges.	144
Fig. 6 - 43: Monochromatic images of degraded plan-view sample PB-7 (#999B).	145
Fig. 6 - 44: Linescans showing intensity versus lateral position, for three wavelengths.	145
Fig. 6 - 45: The spectrum can be fit well with two gaussians.	146
Fig. 6 - 46: Table summarizing analysis of gaussian fitting of plan-view spectra.	147
Fig. 6 - 47: Cross-sectional CL spectra from wafer (#999B), before and after degradation.	148
Fig. 6 - 48: Cross-sectional CL spectra from (311)A -oriented wafer (#999B).	148
Fig. 6 - 49: CL images and linescans from (311)A -oriented wafer (#999B) cross sections.	150
Fig. 6 - 50: High-mag TEM of the As / P interface in a red VCSEL. (Courtesy Ray Twisten.)	151
Fig. 7- 1: MBE grown VCSELs after 72-hour, 30 mA burn-in.	158
Fig. 7- 2: MBE VCSEL after aging for thousands of hours.	158
Fig. 7- 3: MBE VCSEL after aging for thousands of hours.	158
Fig. 7- 4: Aged MOCVD VCSEL with dark-line defects.	159
Fig. 7- 5: Large device which failed quickly due to DLDs.	159
Fig. 7- 6: Dielectric mirror VCSEL before and after rapid aging.	159
Fig. 7- 7: Dielectric mirror VCSEL after rapid aging.	160

Fig. 7- 8: Filtered EL of dielectric mirror device. Image contrast has been enhanced.	160
Fig. 8 - 1: Schematic drawing of bottom-emitting, 980 nm pillar VCSEL	161
Fig. 8 - 2: Filtered EL images show cracks due to strain from thick indium solder bumps.	162
Fig. 8 - 3: Additional filtered EL images of undegraded pillar VCSELs	163
Fig. 8 - 5: Schematic drawing of 980 nm UCSB oxide aperture VCSEL structure	165
Fig. 8 - 6: Filtered EL shows $\langle 110 \rangle$ DLDs from corners of the oxide apertures after aging	166
Fig. 8 - 7: Suspected nucleation and growth of $\langle 110 \rangle$ DLDs.	166
Fig. 8 - 8: Schematic drawing of 850 nm Sandia oxide aperture VCSELs.	168
Fig. 8 - 9: Filtered EL images of Sandia VCSELs.	168
Fig. 8 - 10: Drawing of the propagation of damage in aged Sandia devices.	169
Fig. 8 - 11: CL data for an unaged oxide aperture device.	169
Fig. 9 - 1: Anticipated images from suggested experiment.	177
Fig. A - 1: Schematic diagram of NSOM experimental configuration.	184
Fig. A - 2: Spatially-resolved electroluminescence spectra.	185
Fig. A - 3: Data expected from ideal (thin) sample in the absence of waveguiding effects.	185
Fig. A - 4: Comparison of collection effects from thin and thick samples.	186
Fig. A - 5: Spatially-resolved spectra taken in a wide-bandgap DBR sample.	187
Fig. A - 6: Spatially-resolved EL, photocurrent (PC), and PL maps for VCSEL.	187
Fig. A - 7: A comparison of the predicted and measured axial thermal profile.	190
Fig. A - 8: EL image from cross-sectioned VCSEL, showing luminescence from substrate.	190
Fig. B- 1: Steps of cross-sectional sample preparation.	195
Fig. B- 2: Wax reinforcement of the sample.	196
Fig. B- 3: Three directions of tripod orientation.	199
Fig. B- 4: Top and side view of cross-section.	202
Fig. B- 5: Equipment used for final polishing.	202
Fig. B- 6: Small amounts of glue must be used to bond TEM sample to grid.	205
Fig. B- 7: NSOM / SThM sample mounting.	208
Fig. B- 8: Steps for sample preparation of plan view sample from red InGaP VCSEL.	209
Fig. B- 9: Photo of plan-view CL sample after polishing off substrate and most of n-DBR.	213
Fig. B- 10: Etch rates for selective HF-based and Citric-based etches.	214
Fig. B- 11: Etching procedure for selective etching of DBR.	215
Fig. B- 12: Image of array before (left) and after (right) polishing p-metals off.	219
Fig. B- 13 Removing die from header.	226
Fig. B- 14: Importance of using thin glue for embedding samples.	227
Fig. B- 15: Clamping fixture used for sample preparation.	228
Fig. B- 16: Steps for embedding a single die in a solid matrix.	228
Fig. B- 17: Top-view of die prepared for FIB sample preparation.	230
Fig. B- 18: Three-dimensional view of mounted FIB sample on cutback grid.	230
Fig. B- 19: TEM image of normally degraded VCSEL after cross sectioning by FIB.	233
Fig. B- 20: TEM showing precipitates in the AIAs layer of the n-DBR.	233
Fig. B- 21: TEM of slip dislocations in p-DBR of a normally-degraded VCSEL.	233
Fig. C - 1: EBIC images of damaged GaAs (left) and InGaAs (right) QW lasers after aging.	238
Fig. D - 1: Hazard rate for human, in percent chance of death per year (after ref. [1]).	244

Fig. D - 2: Failure rate as a function of time for high-power laser pump diodes (after [3]).	245
Fig. D - 3: Predicted failure rate as a function of time for Honeywell VCSELs at 40°C.	246
Fig. D - 4: Failure rates for VCSELs increase substantially toward the end of lifetime.	246
Fig. D - 5: Increase in drive current as a function of time for gradually-degrading laser diodes.	247
Fig. E - 1: Experimental diagram of cathodoluminescence (CL) system (Courtesy M. Cheng).	250
Fig. E - 2: Simulations of electron profiles in GaAs (after ref. [5]).	251
Fig. E - 3: Resolution versus beam energy for bulk sample, and for samples with QWs.	252
Fig. E - 4: Electron beam spread in GaAs for two different SEM accelerating voltages.	253
Fig. E - 5: Schematic diagram of the importance of volumetric effects in VCSELs.	254
Fig. E - 6: Monochromatic line scan (650 nm) of a red InGaP-QW VCSEL cross section.	254
Fig. E - 7: Monochromatic profiles of cleaved VCSEL structures. (courtesy Dr. M. Cheng).	254
Fig. E - 8: Monochromatic cross-sectional CL images from three devices (Courtesy Dr. Cheng).	255
Fig. E - 9: A plan-view drawing shows crooked polishing plane.	255
Fig. E - 10: Room-temperature plan-view CL spectrum from InGaP-QW red VCSEL.	256
Fig. E - 11: Plan-view image of an undegraded VCSEL with carbon contamination spots.	257
Fig. E - 12: Light is generated by the electron beam in certain types of submounts.	258
Fig. F - 1: Increase in bandgap as a function of increasing Al mole fraction.	261
Fig. F - 2: Absorption as a function of wavelength for various levels of p-doping, at 297 K.	262
Fig. F - 3: Absorption as a function of wavelength for various levels of n-doping at 297 K.	262
Fig. F - 4: Bandgap of $(\text{Al}_x\text{Ga}_{1-x})_{0.5}\text{In}_{0.5}\text{P}$ as a function of aluminum mole fraction x .	264
Fig. F - 5: Band offsets of $(\text{Al}_x\text{Ga}_{1-x})_{0.5}\text{In}_{0.5}\text{P}$ as a function of aluminum mole fraction x .	265
Fig. F - 6: Diagram of energy levels in 10 nm GaInP quantum wells with AlInGaP barriers.	265
Fig. G - 1: Calculated mirror reflectivity spectrum for VCSEL.	267
Fig. G - 2: Explanation for why spectral filters improve contrast.	268
Fig. G - 3: EL images with 10-nm-FWHM bandpass filters at 790 nm and 850 nm.	268
Fig. G - 4: Images from the Olympus IR Plan objective.	270
Fig. G - 5: Line scans through the images shown in Fig. G - 4.	270
Fig. G - 6: Complimentary emission is observed in filtered EL of large VCSEL.	273
Fig. G - 7: Cross section through device shows stimulated emission.	274
Fig. G - 8: Spectral narrowing in smooth sections gives a higher peak.	274
Fig. G - 9: Filtered EL images of multifilamentary VCSEL.	275
Fig. G - 10: Filtered EL images of a large (25- μm -aperture) multifilamentary VCSEL.	276
Fig. G - 11: EBIC images of 15- μm -diameter multi-filamentary VCSELs.	276
Fig. G - 12: Filtered EL of a lasing VCSEL.	277
Fig. H - 1: L-I curves for a device as it is aged.	279
Fig. H - 2: The sub-threshold output and slope efficiency both fall as the device ages.	279
Fig. H - 3: C-V characteristics for VCSELs in various stages of degradation.	282
Fig. H - 4: Drawing of the small amount of depletion-width change occurring in VCSELs.	283
Fig. H - 5: Forward-bias I-V curve for degraded and undegraded devices.	283
Fig. H - 6: Forward-biased I-V curve (log scale).	284
Fig. H - 7: Closeup of "ideal" portion of I-V curve below lasing threshold.	284
Fig. H - 8: Ideality factor for a VCSEL before and after degradation.	285
Fig. H - 9: Reverse-bias I-V curve shows reduced breakdown voltage after aging.	285

Chapter 1: Introduction

Professor Y.H. Lee was quoted as saying that “VCSELs are the most complicated, but cheapest lasers.” My work in this thesis will show that the quote appears to apply not only to the device physics of VCSELs, but also to their large and complex variety of causes of degradation, most of which are unique to VCSELs. Before I launch into the introductory chapter, I would like to again thank all the groups that contributed lasers for my study — without their help this thesis would not have been possible.

1.1. Applications of vertical cavity lasers.

1.1.1 Fiber optic data communications.

The explosive growth of internet use and distributed computing has created a rapid expansion in the demand for high-speed data communications. One reads of the telephone company laying new fiber-optic cables and installing switches as quickly as possible to accommodate modem connections (average connect time: 1 hour) on a network built for voice calls (average connect time: 3 minutes). The future only promises to bring more of the same, with consumers demanding unlimited internet access, faster data connections, and greater use of large graphics files. Much of this demand is addressed by existing telecommunications products, where price-per-transmitter has historically not been a key consideration (since thousands of voice calls could be sent by a single transmitter). By contrast, the vertical cavity, surface emitting lasers (VCSELs) which are the subject of this thesis, are primarily being used for lower-cost, and shorter-distance data communications applications. Links using low-cost, multi-mode optical fiber are being sold by several manufacturers now. Some links use several VCSELs in parallel across a fiber-ribbon cable [1], while others use more elaborate circuitry to drive a single VCSEL at a data rate of over 1 Gb/s [2, 3].

By and large, these low-cost VCSEL-based data links are being sold to larger companies to increase data transfer rates from servers to users, and as backbones on the local area network and internal intranet connections at corporate or campus sites. The requirement for fiber optic communications has historically been one of being able to go at very high speeds (>1 GHz) for relatively long distances

(>1 km), something conventional electronics can't do because of high parasitic losses from coaxial cable [4]. However, there are a number of additional (and less obvious) considerations which are just as important in driving the marketplace to replace electronic data links with their VCSEL-based competitors. These include problems with cross-talk or interference between coax cables, physical constraints due to the bulkiness of having to jam large numbers of coax cables into a single pipe, and ground-loop problems with electronics - none of these are issues with fiber optics.

1.1.2 Future applications.

1.1.2.1 Free-Space Optical Interconnects

The microprocessors on even modestly-priced personal computers are rapidly being held back by limitations on the speed of the data busses that bring them data from memory. As the processor continues to get faster (up to 500 MHz consumer chips have been demonstrated), and the clock speed of the motherboard remains limited to a fraction of the processor speed (usually 60-70 MHz) by high-speed circuit-board design limitations, computers will fail to reach their full potential. Furthermore, as address and data busses become wider, it becomes increasingly difficult to package semiconductor chips with hundreds of output pins, and to design printed circuit boards which allow the signals from those hundreds of pins to be distributed.

One solution which has been proposed to these problems is the use of "Free-Space Optical Interconnects," (FSOI). Such interconnects could be used to send data from one board to another, avoiding transfer-rate limitations which current architectures impose. Many FSOI designs also allow substantial scale-up to permit more parallel channels to be sent, eliminating the packaging problems limiting present designs. VCSEL arrays are an ideal transmitting element for such FSOI designs, with their low-divergence, circular beams, with low dissipated power. The reader is referred to excellent reviews for more details [4, 5].

1.1.2.2 Optical Computing

Certain image processing applications (e.g., edge enhancement or motion detection) can be done more than a million times faster using Fourier imaging

techniques and two dimensional image processing [6]. VCSEL arrays are well suited for use in such applications .

1.2. Advantages of vertical cavity lasers over conventional semiconductor lasers.

While we have discussed some advantages which *optical* data communications and data processing have over more conventional electronic solutions, we have not yet addressed why the well-established, and low-cost semiconductor lasers already available have not been used to meet those needs. After all, compact disk (CD) lasers are being produced at rates of over 5 million per month by one company (Sharp) alone [7], and cost only \$0.50 each. Because of the low cost, CD lasers have been used in most of the first-generation of laser-based data communications links, where well over a million lasers have been sold for this purpose [3]. However, the reliability of CD lasers has generally fallen short ($\sim 7 \times 10^4$ hr) of the desired lifetimes (10^5 – 10^6 hr), and special screening procedures have had to be developed to pick CD lasers with above-average reliability, and then perform a proprietary screening to get above-average reliability ($\sim 2.24 \times 10^5$ hr) [3]. This has increased the drive for VCSEL based data links, which have routinely demonstrated lifetimes in excess of 1,000 khr, as we shall show in section 1.4. Until the first practical VCSEL was demonstrated in 1989, [8, 9] all semiconductor lasers lased in the plane of the active region, and lased along the length of a stripe which had been lithographically defined perpendicular to its lasing facets. We shall refer to this traditional geometry as either "stripe laser" or "in-plane laser" design. Comparison between laser degradation in these traditional designs, versus the way degradation occurs in the VCSEL, will be a major theme of this dissertation. In spite of their low cost and other positive features, stripe lasers also have some shortcomings which VCSELs have been able to overcome.

1.2.1 Low threshold

VCSELs are able to operate with a much smaller active area than an in-plane laser. Gains in semiconductor laser performance have long been primarily due to reductions in the lasing volume. A certain "overhead" in current is required just to bring the active region to transparency due to spontaneous recombination, and the

lower the volume used, the smaller that overhead current is. The VCSELs studied in this work (with a lasing disc roughly $20\mu\text{m}$ in diameter) have an active area about $300\mu\text{m}^2$, while stripe lasers are usually at least $5 \times 300\mu\text{m}$ (i.e., $>1500\mu\text{m}^2$). Stripe lasers are limited from being made much smaller, since they cannot be cleaved much shorter than $200\mu\text{m}$ on a production basis, and so shorter cavities require etched facets, and the performance, cost, and reliability penalties that go with them.

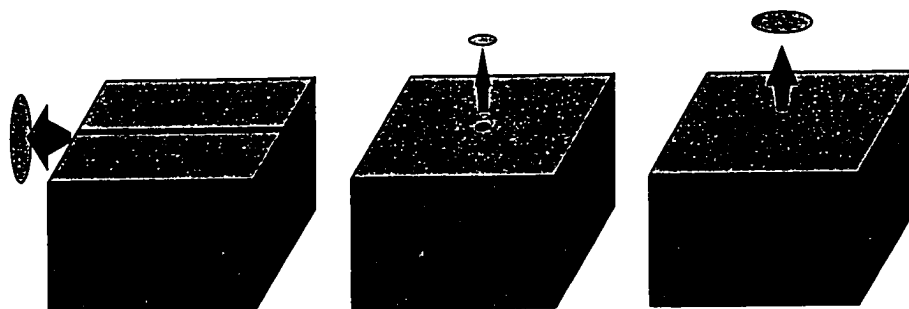


Fig. 1- 1: The active regions of VCSELs are generally considerably smaller than those of stripe lasers, as shown in black on this scale drawing. From left to right, a $300 \times 4\mu\text{m}$ stripe laser; a $20\mu\text{m}$ -diameter proton-implanted VCSEL; and a $2 \times 2\mu\text{m}$ oxide aperture VCSEL. The VCSELs also produce low divergence, circular beams, unlike the stripe laser.

Even smaller active areas are being used in ultra-low threshold VCSELs - as little a $2 \times 2\mu\text{m}$. These very small active areas have allowed thresholds below $40\mu\text{A}$ to be obtained [10], and predictions are for thresholds of only $10\mu\text{A}$ to be reached with further design enhancements [11]. By contrast, the best results obtained with in-plane lasers have been of roughly $145\mu\text{A}$ thresholds, although this geometry has not been pursued for commercial applications [12]. In commercial stripe-laser devices a $4\text{--}10\text{mA}$ threshold is generally considered excellent. A visual comparison of active region areas can be seen in Fig. 1- 1. For VCSELs being used for data communications, 4mA is an average threshold; 40mA is an average threshold for the CD lasers being used [3].

The small pumped area is also advantageous in that the possibility of a dislocation (e.g., from a growth defect or a scratch) being encompassed by the device's lasing area is one to two orders of magnitudes lower.

1.2.2 Beam quality

One of the more important advantages is that VCSELs have a low divergence, circular beam, which allows for 90% fiber coupling efficiency, versus 30% coupling efficiency for the in-plane laser [13]. Stripe lasers have an oblong beam with very fast divergence in the transverse direction (e.g., $f/0.7$) which require special aspheric or multi-element lenses to efficiently collect the light produced. Circularizing the oblong beam is also challenging, and is usually done with four lenses. CD read heads using VCSELs are expected to be \$7 each, versus \$8 for an edge emitting head, with virtually all of the reduced cost coming from simpler beam collimation optics [14]. The VCSEL requires only a simple, one element lens to collimate its circular beam.

1.2.3 Low temperature dependence

Stripe lasers, as mentioned earlier, generally have cavity lengths not less than a few hundred microns, which gives them access to many longitudinal modes within their gain spectrum. (The gain spectrum is usually over 50 nm, and mode spacing is less than 1 nm.) By contrast, the very short ($\sim 2 \mu\text{m}$) cavity length in VCSELs makes longitudinal mode spacing hundreds of nanometers apart, thereby forcing the VCSEL to lase in a single longitudinal mode. Further, this longitudinal mode changes at a rate different ($0.06 \text{ nm} / ^\circ\text{C}$) than the gain shifts ($0.3 \text{ nm} / ^\circ\text{C}$) [15, 16]. By careful design, one can arrange for the gain to start out too short relative to the resonant wavelength when at low temperatures (or operating currents), and shift to wavelengths which are too long at high temperatures [17]. By so doing, the VCSELs can exhibit changes as little as 20% in output power across temperature swings of over 50°C [18]. This is in stark contrast to conventional stripe lasers, which typically suffer from large drops in output power as temperature rises. Sonderstrom et al. cite a typical data communications VCSELs as having an I_{th} temperature coefficient of $0.0\%/^\circ\text{C}$, while the CD lasers tested had a $0.7\%/^\circ\text{C}$ coefficient [3]. The V_f temperature coefficients were -0.01 and $-0.11\%/^\circ\text{C}$, respectively. The VCSEL's ability to hold a steady output power may lead to improvements in system performance, and even cost reductions due to the fact no external temperature stabilizing hardware is needed.

1.2.4 high modulation efficiency

One consequence of the low threshold has been that it is very easy to "fill up" the active region (i.e., the device has a quick turn-on time), and the carrier population also is quickly sapped by stimulated emission once current is turned off (i.e., the device also has a quick turn-off time as well). Record high modulation efficiency results ($>14 \text{ GHz}/\sqrt{\text{mA}}$) have been obtained [19, 20]. The low threshold also leads to a lower jitter time with no pre-bias [21]. Sonderstrom et al. cite the rise and fall times of the typical data communications VCSEL as being 100 ps, while the comparable figure for the CD laser is 400 ps [3].

1.2.5 Low packaging costs

Many companies which have used LED-based data communications products in the past have found the transition to VCSELs to be fairly straightforward. Unlike edge-emitting lasers, VCSELs don't need to be mounted to a precision-manufactured submount (which is particularly tricky for edge-emitters which are mounted p-down). The standard top-emitting design requires no special equipment to mount on a standard package, and is usually stuck down with silver epoxy. By contrast, most edge emitters are mounted using solder preforms, which are somewhat more difficult to work with.

VCSELs are far easier to form in two dimensional arrays. Unlike the "rack-and-stack" procedure used for edge-emitters, a costly procedure with difficult beam collimation, VCSELs naturally form good two-dimensional arrays. These arrays are ideal for the sort of optical computing applications discussed earlier.

1.2.6 Wafer-scale production and testing

The majority of the cost of producing in-plane lasers (often more than 90%) [22] comes after the laser has been grown and processed! While the cost of wafer processing is spread across thousands of lasers produced per wafer, after the devices are cleaved, they must be mounted in coating fixtures one at a time, coated, mounted, and tested, all one at a time. If yield is low, it is generally not known until after all the mounting steps are complete, raising the cost of rejected parts by more than an order of magnitude.

By contrast, when VCSEL processing is complete, no further work is necessary for the VCSELs to be fully tested. Wafer coatings are not needed on each

individual die, since the VCSEL mirrors are established during the epitaxial growth. Entire wafers, with thousands of VCSELs, can be tested by computerized test equipment in just a few hours [23], and bad die or array can be eliminated before any expensive piece handling is needed.

1.2.7 Device coherence properties

As mentioned earlier, VCSELs are inherently single longitudinal mode. By carefully controlling lateral modes with index guiding, particularly using oxide-aperture VCSELs, a single lateral mode can be maintained across a wide range of operating currents and temperatures, with 3.5 mW CW having been demonstrated in a single mode [24]. While >100 mW can be reached with no longitudinal mode hopping in select DFB lasers, DFB lasers generally cost >\$1,000 each, as opposed to costs expected to be <\$10 each for VCSELs. The efficiencies for these single mode VCSELs are also far better than for single mode DFB lasers. Single mode lasers are particularly desirable for long-distance transmission (due to modal dispersion problems with multi-mode lasers), and applications where a pure, low-divergence beam is needed (e.g., laser printers, free-space optical interconnects, etc.)

While it sounds like a disadvantage, broad-area, proton-implanted VCSEL are multi-lateral mode, and fairly incoherent. Further, special VCSELs can be produced with a very broad, 5 nm spectral width [23]. In both cases, many interference effects which would normally be a problem using multi-mode fiber are not a concern, since a small enough fraction of power is in any single mode for interference to affect system performance.

1.2.8 High operating efficiency

The oxide aperture VCSELs are the most efficient lasers produced for low-current operation (i.e., <10–20 mA operation). Power conversion efficiencies (a.k.a. “wallplug efficiencies”) of over 50% have been obtained [25, 26]. Such an efficiency at 1 mW has not been achieved for an in-plane laser.

1.2.9 Radiation hardness and space qualification

Radiation-hardness is an important property for space-based deployment of electro-optic systems. Highly-energetic particles inject a trail of point defects through the device, thereby adding a source of non-radiative recombination. The

small pumped volume of the VCSEL, and high carrier densities, make a fixed non-radiative loss less important. Relative to the stripe lasers and LEDs which have been space-qualified [27], the VCSELs tested have shown at least two orders less sensitivity to large doses of radiation damage [28, 29].

1.3. Potential difficulties with VCSELs.

While VCSELs have a number of promising characteristics, lifetime was not expected to be promising at the time we entered into this research, for a number of reasons.

1.3.1 Small active area

The small active region of the VCSEL relative to the stripe laser leads to increased thermal resistance, and thus high junction temperatures. The layered structure used in VCSELs also has higher thermal impedance by more than 2× laterally and 4–5× vertically (i.e. higher thermal resistance per unit area) due to phonon scattering at interfaces [30, 31]. This high thermal resistance of VCSELs is not an insurmountable problem for data communications applications which require little output power, but will prove to be more of a challenge if VCSELs are to be used for high-power lasers. Typical resistance for a stripe laser is $<200\text{ }^{\circ}\text{C} / \text{W}$. 20- μm -diameter proton-implanted VCSELs have $800\text{ }^{\circ}\text{C} / \text{W}$ thermal resistance [16], with the packaging used often contributing an additional 200-300 $^{\circ}\text{C} / \text{W}$ of resistance. A VCSEL in a data communications application would be operated at 6-10 mA over its lifetime, with 2V applied, and produce less than 1 mW of output power. The 12-20 mW of input waste heat would result in a junction temperature roughly 12-20 $^{\circ}\text{C}$ above the heatsink temperature. As we will show in the following section, the activation energy has been shown to be on the order of 1 eV: in the temperature range of 20-40 $^{\circ}\text{C}$, the degradation rate doubles each time the temperature increases by $\sim 17^{\circ}\text{C}$. In addition to the higher junction temperature of most VCSELs, the operating current density is higher as well. Since degradation rate has been empirically determined to be proportional to current density (as shall be discussed in Chapter 2), the high current density also represents a problem.

For VCSEL applications requiring higher output power, more development work will need to be done to enhance lifetime. For comparable output power,

junction temperatures and current densities are many times those seen in stripe lasers.

1.3.2 Hydrolysis of $\text{Al}_x\text{Ga}_{1-x}\text{As}$ with $x>0.8$.

Many details of the VCSEL structure are potential areas of concern to reliability scientists. The AlAs (indeed any $\text{Al}_x\text{Ga}_{1-x}\text{As}$ alloy with $x>80\%$) is known to have potential instability in the presence of atmospheric moisture: an undesired hydrolysis reaction can take place, turning the alloy into Al_2O_3 over a period of years, and resulting in delamination of the structure [32]. Hydrolysis has been reported as a common failure mechanism in devices without adequate dielectric encapsulation of the epitaxial layers [33, 34]. This presumably is the reason that Motorola has chosen not to use more than 80% aluminum in its DBR layers [35]. However, the lower aluminum fraction is not without negative consequences of its own, including increased thermal resistance due to alloy scattering (i.e., $\text{Al}_8\text{Ga}_2\text{As}$ has thermal conductivity only about half that of AlAs [36]), and a required increase in the number of mirror periods.

1.3.3 Point Defects due to oxygen incorporation, or proton implantation.

In addition to concerns about hydrolysis reactions, the high aluminum fraction in the mirror layers also getters oxygen in the growth chamber [37], and the high doping concentrations also create undesired point defect concentrations. The proton implant, if made too deep, can create very high point defect concentrations close to the quantum well, leading to a potential source of rapid degradation, as demonstrated by Jiang et al. [35].

1.3.4 High fabrication and packaging stresses in some VCSEL designs.

Some VCSELs, such as oxide aperture and pillar VCSELs have posts with very high local stresses near the active region. Epi-down mounting stresses can also create problems, as the glues and solders often cool with high stress applied to the device. As we shall see later, this did actually present a problem with earlier UCSB pillar VCSELs, which was solved by protecting the device structure from direct contact with the solder. However, for the most part, the VCSELs tested have proved to have reliability which far exceeded initial reliability estimates. For data

communications (i.e., low power) applications, VCSELs have excellent reliability which exceeds that of competing compact disc (CD) lasers [38, 39].

1.3.5 Tight growth tolerances for VCSELs

VCSELs also have a few disadvantages in areas not related to potential reliability concerns, including the requirements for exceedingly tight (<1% thickness control) tolerances on epitaxial growth. The majority of VCSEL producers have dealt with this difficulty by performing frequent calibration runs. However, others have responded by developing in-situ growth monitoring [40], improved reactor design, and tighter control of growth rates.

1.4. Background on present VCSEL reliability estimates for 850 nm proton-implanted VCSELs.

We have not sought to estimate VCSEL lifetime ourselves at UCSB for two reasons. First, we do not have appropriate lifetesting ovens. Second, we wish to emphasize the diagnostic tools which we uniquely have, rather than the more tedious job of continually testing and re-testing lasers which are being gradually aged. Thus, we rely on industry for accurate lifetesting, and perform only brief (few hour) tests at UCSB.

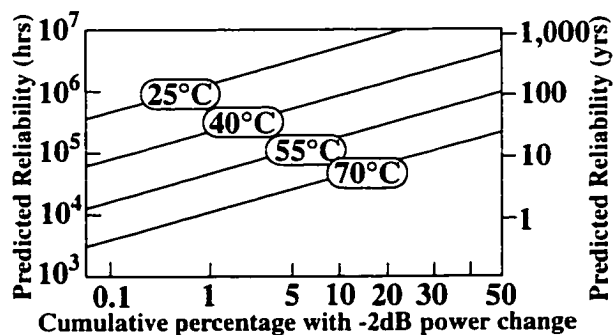


Fig. 1- 2: Estimate of percentage of VCSELs failing, as a function of aging time, for four ambient temperatures (after ref. [41]).

order of magnitude above those expected. This assumed a 40°C ambient temperature, and a 52°C junction temperature. We can see that lifetime for the Honeywell VCSELs has a strong dependence on operating temperature. Before we

This having been said, how we concentrate our efforts depends in large part in how closely a VCSEL comes to meeting its desired lifetime. The first lifetime measurements made by Honeywell showed mean-time to failure (MTTF) estimates of $\sim 5 \times 10^6$ hours, or roughly 500 years (8.76 kh/yr.) that were approximately an

discuss this relationship in more detail, we should note that for the entire rated temperature range (0-70°C), MTTF exceeds the common mission lifetime of 10 years (8.8×10^4 h). Early failure rates (i.e., failure rate over the expected 10-year mission lifetime) become a more useful benchmark than MTTF. This data can be gathered from Fig. 1- 2.

To determine early failure rate from Fig. 1- 2, let us start with the example of finding what percentage of the lasers will fail in ten years, when operated at 55°C ambient. We follow the 55°C line across until it crosses 10 years on the y-axis, and then read the percentage failures of the x-axis: in this case ~4%. While this early failure rate appears surprisingly high given a >100 year MTTF, the failure rate is actually lower than would be expected in LEDs or other devices with a similar MTTF, since the failure distribution is more tightly clustered than for the LED's "exponential distribution," as we shall discuss in Appendix D. What should be

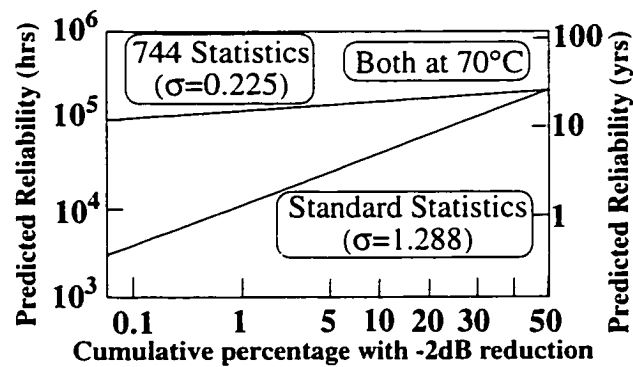


Fig. 1- 3: Failures during the first 10 years are essentially eliminated in the improved Honeywell VCSELs (after ref. [42]).

clear, however, is that raising the MTTF, by itself, would be of relatively little value if it did not also lower early failure rates. In more recent work, the early failures (within 10 years) have been essentially eliminated in the improved designs for data-communications applications [42], as shown in Fig. 1- 3. However, for many high-power and high-

temperature applications, device reliability remains an issue. The early failures should be the focus of failure analysis, as we wish to eliminate the premature failure mode, and not concentrate on making 500-year VCSELs last 800 years (for example). The failure distributions used, and the difference between Weibull and Exponential distributions, are discussed in greater detail in Appendix D.

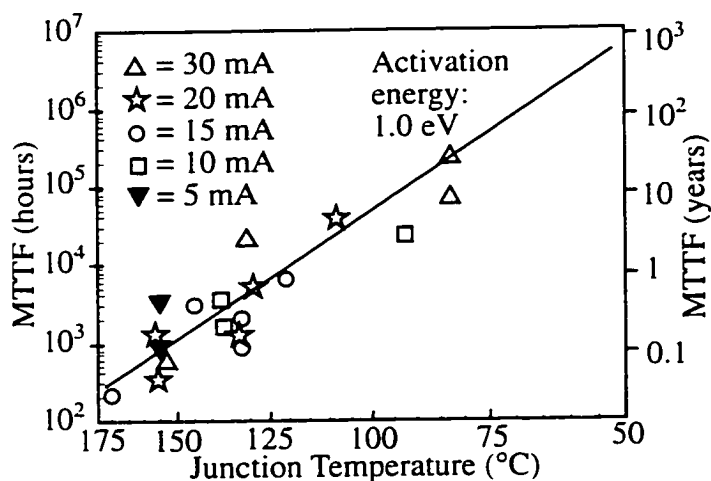


Fig. 1- 4: Variation in estimated device lifetime versus junction temperature, for a variety of drive currents. (After ref. [41])

rate is proportional to current density. (For a fixed laser size, as is the case for these tests, degradation rate would thus be proportional to current.) Honeywell has empirically determined that the degradation rate in their VCSELs is proportional to the *square* of the current [41], after the junction temperature has been accounted for. If we (more than) double the current from 7 to 15 mA, we thus quadruple the degradation rate due to current. We also increase the junction temperature by roughly 12°C by increasing the drive level. The latter increase also roughly quadruples the degradation rate again, for a total 16-fold reduction in reliability by doubling the current from 7 mA to 15 mA. Degradation rate increases even more precipitously for currents above 30 mA [43]. Motorola, with a different structure, has found a very strong ($\propto I^{4.9}$) dependence of device lifetime on current for their proton-implanted VCSEL, even after adjusting for junction temperature rise with current [44].

Fig. 1- 4 shows the dependence of degradation rate on both drive current and ambient temperature. Note that by operating VCSELs at high drive currents, junction temperature quickly rises well above ambient temperature. It has been shown many times in stripe lasers that the degradation

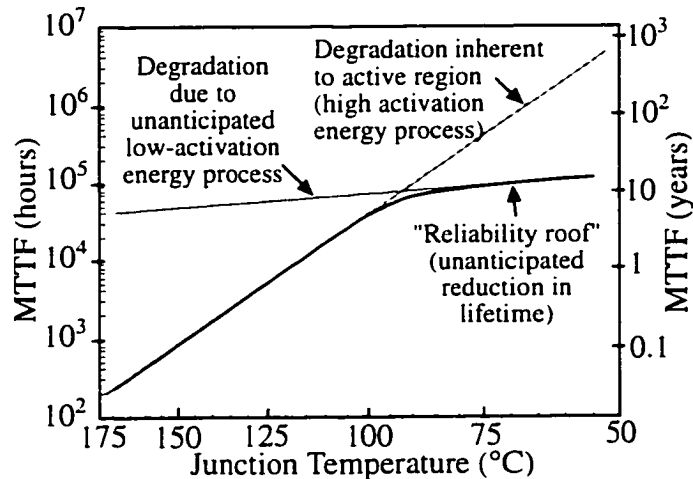


Fig. 1- 5: "Reliability roof" can provide an unanticipated reduction in lifetime when not all failure mechanisms can be accelerated by thermal or current-stress acceleration alone.

The reason that high temperature accelerates device degradation is discussed in greater detail in Chapter 2. Without some such ability to predictably accelerate degradation, we would be hard pressed to extrapolate estimates much beyond the time the devices had been tested (a few years at best when a new generation is released). The

fear of any reliability scientist is the presence of a failure mechanism which has *not* been accelerated with temperature during pre-release qualification, and only becomes noticed in actual operation. This is schematically depicted in Fig. 1- 5. An example of such a failure mechanism is the hydrolysis of high-aluminum layers, mentioned earlier in Section 1.3.2, which has only weak dependence on temperature, and will occur at room temperature with an incubation time of ~10 years [32]. Fortunately, for hydrolysis in particular, high-humidity testing is available for accelerating the oxidation process, and has been performed by most firms selling VCSELs.

1.5. Dissertation overview

1.5.1 Goals of this work

Our goals in this research were to identify the primary failure mechanisms for the VCSELs studied, and if possible, to suggest design changes which might improve device lifetime. As we will show, we believe we have identified a few unexpected causes of failure, and have suggested design improvements which seemed to have reduced the rate of early failures in preliminary testing. In the course of doing many unusual types of characterization, we have also uncovered a better

understanding of VCSEL operation which is relevant not only to VCSEL reliability, but also to improving VCSEL performance generally.

1.5.2 Organization of the dissertation

The variety of different lasers tested, as well as the number of different techniques used, made the choice of a particular organization a difficult one. The effects responsible for laser degradation are separated into different chapters. Within each chapter is the more familiar organization of “introduction, experimental description, results, discussion, conclusions and suggestions for improvement. Further conclusion and discussion is contained in Chapter 9.

In chapter 1, we have discussed background, including how VCSELs compare to conventional stripe lasers, particularly in areas which would affect their reliability. An overview of the reliability tests which have been performed to date was presented, which showed excellent MTTF, but room for improvement in early failure rates, particularly with high temperature or high output power. Due partly to better understanding of the causes of VCSEL failure, the early failures have largely been eliminated for data-communications applications in more recent work.

In chapter 2, the details of degradation physics are discussed, along with what makes devices degrade. This will include descriptions of the types of dark-line defects (DLDs) that cause device failure, the recombination-enhanced defect reactions (REDRs) that cause the DLDs to grow as the device ages, and the ways that traditional stripe lasers fail. Much of the substance is drawn from the field of Material Science, and the cross-disciplinary nature of this work has been an additional challenge.

The early stages of degradation in proton-implanted VCSELs appear to have a very unusual failure mode, where the current is forced toward the periphery of the laser, lowering its efficiency even before true “degradation” of the VCSEL layers takes place. We present the evidence for this in Chapter 3, including various types of plan-view examination, and cross-sectional electron beam induced current (EBIC). The structure of the standard top-emitting, proton-implanted, 850 nm is presented. The tool of spectrally-filtered electroluminescence is also introduced, which is perhaps the most simple and useful method of VCSEL failure analysis we have found. We also discuss the competition between multiple failure mechanisms,

and the way aging conditions accelerate some degradation mechanisms more than others.

As aging progresses to the final stages, we find evidence for degradation of the p-DBR. This was also an unexpected finding, and supporting cathodoluminescence (CL) and transmission electron microscopy (TEM) results are presented in chapter 4.

While the results of Chapter 3 and 4 show *what* happens in degraded VCSELs, the driving mechanism is not clear from those measurements alone. In Chapter 5, the results of spectroscopic measurements are introduced. These measurements have been our primary tool in identifying the cause of degradation, and in suggesting changes which have reduced early failure rates in preliminary testing.

Red InGaP-based VCSELs have historically had poor (<1 year) lifetimes. Analysis, primarily by cathodoluminescence, shows that the primary failure mechanism is the same for red VCSELs as the “current-shunting” mechanism discussed in Chapter 3. However, additional findings, in terms of alloy ordering, device microstructure, and bias-induced annealing are unique to the red VCSEL, and are also discussed in Chapter 6. In particular, we are able to improve device lifetime by more than an order of magnitude by bias-annealing before aging the VCSELs.

Chapter 7 shows the various types of degradation observed from a variety of different pre-production proton-implanted VCSELs. Even devices with a structure nominally identical to one another can show a surprisingly wide variety of different failure modes, indicating that the details of the growth technique and subtle variations in method of processing may be quite important to producing reliable VCSELs.

Index-guided VCSELs, including both pillar and oxide-aperture VCSELs, are briefly discussed in Chapter 8. The effects of strain, from packaging with the pillar VCSEL, or from the oxide apertures themselves, appear to play an important role in the degradation process for these types of lasers

In chapter 9, we conclude with a brief summary of our work, and suggestions for future work.

Appendix A deals with experiments which have been done with cross-sectional samples I've prepared. While the reliability-related experiments originally planned did not come out as hoped, the experiments yielded useful information about VCSELs generally. Two types of scanning probe microscopy are covered: Near-Field Scanning Optical Microscopy (NSOM) and Scanning Thermal Microscopy (SThM).

Appendix B provides full details on sample preparation. While far more detailed than other papers I've seen published, it still contains just enough detail to allow experienced researchers to reproduce my results.

Appendix C discusses a topic which I believed would be the core of my thesis going in: use of strained-layer quantum wells to extend device lifetime. I ended up being more involved in failure analysis, and focused more on the unexpected p-DBR degradation. However, once the p-DBR degradation has been eliminated as a cause of early device failure, enhancement of active region lifetime through strained-layer epitaxy may be a logical next step.

Appendix D gives details on the life testing which has been done on proton-implanted GaAs-QW VCSELs. It also explains the difference between various failure distributions, and points out the importance of choosing the correct model if an accurate estimate of device lifetime is to be obtained.

Appendix E gives supporting information to allow the reader to interpret the electron microscopy images. A number of microscopy artifacts, which could lead to serious errors in data interpretation, are discussed, along with limitations of the techniques and equipment used.

Fundamental materials data on the bandgap of AlGaAs and AlGaInP, to support our interpretation of CL spectral peaks, is contained in Appendix F.

Appendix G contains a brief discussion of why spectrally-filtered electroluminescence works, and how images at different wavelengths should be interpreted.

Finally, Appendix H contains data on how L-I, I-V, and C-V characteristics change with time. We also discuss methods for analyzing these characteristics.

References for Chapter 1:

- [1] D. Bursky, "Parallel optical links move data at 3 Gbits/s," *Electronic Design*, vol. 42, pp. 79-80, 82, 1994.
- [2] L. Wirbel, "Components, lasers in for long, short haul," *E.E. Times*, vol. March 4, 1996, 1996.
- [3] R. Soderstrom, K. Jackson, and D. Kuchta, "New 850 nm VCSELs and CD-type lasers provide interoperable low cost data links," presented at IEEE Lasers and Electro-Optics Society 1995 Annual Meeting., San Francisco, CA, USA, 1995.
- [4] M. R. Feldman, S. C. Esener, C. C. Guest, and S. H. Lee, "Comparison between optical and electrical interconnects based on power and speed considerations," *Applied Optics*, vol. 27, pp. 1742-51, 1988.
- [5] F. A. P. Tooley, "Challenges in optically interconnecting electronics," *IEEE Journal on Selected Topics in Quantum Electronics*, vol. 2, pp. 3-13, 1996.
- [6] H. S. Hinton, B. Soffer, F. A. P. Tooley, and K.-i. Yukimatsu, "Optical computing: Introduction by the feature editors," *Applied Optics*, vol. 33, pp. 1335, 1994.
- [7] "Industry News," *Compound Semiconductor*, vol. 2, pp. 8, 1996.
- [8] J. L. Jewell, A. Scherer, S. L. McCall, Y. H. Lee, S. J. Walker, J. P. Harbison, and L. T. Florez, "Low-threshold electrically pumped vertical cavity surface-emitting microlasers," *Electronics Letters*, vol. 25, pp. 1123-1124, 1989.
- [9] R. S. Geels, S. W. Corzine, J. W. Scott, D. B. Young, and L. A. Coldren, "Low threshold planarized vertical-cavity surface-emitting lasers," *IEEE Photonics Technology Letters*, vol. 2, pp. 234-6, 1990.
- [10] D. L. Huffaker, L. A. Graham, H. Deng, and D. G. Deppe, "Sub-40 μ A Continuous-Wave Lasing in an Oxidized Vertical-Cavity Surface-Emitting Laser with Dielectric Mirrors," *IEEE Photon. Technol. Lett.*, vol. 8, pp. 974-976, 1996.
- [11] Personal communication with Eric Hegblom
- [12] H. Zhao, M. H. MacDougall, P. D. Dapkus, K. Uppal, Y. Cheng, and G.-M. Yang, "Submilliampere Threshold Current InGaAs-GaAs-AlGaAs Lasers and Laser Arrays Grown on Nonplanar Substrates," *IEEE Journal of Selected Topics in Quantum Electronics*, vol. 1, pp. 196-202, 1995.
- [13] K. Tai, G. Hasnain, J. D. Wynn, R. J. Fischer, Y. H. Wang, B. Weir, J. Gamelin, and A. Y. Cho, "90% coupling of top surface emitting GaAs/AlGaAs quantum well laser output into 8 μ m diameter core silica fibre," *Electronics Letters*, vol. 26, pp. 1628-9, 1990.
- [14] Personal Communication with Hyun Kuk Shin of Samsung Electronics.
- [15] R. A. Morgan, M. K. Hibbs-Brenner, T. M. Marta, R. A. Walterson, S. Bounnak, E. L. Kalweit, and J. A. Lehman, "200 degrees C, 96-nm wavelength range, continuous-wave lasing from unbonded GaAs MOVPE-grown vertical cavity surface-emitting lasers," *IEEE Photonics Technology Letters*, vol. 7, pp. 441-3, 1995.
- [16] J. M. Catchmark, R. A. Morgan, K. Kojima, R. E. Leibenguth, M. T. Asom, G. D. Guth, M. W. Focht, L. C. Luther, G. P. Przybylek, T. Mullally, and D. N. Christodoulides, "Extended temperature and wavelength performance of vertical cavity top surface emitting lasers," *Applied Physics Letters*, vol. 63, pp. 3122-4, 1993.
- [17] D. B. Young, J. W. Scott, F. H. Peters, M. G. Peters, M. L. Majewski, B. J. Thibeault, S. W. Corzine, and L. A. Coldren, "Enhanced Performance of offset-gain high-barrier vertical-cavity surface-emitting lasers," *IEEE Journal of Quantum Electronics*, vol. 29, pp. 2013-2022, 1993.

- [18] T. Wipiejewski, D. B. Young, M. G. Peters, B. J. Thibeault, and L. A. Coldren, "High performance vertical-cavity surface-emitting laser diodes with a Au-plated heat spreading layer," *45th Electronic Components and Technology Conference 1995 Proceedings.*, pp. 401-5, 1995.
- [19] K. L. Lear, V. M. Hietala, H. Q. Hou, J. Banas, B. E. Hammons, J. Zolper, and S. P. Kilcoyne, "Small and large signal modulation of 850 nm oxide-confined VCSELs," *CLEO '97*, pp. 193-194, 1997.
- [20] B. J. Thibeault, K. Bertilsson, E. R. Hegblom, E. Strzelecka, P. D. Floyd, R. Naone, and L. A. Coldren, "High-Speed Characteristics of Low-Optical Loss Oxide-Apertured Vertical-Cavity Lasers," *IEEE Photonics Technology Letters*, vol. 9, pp. 11-13, 1997.
- [21] D. M. Cutrer and K. Y. Lau, "Ultralow power optical interconnect with zero-biased, ultralow threshold laser-how low a threshold is low enough?," *IEEE Photonics Technology Letters*, vol. 7, pp. 4-6, 1995.
- [22] 90% estimate based on McDonnell Douglas Cost Model maintained by Thomas Bonham. This high fraction of packaging costs has been kept under control by utilizing low-cost off-shore production, or automating the device handling and coating processes.
- [23] R. A. Morgan and M. K. Hibbs-Brenner, "Vertical-cavity surface-emitting laser arrays," *Proc. of SPIE*, vol. 2398 (Circular-Grating Light-Emitting Sources), pp. 65-93, 1995.
- [24] K. D. Choquette, H. Q. Hou, G. R. Hadley, K. M. Geib, D. Mathes, and R. Hull, "High Power Single Transverse Mode Selectively Oxidized VCSELs," *Proc. of '97 LEOS Summer Topicals*, pp. 73-74, 1997.
- [25] K. L. Lear, K. D. Choquette, R. P. Schneider, Jr., S. P. Kilcoyne, and K. M. Geib, "Selectively oxidised vertical cavity surface emitting lasers with 50% power conversion efficiency," *Electronics Letters*, vol. 31, pp. 208-9, 1995.
- [26] R. Jäger, M. Grabherr, C. Jung, R. Michalzik, G. Reiner, B. Weigl, and K. J. Ebeling, "57% wallplug efficiency oxide-confined 850 nm wavelength GaAs VCSELs," *Electronics Letters*, vol. 33, pp. 330-331, 1997.
- [27] B. D. Evans, H. E. Hager, and B. W. Hughlock, "5.5 -MeV Proton Irradiation of a Strained Quantum-Well Laser Diode and a Multiple Quantum-Well Broad-Band LED," *IEEE Transactions on Nuclear Science*, vol. 40, pp. 1645-1654, 1993.
- [28] H. Schöne, R. F. Carson, A. H. Paxton, and E. W. Taylor, "AlGaAs Vertical Cavity Surface Emitting Laser Responses to 4.5 MeV Proton Irradiation," *Submitted to IEEE Photonics Technology Letters*, 1997.
- [29] R. A. Morgan, J. A. Lehman, M. K. Hibbs-Brenner, Y. Liu, and J. P. Bristow, "Vertical-cavity surface-emitting lasers: The applications," *Proc. of SPIE*, vol. 3004 (Fabrication, testing, and reliability of semiconductor lasers II), pp. 91-103, 1997.
- [30] T. Wipiejewski, M. G. Peters, D. B. Young, B. J. Thibeault, G. A. Fish, and L. A. Coldren, "Thermal resistance of etched-pillar vertical-cavity surface-emitting laser diodes," *Proc. of SPIE*, vol. 2691, pp. 171-182, 1996.
- [31] T. Wipiejewski, M. G. Peters, B. J. Thibeault, D. B. Young, and L. A. Coldren, "Size-Dependent Output Power Saturation of Vertical-Cavity Surface-Emitting Laser Diodes," *IEEE Photonics Technology Letters*, vol. 8, pp. 10-12, 1996.
- [32] J. M. Dallesasse, N. El-Zein, J. N. Holonyak, K. C. Hsieh, R. D. Burnham, and R. D. Dupuis, "Environmental degradation of $\text{Al}_x\text{Ga}_{1-x}\text{As}$ -GaAs quantum-well heterostructures," *Journal of Applied Physics*, vol. 68, pp. 2235-2238, 1990.
- [33] Personal communication with Mary Crawford of Sandia National Labs
- [34] Personal communication with Mary Hibbs-Brenner of Honeywell Technology Center

- [35] W. Jiang, C. Gaw, P. Kiely, B. Lawrence, M. Lebby, and P. R. Claisse, "Effect of proton implantation on the degradation of GaAs/AlGaAs vertical cavity surface emitting lasers," *Electronics Letters*, vol. 33, pp. 137-139, 1997.
- [36] S. Adachi, "GaAs, AlAs, and $\text{Al}_x\text{Ga}_{1-x}\text{As}$: Material parameters for use in research and device applications," *Journal of Applied Physics*, vol. 58, pp. R1-29, 1985.
- [37] T. Achtnich, G. Burri, and M. Illegems, "Study of oxygen incorporation in AlGaAs layers growth by molecular-beam epitaxy," *Journal of Vacuum Science & Technology A (Vacuum, Surfaces, and Films)*, vol. 7, pp. 2537-41, 1989.
- [38] J. K. Guenter, R. A. Hawthorne, D. N. Granville, M. K. Hibbs-Brenner, and R. A. Morgan, "Reliability of proton-implanted VCSELs for data communications," *Proc. of SPIE (Fabrication, Testing, and Reliability of Semiconductor Lasers)*, vol. 2683, pp. 102-13, 1996.
- [39] R. A. Hawthorne, III, J. K. Guenter, D. N. Granville, M. K. Hibbs-Brenner, and R. A. Morgan, "Reliability study of 850 nm VCSELs for data communications," *34th Annual Proceedings of International Reliability Physics Symposium*, pp. 203-10, 1996.
- [40] P. Pinsukanjana, A. Jackson, J. Tofte, K. Maranowski, S. Campbell, J. English, S. Chalmers, L. Coldren, and A. Gossard, "Real-Time Simultaneous Optical-Based Flux Monitoring of Al, Ga, and In Using Atomic Absorption for Molecular Beam Epitaxy," *Journal of Vacuum Science and Technology B*, vol. 14, pp. 2147-2150, 1996.
- [41] Applications Note entitled "Reliability of Honeywell 850 nm VCSEL," by Robert N. Hawthorne, III, dated March 1997
- [42] M. K. Hibbs-Brenner, "VCSEL research, development, and applications at Honeywell," presented at '97 LEOS Summer Topicals, Montreal, Canada, 1997.
- [43] Personal Communication with James Guenter of Honeywell MICRO-SWITCH
- [44] C. A. Gaw, W. Jiang, M. Lebby, P. A. Kiely, and P. R. Claisse, "Characteristics of VCSELs and VCSEL arrays for optical data links," *Proc. of SPIE*, vol. 3004 (Fabrication, Testing, and Reliability of Semiconductor Lasers II), pp. 122-133, 1997.

Chapter 2: Background information on semiconductor laser degradation processes.

As lasers degrade, they often show so-called “dark-line defects” which grow across the device. The “dark-line defects,” or DLDs, are so named because when viewing the electroluminescence from the device, they emit no light. Typically, these DLDs begin in the active region, either at a threading dislocation or at a nick in the cleaved edge, or at a point of high stress. This will often be distant from the electrically pumped area. The DLDs then grow inward toward the lasing region, and travel faster as they get closer to the stripe [1]. When they finally reach inside the stripe itself, they terminate lasing, and the device rapidly reaches its failure criterion.

Extensive TEM studies have shown that DLDs are generally caused by the growth of dislocations [2]. Both glide and climb dislocations have been observed.

We are fortunate to have an extensive body of work published on the degradation of stripe lasers. This work provides us a starting point for our studies of VCSELs. We were surprised to see that VCSELs degrade in very fundamentally different ways than stripe lasers, as we shall discuss in more detail in Chapter 3 and 4. Here, we discuss first the two types of DLDs: $\langle 100 \rangle$ DLDs (i.e., dislocation climb) in section 2.1, and $\langle 110 \rangle$ DLDs (i.e., dislocation glide) in section 2.2. In section 2.3, we discuss commonly-observed gradual degradation mechanisms in stripe lasers and LEDs. Gradual degradation will be discussed in greater detail in Chapter 3, where we will show that VCSELs degrade in a very different manner than stripe lasers. Finally, in section 2.4, we discuss the electrical and optical consequences of defects and dislocations in semiconductor lasers.

2.1. Dislocation climb, and $\langle 100 \rangle$ dark-line defects

While the reader can be forgiven for thinking the following discussion of dislocation properties sounds rather dry and unnecessary, the origin of the dislocations has a direct bearing on how they are best eliminated, and thus on how to make longer-lived devices. I have sacrificed a full treatment of the complex character of the III-V dislocations in the interest of simplicity. In particular, the simple drawings which follow depict crystals with only a single type of atom (rather than depicting the actual group III and group V sublattices), and do not discuss the dissociation of simple dislocations into their associated partial dislocations. For a

more complete discussion of dislocation properties in III-V semiconductors, the reader is referred to Petroff's most recent review article [2], or Swaminathan and Macrander [3, 4], or other more general texts [5, 6]. It is hoped that the material that follows is to explain the relevant features of how dislocations grow and affect device degradation, and serve as a bridge to the more complex material for those interested in the details.

2.1.1 Recombination-enhanced defect motion (REDM).

Recombination-enhanced dislocation motion (REDM) refers to the large increase ($>10^6 \times$) in the mobility of dislocations due to carrier recombination. This mechanism is also known as the "photoplastic effect." Such an enhancement can be provided in a number of ways: electron-beam pumping has provided perhaps the quantitative measurements of defect growth enhancement [7]. Laser pumping has also been used [8, 9]. Most relevant to the case of laser degradation, however, is the observation of defect motion during normal forward-biased operation of the device. The current-dependence of defect motion has been observed [10]; recombination of interstitials and vacancies (i.e., recombination-enhanced annealing) in irradiated GaAs has also been studied [11]. The recombination-enhancement of defect motion applies to both dislocation climb (REDC) and dislocation glide (REDG), and the mechanisms are similar.

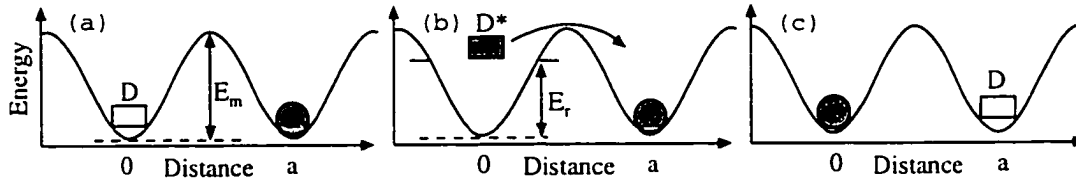


Fig. 2- 1: Schematic of the recombination-enhanced defect motion (REDM) process. (a): The barrier to defect motion is typically ~ 2 eV in GaAs, and is very unlikely to be overcome with thermal energy alone. (b): A non-radiative event can bring the defect to an excited state (up to 1.4 eV above the ground level in GaAs). (c): Migration over the barrier only requires energy $E_m - E_r$ from the excited state. (After Petroff, ref. [12])

The activation energy (i.e. the temperature dependence) of the defect motion is reduced in the presence of recombination. The reduction is usually a significant fraction of the bandgap of the material. Presumably, the energy of recombination (1.4 eV for GaAs) is able to contribute the majority of the energy (2.0 eV) needed to overcome the Peierls barrier which blocks defect motion (Fig. 2- 1). Khait et al.

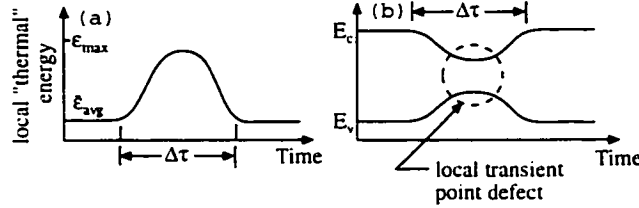


Fig. 2- 2: (a): Local "thermal" (or elastic energy from lattice vibrations) rises well above normal during the short-lived energy fluctuation. (b): The "virtual vacancy" created by the SLEF is capable of capturing carriers and holes, and encouraging non-radiative recombination. (After Khait et al., ref. [13])

have explained dislocation growth in terms of short-lived energy fluctuations (SLEFs) [13, 14]. Such fluctuations can be produced by a multi-phonon event causing a large displacement of lattice atoms from their normal position. Once such a displacement has occurred, it creates (for a short

time $\Delta\tau$) a virtual point defect, which includes a carrier well for both electrons and holes (Fig. 2- 2). If the virtual point defects captures a carrier during its lifetime $\Delta\tau$, non-radiative emission can occur. The energy from this recombination can further extend the already-stretched atomic bonds, and push the atoms involved over the

Peierls barrier.

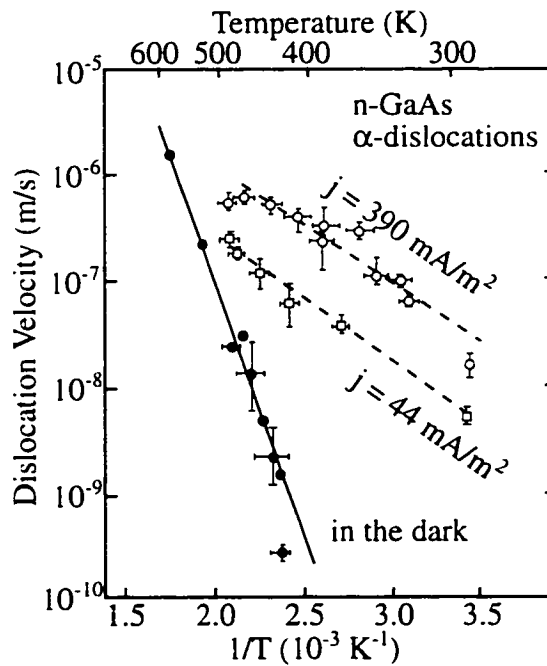


Fig. 2- 3: Arrhenius plot showing propagation velocity of $\langle 110 \rangle$ -type α glide dislocations in GaAs, under electron-beam excitation. Dislocation velocity is directly proportional to pumping intensity (After Maeda et al., ref [7])

DLD growth velocity is proportional to the injected current density, which has been shown both in controlled studies with electron-pumping (Fig. 2- 3) [7, 15], as well as observed empirically in laser degradation studies [16, 17].

For a more detailed explanation of recombination-enhanced annealing and degradation reactions, the reader is referred to the work of Maeda [7, 15], and excellent reviews by Kimerling [18] and Lang [19].

2.1.2 Structural characteristics of $\langle 100 \rangle$ DLDs



Fig. 2- 4: A plan-view (i.e., top-view) TEM image of a $\langle 100 \rangle$ DLD network growing from a threading dislocation labeled "D". (After Petroff et al., Ref.[20].)

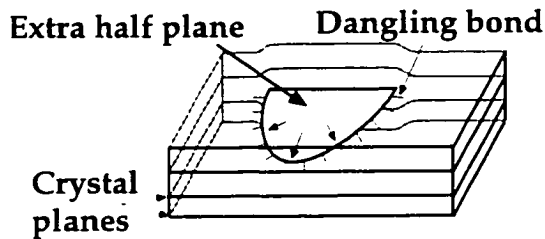


Fig. 2- 5: Simplified drawing of an interstitial half-loop forming a climb-type dislocation. Arrows on half plane show the direction of growth.

Perhaps the most common cause of failure in early stripe lasers were the so-called $\langle 100 \rangle$ DLDs, which generally propagate in the active layer, and appear in EL imaging to travel along the $\langle 100 \rangle$ direction, at a 45° angle to the cleaved facets (which are along the $\langle 110 \rangle$ axes). These $\langle 100 \rangle$ DLDs have been shown by TEM analysis to be made of edge dislocation dipoles formed by dislocation climb as shown in Fig. 2-4. In its simplest form, one can think of these dislocations as being made of an extra half-plane, which has unsaturated bonds at its edges acting as efficient recombination centers. In addition, there is evidence to suggest that point defects and traps are clustered in the vicinity of DLDs, and the traps and defects act as additional recombination and absorption centers. A very simplified drawing of this is, which ignores the complications of the compound semiconductor structure, is shown in Fig. 2- 5. An extra half-plane must be inserted on both the group III and

Perhaps the most common cause of failure in early stripe lasers were the so-called $\langle 100 \rangle$ DLDs, which generally propagate in the active layer, and appear in EL imaging to travel along the $\langle 100 \rangle$ direction, at a 45° angle to the cleaved facets (which are along the $\langle 110 \rangle$ axes). These $\langle 100 \rangle$ DLDs have been shown by TEM analysis to

the group V sublattice to maintain charge balance. The reader is referred to ref. [2] for a more detailed “atomic scale” drawing of the $\langle 100 \rangle$ DLD.

The $\langle 100 \rangle$ DLDs typically nucleate from either threading dislocations (as shown in Fig. 2- 4), or from damage along the device edges, as will be shown later in Section 2.1.6. Threading dislocations in GaAs-based devices are relatively uncommon now that nearly defect-free substrates are widely available. However, in the early days of high etch-pit density (high-EPD) substrates, nucleation of $\langle 100 \rangle$ DLDs from threading dislocations (which grew from the numerous substrate defects) was the primary cause of failure. It is still the primary cause of failure for II-IV ZnSe lasers today. TEM characterization has been used to show that the $\langle 100 \rangle$ DLDs are of interstitial character in the $\{110\}$ planes, with Burgers vector $\mathbf{b} = (a/2)\langle 011 \rangle$ or $(a/2)\langle 101 \rangle$ inclined at 45 degrees to the (001) heterojunction plane [9, 20]. The dislocation periodically jogs up or down (in a “sawtooth” manner) to stay near the active region, since the $\{110\}$ planes are 45° off the $\{100\}$ junction plane, and force the dislocation to ride up or down across the junction plane as the DLD grows [21]. The dislocation extends by the expansion of the extra half plane shown in Fig. 2- 5, which can happen either by attracting interstitials, or emitting vacancies, as we shall discuss in more detail below. Growth of an interstitial plane by vacancy emission, is depicted in Fig. 2- 6. Absorption of an interstitial is much more straightforward: an extra atom would simply migrate to the “dislocation core” site and attach itself at the end.

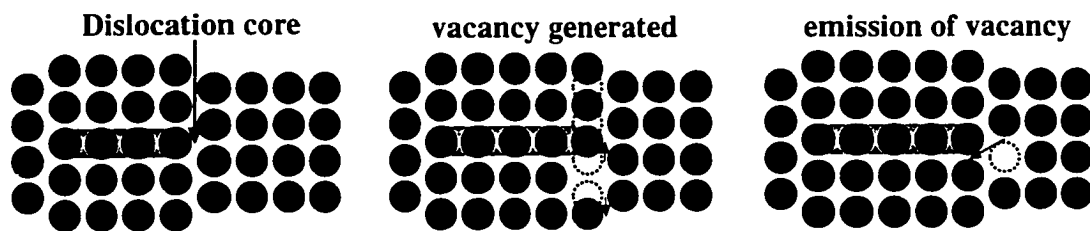


Fig. 2- 6: Simplified sequence showing the growth of the interstitial half plane through dislocation climb. The original lattice is shown at the left, with the half-plane outlined in gray. In the center image, a vacancy is generated at the dislocation core, with the original positions of the atoms shown by the dotted lines, and atomic movement depicted by arrows. In the right image, the vacancy is shown moving toward the right edge of the crystal, where it will be emitted. Note the extension of the half-plane from 4 atoms to 5; this growth is at the root of dislocation climb, and $\langle 100 \rangle$ DLD extension more generally.

2.1.3 Nucleation of $\langle 100 \rangle$ (DLDs).

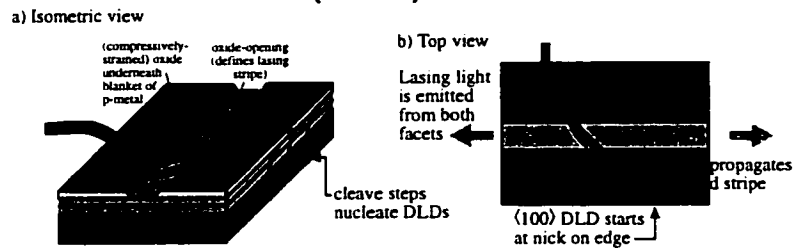


Fig. 2- 7: Schematic view of $\langle 100 \rangle$ DLD originating from a microstep on the cleaved edge, and traveling inward toward the lasing stripe. Basic details of oxide-stripe laser can also be seen.

$\langle 100 \rangle$ DLDs frequently originate from scratches on the surface (e.g. tweezer marks) or nicks from cleaving [22] or sawing damage. This is depicted schematically in Fig. 2- 7. The experimental observations can be seen in Fig. 2- 8, which shows a series of electron-beam-induced current (EBIC) images of degraded stripe lasers [1, 23]. These EBIC images are taken from the top, and show $400 \times 600 \mu\text{m}$ die, with $60 \times 600 \mu\text{m}$ stripes where a $0.12\text{-}\mu\text{m}$ -thick SiO_2 insulator layer has been wet etched away to allow the p-metal to make contact. The wires with the circular blobs on the end are gold wire bonds to make contact; the lasing stripes appear brighter than the remainder of the die, since the stripes do not have the oxide reducing the energy of the impinging injected carriers. In EBIC, electron-hole pairs created in the depletion region of undegraded material are subsequently collected as a current, which is then amplified for imaging. Electron-hole pairs created near recombination centers or dark line defects recombine before they can be collected, thus causing those areas to appear dark. Note that in all cases, the damage appears to originate at the edges, and travel in toward the stripe. When the DLD crosses the stripe, it terminates lasing. It has been empirically shown that by increasing die size, the time it takes for this DLD propagation to take place from the sides can be greatly extended, and thus the device reliability improved [1]. In the lower right image of Fig. 2- 8, two interesting effects are noted: first, DLD propagation stops at the edge of oxide, attributed to “dislocation pinning” by compressive strain as will be mentioned in section 2.1.6.1, and discussed in greater depth in Appendix C. Second, note the darkening at the device facets, which we will come back to later in Section 2.3.

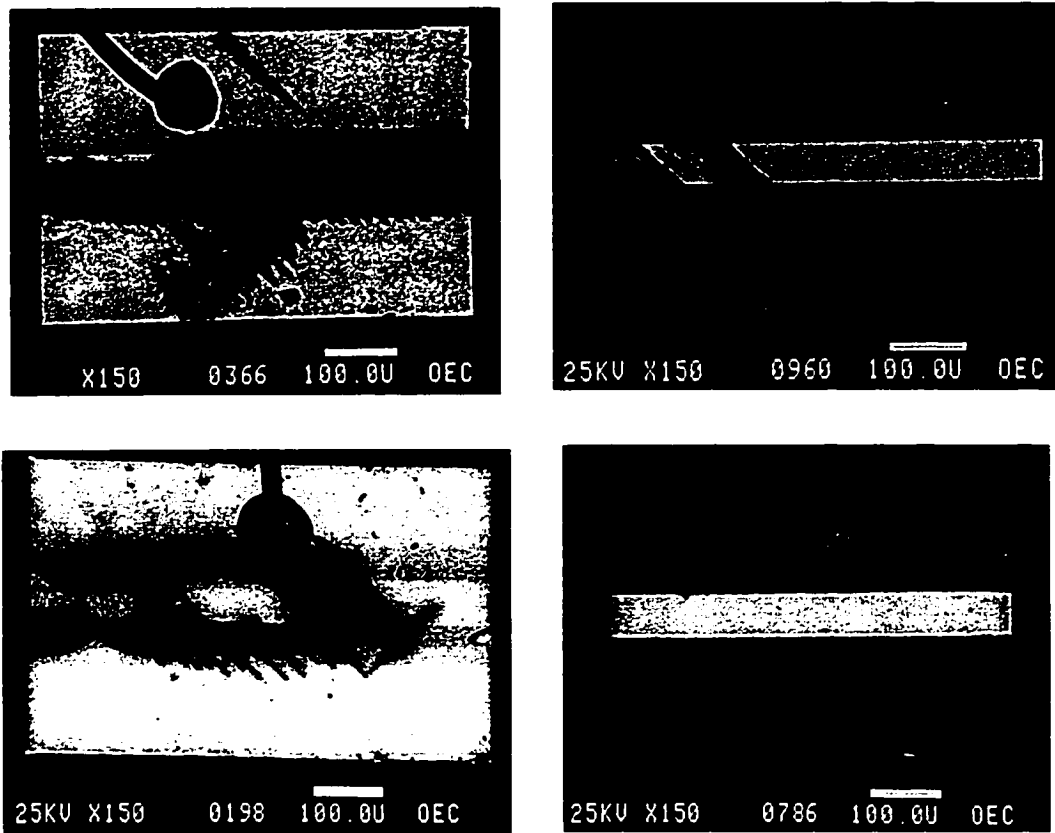


Fig. 2- 8: EBIC images of various types of degraded stripe lasers. Note the dependence of dislocation character on aluminum mole fraction and quantum well thickness. (Upper left: 4 nm GaAs QW; upper right: 10 nm GaAs QW; lower left, 12 nm $\text{Al}_{0.12}\text{Ga}_{0.88}\text{As}$ QW; lower right, 12 nm $\text{Al}_{0.08}\text{Ga}_{0.92}\text{As}$ QW.)

The difference in character of dislocations in the various device types is not understood, and Waters et al. made no attempt to explain their intriguing observations [1, 23]. While fractal theory could be used to model the growth of the DLD networks, and understand their growth better, I am unaware of any attempts to do so to date.

2.1.4 Intrinsic versus extrinsic theory of dislocation climb in DLD growth

Two competing theories have been used to explain the dislocation climb responsible for the growth of $\langle 100 \rangle$ DLDs. The extrinsic theory postulates that large numbers of gallium interstitials or interstitial complexes which are grown into the crystal are absorbed by the dislocation, and arsenic vacancies are emitted [24]. This

theory has the advantage of explaining why devices grown with low V-III ratios (which would be expected to have a higher gallium interstitial concentration) have relatively poor reliability [25, 26]. In addition, Petroff et al. have observed that dislocation networks seemed concentrated at interfaces [21], where point defect concentrations are measurably higher [27]. (However, concentration of dislocations at interfaces could also be explained by many effects other than high point defect concentrations, such as stress, carrier concentration due to band-bending effects, etc.) Additional evidence for the extrinsic theory includes the absence of electron-beam induced dislocation climb in clean material, versus strong climb motion in material which had high point defect concentrations created by megavolt electron irradiation [28].

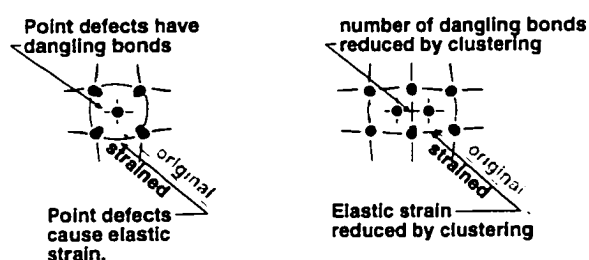


Fig. 2- 9: Interstitials (or vacancies) can reduce the number of dangling bonds, as well as the strain energy, by clustering together.

We show a greatly simplified two-dimensional diagram of an interstitial and an interstitial pair in Fig. 2- 9. Less bending (elastic energy) is required for an interstitial pair than for two separate single interstitials. In addition, the interstitial can electronically bond to

one another, reducing the number of dangling bonds. Therefore, we see that it is energetically favorable for two point defects which come into contact to cluster together.

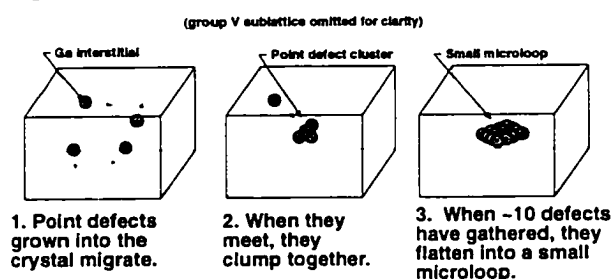


Fig. 2- 10: Three steps to microloop formation, according to extrinsic theory. A group-V half plane is also created by vacancy emission, but is omitted from this diagram for clarity.

This clustering action is believed to be how microloops form by dislocation climb, at least according to the extrinsic theory. A simplified diagram of this is shown in Fig. 2- 10. When the point defect clusters become large enough, it is energetically favorable for them to flatten in a microloop.

This process has been extensively studied in metals, and is described in texts on

dislocation theory [29, 30]. These microloops can be observed along the edges of $\langle 100 \rangle$ DLD networks, and trailing behind $\langle 110 \rangle$ DLDs. They are also often responsible for gradual degradation, as we shall discuss later.

The intrinsic theory, which posits that both gallium and arsenic vacancies are emitted from the dislocation core, is supported primarily by the theoretical calculations of Baraff [31] which claim that interstitials are energetically unfavorable, thus favoring the vacancies-only nature of the intrinsic theory [32]. Some researchers have found agreement with the general trends predicted by Baraff [33, 34], while other more recent work has cast some doubt on the accuracy of these calculations [35]. At any rate, while it is ignored by recent reviews of laser reliability, arguments about the very large number of interstitials needed by the extrinsic theory are just as important, and are easier to experimentally verify.

As even proponents of the extrinsic theory have noted [2], the very high concentrations of interstitials required ($>10^{19} \text{ cm}^{-3}$) seem somewhat unlikely in light of the annealing and TEM measurements estimating their concentration at $2 \times 10^{17} \text{ cm}^{-3}$ [8]. Furthermore, experiments have been done in material which has been thoroughly annealed at 880°C to allow all interstitials to anneal into microloops, and such microloop formation was allowed to totally saturate. Presumably, dislocation climb via interstitials could not take place once all interstitials had been precipitated out if the extrinsic theory were strictly true. However, optical pumping was observed to cause dislocation climb in such annealed samples, indicating that perhaps interstitial absorption wasn't a necessary part of dislocation climb [8]. Petroff et al. have shown using electron-beam-enhanced recombination that vacancies are diffusing away from the dislocation core. Near the edge of recently-formed (interstitial-type) dislocations, the recombination-enhanced defect motion (REDM) due to the electron beam allows vacancies to coalesce into (vacancy-type) microloops. (To clarify the physical picture, if the extra half plane is like a piece of cheese being wedged into the lattice, the vacancies are like bubbles that can gather to create a small "hole" where the extra half plane doesn't exist. Then the electron-beam-irradiated dislocation plane looks more like Swiss cheese!) Further from the leading edge of the $\langle 100 \rangle$ DLD, no such microloops are observed, presumably because the point defects have had more time to diffuse away from the dislocation,

and are thus more dispersed [9, 24]. Woolhouse has discussed additional mechanisms (e.g., electromigration and thermomigration) which further enhance point defect migration [36].

Having stated some of the weaknesses of the extrinsic theory, the intrinsic theory leaves one to the rather hopeless (and false) conclusion that the speed of dislocation growth, and thus degradation rate, cannot be improved by adjusting growth parameters, since it is intrinsic to the material itself. This conclusion is at odds with the general experience of most crystal growers, who have widely accepted the importance of proper growth parameters in making reliable devices. Perhaps some heretofore undescribed combination of the two theories could explain the observed dependence of reliability on V-III ratios without requiring energetically unfavorable numbers of grown-in defects in the original material. Although only claiming to address dislocation climb in gradually-degraded structures, and not DLD growth, Kondo et al. propose a model that differs from both the extrinsic and intrinsic models. They call for the necessary point defects to be generated at deep levels, creating interstitial-vacancy pairs [37]. The interstitials generated from these deep levels could then coalesce to form either a $\langle 100 \rangle$ DLD (if there were enough of them) or the small microloops which are observed in gradual degradation. Kondo's theory has the advantage of being strongly dependent on initial material quality, without needed huge number of grown-in interstitials, since the interstitials are generated at the deep-level centers [37].

2.1.5 Dependence of degradation on growth conditions

As mentioned earlier, growing with a low V-III ratio is a known cause of poor device reliability [25, 26]. This variation of degradation rate as a function of point defect concentrations appears to be inconsistent with the "intrinsic theory." Experiments using DLTS to monitor hole traps associated with point defects have shown that in LPE-grown stoichiometric LEDs (i.e., ones with balanced V-III ratios), the point defects are able to annihilate each other, and device performance improves, perhaps in a manner similar to the improvement in performance from annealing which we will describe in red VCSELs in Chapter 6. On the other hand, devices which were arsenic deficient degraded quickly, and trap concentrations increased, presumably due to point defect emission from dislocation growth [38].

Hayakawa et al. experimented with the V-III flux in MBE, and found that the degradation rate increased by more than an order of magnitude if the V-III flux ratio were lowered to 2 from its optimum value of 3. Initial material quality, as monitored by PL efficiency, was also affected by V-III ratio [25]. Chaly et al. have also found that MBE growth in the “growth-forbidden-gap” (i.e. $<700\text{ }^{\circ}\text{C}$ for their conditions and structure, using As_4 as a group V source) produced a 6-fold reduction in lifetime when comparing a device grown at $660\text{ }^{\circ}\text{C}$ with one grown at $700\text{ }^{\circ}\text{C}$, and a 3-fold reduction in life for a device grown at $680\text{ }^{\circ}\text{C}$ [39]. Low V-III ratios are used in MOCVD to reduce the cost of gasses consumed in wafer growth, as well as to maximize time between hazardous arsine (or phosphine) bottle changes. Dalby et al. have shown the importance of growth temperature to lifetime in MOCVD-grown InAlGaAs QW devices, which produced $<200\text{h}$ lifetimes at the $675\text{ }^{\circ}\text{C}$ growth temperature which was optimum for InGaAs [40, 41]. The addition of aluminum required considerably higher growth temperatures to prevent oxygen incorporation; the best reliability devices (with many thousand hour lifetimes) had to be grown within a $20\text{ }^{\circ}\text{C}$ -wide window, which makes InAlGaAs one of the more difficult types of epitaxy to grow reliably. This dependence of reliability on growth conditions provides strong support for the extrinsic theory of degradation.

There is also a well-known correlation between impurity concentrations and dislocation growth. Ishii et al. performed experiments where oxygen was intentionally introduced into the flowing hydrogen of their LPE apparatus, raising it from 0.03 parts-per-million (PPM) to 5 PPM. The addition of oxygen increased the etch pit density more than three orders of magnitude, and reduced the lifetime from 10^5 h to $<10\text{ h}$ [42]. Elaborate molecular sieves and filtration systems are used in MOCVD to minimize the amount of oxygen and water vapor introduced; the source materials used are without exception the purest available. The needs of crystal growers have driven material purification technology for decades.

Even after steps have been taken to minimize the oxygen introduced into the system, gettering of the oxygen which then remains can be useful. A small amount of aluminum in the active region ($\text{Al}_{0.04}\text{Ga}_{0.96}\text{As}$) produced improved lifetime when compared with devices having a pure GaAs active region [42]. Because of this, most LPE-grown double-heterostructure (DH) lasers use at least a small amount of

aluminum in their active region. Other gettering techniques can involve using different dopants [43]. Using off-axis substrates can also minimize oxygen incorporation [44].

2.1.6 Elimination of dislocation climb in InGaAs and InGaAsP active regions

2.1.6.1 “Defect pinning” in compressively strained quantum wells

By growing compressively strained quantum wells it is possible to totally eliminate the $\langle 100 \rangle$ DLDs, along with the early failures (i.e., “infant mortalities”) the DLDs cause [16, 45]. While most authors cite the paper by Kirkby et al. as explaining this “dislocation pinning” [46], it was written to explain effects observed in liquid-phase epitaxy (LPE), and seems inappropriate for explaining “pinning” in material which has been grown by abrupt-interface epitaxial techniques such as MBE or MOCVD. Furthermore, true dislocation pinning applies not only to climb dislocations, but also to glide dislocations — however, $\langle 110 \rangle$ glide dislocations are *not* pinned in InGaAs QW material, and continue to grow [16]. More plausible mechanisms for the elimination of $\langle 100 \rangle$ DLDs with indium have only recently been proposed [47, 48], although there is a great deal of research which needs to be done to more fully understand and take advantage of this important phenomenon. Maeda et al. also propose that strained quantum wells may be able to inhibit not only dislocation climb, but also dislocation glide [15]. However, it is not clear that $\langle 110 \rangle$ dislocation glide is occurring any more slowly in InGaAs than it does in GaAs [16]. 850 nm VCSELs with strained InAlGaAs quantum wells have only recently been produced [49, 50], and may prove valuable in reducing infant mortality rates [45]. An additional benefit of the strained-layer quantum well is the reduction in heavy-hole mass, which increases differential gain and thus the obtainable modulation frequency [51]. Appendix C of this thesis deals with the issue of strained quantum wells in more detail.

2.1.6.2 Elimination of dislocation climb in long-wavelength InGaAsP / InP devices

$\langle 100 \rangle$ DLDs are also not observed in long-wavelength (1.3–1.55 μm) InGaAsP semiconductor lasers grown on InP substrates. One explanation for this is that recombination does not take place at the dislocation core, since it appears that

unlike AlGaAs alloys, InGaAsP lattice matched to InP does not have mid-gap defect states. Dow et al. [52] have found in theoretical modeling that the defect states at dislocations are in the conduction band. Note that this does not necessarily apply to the shorter wavelength (0.81 μm) InGaAsP lattice matched to GaAs substrates [52], in which dislocations *have* been observed [53].

The fact dislocation climb does not take place in long-wavelength InGaAsP lasers was dramatically demonstrated by Ueda in an experiment where such lasers were intentionally grown on substrates with a high density of threading dislocations. In GaAs / AlGaAs lasers, using low-quality substrates such as this would be guaranteed to produce extremely low lifetime, and nucleate a large density of $\langle 100 \rangle$ climb DLDs as discussed above. However, the lifetime of the InGaAsP lasers on poor quality InP substrates was still excellent [53].

The hardness of long-wavelength InGaAsP devices may help to explain why even fused-wafer VCSELs which had not been optimized for reliability show little degradation over thousands of hours of life testing at UCSB [54]. The reader is referred elsewhere for reviews of degradation in InGaAsP devices, which we shall not be dealing with further [53, 55-58].

2.2. Dislocation glide, and $\langle 110 \rangle$ dark-line defects

2.2.1 Structure and growth of $\langle 110 \rangle$ DLDs

We start this section by describing dislocation glide. Dislocation glide is fundamentally different from dislocation climb, in that glide is classified as a “conservative” process, meaning that the dislocation plane only shifts over, and doesn’t absorb or emit material (i.e., it doesn’t grow or shrink) as it would with dislocation climb. On a macroscopic scale, dislocation glide is the process responsible for the plastic deformation observed in materials when their elastic limit is exceeded. The applied strain is crucial in such glide processes, and it plays an important role in the formation of $\langle 110 \rangle$ DLDs. While the control of $\langle 100 \rangle$ DLDs primarily focuses on optimizing growth conditions, and eliminating mechanical damage to the surface and edges, $\langle 110 \rangle$ DLD elimination focuses primarily on eliminating stress inherent in the design (e.g., dielectrics, metals, mesa etches, etc.) and packaging (e.g., soldering stresses). We observed $\langle 110 \rangle$ DLDs nucleating from

both oxide aperture stress, and from stress due to indium solder, as we shall show in Chapter 8.

Fig. 2- 11 shows how the glide process starts and propagates on an atomic scale. First, a single atomic bond, under stress from the applied shear force, steps over to the adjacent atomic plane. This formation of the “double kink” is the most difficult part of the process, since the line tension is pulling the dislocation back from both sides. Next, the kinks can propagate away from each other, which involves less elastic and electronic stress than the original double kink formation did: on one side the plane is being pulled forward, and on the other it is being pulled back. The applied shear (if large enough) is also encouraging propagation of the double kink. (If the shear force is inadequate, on the other hand, the dislocation line tension may cause the kinks to be attracted to each other, and for the plane to return to its original position.) Extensive experimentation has shown that while the *formation* of the double kink *is* aided by recombination enhancement, but that the *propagation* of the kink is *not* affected by recombination effects [15].

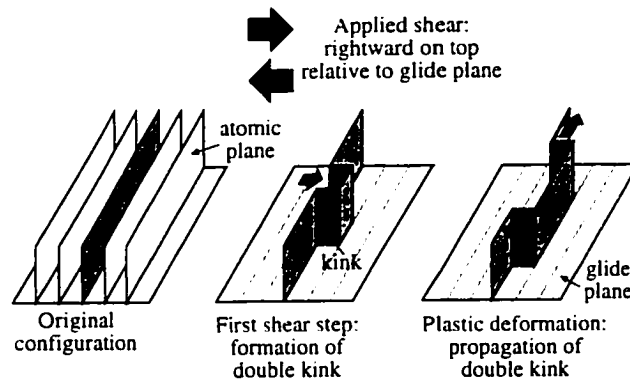


Fig. 2- 11: Dislocation glide process for an undissociated dislocation. First, a single atomic bond steps over to the next plane in response to the applied shear stress (center; adjacent planes hidden for clarity). Then, propagation of the double kink allows the rest of the atomic plane to glide to the right.

Fig. 2- 12 shows a $\langle 110 \rangle$ DLD originating at the high-stress corner of an edge-emitting laser. The design depicted has an opening in a PECVD-deposited, 120-nm-thick layer of SiO_2 . An opening in the oxide layer is created using photolithography, and a p-metal contact is then deposited uniformly on the wafer. The resulting device receives current only under the oxide opening. The PECVD oxide has significant compressive stress, which affects its operating characteristics

(such as mode shape) via strain-related index changes [59]. The oxide stress also affects the degradation rate [60].

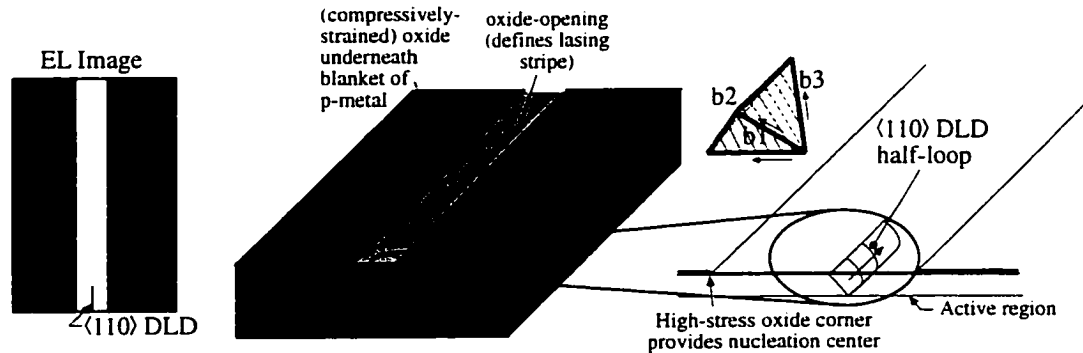


Fig. 2- 12: Propagation of $\langle 110 \rangle$ DLD in an oxide-stripe laser. A typical EL image would be as seen at the left, with the DLD lengthening as the device degraded. Glide is along the 111 plane, and starts at the facet. The $\langle 110 \rangle$ DLD then lengthens away from the facet and toward the center. The Burger's vector can be along any one of the three axes depicted on the Thompson's Tetrahedron.

Note that the DLD grows across a 111 slip plane. Some point defects and dislocation loops are left behind in the wake of the glide dislocation. These defects will contribute to recombination. Edges of the dislocation may form climb networks [53]. $\langle 100 \rangle$ (climb) DLD networks have been observed nucleating from $\langle 110 \rangle$ DLD networks [10, 53]. A higher magnification picture of a glide dislocation is shown in Fig. 2- 13.

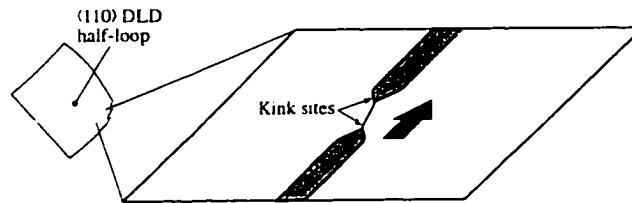


Fig. 2- 13: Microscopic view of the stacking-fault ribbon making up the bottom end of a glide dislocation for the $\langle 110 \rangle$ DLD. Note the electrically-active kink sites, which act as non-radiative centers.

The glide dislocation shown in Fig. 2- 13 is not a simple dislocation: rather, it has (in most areas) broken into a pair of dislocations ("dissociated"), a process which is energetically favorable in III-V compounds [5, 61]. The resulting pair of dislocations ("Shockley partials") are separated by approximately 6 nm, with a "stacking fault ribbon" in-between [2]. The resulting reconstruction of the dislocation core greatly reduces the detrimental electrical activity of the $\langle 110 \rangle$ DLD; it

is clear from measurements that only a small fraction of the available sites are electrically active [62]. The kink sites (which represent fewer than 1% of the sites along the dislocation) are considered electrically active. Generally, though, the $\langle 110 \rangle$ DLDs are considered more benign, since they are both slower growing, and less electrically active, than the $\langle 100 \rangle$ DLDs. The activation energy for dislocation glide (i.e. $\langle 110 \rangle$ DLD growth) is at least 0.3 eV, versus the 0.1 eV dislocation climb ($\langle 100 \rangle$ DLD growth) [21]. The microloops which are associated with gradual dislocation are left in the wake of the $\langle 110 \rangle$ DLD as the glide process takes place; dislocation climb (including $\langle 100 \rangle$ DLD formation) frequently nucleates from the ribbon.

2.2.2 Effects of stress on $\langle 110 \rangle$ DLD growth

Kamejima et al. have applied stresses at various axes to laser diodes to study $\langle 110 \rangle$ dark-line defects. For the standard $\{100\}$ substrate with $\{110\}$ facets, they have observed that the DLDs propagate perpendicular to the applied stresses [10]. A threshold stress, below which dislocation glide was slow or non-existent, was also observed. Maeda also studied the enhancement of dislocation glide with electron-beam assisted recombination in the presence of external stresses and also found a strong relationship between applied stress and dislocation glide [7].

Controlling applied fabrication and packaging stresses is absolutely essential to the control of glide dislocations. One of the main sources of device stress is from surface dielectrics. Goodwin et al. were able to correlate dielectric stress (controlled by varying the oxide thickness) and the degradation rate [60]. Others have found that the stress from AlGaAs ridges accelerates degradation directly under the ridge edges [63-66]. We shall show in Chapter 8 how packaging stresses in pillar VCSELs with thick indium solder reduced the lifetime to nearly zero, and how redesigning the packaging to protect the pillar from the indium eliminated the problem.

2.2.3 Dependence of dislocation glide on doping

One of the more intriguing effects in dislocation glide is the enhancement of crystal hardness using n-doping. Patel et al. have done theoretical modeling on silicon to show how as the Fermi level increases (i.e., as the material becomes more

n-type), kink motion and thus dislocation glide become more difficult [67]; Hirsch has also presented a simple model with good agreement to the data [68]. A number of researchers have observed that n-type GaAs is physically harder than undoped GaAs, which in turn is harder than p-type material, using indentation tests [69]. For example, Swaminathan found (Si) n-doped GaAs crystals to have a yield strength of 21 kgf/mm² at 250 °C, while semi-insulating (Cr-doped) material had a yield strength of 11.5 kgf/mm², and (Zn-doped) p-type material had only a 9.5 kgf/mm² yield strength [70]. Wang et al. have also done calculations showing that for dislocation climb, n-doping lowers vacancy concentrations, and slows $\langle 100 \rangle$ DLD growth as well [48].

The effects of doping on the velocity of glide dislocations is far more dramatic, with Ninomiya et al. observing a 3 \times reduction in α -type glide dislocation velocity in n-type GaAs with 2×10^{18} cm⁻³ doping relative to velocity in p-type samples. For β -type glide dislocations, the difference was even more pronounced, with a 3,000 \times reduction (!) [71]. This may be significant to the fact that, although we observe dislocations in the p-DBR, we see no evidence of dislocations in the n-DBR. Kajimura et al. observed an order of magnitude increase in lifetime of LPE grown devices with a Te-doped active region [72] relative to devices with an undoped active region.

2.3. Gradual degradation in LEDs and stripe lasers.

2.3.1 Microloop formation

If dark-line defect formation, and rapid degradation is avoided, the normal failure mode involves the gradual reduction in active region efficiency, and an increase in internal loss, through the introduction of microloops. The microloop formation process starts when point defects cluster together, as described earlier in section 2.1.4. Microloops grow to 15-50 nm in size [37] through the dislocation climb process described in section 2.1. (However, a different Burger's vector, namely $(a/3)\langle 111 \rangle$, was observed in the microloops [37], rather than the $(a/2)\langle 011 \rangle$ vector observed in the $\langle 100 \rangle$ DLDs.) TEM images of these microloops in the active regions of gradually-degraded devices have been published by Petroff [21] and by

Ueda [37, 58]. The concentration of carrier traps also increases as the device degrades [37, 38]; these traps will also contribute to the degradation device even if they don't combine into larger, observable structures.

2.3.2 Gradual degradation on stripe lasers is concentrated near facets.

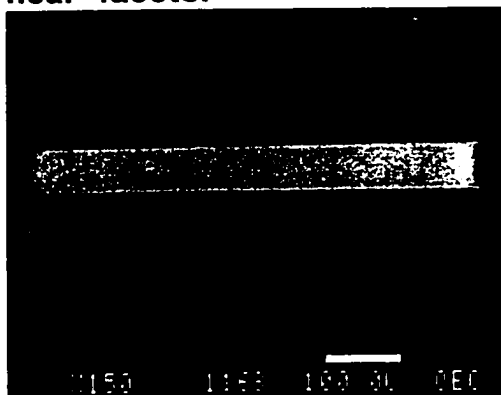


Fig. 2- 14: EBIC image showing degradation concentrated near facet regions (after ref. [1]).

It has long been realized that degradation rates for in-plane lasers are highest near the facets, and that effective facet coating is a key to making long-lived lasers [72]. Presumably, this has to do with the fact that a) the surface at the facets serves as an infinite source of point defects, and b) surface recombination takes place at the facets, which creates local heating, thereby accelerating the degradation process [73]. Fritz et al. found that the gradual degradation was concentrated in the 15 μm nearest to the facets [74]. This was determined through characterization of degraded devices by EBIC, as shown in Fig. 2- 14 [1].

Experiments have been done to determine the amount of degradation in the central portion of the device versus that near the facets. The facet regions were cleaved off of devices which had been aged to failure, and the performance was then compared to unaged devices cleaved to the same dimensions. Little difference was found in performance, indicating that very little degradation had taken place in the central portion of the device, and almost all of the degradation had been concentrated near the facets [75].

For 980 nm erbium-pump lasers, which need 100–200 mW of single-mode power from a 3–5 μm -wide stripe laser, excellent facet coating (or other method of forming a “window laser” [76]) is essential to making a reliable device. The most cost-effective way of preventing the facet degradation shown above in Fig. 2- 14 is a proprietary process developed by IBM, called the “E2” facet coating process [77]. Gradual degradation near the facets appears to have been totally eliminated by this method. The E2 process has been widely licensed, and the resulting lasers have

shown outstanding reliability all the way up to 300 mW [78-80]. Using non-absorbing facet coatings (e.g., replacing Si with non-absorbing TiO_2 at the back facet's high-reflectivity coating) has also been found to be important [78].

2.4. Effects of dark-line defects on devices

2.4.1 Optical Characteristics of DLDs

For a laser to function efficiently, it is obvious it can't tolerate much absorption within its lasing cavity, and still continue to lase. For in-plane lasers, typical average internal cavity losses are on the order of 3 cm^{-1} , while gain might average 30 cm^{-1} (gain is 1000 cm^{-1} within the quantum well, which only sees 3% of the traveling mode at any given time). The disruption in the periodicity of the crystal lattice from the dislocation creates mid-gap states which have significant photo-absorption cross sections [81, 82]. In addition, the dislocation itself is surrounded by traps and point defects which themselves have significant photo-absorption cross-sections. Further, the electrical effects of the dislocation and accompanying traps cause a shrinkage of the bandgap within one diffusion length of the dislocation — thus even undamaged material close to the dislocation contributes to increased laser loss, and a fall of in device performance. These effects are shown schematically in Fig. 2- 15.

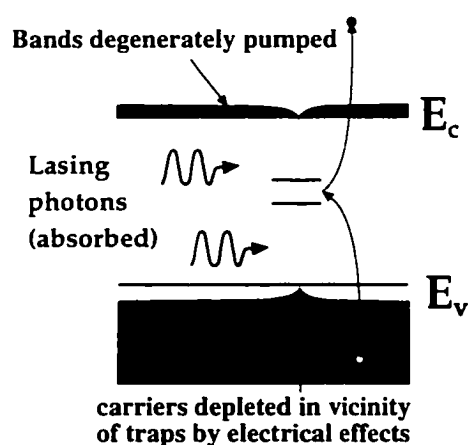


Fig. 2- 15: Band diagram (E_g vs. x) for a degraded laser, showing how device degradation adds optical cavity loss through trap photoabsorption.

Optical measurements have been performed on degraded lasers, and comparison was made with the same devices before degradation. Notable changes in the absorption spectrum have been observed [83]. In fact, while the changes in electrical characteristics were significant at small currents, during the high-pumping conditions needed for lasing, the optical loss was found to be much more important to the reduction in device performance [84]. The presence of sub-bandgap absorption can also be observed by the dramatic increase in the collected

photocurrent collected at sub-bandgap photon energies in degraded devices [85, 86].

An analysis performed at IBM with estimated the changes in device threshold and slope efficiency after initial device burn-in as being due to a 3000 cm^{-1} loss in the $15 \text{ }\mu\text{m}$ next to the facets [75]. This represented a low enough total overall fraction of the cavity volume that it was accompanied by only a 10% drop in output power. However, as the device degrades, the concentration of microloops and defects in the near-facet region continues to increase, and with it, the internal loss of the device and the heat generated increases, further driving the degradation process.

2.4.2 Electrical Characteristics of DLDs

In addition to the dark-line defects creating increased optical loss for lasers, they also reduce carrier concentrations in their vicinity, and provide a non-productive parallel recombination path which competes with the desired stimulated emission path. This is shown schematically in Fig. 2- 16.

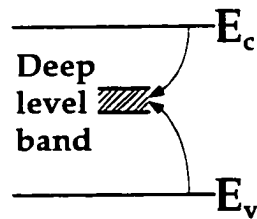


Fig. 2- 16: Unsaturated bonds from the dislocation, and surrounding impurities and deep levels, increase non-radiative rate in the vicinity of the dark line defect.

As many authors have remarked, surprisingly little is known about the electrical properties of dislocations [87]. It is believed that the stress field from the dislocations attracts or creates an elevated concentration of traps surrounding the dislocation. These traps may be as responsible for the properties of the DLD as

the dislocation itself. In fact, there is some evidence that “clean” dislocations (i.e., ones which were manufactured specifically to avoid impurity or trap generation) in certain planes have little or no recombination associated with them [62]. A number of difficulties prevent more accurate fundamental studies from being performed.

Most of the difficulties appear to stem from the extraordinarily small size scale under study. The devices themselves are no larger than a grain of sand, and the active areas are almost too small to be seen or studied. The dislocations are (at least ideally) due to only one extra half-plane of atoms, located a large number of atomic planes beneath the surface. Very few analytical techniques are suitable for

measuring the properties of dislocations; none are suitable for in-situ or non-destructive work.

Scanning DLTS was used in past work to identify impurities or traps in the neighborhood of dislocations [88, 89]. In one report by Lang et al. a reduction in the concentration of DX centers was observed in the vicinity of the dislocation, implying that the DX centers may have been consumed by the defect formation process [88, 89]. Others have also found changes in the trap concentrations in degraded VCSELs [37, 38].

References for Chapter 2:

- [1] R. G. Waters, "Diode laser degradation mechanisms: a review," *Progress in Quantum Electronics*, vol. 15, pp. 153-74, 1991.
- [2] P. M. Petroff, "Defects in III-V Compound Semiconductors," *Semiconductors and Semimetals*, vol. 22, Part A, pp. 379-403, 1985.
- [3] V. Swaminathan and A. T. Macrander, "Section 7.5. "Photonic Devices"," in *Materials aspects of GaAs and InP based structures*. Englewood Cliffs, NJ: Prentice Hall, 1991, pp. 524-549.
- [4] V. Swaminathan and A. T. Macrander, "Section 6.7. "Dislocations"," in *Materials aspects of GaAs and InP based structures*. Englewood Cliffs, NJ: Prentice Hall, 1991, pp. 427-456.
- [5] D. Hull and D. J. Bacon, *Introduction to Dislocations*, 3rd ed. Oxford, UK: Pergamon, 1984.
- [6] K. W. Böer, *Survey of Semiconductor Physics*, vol. 1. New York, NY: Van Nostrand Reinhold, 1990.
- [7] K. Maeda, M. Sato, A. Kubo, and S. Takeuchi, "Quantitative measurements of recombination enhanced dislocation glide in gallium arsenide," *Journal of Applied Physics*, vol. 54, pp. 161-8, 1983.
- [8] P. W. Hutchinson, P. S. Dobson, B. Wakefield, and S. O'Hara, "The generation of point defects in GaAs by electron-hole recombination at dislocations.," *Solid-State Electronics*, vol. 21, pp. 1413-1417, 1978.
- [9] P. M. Petroff, L. C. Kimerling, and W. D. Johnston, Jr., "Electronic excitation effects on the mobility of point defects and dislocations in GaAlAs-GaAs heterostructures," *Institute of Physics Conference Serial*, vol. 31 (Radiation Effects in Semiconductors), pp. 362-7, 1977.
- [10] T. Kamejima, K. Ishida, and J. Matsui, "Injection-enhanced dislocation glide under uniaxial stress in GaAs-(GaAl)As double heterostructure laser," *Japanese Journal of Applied Physics*, vol. 16, pp. 233-40, 1977.
- [11] D. V. Lang, L. C. Kimerling, and S. Y. Leung, "Recombination-enhanced annealing of the E1 and E2 defect levels in 1-MeV-electron-irradiated n-GaAs," *Journal of Applied Physics*, vol. 47, pp. 3587-3591, 1976.
- [12] P. M. Petroff, "Physics and materials issues behind the lifetime problem in semiconductor lasers and light emitting diodes," *Proc. of SPIE*, vol. 2683 (Fabrication, Testing, and Reliability of Semiconductor Lasers), pp. 52-8, 1996.

- [13] Y. L. Khait, J. Salzman, and R. Beserman, "Kinetic model for material structural changes and gradual degradation in semiconductor lasers and light emitting diodes," *Proc. of the SPIE*, vol. 1038 (Sixth Meeting in Israel on Optical Engineering), pp. 531-8, 1988.
- [14] J. Salzman, Y. L. Khait, and R. Beserman, "Material evolution and gradual degradation in semiconductor lasers and light emitting diodes," *Electronics Letters*, vol. 25, pp. 244-6, 1989.
- [15] K. Maeda, Y. Yamashita, N. Maeda, and S. Takeuchi, "Radiation enhanced dislocation glide and rapid degradation," *Materials Research Society Symposium Proceedings*, vol. 184 (Degradation Mechanisms in III-V Compound Semiconductor Devices and Structures Symposium), pp. 69-80, 1990.
- [16] K. Fukagai, S. Ishikawa, K. Endo, and T. Yuasa, "Current density dependence for dark-line defect growth velocity in strained InGaAs/AlGaAs quantum well laser diodes," *Japanese Journal of Applied Physics, Part 2 (Letters)*, vol. 30, pp. L371-3, 1991.
- [17] R. G. Waters and R. K. Bertaska, "Degradation phenomenology in (Al)GaAs quantum well lasers," *Applied Physics Letters*, vol. 52, pp. 179-81, 1988.
- [18] L. C. Kimerling, "Recombination enhanced defect reactions," *Solid State Electronics*, vol. 21, pp. 1391-1401, 1978.
- [19] D. V. Lang, "Recombination-enhanced reactions in semiconductors," *Annual review of materials science.*, vol. 12, pp. 377-400, 1982.
- [20] D. Petroff, W. D. Johnston, Jr., and R. L. Hartman, "Nature of optically induced defects in $\text{Ga}_{1-x}\text{Al}_x\text{As}$ -GaAs double-heterojunction laser structures," *Applied Physics Letters*, vol. 25, pp. 226-8, 1974.
- [21] P. M. Petroff, "Device degradation and recombination enhanced defect processes in III-V semiconductors," *Semiconductors and Insulators*, vol. 5, pp. 307-319, 1983.
- [22] R. Ito, H. Nakashima, S. Kishino, and O. Nakada, "Degradation sources in GaAs-AlGaAs double-heterostructure lasers," *IEEE Journal of Quantum Electronics*, vol. QE-11, pp. 551-556, 1975.
- [23] R. G. Waters and R. K. Bertaska, "Dark-line observations in failed quantum well lasers," *Applied Physics Letters*, vol. 52, pp. 1347-8, 1988.
- [24] P. M. Petroff and L. C. Kimerling, "Dislocation climb model in compound semiconductors with zinc blende structure," *Applied Physics Letters*, vol. 29, pp. 461-463, 1976.
- [25] T. Hayakawa, K. Takahashi, T. Suyama, M. Kondo, S. Yamamoto, and T. Hijikata, "Effect of group V/III flux ratio on the reliability of GaAs/Al_{0.3}Ga_{0.7}As laser diodes prepared by molecular beam epitaxy," *Applied Physics Letters*, vol. 52, pp. 252-4, 1988.
- [26] R. G. Waters and D. S. Hill, "Influence of V/III variation on $\text{Al}_x\text{Ga}_{1-x}\text{As}$ quantum well lasers grown by metalorganic chemical vapor deposition," *Journal of Electronic Materials*, vol. 17, pp. 239-41, 1988.
- [27] P. Krispin, R. Hey, and H. Kostial, "Intrinsic origin and composition dependence of deep-level defects at the inverted GaAs/ $\text{Al}_x\text{Ga}_{1-x}\text{As}$ interface grown by molecular-beam epitaxy," *Journal of Applied Physics*, vol. 77, pp. 5773-5781, 1995.
- [28] L. C. Kimerling, P. Petroff, and H. J. Leamy, "Injection-stimulated dislocation motion in semiconductors," *Applied Physics Letters*, vol. 28, pp. 297-299, 1976.
- [29] D. Hull and D. J. Bacon, "Section 3.7: Experimental Observation of Climb," in *Introduction to Dislocations*, 3rd ed. Oxford, UK: Pergamon, 1984, pp. 62-63.
- [30] F. R. N. Nabarro, "6.1.1 Point Defects and Dislocation Climb," in *Theory of Crystal Dislocations*. Mineola, N.Y.: Dover, 1967, pp. 341-349.
- [31] G. A. Baraff and M. Schluter, "Electronic structure, total energies, and abundances of the elementary point defects in GaAs," *Physical Review Letters*, vol. 55, pp. 1327-1330, 1985.

- [32] S. O'Hara, P. W. Hutchinson, and P. S. Dobson, "The origin of dislocation climb during laser operation," *Applied Physics Letters*, vol. 30, pp. 368-371, 1977.
- [33] A. Uedono, S. Fujii, L. Wei, and S. Tanigawa, "Vacancies and interstitial clusters in as-grown GaAs probed by positron annihilation," *Institute of Physics Conference Serial*, vol. 129 (Int. Symp. GaAs and related Compounds), pp. 513-518, 1993.
- [34] W. Walukiewicz, "Mechanism of Fermi-level stabilization in semiconductors," *Physical Review B*, vol. 37, pp. 4760-4763, 1988.
- [35] C.-H. Chen and T. Y. Tan, "On the validity of the amphoteric-defect model in gallium arsenide and a criterion for Fermi-level pinning by defects," *Applied Physics A*, vol. 61, pp. 397-405, 1995.
- [36] G. R. Woolhouse, "Degradation in injection lasers," *IEEE Journal of Quantum Electronics*, vol. QE-11, pp. 556-561, 1975.
- [37] K. Kondo, O. Ueda, S. Isozumi, S. Yamakoshi, K. Akita, and T. Kotani, "Positive feedback model of defect formation in gradually degraded GaAlAs light emitting devices," *IEEE Transactions on Electron Devices*, vol. ED-30, pp. 321-326, 1983.
- [38] J. Zhou, Q. Zhan, Z. Fu, D. Lü, L. Guan, and H. Chen, "Behavior of types A and B hole traps in n-type GaAs during long-period operation," *Solid-State Electronics*, vol. 35, pp. 1325-1329, 1992.
- [39] V. P. Chaly, M. I. Etinberg, G. A. Fokin, S. Y. Karpov, V. Myachin, A. Y. Ostrovsky, Y. V. Pogorelsky, I. Y. Rusanovich, A. Sokolov, A. P. Shcurko, N. A. Strugov, and A. L. Ter-Martirosyan, "A degradation rate study of MBE-grown high-power AlGaAs laser diodes," *Semiconductor Science and Technology*, vol. 9, pp. 345-8, 1994.
- [40] J. A. Baumann, R. J. Dalby, R. G. Waters, S. L. Yellen, C. Harding, and A. Shepard, "Growth of InAlGaAs strained quantum well structures for reliable 0.8 μm lasers," *Journal of Electronic Materials*, vol. 23, pp. 207-16, 1994.
- [41] J. Baumann, S. Yellen, R. Juhala, A. Shepard, C. Harding, R. Dalby, and R. Waters, "Strained quaternary InAlGaAs 810 nm lasers," *Proc. of SPIE*, vol. 1850 (Laser Diode Technology and Applications V), pp. 203-14, 1993.
- [42] M. Ishii, H. Kan, W. Susaki, H. Nishiura, and Y. Ogata, "Reduction of crystal defects in active layers of GaAs-AlGaAs double-heterostructure lasers for long-life operation," *IEEE Journal of Quantum Electronics*, vol. QE-13, pp. 600-604, 1977.
- [43] N. Chand, S. N. G. Chu, and A. S. Jordan, "Migration and gettering of Si, Be, and ambient-related O in AlGaAs/GaAs laser structures," *Journal of Vacuum Science and Technology, B*, vol. 10, pp. 807-11, 1992.
- [44] N. Chand, A. S. Jordan, S. N. G. Chu, and M. Geva, "Residual oxygen levels in AlGaAs/GaAs quantum-well laser structures: effects of Si and Be doping and substrate misorientation," *Applied Physics Letters*, vol. 59, pp. 3270-2, 1991.
- [45] R. G. Waters, D. P. Bour, S. L. Yellen, and N. F. Ruggieri, "Inhibited dark-line defect formation in strained InGaAs/AlGaAs quantum well lasers," *IEEE Photonics Technology Letters*, vol. 2, pp. 531-3, 1990.
- [46] P. A. Kirkby, "Dislocation pinning in GaAs by the deliberate introduction of impurities," presented at 1974 International Semiconductor Laser Conference, Atlanta, GA, USA, 1974.
- [47] A. A. Hopgood, "Vacancy-controlled model of degradation in InGaAs/AlGaAs/GaAs heterostructure lasers," *Journal of Applied Physics*, vol. 76, pp. 4068-71, 1994.
- [48] H. Wang, A. A. Hopgood, and G. I. Ng, "Analysis of dark-line defect growth suppression in $\text{In}_x\text{Ga}_{1-x}\text{As}/\text{GaAs}$ strained heterostructures," *Journal of Applied Physics*, vol. 81, pp. 3117-3123, 1997.

- [49] J. Ko, B. J. Thibeault, Y. Akulova, E. R. Hegblom, B. D. Young, and L. A. Coldren, "MBE-grown Strained AlInGaAs/AlGaAs Vertical Cavity Lasers with Low Threshold Currents and High Output Power.," *Proc. of IEEE LEOS '96*, pp. 388-389, 1996.
- [50] J. Ko, E. R. Hegblom, Y. Akulova, and B. J. Thibeault, "Low-threshold 840-nm laterally oxidized vertical-cavity lasers using AlInGaAs-AlGaAs strained active layers.," *IEEE Photonics Technology Letters*, vol. 9, pp. 863-865, 1997.
- [51] L. A. Coldren and S. W. Corzine, "Appendix 8.4, Band Structure in Quantum Wells," in *Diode Lasers and Photonic Integrated Circuits, Wiley Series in Microwave and Optical Engineering*. New York, NY: John Wiley - Interscience, 1995, pp. 494-507.
- [52] J. D. Dow and R. E. Allen, "Role of dangling bonds and antisite defects in rapid and gradual III-V laser degradation.," *Applied Physics Letters*, vol. 41, pp. 672-674, 1982.
- [53] O. Ueda, *Reliability and degradation in III-V optical devices*. Norwood, MA: Artech House, 1996.
- [54] Near Margalit, Life testing currently in progress (unpublished)
- [55] S. N. G. Chu, "Transmission electron microscopy of InP-based compound semiconductor materials and devices," *Annual review of materials science, volume 20*, pp. 339-63, 1990.
- [56] S. N. G. Chu, S. Nakahara, L. C. Luther, and H. W. Krautter, "Defect mechanisms in degradation of InGaAsP long-wavelength edge-emitting light-emitting diodes," *Journal of Applied Physics*, vol. 69, pp. 6974-8, 1991.
- [57] S. N. G. Chu and S. Nakahara, "Cross-sectional transmission electron microscopy parallel to the active stripe of degraded buried heterostructure distributed feedback laser devices," *Applied Physics Letters*, vol. 62, pp. 817-19, 1993.
- [58] O. Ueda, "Degradation of III-V Opto-Electronic Devices," *J. Electrochem. Soc.*, vol. 135, pp. 11C-22C, 1988.
- [59] P. A. Kirkby, P. R. Selway, and L. D. Westbrook, "Photoelastic waveguides and their effect on stripe-geometry GaAs/Ga_{1-x}Al_xAs lasers," *Journal of Applied Physics*, vol. 50, pp. 4567-79, 1979.
- [60] A. R. Goodwin, P. A. Kirkby, I. G. A. Davies, and R. S. Baulcomb, "The effects of processing stresses on residual degradation in long-lived Ga_{1-x}Al_xAs lasers," *Applied Physics Letters*, vol. 34, pp. 647-9, 1979.
- [61] K. W. Böer, "Chapter 24, Defect States and Band States," in *Survey of Semiconductor Physics*, vol. 1. New York, NY: Van Nostrand Reinhold, 1990, pp. 633-643.
- [62] P. M. Petroff, R. A. Logan, and A. Savage, "Nonradiative recombination at dislocations in III-V compound semiconductors," *Physical Review Letters*, vol. 44, pp. 287-91, 1980.
- [63] P. W. Epperlein, A. Fried, and A. Jakubowicz, "Stress-induced defects in GaAs quantum well lasers," presented at Proceedings of the Seventeenth International Symposium, Jersey, UK, 1990.
- [64] I. Rechenberg, G. Beister, F. Bugge, G. Erbert, S. Gramlich, A. Klein, J. Maege, M. Pilatzek, U. Richter, S. S. Ruvimov, H. Treptow, and M. Weyers, "Potential sources of degradation in InGaAs/GaAs laser diodes," *Mater. Sci. Eng. B, Solid-State*, vol. B28, pp. 310-13, 1994.
- [65] S. Ruvimov, A. Klein, U. Richter, I. Rechenberg, K. Scheerschmidt, and J. Heydenreich, "TEM study of the rapid degradation of pump laser diodes," *Physica Status Solidi A*, vol. 146, pp. 415-24, 1994.
- [66] A. Jakubowicz, "Material and fabrication-related limitations to high-power operation of GaAs/AlGaAs and InGaAs/AlGaAs laser diodes," *Materials Science and Engineering B*, vol. 44, pp. 359-363, 1997.

- [67] J. R. Patel, L. R. Testardi, and P. E. Freeland, "Electronic effects on dislocation velocities in heavily doped silicon.," *Physical Review B*, vol. 13, pp. 3548-57, 1976.
- [68] P. B. Hirsch, "A mechanism for the effect of doping on dislocation mobility," *Journal de Physique*, vol. 40, pp. C6-117-121, 1979.
- [69] V. Swaminathan, W. R. Wagner, and P. J. Anthony, "Effect of n- and p-type doping on the microhardness of GaAs, (Al,Ga)As and Ga(As,Sb) active layers in 0.82 and 0.87 μm injection lasers," *Journal of the Electrochemical Society*, vol. 130, pp. 2468-2472, 1983.
- [70] V. Swaminathan and S. M. Copley, "Temperature and orientation dependence of plastic deformation in GaAs single crystals doped with Si, Cr, or Zn," *Journal of the American Ceramic Society*, vol. 58, pp. 482-485, 1975.
- [71] T. Ninomiya, "Velocities and internal friction of dislocations in III-V compounds," *Journal de Physique*, vol. 40, Colloque C6, pp. C6/143-145, 1979.
- [72] T. Kajimura, "Degradation mechanisms of $\text{Ga}_{1-x}\text{Al}_x\text{As}$ visible diode lasers," *Journal of Applied Physics*, vol. 51, pp. 908-13, 1980.
- [73] P.-W. Epperlein, "Micro-temperature measurements on semiconductor laser mirrors by reflectance modulation: a newly developed technique for laser characterization.," *Japanese Journal of Applied Physics*, vol. 32, pp. 5514-5522, 1993.
- [74] W. J. Fritz, L. B. Bauer, and C. S. Miller, "Analysis of aluminum gallium arsenide laser diodes failing due to nonradiative regions behind the facets," *Proc. of the Intl. Reliability Physics Symposium 1989*, pp. 59-64, 1989.
- [75] E.-E. Latta, A. Moser, A. Oosenbrug, C. Harder, M. Gasser, and T. Forster, "Operational limits of GaAs-based single quantum well laser diodes," *IEEE Journal of Quantum Electronics*, vol. (submitted for publication, and then withdrawn), 1991.
- [76] D. F. Welch, W. Streifer, and D. R. Scifres, "High power single mode laser diodes," *Proc. of the SPIE*, vol. 1043 (Laser Diode Technology and Applications), pp. 54-60, 1989.
- [77] M. Gasser and E. E. Latta, "Method for mirror passivation of semiconductor laser diodes (U.S. patent #5,063,173)," . USA: International Business Machines Corporation, Armonk, N.Y., 1991.
- [78] A. Oosenbrug and A. Jakubowicz, "Operational Stability of 980 nm Pump Lasers at 200 mW and above.," *Proc. of SPIE*, vol. 3004 (Fabrication, Testing, and Reliability of Semiconductor Lasers II), pp. 62-70, 1997.
- [79] H. P. Meier and V. Graf, "Research lab converts to diode laser manufacturer," *Laser focus world*, vol. Oct. 1996, pp. 51-56, 1996.
- [80] G. Grasso, F. Magistrali, G. Salmini, A. Ossenbrug, A. Jakubowicz, D. Darby, and P. Whitney, "Qualification-testing and field-reliability results for 980 nm pump lasers," *Optical Fiber Conference Technical Digest*, vol. OFC-95, pp. 232-233, 1995.
- [81] K. W. Böer, "Chapter 20, Optical Absorption at Lattice Defects," in *Survey of Semiconductor Physics*, vol. 1. New York, NY: Van Nostrand Reinhold, 1990, pp. 491-530.
- [82] D. Redfield and R. H. Bube, *Photoinduced defects in semiconductors*. Cambridge, U.K.: Cambridge University Press, 1996.
- [83] T. L. Paoli and B. W. Hakki, "cw degradation at 300°K of GaAs double-heterostructure junction laser. I. Emission spectra," *Journal of Applied Physics*, vol. 44, pp. 4108-4112, 1973.
- [84] B. W. Hakki and T. L. Paoli, "cw degradation at 300°K of GaAs double-heterostructure junction lasers. II. Electronic gain," *Journal of Applied Physics*, vol. 44, pp. 4113-4119, 1973.
- [85] C. H. Henry, P. M. Petroff, R. A. Logan, and F. R. Merritt, "Catastrophic damage of $\text{Al}_x\text{Ga}_{1-x}\text{As}$ double-heterostructure laser material," *Journal of Applied Physics*, vol. 50, pp. 3721-32, 1979.

- [86] A. Richter, J. W. Tonn, C. Lienau, and J. Luft, "Optical near-field photocurrent spectroscopy: a new technique for analyzing microscopic aging processes in optoelectronic devices," *Applied Physics Letters*, vol. 69, pp. 3981-3, 1996.
- [87] A. Ourmazd, "The electrical properties of dislocations in semiconductors," *Contemporary Physics*, vol. 25, pp. 251-268, 1984.
- [88] P. M. Petroff, "Point defects and dislocation climb in III-V compounds semiconductors," *Journal de Physique*, vol. 40, pp. C6/201-5, 1979.
- [89] D. V. Lang, P. M. Petroff, R. A. Logan, and W. D. Johnston, Jr., "Recombination-enhanced interactions between point defects and dislocation climb in semiconductors," *Physical Review Letters*, vol. 42, pp. 1353-6, 1979.

Chapter 3: The early stages of degradation

The previous chapter discussed dark-line defects and microloops — coherent structures of point defects which are easily observable, and have strong (and usually very serious) consequences to laser lifetime. Because such DLD and “dark-area defect” structures are easy to observe, they have been studied for as long as lasers and LEDs have been around (i.e., since the early 60’s). However, in many well-made lasers such coherent defect structures are never observed. It is possible, and perhaps even likely with some designs, that device may fail without the presence of a single such DLD or microloop. In such a case, we must look to point defects and carrier traps to explain the failure of the device. We have found substantial evidence, at least for rapidly-degraded Honeywell VCSELs, that the devices never suffer any measurable degradation of their active region during their aging process, until well after they have already exceeded failure criteria. The mechanism we will discuss for their failure, was originally proposed by scientists at Honeywell MICRO SWITCH. We refer to this as the “current shunting” failure mechanism, which calls for passivation of the DBR mirror(s) near the device center to raise the resistivity of the center, and push the current toward the outside of the device, where it is unable to contribute usefully to the lasing process. This mechanism has never before been described in the literature, and appears to apply uniquely to VCSELs.

While not many papers on laser degradation have described failures which are trap-mediated in a thorough manner, we focus on a few of the most valuable results in this area in section 3.1. Next, in section 3.2 we describe the 850 nm top-emitting VCSEL which was the primary focus of this thesis. In section 3.3 we discuss two key assumptions which have been called into questions by the data presented in this chapter; we also describe the aging conditions used for rapid device degradation. Results for two methods of plan-view examination (CL and EL) which would be expected to give similar results (but don’t) are presented in sections 3.6 and 3.5, along with supporting evidence from cross-sectional EBIC characterization in section 3.4. We briefly mention C-V and I-V characterization in section 3.7. We conclude with our discussion (section 3.8), where the proposed failure mechanism is presented. This mechanism is consistent with our experimental observations, but contradicts some of our previous assumptions about the nature of degradation.

3.1 Background on traps and donor passivation during gradual degradation.

Madhava-Menon, Petroff, and Waters studied early GRIN-SCH SQW stripe lasers grown at McDonnell Douglas, and found an anomalous temperature dependence [1]. Degradation rates at 100 K were over $3 \times$ *higher* than at room temperature (!) The mechanism proposed to explain this reverse temperature dependence involved carrier traps in the GRIN-SCH confinement layers adjacent to the quantum well. At low temperature, carriers in these traps recombined in non-radiative processes, thereby driving degradation and $\langle 100 \rangle$ DLD growth. At high temperatures, it was postulated that carriers were thermally re-emitted from the traps before they had time to recombine non-radiatively, and were subsequently collected by the quantum well, which had far fewer traps in it than the GRIN-SCH layers had in them. The anomalous temperature dependence of degradation rate was not subsequently observed on any other McDonnell Douglas wafers, but the results left the designers of space-based laser systems with uncertainty about how to assure reliability in a device without confidence in conventional accelerated-temperature testing, so they swore off quantum well lasers for many years to come.

Martins et al. have used EBIC and CL profiling to study the passivation of dopants during gradual degradation [2]. They describe a three-step process to degradation. First, a defect complex (which they believe is $\text{Si}_{\text{Ga}}-\text{V}_{\text{Ga}}$) results in donor passivation in the GRIN-SCH confinement layers. This starts at the p-n junction, which is generally *not* exactly aligned at the quantum well in most devices. For most devices, background doping places the p-n junction at the top or bottom the confinement layers (at the top of the n-DBR or the bottom of the p-DBR in our case). As the dopants become passivated, the band bending changes, with a “virtual anode” (i.e., a band-energy minimum) forming between the junction and the QW, and moving toward the active region, and the “passivation front” also moving closer to it. The second stage of degradation starts when the virtual anode reaches the active region, and defect complexes start to form within the QWs (not just in the cladding layers), reducing the active region’s efficiency. Finally, in the third stage, the local heating from the non-radiative recombination promotes dark-line defect growth, which in turn cause device failure. The evidence from Martins et al. suggests that DLDs are not generated until the late stages of degradation are reached,

which is consistent with our observations. The dopant passivation model they propose may be similar to the mechanism we believe is causing increased resistance in the device center, and shunting current toward the edges of the device which act as low-resistance parallel paths. This paper has many other valuable elements which recommend it: one of the few plausible (and experimentally-verified) band diagrams for a GRIN-SCH structure; some of the best EBIC modeling seen for a laser structure; and a valuable concept: the "virtual anode," which can act as a carrier-trapping pocket which contributes to aging in the laser's confinement layers.

Kondo et al. propose a similar three-step process [3]. First, the deep-levels associated with point defects act as non-radiative centers. Second, vacancy-interstitial pairs are generated by the energy of recombination at the non-radiative centers. Third, more recombination centers are formed by the newly-created point defects. In addition, the interstitials are able to cluster to create either $\langle 100 \rangle$ DLDs, or the microloops observed in gradually-degraded devices. They provide substantial DLTS and TEM data to back up their model [3].

Many others have used deep-level transient spectroscopy (DLTS)[4] to study how trap populations vary (usually rise) as the device ages [5-10]. It is somewhat surprising, given the amount of work which has taken place, that the authors involved have not been able to definitively identify whether the intrinsic or extrinsic model (discussed in Chapter 2) is responsible for dislocation climb. Taken as a whole, the work discussed above provides a more than adequate precedent for carrier sites being passivated and the resulting current flow being modified, as we propose in the discussion at the end of this chapter.

3.2 Description of VCSEL structure studied

The VCSELs which were the primary focus of this work were provided by Robert A. Morgan and Mary K. Hibbs-Brenner of the Honeywell Technology Center, in Plymouth, Minnesota, as well as aged VCSELs which were provided by James Guenter of Honeywell MICRO SWITCH of Richardson, Texas. I am deeply indebted to them, not only for these samples, but for the continuing support they provided during my analysis. The growth and processing are consistent with the proton-implanted, top-emitting, 850 nm multi-mode VCSEL design widely used for data communication applications.

The structure is grown in an unmodified Aixtron 200/4 MOCVD reactor, on 3"-diameter n⁺GaAs substrates oriented 2° off the 100 orientation toward the ⟨110⟩. Growth pressure is 200 mBar, and growth temperature is 750°C. After a thin n-GaAs buffer layer is grown, 30 1/2 λ/4 DBR pairs of Al₁₆Ga₈₄As / AlAs are grown for a 99.9% reflective bottom mirror. Doping in the layers is 1×10¹⁸ cm⁻³ of Te, while the doping level rises to 2-3×10¹⁸ cm⁻³ in the 10-nm-wide graded transitions between the Al₁₆Ga₈₄As and the AlAs, in order to minimize interface resistance.

Above the n-DBR, a 1-λ optical cavity is formed primarily of Al_{0.6}Ga_{0.4}As. At the center of this cavity are three 7-nm-thick GaAs quantum wells (QWs) which provide the gain. The quantum wells are separated by 10-nm-thick Al₂₅Ga₇₅As barrier layers which contain carriers from the quantum wells.

Finally, 22 p-DBR Al₁₆Ga₈₄As / AlAs pairs are grown for a 99.8% reflective upper mirror, with doping levels and grading as indicated above for the n-DBR. The p-dopant used is zinc. Further details of the growth of the structure have been published elsewhere [11, 12].

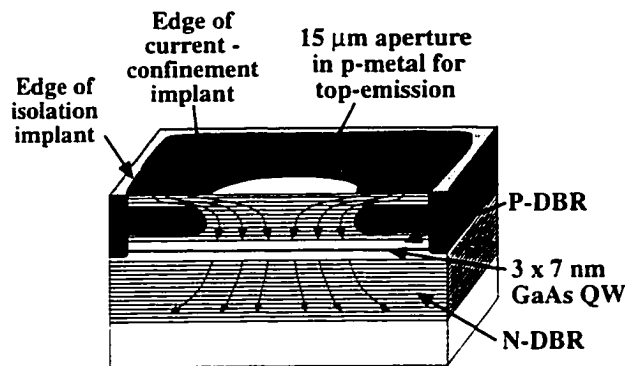


Fig. 3- 1: Schematic cross-section of the proton-implanted, top-emitting VCSEL structure which was the primary type of device studied in this thesis. Arrows inside the structure show the direction of current flow.

As detailed by Morgan et al. [13], the processing of this wafer includes: 1) the formation of the 40-μm-square p-ohmic contact with a 15 μm aperture through the middle for lasing emission; 2) a shallow ("current-confining") proton implant, with a 20 μm aperture to force current flow through the device center; 3) dielectric deposition; 4) a deep

("isolation") proton implant through the active region to prevent leakage between adjacent devices; 5) n-metallization; and 6) interconnect metallization of the contact traces and wire bond pads. The devices are tested by a computerized probe station. Good devices (with over 99.8% device yields and 94% array yields being observed [12]) are separated by sawing, and then packaged. The resulting devices have

threshold currents of 2.5 mA, and peak power > 5.5 mW, and very low threshold voltages averaging 1.68V, which are indicative of the optimized low-resistance DBRs [13]. A schematic view of the structure is shown in Fig. 3- 1.

The relative dimensions of the proton implants can be established by cleaving (or polishing) a device down the center, and then stain etching. The stain etches used included the "A-B etch," [14] and a Nitric/Peroxide/Water etch. The resulting image is seen in Fig. 3- 2.

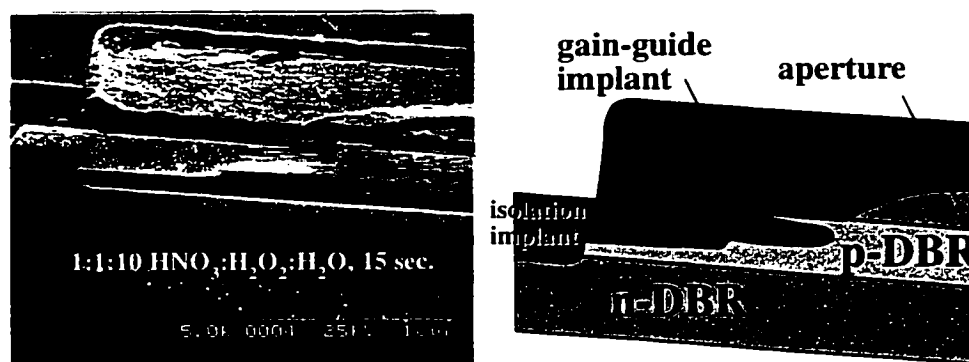


Fig. 3- 2: SEM of the left side of a stain-etched VCSEL cross section. A drawing, showing the features described earlier, is seen on the right.

Nominal operating current is in the range of 6-10 mA. The device is multi-lateral mode, with little enough power in any given mode that modal interference effects, and mode switching noise, are not problems in data communications through multi-mode fiber. More details about the design and performance of these VCSELs have been published elsewhere [13, 15]. They are also the first VCSELs to be sold as individual components from a major manufacturer [16].

3.3 Key assumptions, and aging conditions

3.3.1 Inconsistencies in results may be explained by questioning two key assumptions.

3.3.1.1 Assumption #1: The failure mechanisms in slightly aged VCSELs can be deduced by studying totally aged VCSELs.

Two assumptions were made during the early part of this work, both of which have more recently been called into question. First, we assumed that we could deduce the cause of failure (defined as where output power drops by 2 dB, or 37%, at 10 mA) by studying deeply or totally degraded VCSELs which had been aged far beyond this small amount of degradation. The failure criterion only calls

for an increase in the threshold of $\sim 1.4\times$, or a small drop of the peak power of $\sim 13\%$. By contrast, most devices studied were aged until the peak power fell by a minimum of 50-70%, which is far beyond the point at which the system would have failed. Many of the devices examined by Michael Cheng were aged until they no longer lased at all (i.e., they suffered a 100% drop in peak power, and then were even further aged beyond that point).

We assumed that if DLDs are observed in the totally degraded VCSELs, that the DLDs were simply shorter or less dense earlier in the degradation process, but were nonetheless responsible for device failure. The course of failure, however, may well be more complex than originally thought, as we have more recently discovered through the multi-stage processes supported by the work of Martins et al. [2]. This assumption is discussed in greater detail in the final section of this chapter.

3.3.1.2 Assumption #2: Rapidly-aged VCSELs fail due to the same causes as normally-aged VCSELs.

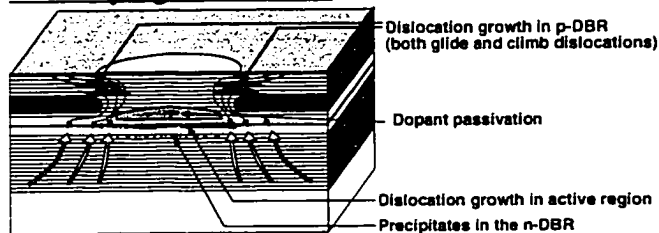


Fig. 3- 3: A number of failure mechanisms were observed to progress at similar speeds, making it difficult to assume only a single mechanism mattered.

Our second assumption was that very rapid degradation, where the laser was operated at a current past where lasing was extinguished (junction temp $> 200\text{ }^{\circ}\text{C}$), would cause the VCSELs to fail by the same mechanism as gradual

degradation. As we shall see later, this rapid degradation may well under-emphasize the actual degradation appearing in the mirror region and active layers, and overemphasize the “current shunting” mechanism that is the focus of this chapter. Nevertheless, work done independently at Honeywell on gradually-degraded devices also supports the current-shunting mechanism, so it is not purely a product of the high-current aging conditions used. The assumption that extremely rapid aging is a valid method of degrading devices is acceptable, provided only a single mechanism dominates the device failure at both the normal and accelerated conditions. However, when *multiple* failure mechanisms are operating across the same time scale, some failure mechanisms are likely to be accelerated more than

others, as aging conditions are changed. We show the main failure mechanisms observed in the normal Honeywell 850 nm VCSELs in Fig. 3- 3.

3.3.2 Rapid aging conditions used

3.3.2.1 Junction temperature dependence on drive current

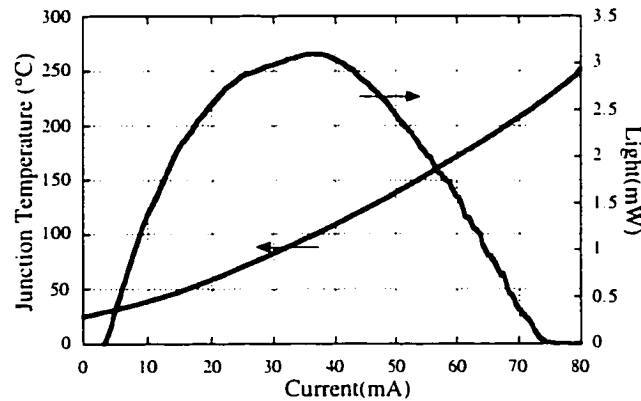


Fig. 3- 4: Increase in junction temperature versus drive current.

Measurements

on similar VCSELs have shown that the thermal resistance is $\sim 0.8^\circ\text{C}/\text{mW}$ [17]. By using the formula $T_j = T_a + R_{th}(IV - P_{out})$, where T_j is the junction temperature, R_{th} is the thermal resistance, I and V are the applied current

and bias voltage, respectively, and P_{out} is the output power, we are able to estimate the junction temperature. The resulting curve of junction temperature rise versus drive current is shown in Fig. 3- 4. The curve was taken at room temperature; unless otherwise specified, ambient temperature for rapidly degraded VCSELs was $\sim 25^\circ\text{C}$. Measurable amounts of degradation (we generally targeted a 1.3–4 \times increase in threshold) could be obtained by aging at 60 mA ($J=19\text{ kA}/\text{cm}^2$; $T_j = 170^\circ\text{C}$) for 24 hr, at 70 mA ($J=22\text{ kA}/\text{cm}^2$; $T_j = 210^\circ\text{C}$) for 0.5-1 hr, or at 80 mA ($J=25\text{ kA}/\text{cm}^2$; $T_j = 250^\circ\text{C}$) for 1-2 minutes. By contrast the “gradually-degraded” or “normally-degraded” VCSELs analyzed in this thesis (which were obtained from Honeywell MICRO SWITCH) were aged at currents usually 15–20 mA, and temperatures of 80–125 $^\circ\text{C}$, for 2,000–6000 hr. In this case, the current is only $\sim 2\times$ the normal operating current, and the aging acceleration factor is 3–5 orders of magnitude more gradual than for our rapid acceleration.

3.3.2.2 Degradation rate versus drive current.

The studies of degradation rate performed to date have found that degradation rate varies $\propto I^2$, above and beyond the acceleration expected due to junction heating alone. We will discuss this in more detail in Appendix D [18]. Above 30 mA, degradation rates may be even higher than would be predicted. This

is consistent with the model we propose for the driving force of degradation in Chapter 5, where the high-energy spontaneous emission is responsible for aging. This spontaneous emission is relatively flat across the normal range of operating currents, but rises rapidly above 30 mA.

In particular, we empirically observed a very rapid increase in degradation rate above the point where output power was totally quenched (i.e., at currents above the point where output power dropped to <0.5 mW, small increases in current would cause dramatic increases in degradation rate).

3.4 Cross-sectional EBIC

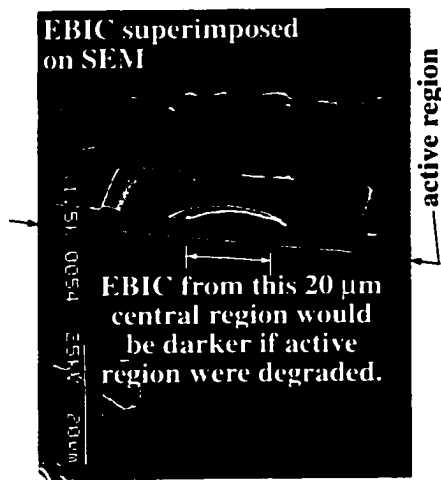


Fig. 3- 5: EBIC Image of aged and cleaved VCSEL shows no evidence of degradation.

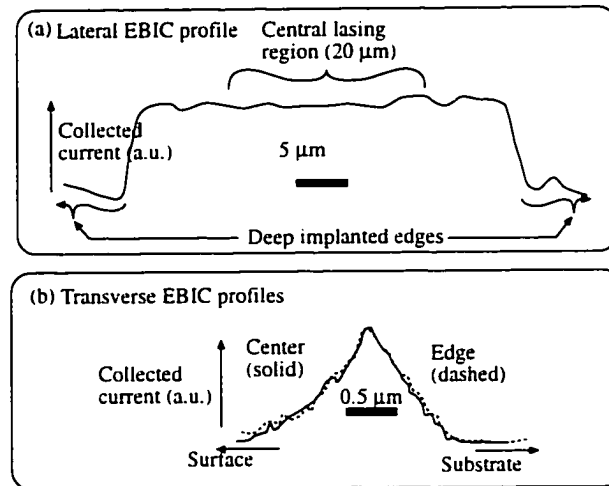


Fig. 3- 6: Collected current linescans of the VCSEL from side-to-side (a); and from top-to-bottom (b). Note no reduction in current collection efficiency in the center relative to the edge.

We were able to verify our conclusion that no true degradation takes place in the active region by using charge-collection microscopy (a.k.a. EBIC, or electron-beam induced current). EBIC, with its ability to detect dark-line defects or trap concentrations, was discussed earlier in Chapter 2. Here, we use EBIC to examine devices which were rapidly aged at high currents until threshold increased by a factor of $2 \times$, and then cleaved along their centerline. The cross sections of the devices were examined at 15–20 kV. As we discuss in Appendix E, this only excites an area within $\sim 0.3 \mu\text{m}$ of the surface. The resulting EBIC profile appears totally uniform throughout the entire $40\text{-}\mu\text{m}$ area between the deep-implant boundaries, and shows no evidence of dark-line defect growth or degradation (Fig.

3- 5). This can be verified more quantitatively in the lateral and transverse collected-current profiles which were obtained by digitizing the collected current (Fig. 3- 6). If dark-line defect formation had degraded the central part of the active region, in the manner which we had expected from the EL images or the cross-sectional TEM, the central 20 μm of the EBIC image should have been dark.

3.5 Plan-view CL and PL imaging.

The plan-view electroluminescence imaging to be discussed in the following section has an important limitation: the light generated by EL all originates from the active region. As such, EL is not capable of examining degradation in the mirrors. By contrast, photoluminescence (PL) and cathodoluminescence (CL), *are* both capable of exciting luminescence in bulk layers far from the depletion region (e.g., the p-DBR).

3.5.1 Top-view photoluminescence microscopy

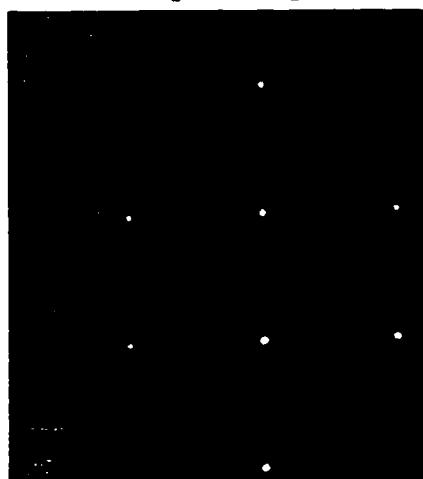


Fig. 3- 7: Unfiltered PL image of VCSEL with p-metal polished off. Bright spots are unimplanted regions, located $\sim 600 \mu\text{m}$ apart.

A number of authors have used photoluminescence microscopy to study dislocation contrast in devices with DLDs [19-21]. In such measurements, the excitation laser is either defocused to provide uniform excitation across a field, or it is systematically rastered across the field of view. Optical filters are used to block light from the excitation line, and monitor photoluminescence (PL) excited in the sample. PL intensity in the vicinity of dislocations is lower due to the parallel non-radiative recombination carrier recombination paths presented by the dislocation and surrounding defects.

PL has one important difference from CL (among many others): extremely shallow penetration depth. Using an Ar^+ laser (514 nm), the nominal photon penetration depth is on the order of 10 nm [22], versus $\sim 12 \mu\text{m}$ for CL operating at 120 keV. Thus, CL creates a nearly uniform carrier density through all device layers, and would likely miss individual dislocations or networks that weren't sufficiently dense, while the PL allows us to isolate just the very top of

the structure for imaging. Given the TEM evidence (to presented in Chapter 4) of glide dislocations originating from the p-contact at the top edges of the device, examination of the near-surface area was a prime goal. In practice, the PL-generated carriers diffuse down from the surface, particularly as pumping intensity is increased, so analysis is not quite as confined to the surface as might be originally expected on the basis of photon penetration depth alone. This is shown in Chapter 5. Using samples with the p-metals polished off, it was hoped that dislocations originating in the p-contact layer (at the top of the p-DBR) could be observed.

Two systems were used for imaging: the first was a very simple system, with a 2 mW unfocussed HeNe (633 nm) laser exciting the device off-axis, and a Si CCD camera imaging it. The resulting PL image is shown in Fig. 3- 7. Unfortunately, when magnification was increased to allow imaging of a single device, the brightness was inadequate to acquire an image.

A second system used a rastered Ar⁺ laser (514 nm) with a <0.5 μm spot to generate PL light, which was detected by a detector with a lock-in amplifier, and the data subsequently was assembled into an image. No dark lines or non-uniformity were observed in the resulting image of aged devices. No image could be made in the shallow-implanted area, since the PL intensity had fallen by at least 4–5 orders of magnitude (i.e., below the noise floor) due to the effects of implant damage. This lack of evidence of degradation is consistent with the explanation of device aging which we will subsequently offer, and is also consistent with our CL observations of rapidly-degraded devices.

3.5.2 Top-view CL observations of degraded VCSELs

An excellent method for monitoring potential degradation in the p-DBR is the use of quantitative cathodoluminescence (CL) data. In such an experiment, CL spectra are taken from degraded and undegraded devices from the same sample, preferably during the same data run to avoid problems with drift in the system sensitivity. In the case of separate samples the spectra can be normalized by a feature which is assumed not to change, such as the CL efficiency of the GaAs substrate. For all the CL results which follow other than those of Fig. 3- 8, the samples were all on the same chip (and thus at the same height on the stage, and therefore having equal coupling efficiencies).

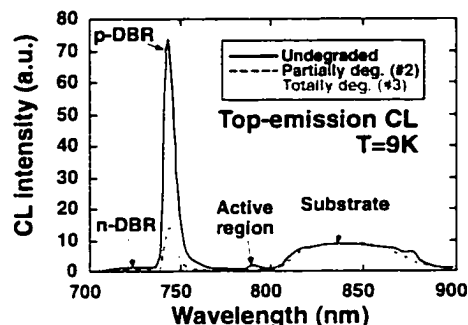


Fig. 3- 8: Top-emitting CL Spectra of normally-degraded VCSELs show dramatic reductions in CL efficiency of the p-DBR after aging, suggesting the formation of DLDs in the active region. (After ref [23])

Michael Cheng earlier used the same quantitative CL technique to determine whether the CL efficiency of p-DBRs had fallen in normally-degraded VCSELs, and found a very dramatic decrease in the aged devices, as we show in Fig. 3- 8 [23, 24]. These VCSELs had been aged for 2–3,000 hours at near-normal currents and 125°C ambient temperature. The “partially-degraded” device had aged until its threshold tripled, while the “totally-degraded” device no longer lased.

However, given the inconsistency with the results taken of plan view samples described below (where little change was observed in degraded devices) Cheng’s CL experiment was replicated, except with rapidly degraded VCSELs, rather than VCSELs which had been gradually-aged. We first using the same (newer) sample (#602) as used in our recent work, and then again repeated with the same sample (#469) Cheng examined earlier. The results were the same every time: no evidence of degradation was observed in the p-DBRs, except in the totally-degraded devices, or the devices which were aged more slowly (i.e., devices which began to approach the “normally-degraded” devices). The spectral efficiencies of all the devices were within 10% of each other (Fig. 3- 9).

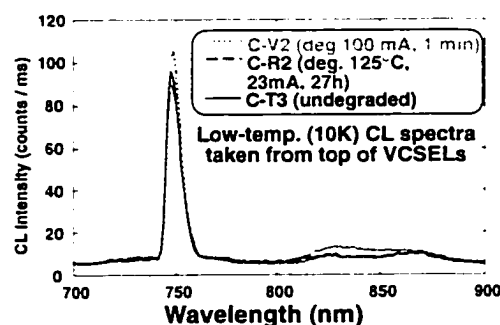


Fig. 3- 9: Top-emitting CL spectra of rapidly-degraded VCSELs shows little change in CL efficiency after aging, consistent with no non-radiative centers forming in the device.

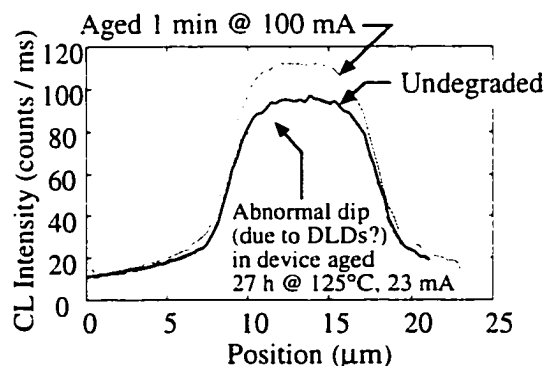


Fig. 3- 10: CL linescans taken from the top of rapidly degraded VCSELs show some signs of dislocation formation in device aged overnight.

Some evidence of DLDs can be seen in the device aged overnight (Fig. 3- 10). There are three possible explanations for this inconsistency of results.

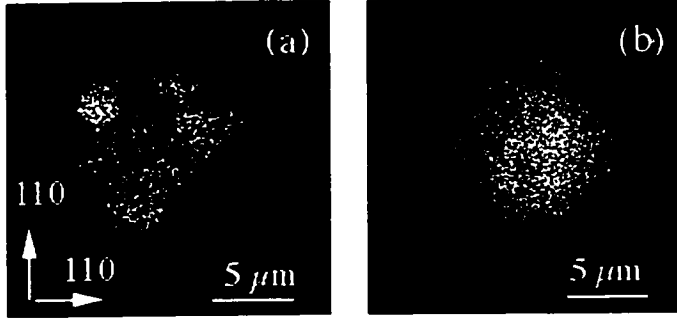


Fig. 3- 11: Monochromatic CL images of p-DBRs in VCSELs before degradation (right) show uniform luminescence, while after degradation (left), dislocation networks can be observed (after Ref [23]).

The first explanation could be experimental error. If the gradually-degraded devices examined had been taken from different parts of the wafer, and DBR wavelength varied (it often does by up to 20 nm across a single wafer), the 748 nm peak could be in the center of

a reflectivity null for one device, and between nulls for another device. This could create substantial differences in CL signal, even if no degradation had taken place. No measurement of lasing wavelength was made before performing the measurements to check for this possibility. However, we reject this first hypothesis, since Cheng was able to image dislocations in the monochromatic image of the totally degraded device (Fig. 3- 11) [23], which is an independent sign of true degradation. The other two explanations, calling into question some of our earlier assumptions about rapid aging being similar to gradual aging; and of deep degradation being similar in nature to partial degradation, will be discussed in more detail in the final section of this chapter.

3.5.3 CL of active region after removal of substrate and n-DBR

The top-emitting quantitative CL experiments discussed in the previous section had a number of advantages. They required no sample preparation to the VCSELs, and because the die were left in their as-fabricated state, a direct quantitative comparison could be made from one die to the next. Because no sample preparation was required, even the small die aged by Honeywell MICRO SWITCH could be used.

However, the experiment also had several limitations. First, the thickness and high reflectivity of the upper mirror prevents us from observing more than a weak signal from the active region [23, 24]. Thus, no useful monochromatic image

of the active region could be formed in top-emitting CL of unthinned devices. Furthermore, only the central region of the p-DBR can be imaged. We cannot see dislocations under the p-contact, since light generated there is blocked from escaping into the CL system.

For these reasons, several months were spent developing sample preparation techniques to allow us to look at degraded VCSELs in plan view. We wished to look for external nucleation sites for the dark areas shown in the electroluminescence images (Section 3.6.2). To identify defect nucleation sites, plan view imaging is essential. If only a single external dislocation nucleated the entire dislocation network in the active region, our chances of being lucky enough to capture the evidence in a cross sectional sample (which contains much less than 0.5% of the volume of interest) would be vanishingly small. Being able to see the entire active region in plan view (as shown in the EBIC images of Chapter 2) is of great value. Taken together with the cross-sectional CL results, the plan view images produce a much more complete picture of what's taking place.

Arrays approximately 3x5 mm were used, and five different aging conditions were used to allow us to see how device degradation proceeds as the VCSEL ages. Fortunately, a similar high-current aging stress nearly always caused similar change in performance. A typical sample set would contain a sample where the device had been aged to cause a 20, 50, 100, 200, and 400% increases in threshold current. Each device had unique identification letters in the interconnect metal, making device identification and record keeping simple.

The devices were then mounted p-side down on a small piece of AlN with Allied Hi-Tech Epoxy 110, which cures in just a few minutes at 120°C. The substrate was then removed using a series of progressively finer grades of mylar-backed diamond paper. Most of the n-DBR layers were also removed. We found the best results were obtained by leaving several n-DBR pairs, though. Presumably this is because the remaining pairs create a resonant cavity, without having so many pairs that it is difficult for light to escape. The final sample preparation step was to provide a brief polish to the n-DBR with a dilute Br:Methanol solution (1:1000) using a Buehler Chemomet pad. This provided a specular and virtually scratch-free surface finish. As a whole, the technique removed over 400 μm of substrate

material, and yet we were able to stop with a precision of a few mirror pairs (i.e., $\sim \pm 0.25 \mu\text{m}$). A more detailed description of the sample preparation is contained in Appendix B.

All cathodoluminescence was performed at low temperature (10 K) using liquid helium cooling, to minimize spectral broadening, and allow clear monochromatic imaging. The cooling also provided an enhancement of observed intensity of approximately two orders of magnitude by reducing non-radiative recombination, which is also important to improving the quality of the data. Details of the CL imaging can be found in Appendix E.

A large number (over a dozen) devices at various stages of degradation were examined in detail on two separate samples. Spectra were taken at a number of different locations on each VCSEL, and monochromatic line scans and images were also taken at several key wavelengths for each device. We expected to find dislocations in the active region, consistent with the degradation observed by EL (section 3.4.2), and the TEM images taken by Cheng showing such dislocations [23]. We also expected to see evidence of p-DBR degradation, consistent with the finding of Cheng [23, 24]. However, our actual observations were that the results from degraded and undegraded devices were virtually identical. No significant degradation was observed in any layer of the device, which was initially deeply disturbing, but led to our acceptance of the “current-shunting” failure mechanism

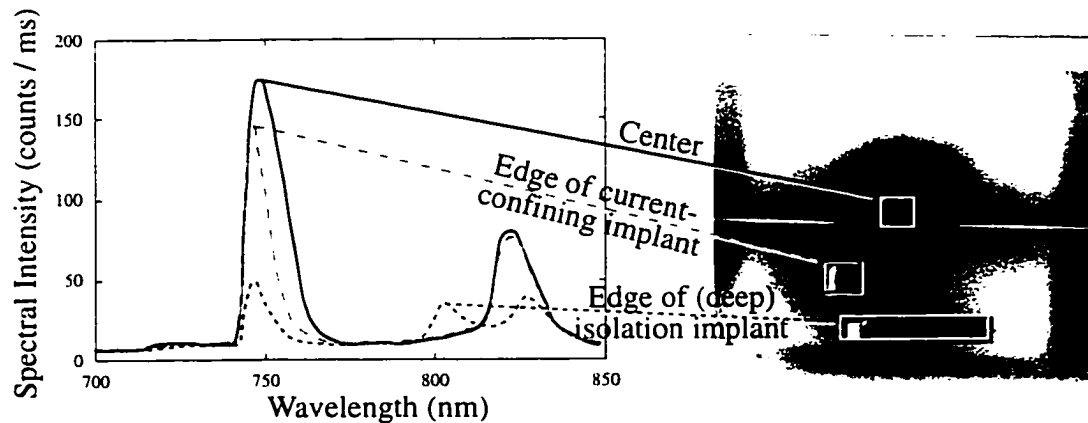


Fig. 3- 12: CL Spectra taken at three different points from a deeply degraded plan-view sample. The locations the spectra were collected at are shown with boxes on the SEM image at right, which shows the p-metal through the remaining $\sim 3.5 \mu\text{m}$ of AlGaAs epitaxial material.

proposed earlier by Honeywell MICRO SWITCH, and discussed in detail below.

We show the spectrum from a deeply degraded VCSEL in Fig. 3- 12 (which had been aged at 82 mA for 1 minute, until the threshold current nearly quadrupled from 3.4 mA up to 12.5 mA).

A number of spectral peaks can be easily recognized by referring to our cross-sectional CL results [23, 25], which will be presented in Chapter 4, or by using the bandgap data on AlGaAs presented in Appendix F. The n-DBR spectrum appears as a low, broad peak at 725 nm. The p-DBR is a sharp, high peak at 745 nm. The active region appears at 823-825 nm, somewhat longer in wavelength than the 795-800 nm observed in cross-sectional CL samples. This longer wavelength is likely due to a resonator effect: while the gain peak shifts toward shorter wavelength at the rate of 0.28 nm per °C reduction in temperature, the resonator wavelength only shifts at 0.056 nm / °C [17]. Thus, given that a cavity resonance with the remaining n-DBR pairs is likely taking place, we would expect the peak wavelength to shift to shorter wavelengths more slowly than the shift of the GaAs itself. An additional peak at 800-810 nm is visible, particularly around the edges where the deep isolation implant has taken place. We believe that proton-enhanced intermixing

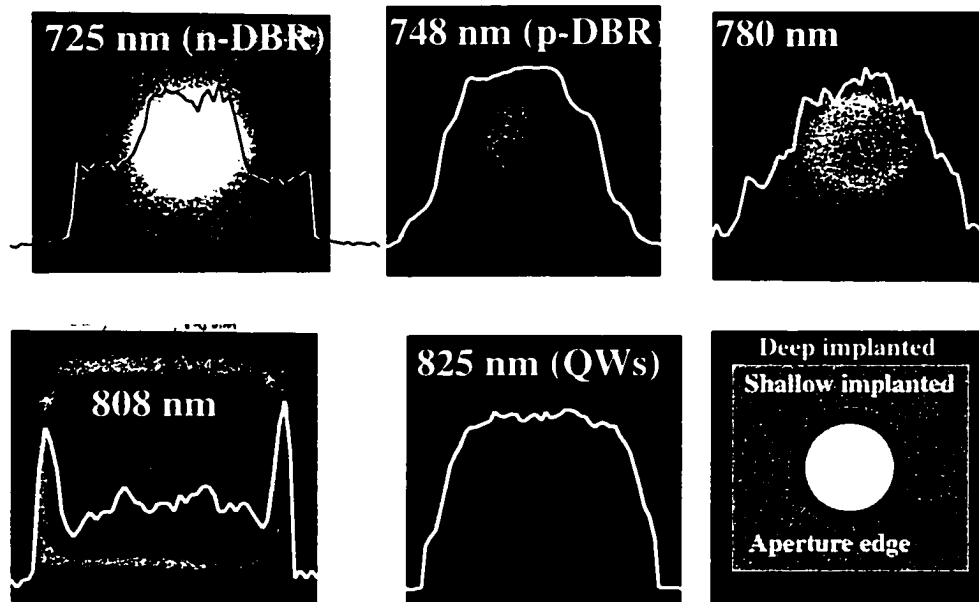


Fig. 3- 13: Monochromatic CL images of deeply degraded plan-view sample. See text for discussion. At bottom right is a scale figure showing the 15 μm aperture, the 20 μm diameter (shallow) current-confining implant, and the 40 μm square defining the (deep) isolation implant.

[26], with photo-annealing as a driving force [27], is causing intermixing between the GaAs QW and the neighboring $\text{Al}_{0.25}\text{Ga}_{0.75}\text{As}$ barrier layers, and thus raising the energy levels slightly in these areas.

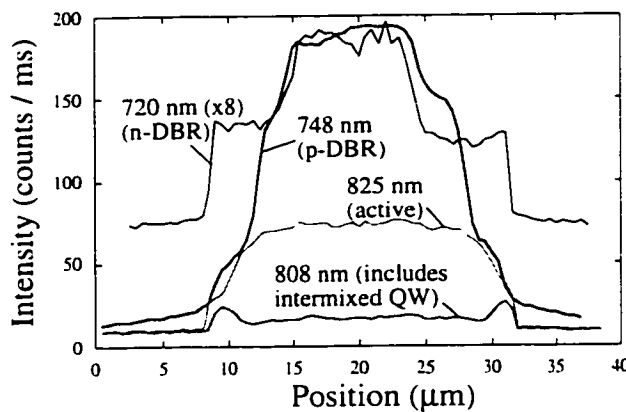


Fig. 3- 14: Plan-view CL linescans of deeply degraded VCSEL G-60. Note the uniform profiles across the center of the device. These linescans were virtually identical, both qualitatively and quantitatively, to line scans from undegraded devices.

Monochromatic images of the device are seen in Fig. 3- 13. To our dismay, no dark central area was observed in the quantum well image at 825 nm, as we would expect from our EL results with a semitransparent contact (Section 3.6.2). In fact, the CL spectra taken in the center of each device were virtually identical, showing no difference between aged and unaged devices. The 825 nm linescan,

which is superimposed on the image, and also shown in Fig. 3- 14, showed no measurable reduction through the center of the device either.

As expected, the image of the n-DBR was uniform. It showed twice the signal in the central area that was observed elsewhere; possibly spectral overlap from the stronger p-DBR luminescence enhanced the central intensity. No DLDs or signs of non-uniform degradation were observed.

The biggest difference seen between aged and unaged devices was observed in the p-DBR (748 nm) images and linescans. Small non-uniformities, of the sort seen in the monochromatic image (Fig. 3- 13), could be observed if extreme contrast settings were used. The amplifiers were set for high contrast in the image shown, with the black level set at ~160 counts or higher, and the white level set to roughly 200 counts. Thus the “dark-line” seen on the right side actually has very little contrast in the sample. An increase in diameter of a few microns (>10%) was observed in the p-DBR images and line scan profiles after aging. This increase at the edges is not surprising, given the annealing of proton implant damage which would be expected at the edges of the current-confinement implant, but which has

not been observable until now, since few have been able to see beneath the p-contact.

The edges of the deep proton implant are observable at 808 nm, as discussed above. The edges of the shallow proton implant are visible at 780 nm; we do not have an explanation for why this wavelength provides contrast for the current confinement implant. No evidence of dislocation growth nucleating from either of the proton implants was observed in any of the aged VCSELs, which would have been evident as dark lines through these rings or boxes.

The lack of evidence for degradation in the active region was initially particularly disturbing in light of the fact that these devices were from the same wafer, and were degraded in a manner identical to those shown in the EL images with the semitransparent contact, which showed a dark central core (Fig. 3- 19). This result cannot simply be written off, since over a dozen devices and several different samples were used to replicate the result, with very consistent results. At this point, we gave more serious consideration to the failure mechanism proposed by Honeywell MICRO SWITCH, which called for failure through current shunting, without any reduction in radiative efficiency from the device layers.

3.6 Electroluminescence imaging of aged VCSELs

The mainstay of failure analysis from VCSELs and LEDs is generally electroluminescence imaging. It is simple, requires no sample preparation, and is non-destructive. By electroluminescence imaging, we mean microscopic imaging of the light emitted from the device when a small (sub-threshold) forward bias is applied currents, which would also sometimes be referred to as “nearfield imaging.” An Olympus “MIRPlan” 80x objective was used for this purpose [28]. It proved to have twice the resolution of the next best objective tested since its design was optimized for infrared rather than visible light. A standard CCD camera and frame grabber were used to acquire the images, giving approximately 4-6 bits of useful resolution. The highly-reflective DBRs above and below the active region of VCSELs, while required for operation, significantly reduce the visibility of dark-line defects and other features. This is well illustrated with examples in Chapter 7. Fortunately, by using standard 10 nm FWHM bandpass filters, we were able to image light escaping from the mirrors’ reflectivity nulls, which gave a far clearer

picture. This is because most of the light (at say, 790 nm) could escape directly from the device, giving a clear image. However, the unfiltered light was peaked at 850 nm, and would take on average 500 passes to escape the 99.8% reflective p-DBR. During the 500 passes, it would be likely to “walk” laterally from one side of the device to the other before leaving the cavity, and the escaping photons would be consistent with the average of the cavity gain in degraded and undegraded areas. The unfiltered image thus is “homogenized”, and often fails to show dark lines and other features which can be clearly observed using filters at the reflectivity nulls. Filtered electroluminescence imaging is discussed in more detail in Appendix G.

3.6.1 EL Imaging without sample preparation

I have never observed dark-line defects in the standard 850 nm Honeywell VCSELs which are the focus of this thesis. (However, DLDs have been observed in nominally identical VCSELs from other sources, as discussed in Chapter 7.) The degradation which is observed appears to be a featureless darkening, which is generally more pronounced along one side than the other. This can be seen in Fig. 3- 15. These VCSELs were aged over thousands of hours at near-normal operating currents (20-30 mA), and high (80-100°C) temperatures by Honeywell MICRO SWITCH.

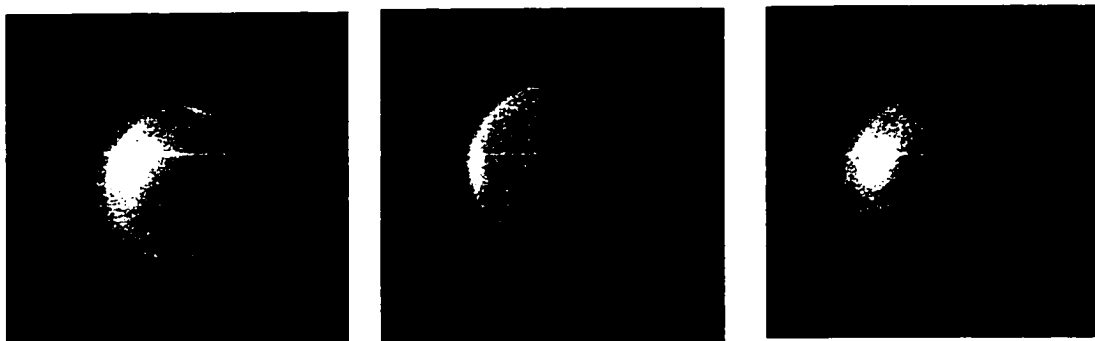


Fig. 3- 15: Filtered electroluminescence images of three different 850 nm VCSELs which were aged over thousands of hours. Images were taken well below threshold, (800 μ A) using a 780 nm bandpass filter.

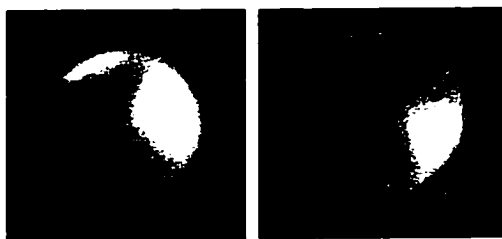


Fig. 3- 16: Filtered EL of two VCSELs from another lot of normally degraded VCSELs showing greater structure to their degradation.

A less-uniform degradation was observed from lasers degraded in a separate batch (Fig. 3- 16); again these were aged at near-normal currents and high temperatures for thousands of hours, and imaged at 780 nm.

3.6.2 Plan-view EL imaging through semi-transparent metals

An obvious limitation of this EL technique is the inability to see what's happening outside the device aperture opening. Given that the degradation appears to be starting outside the aperture, and then traveling inward, this is a serious limitation on our ability to discover where the degradation is originating. Since we showed in the previous chapter that for many stripe lasers, degradation starts at the die edges (or perhaps the deep proton-implant edges in this case) and then travels inward, we would like to be able to see if the dark area were nucleating at a particular region. If it was consistently doing so, identifying the source of dark-area nucleation would be the first step in allowing us to eliminate that degradation source.

We thus prepared several devices for semitransparent contacts by rapidly aging several devices in an array, and then polishing the p-metals off using 0.05 μm alumina grit. A layer of pure In_2O_3 was then deposited by Eric Tarsa. (Indium Tin Oxide, or ITO, which is usually 90% In_2O_3 / 10% SnO_2 , is more common for commercial applications and has lower resistance, but was not used at for this sample because the reactor was being used to study pure epitaxial layers of Indium Oxide. Details of the semi-transparent contact are in Appendix B.) After the In_2O_3 layer was subsequently annealed to increase the oxygen content, filtered electroluminescence measurements were taken (Fig. 3- 17).

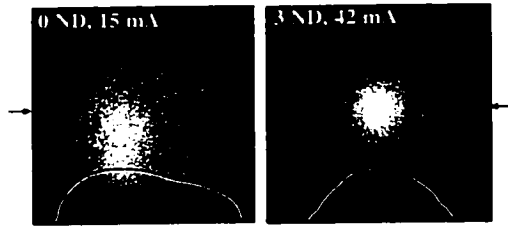


Fig. 3- 17: Electroluminescence images from undegraded VCSELs with semi-transparent In_2O_3 contact. Linescans of intensity versus lateral position (taken through the device center) are shown. The right image is attenuated by three orders of magnitude (3 ND filter); the current shown was divided (perhaps not equally) across the 15 VCSELs in the array, and thus both samples are still below threshold.

As expected, the image from the undegraded samples was a featureless square of nearly $40\ \mu\text{m}$ dimension within the boundaries of the deep proton implant. As higher currents were used, current crowding becomes a factor, and the lateral voltage drop for holes traveling to the edge of the device through the p-DBR layers increases in proportion to the current. This lateral voltage drop reduces the voltage at the edges relative to that in the center. The constriction caused by the $20\ \mu\text{m}$ -diameter current confinement aperture thus is evident in the EL images.

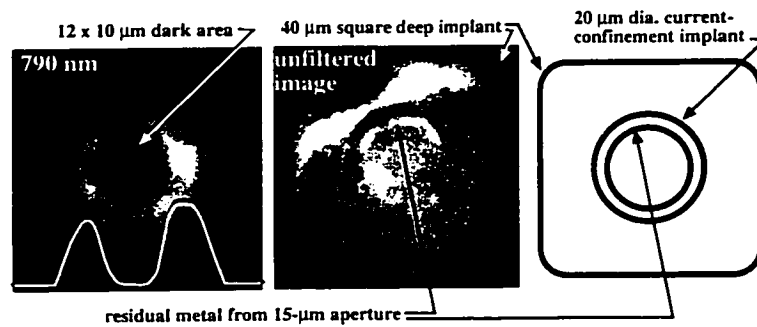


Fig. 3- 18: EL images from a degraded VCSEL with semi-transparent contact. 790 nm image shows dark central area, plus dark ring at top left where p-metal remained. Central image, without filtering, was taken at much lower current, and is thus more uniformly illuminated. Remaining metal is clearly visible. Drawing at right on same scale shows nominal size of implants and aperture.

Due to poor sample preparation and relatively small samples, only a few degraded samples were imaged. Images from one wafer are seen in Fig. 3- 18. As with the standard (opaque-contact) samples, the unfiltered images were all featureless; a 790 nm bandpass filter was useful for obtaining image contrast. A better image was obtained from a second wafer, and is shown in Fig. 3- 19.

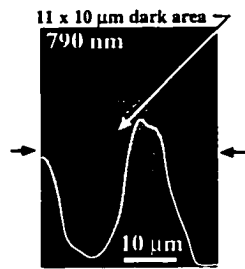


Fig. 3- 19: Filtered EL from a degraded VCSEL with a semi-transparent contact shows a dark central core, with an undegraded periphery. The dark line observed from the upper portion is due to a surface scratch from the sample preparation.

While our conclusions are tentative due to the small number of samples, and the interference from surface scratches, no evidence was available that the dark area is nucleated from proton implant damage at the edge of the deep implant, or from sawing damage at the die edges. The fact the degradation appeared to

preferentially start at one side of the aperture may have been due to the inevitable small mis-alignments between the aperture and the current confinement implant. Presumably, the darkening will be radially symmetric with the implant, and the non-centered aperture will expose brighter and dimmer edges. This hypothesis seems to have been well supported in a systematic study of EL from aged red VCSELs (see chapter 6 for details), where the darkening always came from the same side of the device in every aged device. If there were truly another cause of the darkening being more prominent on one side than the other (such as external nucleation of degradation), we would expect to see darkening coming from different sides of the device.

3.7 C-V and I-V characterization

One weakness of many of the techniques used to characterize degraded lasers is that they are fairly poor at detecting uniform degradation. While virtually all techniques (EL, CL, EBIC, TEM, PL microscopy, etc.) can image dark-line defects, most are incapable of detecting, say, a uniform 20% drop in efficiency due to an increased concentration of non-radiative centers. (In principle, perhaps with special calibration structures and true quantitative data collection methods, this could change; however, the comment holds true for the way the techniques are generally implemented and used only for qualitative information.)

Capacitance-voltage (C-V) and current-voltage (I-V) techniques are measurable to high accuracy, and are both affected by distributed point defects. They have successfully been used to characterize degradation in stripe laser diodes in

the past. While we are not able to draw any conclusions about what the cause of failure is using our C-V or I-V characterization, we were able to rule out causes which are inconsistent with the experimental results. The results are discussed in Appendix H.

3.8 Discussion of degradation mechanisms occurring early in the device lifecycle

We shall discuss below a failure mechanism, initially proposed by Honeywell MICRO SWITCH, which appears to explain our experimental observations far better than conventional stripe-laser models do. To the best of our knowledge, although some aspects of this mechanism have been observed in stripe lasers and LEDs [2], it has never been designated the primary cause of failure in such devices.

3.8.1 The “Current Shunting” or “Dopant Passivation” mechanism of VCSEL degradation.

If we take the evidence of totally-degraded VCSELs from Michael Cheng (Ch. 4), plus the EL results earlier in the chapter (Sect. 3.6.2), and add what's known about degradation in stripe lasers (Ch. 2), we reach the conclusion that by far the most likely explanation of failure is the growth of a dislocation network in the central portion of the VCSEL's active region. This is shown on the left side of Fig. 3- 20. However, when we also consider the CL and EBIC experiments described earlier in this chapter on partially-degraded VCSELs, which show no evidence of dislocation growth, we must seriously consider the alternate failure mechanism on the right side of Fig. 3- 20. The right side shows that the central portion of the p-DBR or the n-DBR becomes passivated as a consequence of device aging. It is very likely that, depending on the background doping near the quantum wells, and the physics of degradation, only one DBR or the other would show strong passivation; however, we do not have sufficient evidence to say which of the DBRs is responsible. This then increases the effective resistance in the device center, which encourages the carriers to follow the lower resistance parallel paths available toward the edges of the device. It is unclear whether this passivation takes place as a result of defect complexes, as discussed in Martins [2], or whether the passivation is due to the migration of the abundant amounts of hydrogen in the device from proton implantation. It does seem to be the case that perhaps the passivation process is

photo-pumped, since patterns are often observed which look suspiciously like the shapes of the modes which were lasing during the aging process.

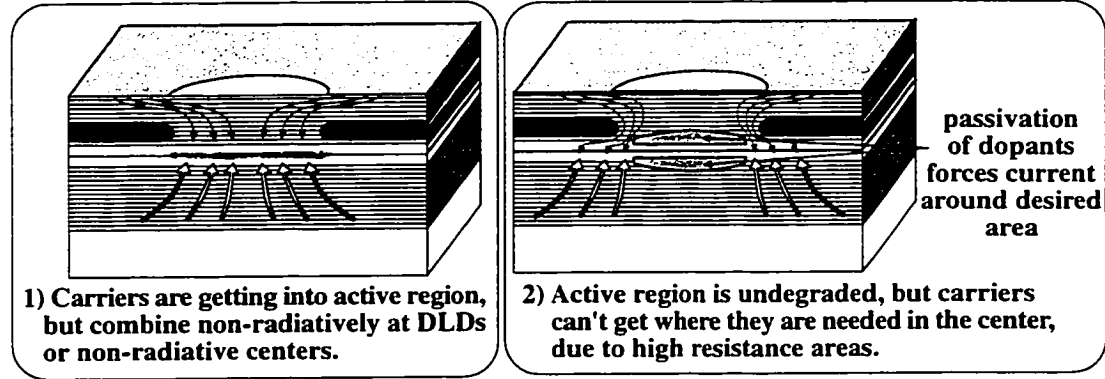


Fig. 3- 20: Two competing models to explain declining EL efficiency in device center. The left model is conventional, but the right model fits the data better.

The “current shunting” model of device failure is consistent with all the observations published in this Chapter. Further, with some critical re-examination of our two key assumptions (see the discussion below), it is consistent with *all* experimental data taken to date.

An explanation of the difference between the working of plan-view cathodoluminescence and transparent-contact electroluminescence results would be valuable at this point. CL is able to *directly* inject carriers into the device uniformly, and largely without regard to the resistance or internal fields encountered under device operation. As such, the uniform luminescence observed in CL and the uniform current collection by EBIC is an indication that dislocations or non-radiative centers do *not* exist in the active region of rapidly-degraded devices, and are not strongly evident in other layers. By contrast, EL is dependent not only on the radiative efficiency of the active region, but also on the availability of a current-delivery mechanism. Since current can't get the center of the (undegraded) active region in EL, it appears dark. Thus, the “current-shunting” model is able to explain both the non-uniform EL and the uniform CL images.

Future work should first attempt to *directly* verify current shunting, and show a reduction in the fraction of activated dopants — our present evidence is *indirect*, since it only shows that the device has degraded without any evidence of dislocations or non-radiative centers. As we shall discuss in Chapter 9, a variety of

different techniques (such as scanning capacitance microscopy, or "SCM") exist for taking two-dimensional doping profiles. However, this requires either cleaving or cross-sectioning the device, where the cross sectioning requirements may be far stricter than those for our previous samples, given the extremely surface-sensitive nature of SCM. Once dopant passivation had been verified in aged devices, other aged devices could be annealed before cleaving. This would drive off excess hydrogen, presumably without affecting defect complexes which form with dopants, and allow us to find which one of the two explanations is more likely.

3.8.2 Additional support for "current-shunting" failure mechanism from Honeywell MICRO SWITCH

We are not the first to postulate the failure mechanism discussed in this section: credit for that goes to scientists at Honeywell MICRO SWITCH, particularly James Guenter, Robert Biard, and Ralph Johnson. Two major pieces of evidence drove them to this conclusion: first, the quantum efficiency of the device at very low drive levels remains unchanged after degradation.

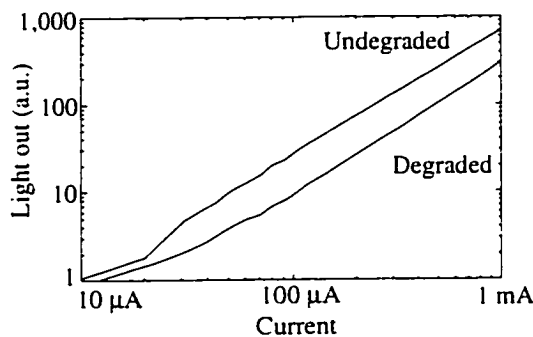


Fig. 3- 21: Low-current L-I curve of a VCSEL before and after degradation shows a ~3x drop in light out at 100 μ A, but little change at 10 μ A.

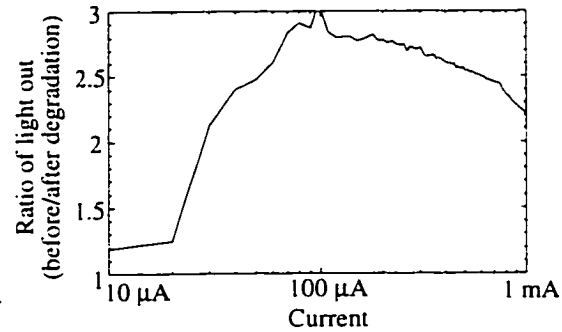


Fig. 3- 22: Ratio of light out before / after degradation, versus current. The fact there isn't a significant drop at low currents after aging is taken as evidence that the active region has not degraded.

Light versus voltage (L-V) characteristics below 1.4 V, and light versus current (L-I) characteristics below 100 μ A do not change much after aging, as we see in Fig. 3- 21. We can also compare the ratio of the light out before and after aging (Fig. 3- 22), where we are able to see that at very low currents the efficiency is almost unchanged. When true degradation takes place inside the active region, such as the creation of non-radiative centers, or dark-line defects, the active region efficiency would be expected to drop across the full range of operation.

The second observation supporting a different failure mechanism comes from careful analysis of the subthreshold L-V and I-V characteristics above the aforementioned drive levels, yet below threshold. Normally, radiative recombination in an ideal device should increase in current as $I(V)=I_0\exp(qV/kT)$ (i.e., 1 decade per 60 mV increase), as we discuss in Appendix H. However, at currents below this ideal regime, non-radiative current, of the sort expected at the deep-implant edges, increases more slowly: $I(V)=I_0\exp(qV/2kT)$ (i.e., 1 decade per 120 mV). The total current can be analyzed as the sum of radiative and non-radiative components [7, 29]. In undegraded devices of various sizes, the non-radiative current scales as the length of the deep-implant perimeter, while the radiative current scales as the area of the device, further supporting this interpretation. An analysis of aged devices suggests that current is being shunted off to the non-radiative deep-implant edges, and that the effective device area has been reduced after aging. The proposed change is an increase in the resistance of the p-DBR in its center, which then causes the current to flow through the lower-resistance parallel paths around the device center.

3.8.3 Assumptions about the nature of degradation revisited.

Earlier, we discussed two key assumptions we had made, the first being that degrading a device over a period of minutes or hours would cause degradation by the same failure mechanism that the device would experience under actual operation. This assumption has been widely used in experiments in the past, and is generally valid, providing a single, dominant failure mechanism is present. However, where multiple failure mechanisms are present (and we have certainly found many even in single devices), then the assumption must be called into question. Given that the different accelerating factors (including current density, carrier concentrations, temperature, and optical pumping density) will not all increase in lockstep with one another, it is not reasonable that the same acceleration factor can be achieved for each of the multiple failure mechanisms. Thus, *any* acceleration will not accurately display the true case in a device normally operated. However, given that acceleration of some sort *must* be used to obtain failures in a timely fashion, there is a strong argument that lower acceleration factors will more closely show what the true nature of degradation will be. Given the observation that currents in excess of

30 mA no longer degrade devices at the rates predicted by the published Arrhenius plots [30], using currents at or below 30 mA (along with thermal acceleration) is probably wise. However, as stated earlier, we did not have a burn-in station capable of aging arrays under high-temperature conditions. A few experiments were done with degradation overnight on a hot plate with 20-30 mA and 150 °C⁺ surface temperatures (as opposed to our very-high-current aging at 25°C ambient). These experiments produced virtually the same results (i.e., no degradation observed by CL) as the results seen by high-current aging, as we shall discuss. Note that in many cases (such as those devices show in Chapters 7 and 8), a single failure mechanism related to DLD growth in the active region appears to be responsible for device degradation; in such cases high acceleration rates appear to be justified.

To be more specific about the acceleration mechanisms which are important to device aging, the optical pumping, which is believed to be a key factor in p-DBR degradation, at first becomes more prominent as current is increased above 30 mA, (as discussed in Chapter 5). However, at biases above 60 mA (almost always used for rapid aging) the extremely high internal temperatures reduce the spontaneous emission efficiency, and non-radiative recombination in the active region takes its place. This provides more thermal acceleration relative to the optical pumping mechanism.

The second key assumption we made was that by studying totally degraded devices, we could discover the cause of degradation for partially-degraded devices which have just passed the “2 dB power drop” [31] failure criterion.

This second assumption was invoked by Michael Cheng after performing a number of “negative” experiments, where no difference could be seen between degraded and undegraded devices. The first cross-sectional cathodoluminescence data run was on an array of 4 aged devices: only one of the four showed any sign of aging; the others all appeared identical to the unaged devices. The first few VCSELs which were examined by TEM were degraded to where peak power dropped by 50–70%: all of them appeared totally undegraded in TEM examination. Other mechanisms for device failure not requiring non-radiative centers (such as those proposed in this chapter), had not been postulated at the time. Thus it was believed that possibly the reason no dislocations were observed was that their density was

insufficient, or that we'd been "unlucky" in not capturing any dislocations in our thin TEM foil. By studying a totally degraded VCSEL with a high density of dislocations, this probability could be reduced. However, our subsequent work, and those of others, make it appear possible that the dislocation propagation only starts well after the device has already passed its failure criterion. In retrospect, Cheng's consistent failure to find any physical evidence of degradation in partially-degraded devices he studied is consistent with the findings of this chapter, and was probably not simply an unlucky accident.

3.8.3.1 Analysis of top-emitting CL results

The best method for studying how aging conditions affect the dislocation growth in the p-DBRs is the top-emitting CL on unprepared samples (Section 3.5.2). We start with a summary of the results in Fig. 3- 23, which encapsulates the results presented earlier in section 3.5.2.

Device	Aging time	Aging current	Ambient aging temperature	Increase in threshold current	Change in top-emitting p-DBR CL efficiency	Resolvable DLDs in p-DBR?
602 C-V2	1 min	100 mA	20 °C	4x	+15%	no
602 C-R2	23 h	23 mA	125°C	2.5x	-10%	yes, barely, in line scan
469 #2	2,000 h	10 mA	125°C	4x	-83%	? (no line scan made)
469 #3	3,000 h	10 mA	125°C	non-lasing	-94%	yes, clearly resolvable

Fig. 3- 23: Summary of results from the top-emitting CL experiments performed on VCSELs aged at various conditions.

Extent	Partial degradation (2-3 x increase in threshold)	Total degradation (no longer lases)
Aging Condition		
Near-normal current (2,000 h+)	"Current Shunting" believed to be primary failure mechanism. Dislocations also observed.	Extensive dislocation growth observed.
Extreme Current (2 min - 24h)	"Current-Shunting" only. No dislocation growth (my primary focus)	"Current Shunting" and traditional degradation (Michael Cheng's work)

Fig. 3- 24: How aging conditions affect VCSEL degradation.

We arrange the findings of Fig. 3- 23 in Fig. 3- 24, along two axes. The y-axis is the acceleration factor used. In the highly-accelerated conditions we used, it appears that the current shunting was accelerated more rapidly than dislocation growth in the p-DBRs. As the acceleration factor is slightly lowered (overnight degradation for C-R2 vs. 1 minute degradation for C-V2 in Fig.

3- 23), we start to see some sign of dislocations. As the acceleration factor is lowered substantially further (thousands of hours, or >100 days), we observe a significant (>80%) drop in CL efficiency. After seeing the difference between rapidly- and gradually-aged devices, it would obviously be preferable to simply study gradually-aged devices. However, at this writing, all such devices are single die, which cannot be used in most of the experiments described. If arrays of closely-spaced devices were aged, as discussed in Chapter 9, this limitation could be overcome in future work.

The other axis of Fig. 3- 24 addresses how deeply devices are degraded before examining them. It seems evident that totally aging devices until they put out no more light increases the importance of DLD growth relative to that of current-shunting. This seems consistent with the aging process described by Martins et al. [2], whereby the passivated region of the cladding layers grows until it encompasses the active region, at which point DLD growth in the active region begins. Thus DLD growth only starts fairly late in the degradation process, and may not be the true cause of device failure. In the next chapter, we will discuss these findings of dark-line defect growth in detail. Even where they do not reflect the true failure mechanism, they give us important information about the "weak points" of the device which we should examine in order to improve VCSEL reliability.

References for Chapter 3:

- [1] E. C. Madhava-Menon, P. M. Petroff, and R. G. Waters, "Degradation kinetics of GaAs quantum well lasers," *Applied Physics Letters*, vol. 54, pp. 2683-5, 1989.
- [2] R. B. Martins, P. Henoc, B. Akamatsu, and J. F. Palmier, "A model for the degradation of Ga(Al)As single-quantum-well lasers," *Journal of Applied Physics*, vol. 70, pp. 554-61, 1991.
- [3] K. Kondo, O. Ueda, S. Isozumi, S. Yamakoshi, K. Akita, and T. Kotani, "Positive feedback model of defect formation in gradually degraded GaAlAs light emitting devices," *IEEE Transactions on Electron Devices*, vol. ED-30, pp. 321-326, 1983.
- [4] D. V. Lang, "Deep-level transient spectroscopy: a new method to characterize traps in semiconductors," *Journal of Applied Physics*, vol. 45, pp. 3023-32, 1974.
- [5] J. Zhou, Q. Zhan, Z. Fu, D. Lü, L. Guan, and H. Chen, "Behavior of types A and B hole traps in n-type GaAs during long-period operation," *Solid-State Electronics*, vol. 35, pp. 1325-1329, 1992.
- [6] T. Uji, T. Suzuki, and T. Kamejima, "Deep-level changes in (Al,Ga)As double-heterostructure lasers degraded during accelerated aging at high temperatures," *Applied Physics Letters*, vol. 36, pp. 655-657, 1980.

- [7] T. V. Torchinskaya, A. A. Shmatov, and M. K. Sheinkman, "Recombination-enhanced transformation of deep centers in red light-emitting AlGaAs diodes," *Physica Status Solidi (A)*, vol. 110, pp. 213-220, 1988.
- [8] M. M. Sobolev, A. V. Aittsovich, S. G. Konnikov, I. V. Kochnew, and B. S. Yavich, "Deep level defects detection in degrading GaAs/AlGaAs quantum well laser," *Material Science Forum*, vol. 143-147, pp. 1547-1552, 1994.
- [9] B. Le Thanh and K. Zdansky, "Investigation of degradation processes in AlGaAs/GaAs light emitting diodes," *Physica Status Solidi A*, vol. 123, pp. 493-500, 1991.
- [10] D. V. Lang, P. M. Petroff, R. A. Logan, and W. D. Johnston, Jr., "Recombination-enhanced interactions between point defects and dislocation climb in semiconductors," *Physical Review Letters*, vol. 42, pp. 1353-6, 1979.
- [11] M. K. Hibbs-Brenner, R. P. Schneider, Jr., R. A. Morgan, R. A. Walterson, J. A. Lehman, E. L. Kalweit, J. A. Lott, K. L. Lear, K. D. Choquette, and H. Juergensen, "Metalorganic vapour-phase epitaxial growth of red and infrared vertical-cavity surface-emitting laser diodes," *Microelectronics Journal*, vol. 25, pp. 747-55, 1994.
- [12] M. K. Hibbs-Brenner, R. A. Morgan, R. A. Walterson, J. A. Lehman, E. L. Kalweit, S. Bounnak, T. Marta, and R. Gieske, "Performance, uniformity, and yield of 850-nm VCSELs deposited by MOVPE," *IEEE Photonics Technology Letters*, vol. 8, pp. 7-9, 1996.
- [13] R. A. Morgan, M. K. Hibbs-Brenner, T. M. Marta, R. A. Walterson, S. Bounnak, E. L. Kalweit, and J. A. Lehman, "200 degrees C, 96-nm wavelength range, continuous-wave lasing from unbonded GaAs MOVPE-grown vertical cavity surface-emitting lasers," *IEEE Photonics Technology Letters*, vol. 7, pp. 441-3, 1995.
- [14] G. H. Olsen and M. Ettenberg, "Universal stain/etchant for interfaces in III-V compounds," *Journal of Applied Physics*, vol. 45, pp. 5112-5114, 1974.
- [15] R. A. Morgan, M. K. Hibbs-Brenner, R. A. Walterson, J. A. Lehman, T. M. Marta, S. Bounnak, E. L. Kalweit, T. Akinwande, and J. C. Nohava, "Producible GaAs-based MOVPE-grown vertical-cavity top-surface emitting lasers with record performance," *Electronics Letters*, vol. 31, pp. 462-4, 1995.
- [16] "Honeywell Micro Switch Offers VCSELs as Catalog Items," in *Compound Semiconductor*, vol. 2, 1996, pp. 12.
- [17] J. M. Catchmark, R. A. Morgan, K. Kojima, R. E. Leibenguth, M. T. Asom, G. D. Guth, M. W. Focht, L. C. Luther, G. P. Przybylek, T. Mullally, and D. N. Christodoulides, "Extended temperature and wavelength performance of vertical cavity top surface emitting lasers," *Applied Physics Letters*, vol. 63, pp. 3122-4, 1993.
- [18] Applications Note entitled "Reliability of Honeywell 850 nm VCSEL," by Robert Hawthorne, III, dated March 1997
- [19] R. Ito, H. Nakashima, S. Kishino, and O. Nakada, "Degradation sources in GaAs-AlGaAs double-heterostructure lasers," *IEEE Journal of Quantum Electronics*, vol. QE-11, pp. 551-556, 1975.
- [20] K. Bohm and B. Fischer, "Photoluminescence at dislocations in GaAs and InP," *Journal of Applied Physics*, vol. 50, pp. 5453-60, 1979.
- [21] I. J. Fritz, P. L. Gourley, L. R. Dawson, and J. E. Schirber, "Electrical and optical studies of dislocation filtering in InGaAs/GaAs strained-layer superlattices," *Applied Physics Letters*, vol. 53, pp. 1098-100, 1988.
- [22] S. Adachi, "Optical Properties of AlGaAs," in *Properties of Aluminum Gallium Arsenide*, S. Adachi, Ed. Stevenage, UK: IEE / INSPEC, 1991, pp. 118-140.

- [23] Y. M. Cheng, R. W. Herrick, P. M. Petroff, M. K. Hibbs-Brenner, and R. A. Morgan, "Degradation mechanisms of vertical cavity surface emitting lasers," *34th Annual Proceedings of International Reliability Physics Symposium*, pp. 211-13, 1996.
- [24] R. W. Herrick, Y. M. Cheng, J. M. Beck, P. M. Petroff, J. W. Scott, M. G. Peters, G. D. Robinson, L. A. Coldren, R. A. Morgan, and M. K. Hibbs-Brenner, "Analysis of VCSEL degradation modes," *Proc. of the SPIE (Fabrication, Testing, and Reliability of Semiconductor Lasers)*, vol. 2683, pp. 123-33, 1996.
- [25] Y. M. Cheng, R. W. Herrick, P. M. Petroff, M. K. Hibbs-Brenner, and R. A. Morgan, "Degradation studies of proton-implanted vertical cavity surface emitting lasers," *Applied Physics Letters*, vol. 67, pp. 1648-50, 1995.
- [26] G. F. Redinbo, H. G. Craighead, and J. M. Hong, "Proton implantation intermixing of GaAs / AlGaAs quantum wells," *Journal of Applied Physics*, vol. 74, pp. 3099-3102, 1993.
- [27] K. McIlvaney, A. McKee, A. C. Bryce, and J. H. March, "Feasibility of monolithic device integration in GaInP/AlGaInP using photoabsorption induced disordering," *Proc. Integ. Photonics Research 1996*, vol. 6, pp. 232-234, 1996.
- [28] Olympus LM594I 80x MS plan ULWD objective was purchased from the Scientific Instrument Company, 5855 Uplander Way, Culver City, CA 90230, (310) 568-9188
- [29] R. F. Pierret, "Section 6.2: Deviations from the ideal," in *Semiconductor Device Fundamentals*. Reading, MA: Addison-Wesley, 1996, pp. 260-281.
- [30] Personal Communication with James Guenter of Honeywell MICRO-SWITCH
- [31] J. K. Guenter, R. A. Hawthorne, D. N. Granville, M. K. Hibbs-Brenner, and R. A. Morgan, "Reliability of proton-implanted VCSELs for data communications," *Proc. of SPIE (Fabrication, Testing, and Reliability of Semiconductor Lasers)*, vol. 2683, pp. 102-13, 1996.

Chapter 4: Late stages of degradation in proton-implanted VCSELs: dislocation growth

In the previous chapter, we discussed what appears to be the primary degradation mechanism for proton-implanted devices, namely the “current shunting” mechanism based on dopant passivation. In this chapter we discuss a number of additional failure mechanisms observed in proton-implanted devices. Among these mechanisms is the surprising observation of degradation in the p-DBR: degradation beyond the immediate vicinity of the active region is not generally observed in traditional stripe lasers. We are confident that the other mechanisms discussed in this chapter are not the cause of failure for partially-degraded VCSELs aged under extreme currents. However, these mechanisms appear to be more important for devices aged under normal conditions, as was discussed earlier in Section 3.8.3. Further, the data in this chapter tell us a great deal about the inner workings of VCSELs, and point out where operating stresses are concentrated. This information should be useful to device designers looking to improve VCSELs in the future. The discussion in this chapter relies heavily on work done by my co-worker at UCSB: Dr. Michael Cheng. I appreciate his permission to reproduce much of his data in this chapter; I have cited the original source in each of the images or spectra.

4.1 Degradation in the active region

We start this chapter with a brief discussion of degradation in the active region. Such degradation is the primary cause of failure for stripe lasers, and was expected to be the primary cause of VCSEL failure before our experimental work was begun. Presumably, if some of the other failure mechanisms mentioned in Chapter 3 and 4 were eliminated, active region degradation would remain as the limiting failure mechanism.

Early double-heterostructure (DH) stripe lasers used proton-implantation for current confinement. Deep proton implantation was known to be a cause of reliability problems. This has also been observed by Wenbin Jiang of Motorola, who has seen that VCSELs with excessively deep current-confining implants have very short lifetimes (<500 h), while normally-implanted devices have long lifetimes ($>10^5$ h) [1].

A JEOL 2000FX operating at 200 kV was used to image the degraded VCSELs. $\langle 220 \rangle$ strong-beam dark field conditions were used for imaging dislocations. Inspection of transparent regions outside the lasing area showed no dislocations, and helped to rule out the possibility of dislocations generated by sample preparation techniques. In addition, no dislocations were detected in similarly-prepared undegraded VCSELs. The sample preparation and capabilities of TEM will be discussed in greater detail in section 4.3.

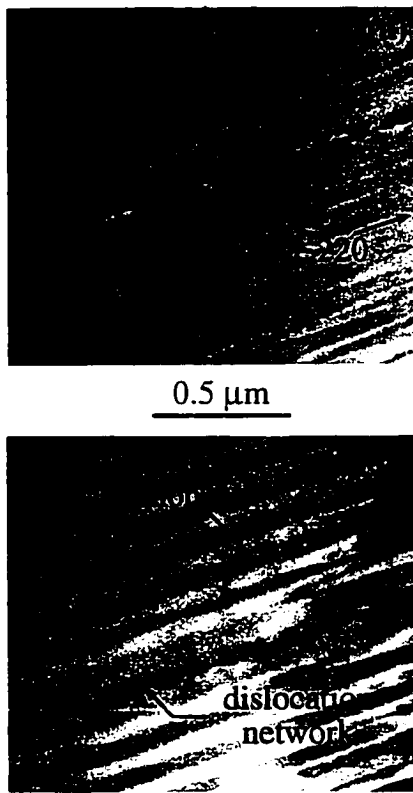


Fig. 4 - 1: TEM images of totally degraded VCSEL cross-section. a): Near edge of current-confinement implant, dislocation network is sparse. b): Near center of device, dislocations are dense. Glide dislocation appears to have penetrated active region, and may have nucleated the dislocation network (After Cheng et al., ref. [2]).

As we can see in Fig. 4 - 1, no such dislocation nucleation is observed near our proton implants. This is not surprising, given that the stain-etch images shown in Fig. 3 show that the peak of the implant is not much deeper than half-way down in the mirror stack (i.e., at least 1 μm above the quantum wells).

The dislocation network is most dense near the center of the device, where current, heat, and photon density are all the highest. It is worth re-iterating that the photos shown in Fig. 4 - 1 were of a *totally* degraded VCSEL; partially-degraded VCSELs showed no dislocations in any layer of the device. This is consistent with the observation offered in the previous chapter that dislocation growth only takes place late in the aging process.

It appears that one of the glide dislocations has traveled from the p-DBR down into the active region in Fig. 4 - 1b. The start and end of the dislocation are not visible, presumably since the dislocation was not perfectly oriented in the plane of the sample ($<0.1 \mu\text{m}$ thick). The glide dislocations may have nucleated the dislocation network in the active region

[3].

4.1.1 strategies for reducing degradation in active region

Many of the strategies appropriate for improving the reliability of the active region were discussed earlier in Chapter 2, and are equally appropriate for stripe lasers and for VCSELs. The most important step that can be taken to reduce degradation in the active region is to optimize growth conditions, to produce optimized stoichiometry. Controlling the precise doping profile in the confinement layers also appears to be important given the possible formation of a “virtual anode” in the immediate vicinity of the active region [4]. Strained quantum well epitaxy can provide an active region immune to dislocation climb [5]. The current-confining implant needs to stay shallow enough to avoid nucleating damage in the active region [1]. Finally, since DLDs may be nucleated by dislocations from the p-DBR, controlling the degradation in the mirrors, as discussed in the following section, may also be important.

4.2 Non-localized observations of degradation by cathodoluminescence

4.2.1 Cross-sectional CL of rapidly degraded devices.

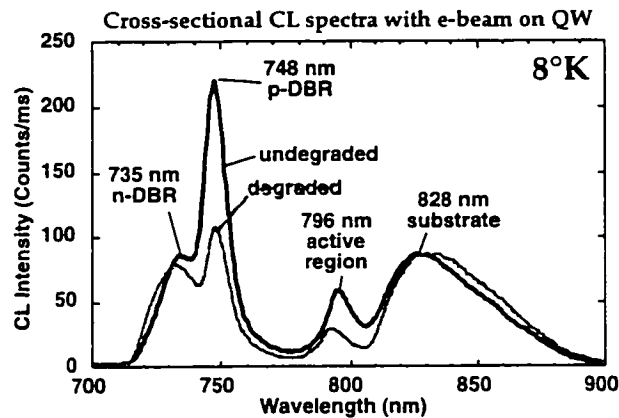


Fig. 4 - 2: Cross-sectional CL spectra of degraded and undegraded VCSELs (after Cheng et al., ref. [6]).

Our earliest work used VCSEL samples which were rapidly degraded at currents well past the roll-over point ($T_j \sim 200^\circ\text{C}$) for on the order of one hour, until their peak output power had dropped by at least 50%, and their lasing threshold had doubled. However, as we shall show in the following chapter, the same degradation phenomena we

observed in the rapidly-degraded samples are also observed in VCSELs degraded over thousands of hours at normal operating currents by Honeywell's MICRO SWITCH division.

These rapidly degraded arrays were either cleaved or polished to allow inspection of their cross sections. Their spectra were taken, allowing identification of four distinct peaks: the n-DBR (735 nm), the p-DBR (748 nm), the active region (796 nm), and the substrate (828 nm), as shown in Fig. 4 - 2 [6]. Basic data on the spectral properties of AlGaAs, and the spectral shifts related to doping, are contained in Appendix F.

Subsequent data studying cross-sectional spectra from undegraded arrays proved that the data from the cross-sectional spectra must be interpreted with some caution. Generally, the beam was focused into a tight raster pattern while the spectrum was being collected, and concentrated as near to the active region as possible. However, since these samples were not stain-etched, the exact location of the active region was not clear as the data was being collected, and the box could easily be centered a half-micron too high or too low, which would significantly change the results. In addition, differences in the exact cleaving or polishing plane, had dramatic effect on the signal collected from the p-DBR (but less from the active region). (See Appendix E for details.) Thus, quantitative comparison of spectra is probably unwarranted (i.e., "...luminescence from the p-DBR drops by exactly 50%"), and the nature of both the sample and equipment do not lend themselves to quantitative comparison.

By then tuning the spectrometer to each of the spectral peaks, we were able to form monochromatic CL images of the different device components. When examining undegraded VCSELs, we were able to see what areas had been proton-implanted, as the implant damage eliminated cathodoluminescence in those areas by providing efficient recombination centers. The unimplanted areas showed uniform luminescence as expected.

The degraded VCSEL cross sections, however, showed a surprising result. The p-DBR, which had not been expected to participate in the degradation process, showed evidence of dark areas in the monochromatic CL image. In addition, as expected, the active region showed reduced luminescence in the central region where current density was highest. No degradation was observed in the n-DBR. The monochromatic images are shown in Fig. 4 - 3 [6, 7].

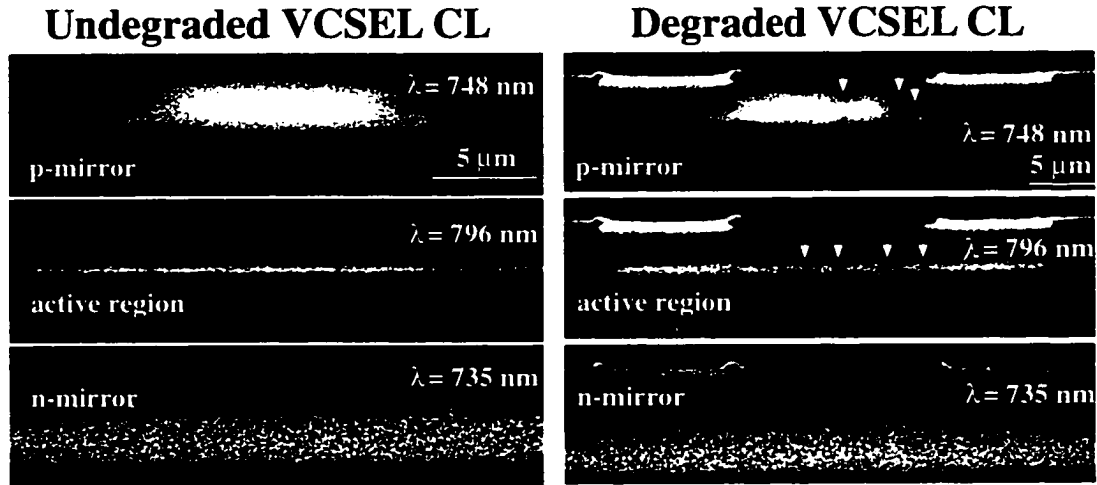


Fig. 4 - 3: Monochromatic images from undegraded VCSEL (left, after Cheng et al., ref. [6]) and rapidly degraded VCSEL (right, after Cheng et al., ref. [7]). The right images are a double exposure of the SEM image (showing the p-contact metallization) and the CL image. The arrows point out degraded regions in the aged device.

The discovery of p-DBR degradation led us to an intensive investigation to uncover the driving mechanism responsible. The mechanism, and the proposed solution, are discussed in greater detail in Chapter 5.

4.2.2 Cross-sectional CL of normally-degraded devices

Due to concerns about the difference between rapid degradation and the true degradation which would be expected under normal operating conditions, I prepared VCSELs which were degraded by Honeywell Micro-Switch for ~6,000 hours at 20 mA and 80 °C. Such devices were prepared by bonding a small glass cover-slip to the top of the die, and then encapsulating the die and header in epoxy. The die and header were then cross-sectioned using the standard polishing procedure discussed in Appendix B. Two devices were examined: a partially-degraded device with a threshold which had more than doubled to ~8.5 mA, and a totally-degraded device which no longer lased.

The spectra are shown in Fig. 4 - 4. The differences in the heights of the p-DBR peaks at 745 nm, and the shape of the substrate peak at 825 nm, are not thought to be significant, given the potential sources of experimental error discussed above and in Appendix E. However, the difference between the n-DBR peaks at 725 nm is so large as to be worth examination. In TEM, small clusters or

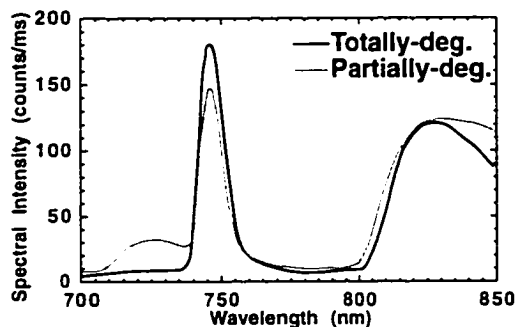


Fig. 4 - 4: CL spectra from normally-degraded VCSELs.

precipitates were observed in the n-DBRs of aged devices, where the current was the most concentrated. However, no reduction in the brightness of this central area could be observed in monochromatic CL imaging at 725–735 nm. Further work is needed in this area; specially-prepared plan-view samples with the p-DBR removed would be one avenue of investigation.

The monochromatic images of the partially- and totally-degraded devices can be seen in Fig. 4 - 5 and Fig. 4 - 6. A gradual fall-off of intensity toward the left

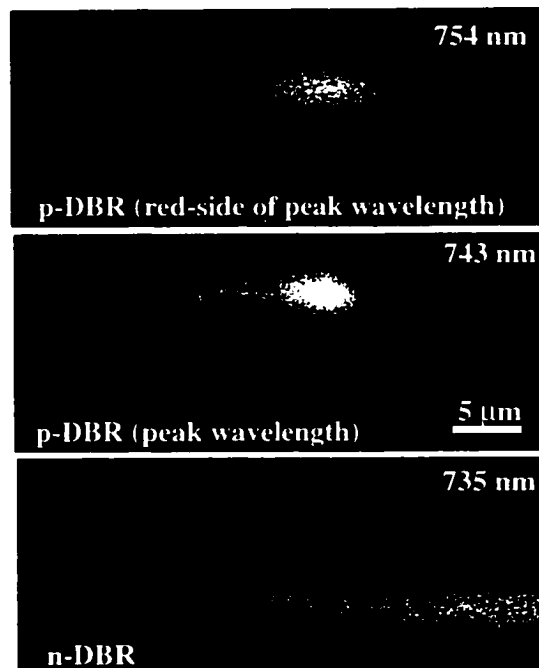


Fig. 4 - 5: Monochromatic CL images of a partially-degraded VCSEL which was aged at near-normal currents.

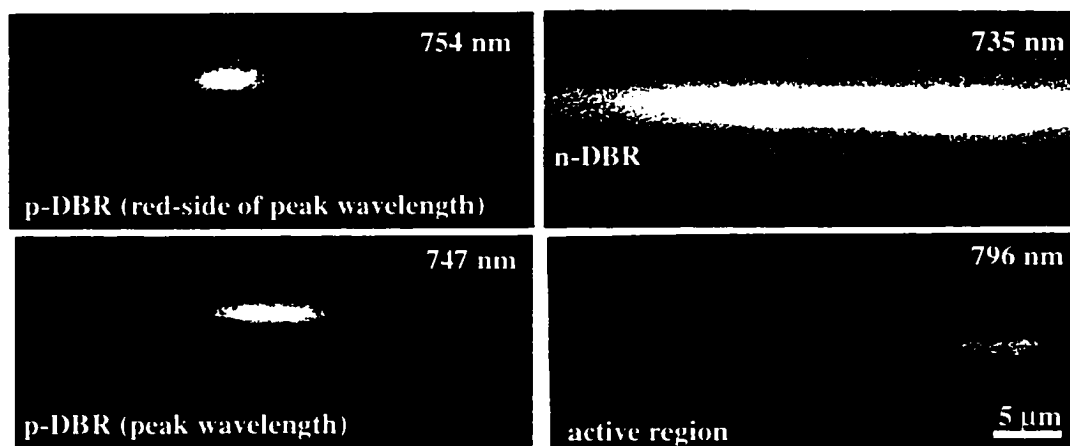


Fig. 4 - 6: Monochromatic CL images of a totally-degraded VCSEL which was aged at near-normal currents.

can be observed in the 735 nm n-DBR images, due to a problem with CL mirror alignment which existed at the time. Non-uniform p-DBR emission can be observed in both devices. In the totally-degraded device, darkening in the center of the active region was observed, consistent with the TEM and CL observations discussed earlier in this chapter. Unfortunately, due to sample charging problems, we were not able to image the active region of the partially-degraded device.

4.3 Analysis of TEM images of degraded devices

4.3.1 General notes on TEM and cross-sectional sample preparation.

Transmission electron microscopy (TEM) is alone among the techniques we used in that it is capable of atomic resolution with well-prepared samples. It can detect individual dislocations, precipitate clusters, microloops, and interface roughness. It is the only technique we used which can show the details of where the dislocations start and where they end — other techniques merely show the general areas affected. Further, unlike other techniques, it is able to identify what the defect type is (i.e., glide or climb dislocations).

TEM has its shortcomings, like all techniques. The sample preparation for VCSELs is nearly impossible, and so the investment per sample is enormous. Thus, conclusions drawn from TEM results usually are based on a couple of “lucky samples.” The TEM is notoriously difficult to learn to use. While CL can identify implanted areas (where luminescence is reduced due to disruption of the lattice) TEM sees only the coherent defect structures (e.g., microloops and dislocations), and is unable to see the proton implant or high trap concentrations, for example. And TEM tells you little or nothing about the internal workings of the device in a dynamic sense (e.g., carrier concentration, resistance or doping profiles, current flow paths, etc.) TEM is merely a structural snapshot at a single point in time — because it is destructive you can’t use it to watch dislocation growth like you can with electroluminescence.

After aging at extreme currents until total device failure, a glass cover slip was bonded on top of the array to protect the top edge of the VCSEL, and the array

was polished down to the middle of the emission openings using a tripod polisher using standard cross-sectioning techniques [8]. The opposite side of the array was dimpled until it was approximately 15 μm thick. The dimpled side of the sample was finally ion milled to electron transparency. Further details of the aging and sample preparation are discussed in detail in Appendix B.

4.3.2 Dislocations at inverted interfaces

4.3.2.1 TEM images of interface dislocations

A TEM image of a cross sectioned device is shown in Fig. 4 - 7. Twin-beam imaging (using the $\langle 220 \rangle$ diffraction vector) was again used to maximize dislocation contrast.

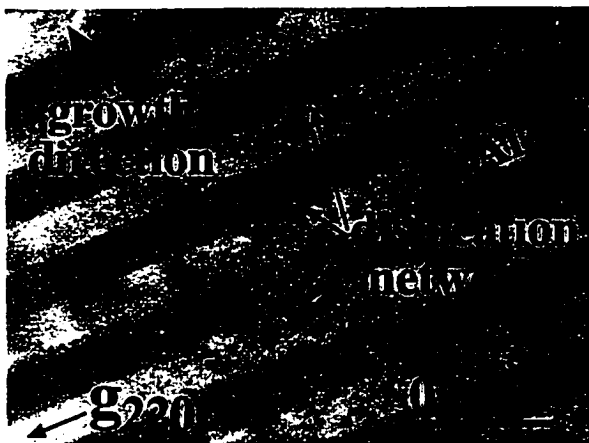


Fig. 4 - 7: TEM Image of climb dislocation networks localized to the inverted interfaces (After Cheng et al., Ref. [7]).

Dislocations can be seen at the "inverted interfaces" where the aluminum fraction is reduced from 100% (pure AlAs) to 16% ($\text{Al}_{16}\text{Ga}_{84}\text{As}$). No defects were observed in the DBR layers themselves, or in the "upstep" where the aluminum fraction is increased. These dislocations were observed about a micron below the device surface, and near the edge of the aperture, where current flow would

be expected to be highest. Weak beam imaging confirmed that the dislocation networks (as well as those shown in Fig. 4) were not single dislocations or dissociated pairs with stacking faults.

4.3.2.2 SIMS data on dopant and impurity trapping at inverted interfaces

One possible explanation for the defects only being present at the inverted interface (i.e., the Al "downstep") is that oxygen or other impurities are getterred by the reactive AlAs layer, floating on its surface during growth. As the aluminum mole fraction is reduced, such impurities end up being incorporated into the graded

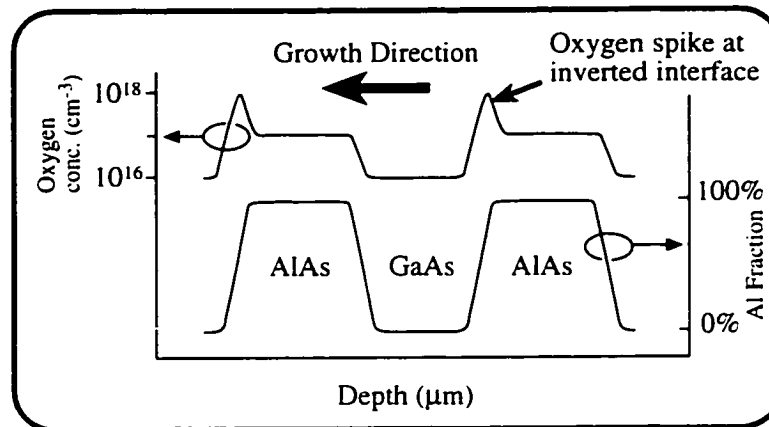


Fig. 4 - 8: SIMS profile of superlattice, showing increased oxygen incorporation in the bulk of the layers, and oxygen "spikes" at the inverted interfaces (After Achtnich et al., ref. [9]).

layer. This oxygen incorporation at the inverted interfaces has been well-documented in studies of MBE growth using SIMS [9, 10], and is shown in Fig. 4 - 8. However, for MOCVD or LPE growth (the technique used to grow the wafers being studied), we have only been able to find a single analogous SIMS study; it did *not* show the high oxygen incorporation at the interfaces seen in MBE [9]. Presumably the hydrogen present in LPE and MOCVD helps to reduce oxygen which would otherwise be present in the growth chamber. Dopant spikes can also be observed at the inverted interfaces (including in MOCVD samples), and may contribute to degradation as well.

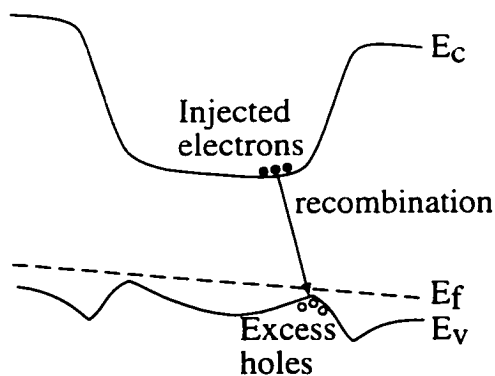


Fig. 4 - 9: Band diagram of VCSEL p-DBR shows charge being trapped preferentially at an interface, thus resulting in localized dislocation growth.

The other explanation for dislocation networks which are localized to the inverted interface would be due to carrier recombination being localized at that interface due to band-bending. Under bias, the band bending would be asymmetric, and would trap charge preferentially at one interface or the other (Fig. 4 - 9). Band-bending has been analyzed previously using mathematical modeling [11, 12], and is reduced with graded interface structures

with optimized doping profiles [13]. One could determine which of the two models (i.e. impurities or trapped charge) was responsible for the DLDs, by artificially aging p-DBRs with a high power laser, while simultaneously applying a forward or reverse bias. Impurity-driven degradation should continue to be concentrated at the inverted interface (“downstep”), regardless of the applied bias. By contrast, degradation due to band bending should be at the inverted interface under forward bias, and should shift to the other (“upstep”) interface as the bias is reversed.

4.3.2.3 PL data showing interface states

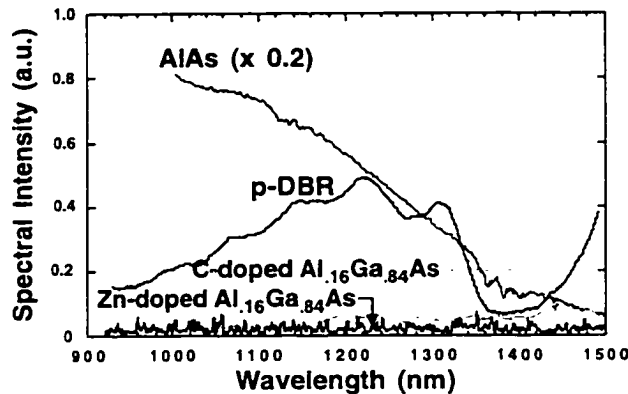


Fig. 4 - 10: Sub-bandgap PL spectra from AlAs, $\text{Al}_{0.16}\text{Ga}_{0.84}\text{As}$, and from a p-DBR.

We used PL to study the deep-level interface states in mirror structures. We obtained a number of samples, both of DBRs, and bulk samples of the DBR constituent alloys (namely AlAs and $\text{Al}_{0.16}\text{Ga}_{0.84}\text{As}$). Perhaps by comparing the spectra, we can see whether the DBR spectrum is simply a composite of its two constituent components or

whether spectral features not common to either component are observed due to DBR interface states. In fact, we do see a peak at $1.22\ \mu\text{m}$ which is not observed in either of the constituents, which could be due to interface states not present in the bulk layers (Fig. 4 - 10). The thick AlAs layer has a very large spectral signature (it had to be reduced 5-fold to fit in Fig. 4 - 10), probably due to build up of oxygen concentrations to progressively higher levels throughout the thick growth, or due to hydrolysis reactions due to atmospheric moisture.

4.3.3 Dislocations from p-contact

In addition to the networks of climb dislocations at the inverted interfaces, long glide dislocations appear to originate at the p-contact, and travel into the center of the device (Fig. 4 - 11). The Burger's vector is $(a/2)\langle 110 \rangle$, as would be expected for glide dislocations. The glide dislocations appear to travel along the path of

highest current flow. While most such dislocations appear to terminate by curling up toward the emitting window, a few appear to have gone down and penetrated the active region. It is possible that they have nucleated dislocations in the active region, as discussed in Section 4.1.

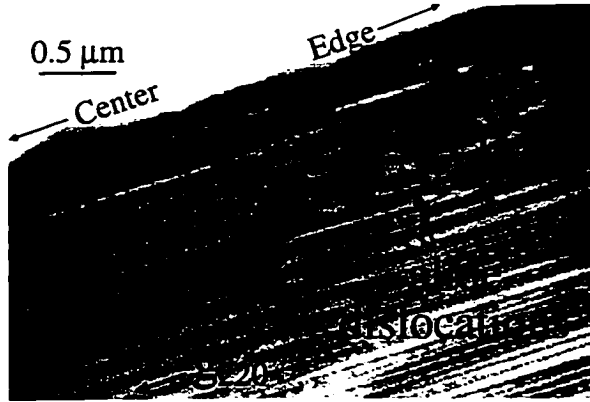


Fig. 4 - 11: TEM image of glide dislocations originating from the p-contact, and traveling toward the center of the device (After Cheng et al., ref. [7])

Extensive efforts were made to prepare the small die aged at normal currents for TEM, due to the concerns about differences between rapid aging (used in the samples above) and gradual aging under more normal operating conditions. In spite of over 6 months full time investment in the task, most of our results were failures, and the few that gave useable samples (by FIB)

appeared to have strain-induced cracking due to p-contact stress. Details of the sample preparation, and a discussion of the difficulties, is contained in Appendix B.

Depending on how dominant the “current shunting” mechanism is, TEM may or may not be useful — devices having failed due to current shunting could easily show a featureless TEM image, and be dislocation-free. To the extent that future TEM work is to be done, gradually-aged *arrays* would be desirable, as we discuss in the Future Work section of Chapter 9.

4.4 Examining p-contact interdiffusion.

Studies of long-wavelength (1.3 and 1.55 μm) InP-based LEDs have shown that reaction between the p-metal and the InP is a major cause of device degradation. Substantial metal diffusion in these long-wavelength LEDs is observed. This can be seen by etching away the semiconductor in a wet etch bath. Most semiconductor etches will not attack p-metals. By examining the metals remaining, it has been observed that spikes taller than 1 μm (i.e., spikes which were penetrating the semiconductor by more than 1 μm) have been observed in aged devices [14, 15].

Further, dark spots in the electroluminescence (EL) image were observed where the metal spikes had penetrated the device. Given the way TEM was able to observe glide dislocations originating at the interface between the p-metal and the p-contact immediately below it [2, 7], it seemed that exploring the stability of the p-contact might be worthwhile.

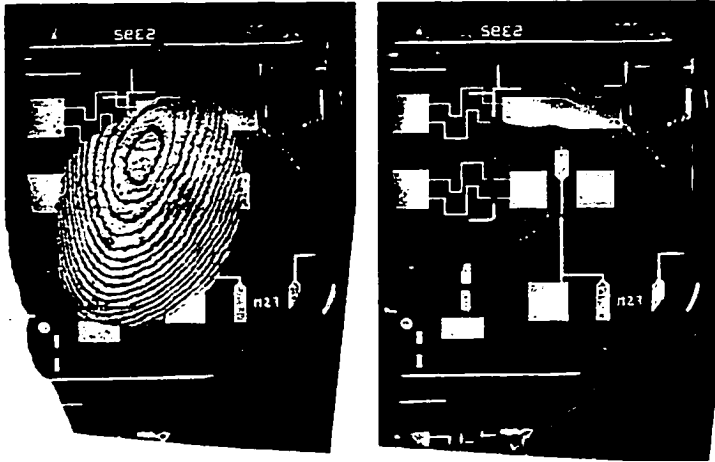


Fig. 4 - 12: Microscope photos of sample to test metal interdiffusion. The rings seen on the left are the remaining 17 p-DBR mirror pairs; in the right image, all the semiconductor has been etched away.

First, arrays of devices were aged at high currents (60-250 mA, where 10 mA would be a normal operating current) to greatly accelerate the aging conditions. Next, the devices were bonded, contact-side down, to a small piece of glass using epoxy, and the substrate was mechanically thinned to 50 - 100 μm . Finally, the samples were wet etched using a solution of 1:1:10 $\text{H}_2\text{SO}_4:\text{H}_2\text{O}_2:\text{H}_2\text{O}$. A sample is shown in Fig. 4 - 12, after 5 minutes of etching in this solution (with over 2 μm of p-DBR remaining) and after 8 minutes of etching (with all the semiconductor removed). Note that the lettering shows up as backward, because we are looking at the remaining metallization *from the bottom*. Samples were then carefully examined using optical,



Fig. 4 - 13: SEM photos of p-metal from aged VCSEL, viewed from underside, after semiconductor has been wet-etched away.

Nomarski, and scanning electron microscopy. The scanning electron microscopy images are seen in Fig. 4 - 13.

Metal interdiffusion could also be observed while the technique of mechanically polishing away the p-contact metal was being developed. While this technique is discussed in greater detail in Appendix B, it involved using a very fine 0.05 μm alumina suspension on a Buhler Chemomet polishing pad to remove the metal with minimal removal of the p-contact layer below. Controllable material removal was assured; larger samples could require more than an hour of polishing to fully remove the p-metals. The top interconnect and dielectric layers would polish off very quickly, and the p-metal, which had interdiffused with the semiconductor, would remain. The p-contact interdiffusion was deep enough that although the oxide and interconnect metals could be peeled off by an epoxy-bonded layer, the p-metal would rip several microns of semiconductor out of the device with it, if it could be removed at all.

The samples were photographed when most, but not all, of the p-metal had been mechanically polished away. They were photographed using both ordinary optical microscopy, as well as Nomarski interference microscopy. Nomarski

microscopy shows height contrasts more sensitively than ordinary microscopy, but distorts natural colors and contrasts. Thus, both types of images are shown (Fig. 4 - 14).

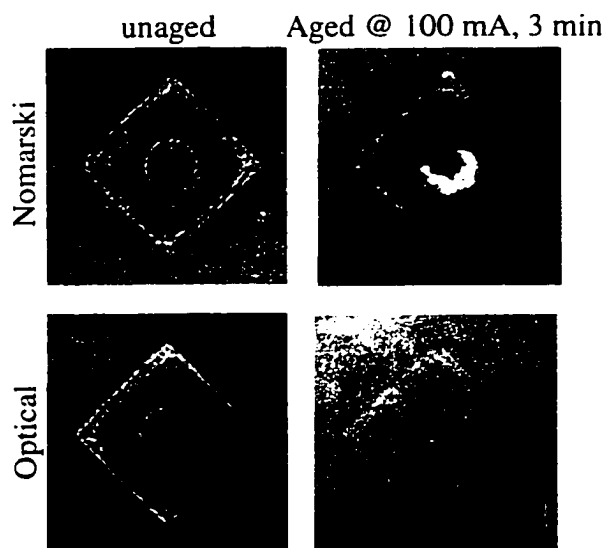


Fig. 4 - 14: Nomarski (top) and optical (bottom) microscope photos are shown of aged VCSELs after the removal of almost all the p-metal. The ring in the center is what remains of the edge of the 15 μm aperture; the square further out is the outer edge of the p-metallization. The left sample was not aged; the right sample was aged at 100 mA for 3 minutes.

While some metal-semiconductor interdiffusion was observed at the p-metal edges even in unaged samples, no further interdiffusion was observed for any reasonable aging condition (i.e., for currents less than 90 mA). The edges of the ring clearly seen in Fig. 4 - 14 demarcating the aperture edges, are not seen in the SEM images of the remaining metal (Fig.

4 - 13). The intermixing in Fig. 4 - 13 is evident only by the *absence* of metal at the edge of the aperture. It is likely that by interdiffusing with soluble Ga and As compounds, the metal at the aperture edge was dissolved in the wet etch solution. It is not known whether the "rough spots" remaining in Fig. 4 - 13 are the sites of glide defect nucleation seen earlier in Fig. 4 - 11. However, it is fair to conclude that no gross intermixing of the sort seen in InP LEDs takes place in the VCSELs we studied. The contacts appeared to be stable as the device aged.

References for Chapter 4:

- [1] W. Jiang, C. Gaw, P. Kiely, B. Lawrence, M. Lebby, and P. R. Claisse, "Effect of proton implantation on the degradation of GaAs/AlGaAs vertical cavity surface emitting lasers," *Electronics Letters*, vol. 33, pp. 137-139, 1997.
- [2] Y. M. Cheng, R. W. Herrick, A. C. Yen, P. M. Petroff, M. K. Hibbs-Brenner, and R. A. Morgan, "Defect-related degradation in vertical-cavity surface-emitting lasers," *To be published*, 1997.
- [3] T. Kamejima, K. Ishida, and J. Matsui, "Injection-enhanced dislocation glide under uniaxial stress in GaAs-(GaAl)As double heterostructure laser," *Japanese Journal of Applied Physics*, vol. 16, pp. 233-40, 1977.
- [4] R. B. Martins, P. Henoc, B. Akamatsu, and J. F. Palmier, "A model for the degradation of Ga(Al)As single-quantum-well lasers," *Journal of Applied Physics*, vol. 70, pp. 554-61, 1991.
- [5] R. G. Waters, D. P. Bour, S. L. Yellen, and N. F. Ruggieri, "Inhibited dark-line defect formation in strained InGaAs/AlGaAs quantum well lasers," *IEEE Photonics Technology Letters*, vol. 2, pp. 531-3, 1990.
- [6] Y. M. Cheng, R. W. Herrick, P. M. Petroff, M. K. Hibbs-Brenner, and R. A. Morgan, "Degradation studies of proton-implanted vertical cavity surface emitting lasers," *Applied Physics Letters*, vol. 67, pp. 1648-50, 1995.
- [7] Y. M. Cheng, R. W. Herrick, P. M. Petroff, M. K. Hibbs-Brenner, and R. A. Morgan, "Degradation mechanisms of vertical cavity surface emitting lasers," *34th Annual Proceedings of International Reliability Physics Symposium*, pp. 211-13, 1996.
- [8] J. Benedict, R. Anderson, and S. J. Klepeis, "Recent developments in the use of the Tripod Polisher for TEM specimen preparation," *Proc. of the Mat. Res. Soc., (Specimen Preparation for Transmission Electron Microscopy of Materials - III)*, vol. 254, pp. 121-40, 1991.
- [9] T. Achtnich, G. Burri, and M. Ilegems, "Study of oxygen incorporation in AlGaAs layers growth by molecular-beam epitaxy," *Journal of Vacuum Science & Technology A (Vacuum, Surfaces, and Films)*, vol. 7, pp. 2537-41, 1989.
- [10] N. Chand, S. N. G. Chu, and A. S. Jordan, "Migration and gettering of Si, Be, and ambient-related O in AlGaAs/GaAs laser structures," *Journal of Vacuum Science and Technology, B.*, vol. 10, pp. 807-11, 1992.
- [11] E. Zeeb and K. J. Ebeling, "Potential barriers and current-voltage characteristics of p-doped graded AlAs-GaAs heterojunctions," *Journal of Applied Physics*, vol. 72, pp. 993-9, 1992.

- [12] R. F. Nabiev and C. J. Chang-Hasnain, "Voltage drop in n- and p-type Bragg reflectors for vertical-cavity surface-emitting lasers," *IEEE Photonics Technology Letters*, vol. 7, pp. 733-5, 1995.
- [13] M. G. Peters, B. J. Thibeault, D. B. Young, A. C. Gossard, and L. A. Coldren, "Growth of Be doped $\text{Al}_x\text{Ga}_{1-x}\text{As}/\text{GaAs}$ mirrors for VCSELs," *Journal of Vacuum Science and Technology B*, vol. 12, pp. 3411-3427, 1994.
- [14] M. Fukuda, O. Fujita, and S. Uehara, "Homogeneous degradation of surface emitting type InGaAsP/InP light emitting diodes," *Journal of Lightwave Technology*, vol. 6, pp. 1808-14, 1988.
- [15] A. K. Chin, C. L. Zipfel, F. Ermanis, L. Marchut, I. Camlibel, M. A. Diguseppe, and B. H. Chin, "The migration of gold from the p-contact as a source of dark spot defects in InP/InGaAsP LED's," *IEEE Transactions on Electron Devices*, vol. ED-30, pp. 304-309, 1983.

Chapter 5: Driving forces responsible for degradation in DBR layers.

While the measurements in other chapters were able to show *how* degradation progressed, the explanations of *why* degradation of the DBR layers occurred has come primarily from the evidence which will be discussed in this chapter. Ordinarily, degradation would not be expected outside the immediate vicinity of the active region, since the cladding and confinement layers are not supposed to have significant minority carrier populations in them. However, using spectral measurements, we were able to establish that significant amounts of carrier recombination are also taking place in the $\text{Al}_{16}\text{Ga}_{84}\text{As}$ layers of the mirrors, and that this recombination was a likely explanation for why degradation of the mirrors was observed.

This being the case, while it is straightforward to detect the spontaneous emission which pumps the mirror layers, it is nearly impossible to distinguish mirror luminescence from the optical pumping which drives the luminescence. While calculations can be used to show that a non-negligible fraction of the active region's spontaneous emission is absorbed by the mirror layers, it can

also be directly detected by near-field scanning optical microscopy (NSOM) experiments, which were done in cooperation with Prof. Buratto's group. The details of these measurements are contained in Appendix A.

Ultimately, these results led to suggested design changes which were able to reduce the early failure rate drastically, as we discussed in Chapter 1.

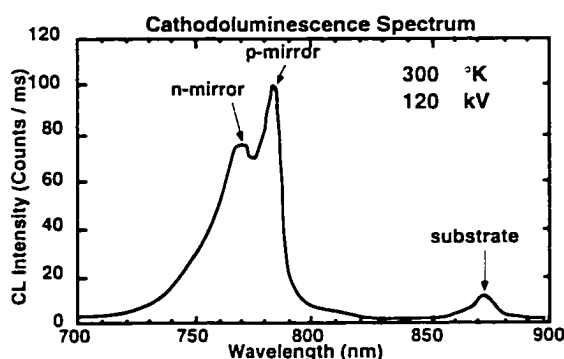


Fig. 5- 1: Cathodoluminescence spectrum of a vertical cavity laser, taken from the top. (Taken by Dr. Michael Cheng, ref. [1])

5.1 Identification of Spectral features

5.1.1 Top-emitting, room temperature, cathodoluminescence spectrum, showing $\text{Al}_{16}\text{Ga}_{84}\text{As}$ luminescence.

As discussed in chapter 3, room-temperature cathodoluminescence of our proton-implanted VCSELs yields peaks at 785 nm from the p-DBR ($\text{Al}_{16}\text{Ga}_{84}\text{As}$),

as well as at 770 nm from the n-DBR [1]. This is shown in Fig. 5- 1. Since all layers are excited almost equally by the electron beam, and the DBRs make up >95% of the epitaxial thickness of the device, CL from the $\text{Al}_{16}\text{Ga}_{84}\text{As}$ layers of the mirrors dominates this spectrum.

5.1.2 Photoluminescence spectra.

We took photoluminescence spectra on a variety of samples for two reasons: first, we wished to establish the luminescence wavelengths of n- and p-type $\text{Al}_{16}\text{Ga}_{84}\text{As}$ independently of any resonance effects which the mirror might play in our observations. Second, we wished to explore the effects of traps or deep-levels in the bulk material and at the interfaces.

5.1.2.1 Description of apparatus and measuring technique.

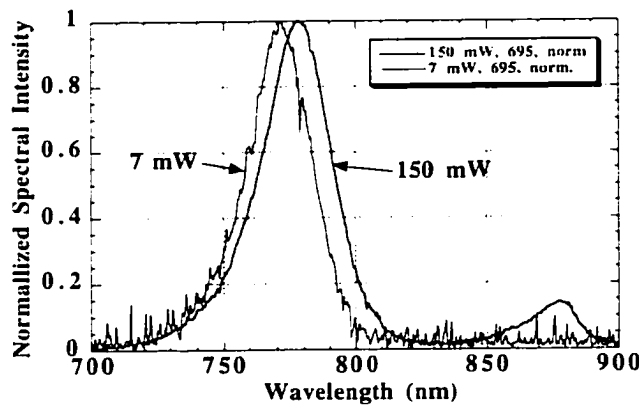


Fig. 5- 2: PL spectra from a bulk p- $\text{Al}_{16}\text{Ga}_{84}\text{As}$ layer at various pump powers.

An Argon-ion laser was used to pump samples, and for most samples, a relatively high beam power was used to maximize signal-to-noise ratio from the weak deep-level emission. The beam was chopped, and a lock-in amplifier was used to detect the resulting signal. The signal was sent through a 0.85m spectrometer,

and then into a North Shore Ge detector, enabling us to detect long wavelengths (up to $1.7\ \mu\text{m}$). The detector was cooled with liquid nitrogen to reduce dark noise. All samples examined were measured at room temperature, since determining room-temperature spectral characteristics was important for the purpose of this work. We also did not want to freeze out donor or deep level states, as we might do by taking low-temperature measurements.

The samples were mounted on a large aluminum block for good heat sinking. The spectrometer was tuned to a peak wavelength, and the focus adjusted to give minimum spot size and maximum signal. In the case of implanted devices,

the sample position also had to be carefully adjusted to take the sample in the non-implanted area in the center of an aperture. We attempted to take spectra in the implanted areas as well, in order to possibly see the deep-level bands from proton implantation, but no signal was obtained. While the absorption lengths for 514 nm light (as from the Ar^+ laser) are very shallow, electrons and holes generated at the surface can diffuse into the deeper layers. This is visible with a p-doped $\text{Al}_{16}\text{Ga}_{84}\text{As}$ sample which was a few microns thick, as seen in Fig. 5- 2. Note that emission from the substrate (at 890 nm) is much more evident at high pumping densities.

5.1.2.2 Band-to-band recombination.

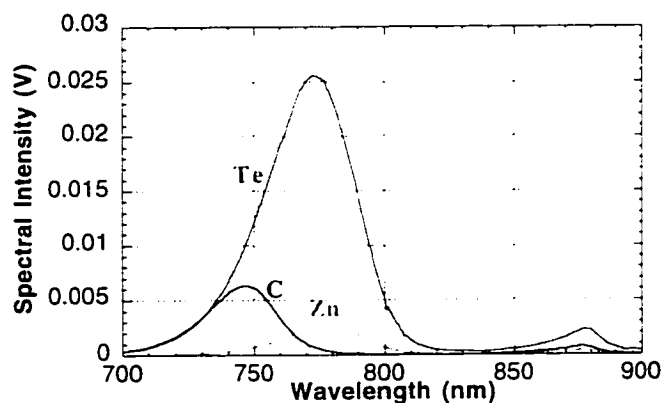


Fig. 5- 3: Spectra from p-doped and n-doped samples.

capable of creating changes in emission wavelength on the order of the 15 nm doping-related shifts we observe. Two spectra, from a p-doped (Zn) and an n-doped (Te) sample are shown in Fig. 5- 3.

Part of our goal in measuring the PL spectra was to obtain data on the doping-related spectral shifts discussed earlier in Chapter 3. For these data to be accurate, compositional control would need to be quite tight, since even small fluctuations in Al-mole-fraction would be

5.1.3 Description of instrumentation for electroluminescence spectra.

5.1.3.1 Experimental setup for taking top-emitting spectra

Taking spectra from a laser in the direction of emission is normally a fairly simple matter, since laser emission is so intense that even with poor coupling, one can acquire data. In our case, however we were attempting to acquire the relatively weak parts of the spectrum, and not just the lasing peak. Thus, we were careful to optimize coupling efficiency: 20–40% of the light could be coupled into the fiber.

An 830 nm graded-index (GRIN) lens with a 0.29 pitch was purchased from Melles Griot, and mounted in a custom brass holder, which held the lens on the end of the multi-mode fiber. The fiber and lens were then mounted to the end of an XYZ translation stage, and rough aligned with the lasing beam using an infrared viewer. The output end of the fiber had an FC-PC ferrule on it: it was attached to a calibrated detector, and the XYZ position of the GRIN lens was adjusted to maximize coupling. The spectra were then generally acquired in two separate sections: from 740-820 nm, and from 820-900 nm. (For reasons that I still do not understand, the HP Optical Spectrum Analyzer (OSA) was able to take these two spectra more rapidly than it was able to take a single spectrum from 740-900 nm). Resolution Bandwidth was 2 nm, which greatly increases the sensitivity relative to normal OSA settings, but gives poor resolution of individual lasing modes. The spectrometer sensitivity was set at -83 dBm, which made for very slow scans (~5 min. each), but gave relatively noise-free data even for parts of the spectra with low power in them. The experimental setup is shown in Fig. 5- 4.

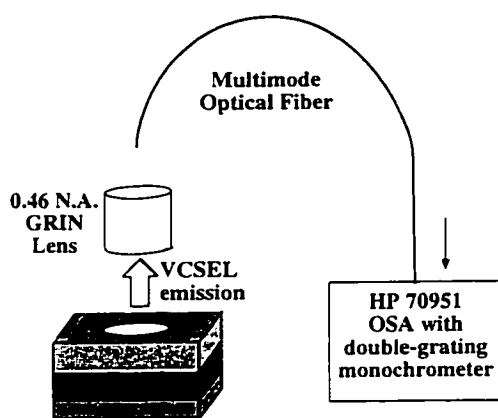


Fig. 5- 4: Experimental setup used to measure top-emitting spectra.

Two Optical Spectrum Analyzers (OSAs) were used for this work: an Ando 6312B, and an HP 70951A. The Ando had the advantage of being able to save data directly to floppy disks, but had only a single pass spectrometer. For many measurements, this was not a disadvantage (e.g., the side emitting measurements, or measurements of spectral shift as a function of temperature change). However, since we were attempting to resolve spectral

features relatively close to the lasing peak for the top-emitting spectra, we generally preferred to use the HP 70951A, due to its double-pass spectrometer. The difference between the instruments can be seen in Fig. 5- 5. Lambertian scattering from the Ando's grating gives an artificially high background, and strongly affects the spectral measurements this close to the lasing peak. By contrast, the second pass on the grating in the HP is able to remove most of the scattered light.

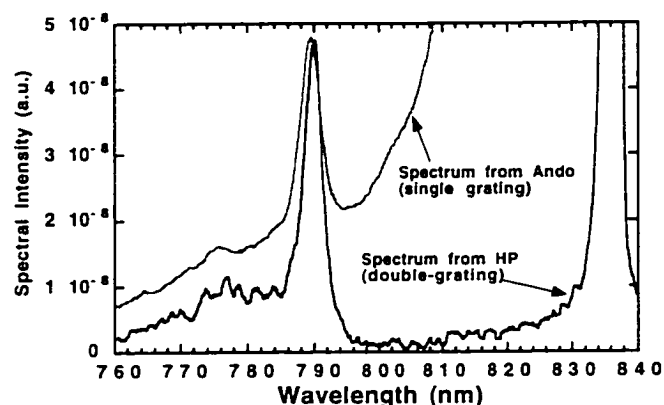


Fig. 5- 5: Spectra taken from the same laser. The intensity was normalized to be the same at the 790 nm peak. Note the strong existence of scattered laser light affecting the measurements from the Ando spectrometer.

5.1.3.2 Dependence of spectra on collecting system's numerical aperture (N.A.).

A sampling of electroluminescence spectra follows. In each case, spectral peaks are observed on the high-energy (short-wavelength) side of the lasing peak. While we no longer believe these peaks are a direct observation of luminescence from the low-bandgap (e.g., $\text{Al}_{16}\text{Ga}_{84}\text{As}$) layers of the DBR [1], the peak is proportional to the optical pumping which drives mirror degradation, and thus is still of interest.

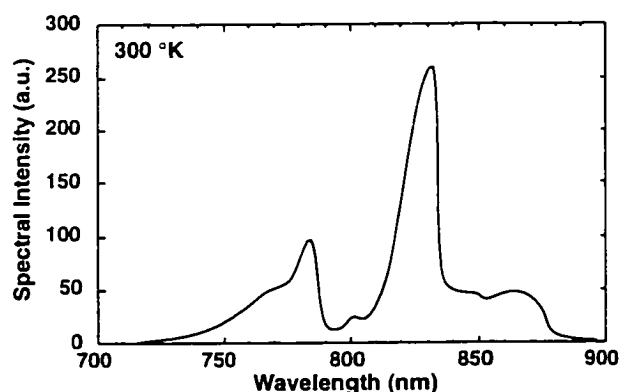


Fig. 5- 6: Electroluminescence spectrum of a laser at 1.4 V, collected in the cathodoluminescence microscope (after ref. [1]).

The first spectrum shown (Fig. 5- 6) was actually collected in the CL system by Michael Cheng [1]. It is of interest not only for historical reasons (as it was the first indication we had of short-wavelength luminescence), but also because of the high numerical aperture of the system used to collect the data. The cathodoluminescence mirror is able

to collect light from over 70° off the normal, while the GRIN lens used for other measurements had a numerical aperture of only 0.25 N.A., or about 15° off-axis.

The asymmetric shape of the spectra, with a softer roll-off to the blue (left) side, is a consequence of this off-angle collection [2], as we shall see again later in this chapter. The peak at 830 nm is at the lasing wavelength. The peaks at 770 and 780 nm are due to high-energy spontaneous emission escaping from the mirror reflectivity nulls. The peak at 870 nm is possibly due to luminescence from the substrate, which is discussed in Appendix A.

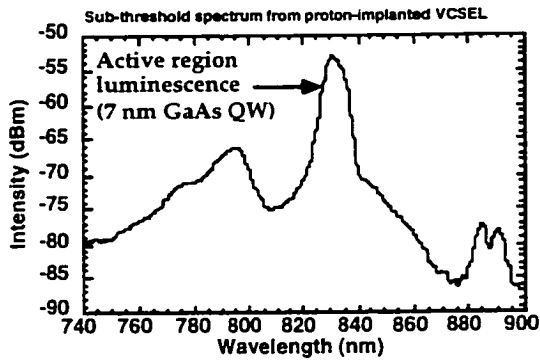


Fig. 5- 7: Sub-threshold spectrum from a multi-filamentary vertical cavity laser. Note the logarithmic scale used on the y-axis; 795 nm peak is ~17 dB lower than the 830 nm peak, and has integrated power about 10 dB lower.

other spectra shown of devices above threshold, the spectral width shown is determined by the bandwidth resolution set on the spectrometers. The true spectral width of the lasing peaks in other laser types is almost always <0.5 nm.

Fig. 5- 8 shows the sub-threshold spectrum from an InGaAs-QW pillar VCSEL. All VCSELs we have

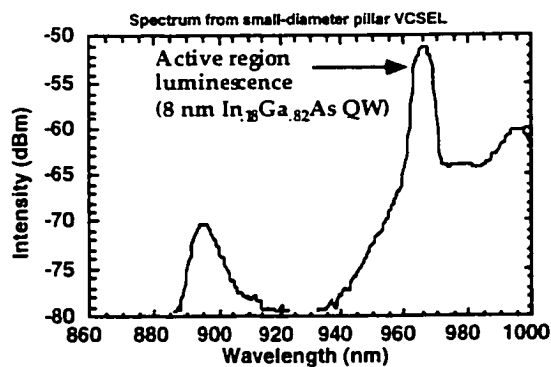


Fig. 5- 8: Sub-threshold spectrum from an InGaAs-QW pillar VCSEL.

The spectrum shown in Fig. 5- 7 is more typical of the results which could be taken with our usual GRIN-lens collection apparatus, where the peak to the left of the active region remained 10 dB or more below the active region peak at sub-threshold currents, as opposed to only 3 dB below in Fig. 5- 6. It is worth noting that the true spectral width of the active region is quite large at 5 nm, with many independent filaments contributing to the lasing spectrum [3]. In all the

observed have a broad enough gain spectrum that spontaneous emission can be observed escaping from the reflectivity nulls. Whether the high energy spontaneous emission is absorbed or not depends on the bandgap of the DBR layers, as we shall discuss later in this chapter. The reflectivity null is slightly further away

from the lasing peak in these lasers: about 60 nm. The mirror's stop-band is wider due to the higher refractive-index contrast between DBR layers.

5.1.3.3 Analysis of shifts in DBR transmission spectra.

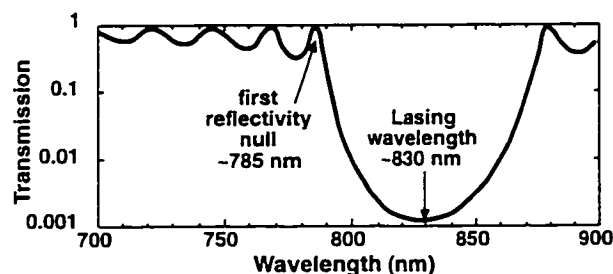


Fig. 5- 9: Mirror transmission versus wavelength. Note that if the maximum reflectivity is at 830 nm, a reflectivity null occurs at 785 nm.

Many past authors have also observed high-energy spontaneous emission escaping from the DBR reflectivity nulls [2, 4, 5]. This occurs because transmission increases to >50% at the reflectivity null some 40-50 nm away from the lasing peak, versus <0.2% at the lasing wavelength,

thus giving more than two orders of magnitude enhancement to escaping spontaneous emission at the reflectivity null. These nulls were co-incidentally at the same wavelength as the mirror emission, as established by CL. The mirror transmission versus wavelength is shown in Fig. 5- 9.

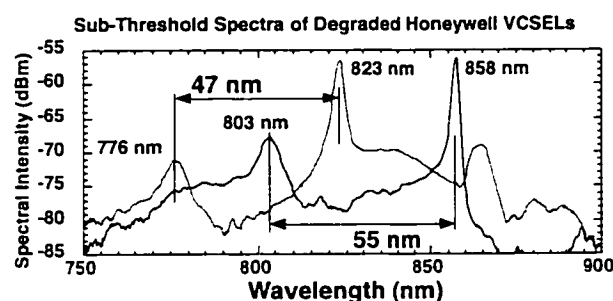


Fig. 5- 10: Spectra from two VCSELs with different resonance wavelengths. Note that the spacing between the secondary peak and the lasing wavelength is approximately constant; the secondary peak does not maintain a fixed wavelength as it would if it were due to luminescence of $\text{Al}_{16}\text{Ga}_{84}\text{As}$, which is fixed at 790 nm, regardless of cavity geometry.

The target wavelength of the VCSELs is 850 nm. The 830 nm samples shown above are edge samples — growth rate declines toward the wafer edges, and resonance wavelength falls with decreasing DBR thickness. Essentially, these thickness differences simply shift the entire reflectivity spectrum, without modifying the shape, or significantly changing the spacing

between the nulls. Two spectra are shown in Fig. 5- 10, allowing us to see that the peak to the left of the lasing peak is almost entirely composed of spontaneous emission escaping from the mirror reflectivity nulls. If the emission from the DBRs were a major contributor to the spectrum (> 20% of escaping power) a peak fixed at

790 nm would be evident (the wavelength seen in the CL spectra), regardless of how the resonance wavelength differs.

This same phenomenon of spectral shifting of the mirror and cavity resonance can be observed by taking off-axis spectral measurements. Since the k -vector of the light increases off-axis, the wavelength decreases. The resulting spectra can be seen in Fig. 5- 11.

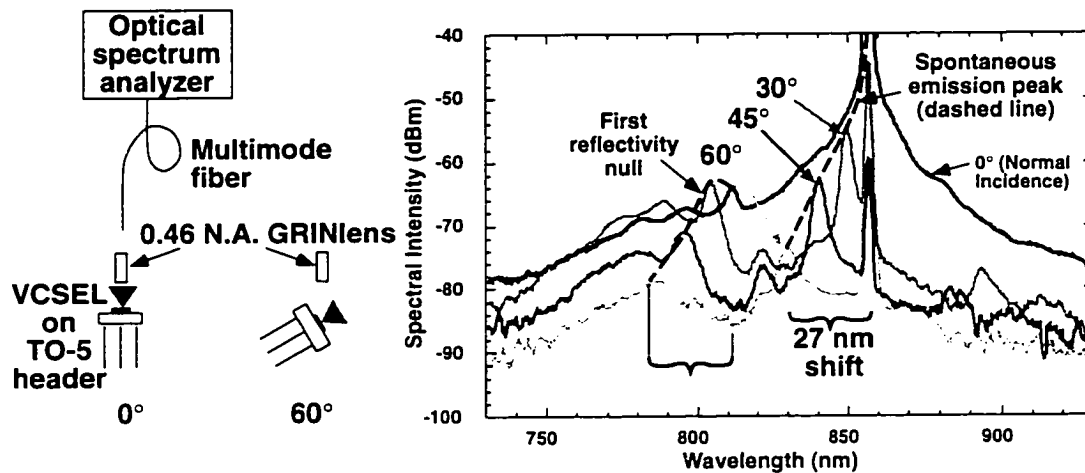


Fig. 5- 11: Spectra taken at four angles. The one labeled “0°” was taken normal to the surface, the others were taken at increasing angles from normal.

5.2 Dependence of spontaneous emission on drive level.

5.2.1 Top-emitting spectra at various current levels.

The reader who had not read the introduction to this chapter could easily come to the incorrect conclusion that perhaps the mirrors aren’t really giving off

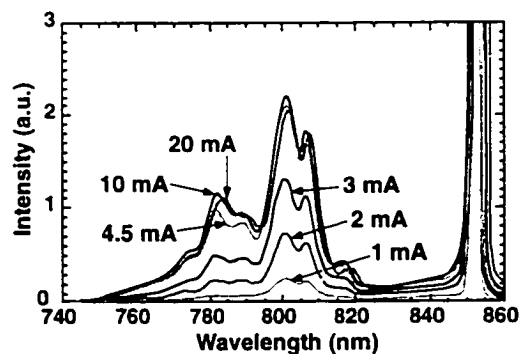


Fig. 5- 12: Spectra from undegraded proton-implanted VCSEL.

luminescence after all — this is not the case. Even if the luminescence from the mirror layers can only be observed directly using NSOM, as discussed at the conclusion of this chapter, it stands to reason that “where there’s smoke, there’s fire.” That is, with emission escaping from the mirror reflectivity nulls at photon energies well above the bandgap of

$\text{Al}_{16}\text{Ga}_{84}\text{As}$, some absorption of this luminescence is to be expected, and will optically pump these layers, thereby introducing unwanted minority carriers in them. Thus, even if we can't directly study the mirror luminescence itself because it is swamped by the optical pumping signal, it is worthwhile studying the high-energy spontaneous emission escaping through the mirrors, as the mirror luminescence would be expected to be roughly proportional to the intensity of this optical pumping source. A typical set of spectra (from Honeywell VCSEL wafer 591, laser L-1V) are shown in Fig. 5- 12. Note that the luminescence rises quickly until threshold is reached (at around 4.5 mA), and is then pinned above threshold. This is discussed quantitatively in the next section.

5.2.2 Integrated power in various spectral bands as a function of current.

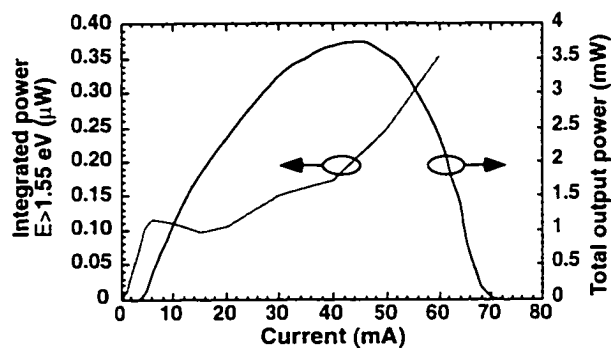


Fig. 5- 13: L-I curve both for total output power from laser (dominated by 850 nm emission), as well as integrated high-energy emission as a function of current.

Studying the EL spectra as a function of drive current also reveals useful information about the nature of the spontaneous emission, and the mirror luminescence it drives. The spontaneous emission rises below threshold, then levels out (once the lasing threshold is reached) with a pinned carrier concentration, and finally starts to rise once again when the L-I curve

starts to roll over (Fig. 5- 13). By integrating the power from 740-820 nm for each of many different currents, we obtain the power from the high-energy spontaneous emission which pumps the luminescence. Note that it *does not* scale with lasing power. Also note that the power is a fraction of a microwatt, which is a few orders of magnitude lower than the lasing power.

5.3 Discussion of driving mechanism for mirror degradation.

5.3.1 Side-emitting electroluminescence spectra from cleaved VCSELs.

The source driving degradation in the mirror layers is believed to be the optical pumping from high-energy spontaneous emission, which is absorbed by the $\text{Al}_{16}\text{Ga}_{84}\text{As}$ layers in the DBRs. It should be noted that the lasing photons have too little energy to be absorbed by DBR layers (although in areas with dislocations, deep levels exist which *can* absorb lasing light). This optical pumping would lead to minority carrier injection in the mirror layers, *which is a pre-requisite to reaction-enhanced defect reactions* [6]. The broad spontaneous emission characteristic of semiconductor lasers provides a significant number of such high-energy photons. The spontaneous emission is best observed by studying VCSEL emission directly from the side, where the spectral characteristics of the mirror will not affect the measured spectrum.

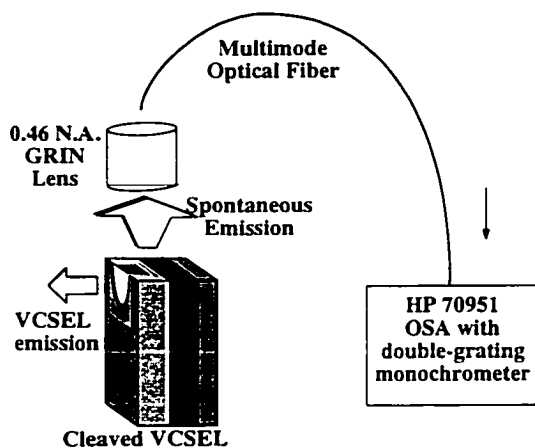


Fig. 5- 14: Schematic of experimental setup for cross-sectional spectra from a cleaved VCSEL.

The cross-sectional spectra can be taken by cleaving a VCSEL in half, and then studying the luminescence coming from the side. Amazingly, the device lases, and even has a lower threshold after being cleaved in half. The experimental configuration is shown in Fig. 5- 14. Thus, a rough approximation of the modal dynamics of a real VCSEL can still be studied. The only caution is that, with the reactive AlAs layers, the cleaved VCSEL must either be coated, or

kept in a desiccator when not in use to prevent hydrolysis of the AlAs. A typical set of spectra is shown in Fig. 5- 15.

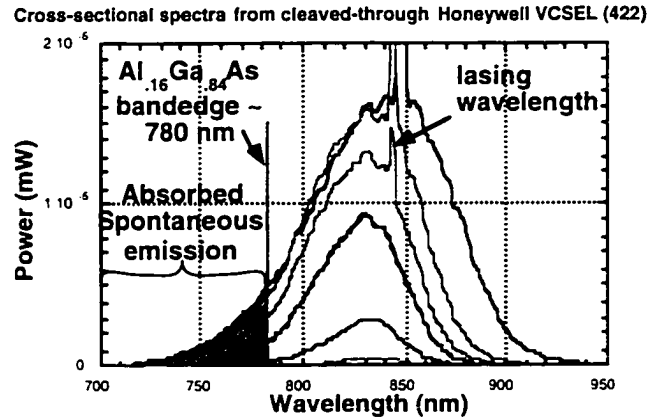


Fig. 5- 15: Cross-sectional spectra from a cleaved VCSEL, taken edge-on. The bandedge, and the light with energy above the bandedge, are shown on the high-energy (short-wavelength) side of the diagram.

As has been observed earlier [4], while the top-emitting spectrum is filtered by the mirror's response function, the cross-sectional spectrum is a fairly accurate depiction of the actual spontaneous emission profile. The spectral profile is quite broad, with a 62 nm full-width at half-maximum (FWHM) at lasing currents (Fig. 2). Luminescence from the n- and p-AlGaAs layers is not directly visible in the cross-sectional spectrum, possibly because such luminescence is overwhelmed by the magnitude of the spontaneous emission which is pumping it.

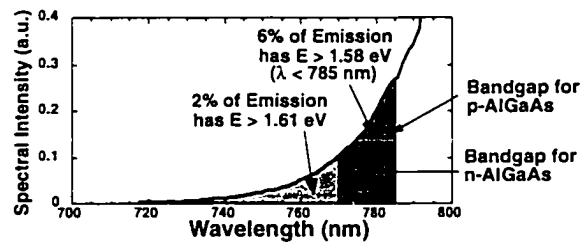


Fig. 5- 16: High-energy tail from the cross-section of a cleaved VCSEL.

We can observe that 6% of the spontaneous emission produced is above the (1.58 eV) bandgap of the p-Al₁₆Ga₈₄As layers in the p-DBR, and thus able to inject minority carriers by optical pumping. The n-Al₁₆Ga₈₄As, by contrast, has less doping-induced band-gap shrinkage,

and thus is capable of absorbing only 2% of the spontaneous emission. This can be seen by examining a close-up of the device spectrum's high energy tail (Fig. 5- 16). By increasing the bandgap of the layers in the DBR pair to Al₂₄Ga₇₆As, we calculated we could obtain a 20-fold reduction in minority carrier injection (Fig. 5- 17). As will be discussed later, we verified that this change to the structure indeed

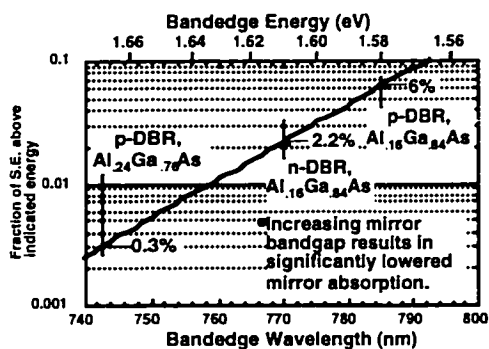


Fig. 5- 17: Reduction in absorbed power expected from increasing bandgap of AlGaAs DBR layer.

eliminated the formation of dark areas in the p-DBR, by examining degraded VCSELs using cross-sectional CL. It also seems to have reduced early failures, causing a reduction in Sigma from 1.29 previously to 0.23 afterward [7]. However, it should also be noted that other changes in growth, fabrication, and screening, have subsequently enabled similar improvements in device reliability without using increased

bandgap mirrors [8].

It should be noted that a number of other possible causes of minority carrier injection can be ruled out by examining how the top-emitting spectra change as a function of current. The short wavelength portion of the spectrum, which includes both high-energy spontaneous emission and the luminescence it creates in the mirror layers, rises with current until laser threshold, and is clamped above threshold. This is the behavior expected of spontaneous emission. We were thus able to rule out a number of other possibilities, including optical pumping by the lasing light, pumping by the barrier layers, or double-photon pumping through mid-gap states.

5.3.2 Strategies for reducing dislocation growth in p-DBRs

In addition to the use of wider-bandgap mirrors, discussed above, a number of other possible opportunities for improving device lifetime are evident from the preceding discussion in Chapters 3,4 and 5. Control of interfacial oxygen and dopant concentration seems important in view of the TEM findings. Carriers may also be trapped in adjacent layers; perfecting the dopant profile to minimize DBR resistance would address this potential cause of degradation. Different dopants may allow better control (e.g., less migration), or give better reliability results. Carbon has replaced beryllium in most HBTs because it is generally more stable. However, Be can be incorporated as a more stable substitutional dopant (rather than being an interstitial dopant) by changing the V-III ratio [9]. Work on reducing metallization stress would likely also prove worthwhile.

5.4 Results from wide-bandgap VCSELs

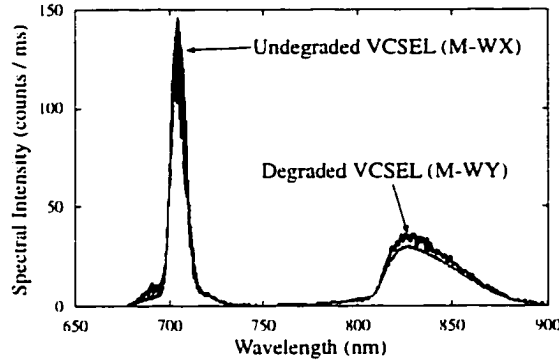


Fig. 5- 18: CL spectra from degraded VCSELs with wide-gap (24%) Al mirrors.

A modified structure with high-bandgap materials ($\text{Al}_{24}\text{Ga}_{76}\text{As}$ rather than $\text{Al}_{16}\text{Ga}_{84}\text{As}$) in the mirrors was then grown and processed at the Honeywell Technology Center. To the extent that mirror degradation is driven by optical pumping from high-energy spontaneous emission, we expect a 20-fold reduction in absorbed power with the wider bandgap mirrors, as was discussed in the previous section. After being rapidly aged, the array was cross-sectioned, and imaged by CL. No dark areas of the sort seen earlier were observed in the p-DBRs, which tends to confirm our hypothesis. While other ways also exist to control DBR degradation, the reduction in the early failure rate is encouraging. Note that the wider bandgap mirrors have not been adopted earlier at least partly because they come with some performance penalties: the lower mole-fraction contrast results in reduced reflectivity per mirror pair, which then requires us to add two more pairs to the p-DBR and three more pairs to the n-DBR.

CL spectra and monochromatic images of degraded VCSELs are shown in Fig. 5- 18 and Fig. 5- 19, respectively. Note that the spectra peak at ~ 705 nm, rather than 745 nm, due to the increased bandgap of $\text{Al}_{24}\text{Ga}_{76}\text{As}$. The CL

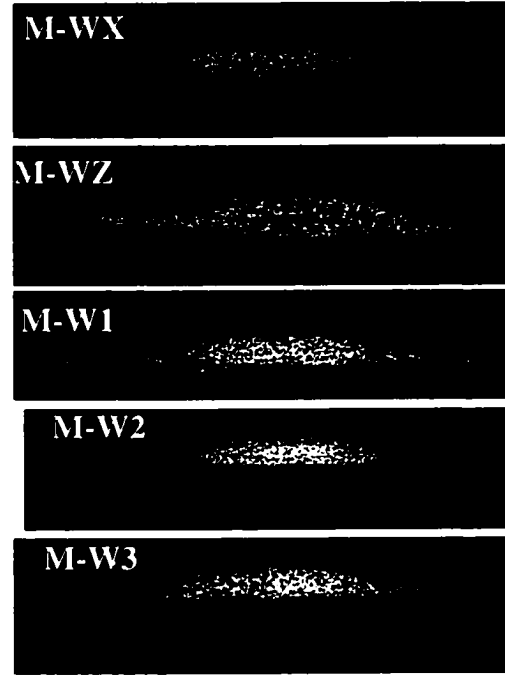


Fig. 5- 19: Monochromatic CL images from undegraded (WX) and degraded (other) VCSELs. Note that no DLDs of the sort seen in Chapter 4 are visible in these devices.

efficiency varied by $\pm 20\%$, but did not appear to be significantly different in aged devices than in unaged devices.

5.5 Observation of deep-levels in VCSEL spectra.

5.5.1 Long-wavelength (sub-bandgap) spectral features of the lasing spectrum.

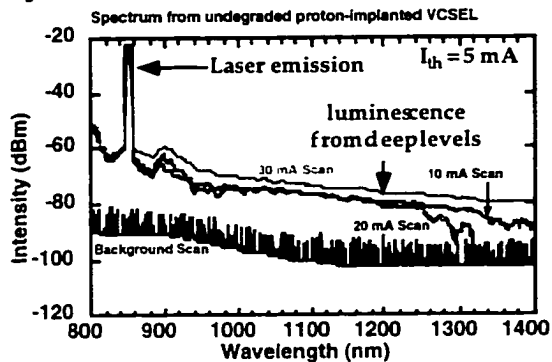


Fig. 5- 20: Long-wavelength spectra from an undegraded VCSEL show significant amounts of luminescence at wavelengths well below the bandgap.

an increasing number of deep levels [10, 11]. It has been observed that deep-levels show primarily non-radiative recombination, so collected photocurrent would be expected to be a better gauge than emitted power. However, we do observe a certain amount of radiative, low-energy emission. While significant amounts of luminescence could be observed at below-band-gap wavelengths, no conclusive results were obtained as to whether deep-level luminescence increased after the device degraded. Due to difficulties in choosing a comparable level for a meaningful comparison (same drive current? same laser output power?) it was difficult to know how to compare the changes in the output power at long wavelengths before and after aging. A typical set of spectra is shown in Fig. 5- 20. (Resolution bandwidth was increased to 5 nm for improved sensitivity, and sensitivity was set to -80 dBm; the reference level was set to -50 dBm.)

A handful of VCSEL spectra were taken all the way out to 1500 nm, in an attempt to view luminescence from deep levels inside the diode. They were studied before and after degradation in an attempt to see if deep level luminescence increased as the device degraded. An increase in collected photocurrent at sub-bandgap wavelengths has been observed after the laser has degraded, giving evidence of

5.5.2 Long-wavelength (sub-bandgap) spectra from cleaved VCSELs.

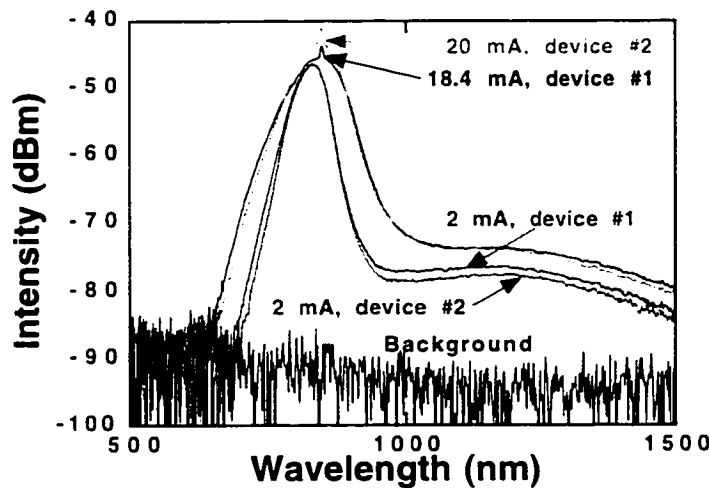


Fig. 5- 21: Long-wavelength spectra from cleaved VCSEL.

Significant

amounts of luminescence could also be observed at wavelengths below the bandgap of the VCSEL in the side-emitting spectrum from cleaved VCSELs (Fig. 5- 21). The observed magnitudes and spectral shapes were similar to those seen in the top-emitting spectra.

References for Chapter 5

- [1] R. W. Herrick, Y. M. Cheng, P. M. Petroff, M. K. Hibbs-Brenner, and R. A. Morgan, "Spectrally-filtered electroluminescence of vertical-cavity surface-emitting lasers," *IEEE Photonics Technology Letters*, vol. 7, pp. 1107-9, 1995.
- [2] M. P. van Exter, A. K. Jansen Van Doorn, and J. P. Woerdman, "Effect of spatial filtering on the spontaneous emission spectrum of a sub-threshold VCSEL," *IEEE Journal on Selected Topics in Quantum Electronics*, vol. 1, pp. 601-5, 1995.
- [3] R. A. Morgan and M. K. Hibbs-Brenner, "Vertical-cavity surface-emitting laser arrays," *Proc. of SPIE*, vol. 2398 (Circular-Grating Light-Emitting Sources), pp. 65-93, 1995.
- [4] D. T. Schaafsma, R. K. Hickernell, and D. H. Christensen, "Measurement and simulation of photoluminescence spectra from vertical-cavity quantum-well laser structures," *Proc. of the SPIE*, vol. 2139 (Quantum Well and Superlattice Physics V), pp. 92-102, 1994.
- [5] D. T. Schaafsma, D. H. Christensen, R. K. Hickernell, and J. G. Pellegrino, "Comparative photoluminescence measurement and simulation of vertical-cavity semiconductor laser structures," *Proc. of the Mater. Res. Soc.*, vol. (Symposium Growth, Processing, and Characterization of Semiconductor Heterostructures. Symposium), pp. 483-8, 1993.
- [6] P. M. Petroff, "Device degradation and recombination enhanced defect processes in III-V semiconductors," *Semiconductors and Insulators*, vol. 5, pp. 307-319, 1983.
- [7] M. K. Hibbs-Brenner, "VCSEL research, development, and applications at Honeywell," presented at '97 LEOS Summer Topicals, Montreal, Canada, 1997.
- [8] Personal Communication with James Guenter of Honeywell MICRO-SWITCH
- [9] D. C. Streit, A. K. Oki, D. K. Umemoto, J. R. Velebir, K. S. Stolt, F. M. Yamada, Y. Saito, M. E. Hafizi, S. Bui, and L. T. Tran, "High-reliability GaAs-AlGaAs HBT's by MBE with Be base doping and InGaAs emitter contacts," *IEEE Electron Device Letters*, vol. 12, pp. 471-473, 1991.

- [10] C. H. Henry, P. M. Petroff, R. A. Logan, and F. R. Merritt, "Catastrophic damage of $\text{Al}_x\text{Ga}_{1-x}\text{As}$ double-heterostructure laser material," *Journal of Applied Physics*, vol. 50, pp. 3721-32, 1979.
- [11] A. Richter, J. W. Tamm, C. Lienau, and J. Luft, "Optical near-field photocurrent spectroscopy: a new technique for analyzing microscopic aging processes in optoelectronic devices," *Applied Physics Letters*, vol. 69, pp. 3981-3, 1996.

Chapter 6: Degradation in red InGaP vertical cavity lasers

6.1 Introduction to red VCSELs

In this chapter, we start by introducing red VCSELs in section 6.1, and describing the structure of the devices studied in section 6.2. General observations of degraded red VCSELs follow in Section 6.3, in which we see that the primary cause of failure for proton implanted red VCSELs appears to be the “current-shunting” mechanism described earlier in Chapter 3. We then discuss two major effects which are not observed in infrared VCSELs. First, the bias-induced annealing of red VCSELs, which is able to significantly extend the lifetime of devices from some wafers, will be analyzed (section 6.4). Second, the observation of spatially-indirect recombination, which is likely related to spatial inhomogeneities, is described (section 6.5). Finally, we discuss how red VCSELs might be improved in section 6.6.

6.1.1 Potential applications of red VCSELs

Several novel applications which cannot be met by near-infrared lasers have recently emerged. First, and most obviously, for display applications (e.g., laser pointers) infrared lasers are not useful, and green and blue lasers are produced only in research laboratories at the time of this writing. By contrast, 5 mW red laser diodes are sold (\$2 each) in quantity for laser pointers. For bar-code readers, visible lasers must be used, since the infra-red properties of the printing inks used cannot be guaranteed, while it is a simple matter to print a high-contrast bar-code pattern at any visible wavelength. For optical storage (including CD's, and now DVD's), shorter wavelength sources can be focused into tighter spots since the diffraction limit is smaller, which allow higher data density to be obtained. Thus, the new DVD standard (650 nm) allows 4.7 GB of data to be stored, vs. 0.64 GB on the old infrared CD standard. For laser printing and other reprographic applications [1], infrared lasers have generally not been very useful, since their low photon energy is simply too weak to break molecular bonds in common photosensitive chemicals. By contrast, red lasers are able to affect a wide variety of useful photochemicals. Finally, the application driving Honeywell Technology Center (among other companies) to make red VCSELs has been data communications through plastic

fibers. Inexpensive plastic fiber has relatively low loss in the red, while loss in the infrared is prohibitively high. The data communications products envisioned would be similar to those described for the infrared VCSELs. Results of a red VCSEL data link have recently been described [2].

6.1.2 A Brief History of Red VCSELs

While red semiconductor lasers were demonstrated over 30 years ago, red VCSELs were first demonstrated (room-temperature, CW) at Sandia in 1993 [3]. Since then, progress has been very rapid, and within one year VCSELs with 10% wallplug efficiencies, and output power of over 2 mW had been demonstrated. Generally the devices had met most other characteristics necessary for the applications discussed above [4], with one exception. That exception was the relatively poor reliability of red VCSELs. While recent breakthroughs at Sandia National Laboratories have allowed operation for over 3,000 h at 1 mW with no measurable degradation [5], red VCSELs with similar reliability have not yet been demonstrated elsewhere. It is worth noting that these initial difficulties with device reliability are to be expected, given the correlation which has been noted between high photon energy and low device lifetimes [6]. However, the need to improve the lifetime to 10^5 hours or better has been a major impediment to commercialization of red VCSELs, which is the reason we got involved in studies of red VCSEL degradation. As we shall see, the physics of device degradation has proved to be quite different from that observed in 850 nm VCSELs.

6.1.3 Background information on alloy ordering in AlGaInP alloys

6.1.3.1 *Why random alloy devices are preferable for most applications.*

A substantial difference between the red InGaP VCSELs, and the 850 nm VCSELs made from AlGaAs, is the importance of alloy ordering and spatial separation of electrons and holes in the former. Alloy ordering, when it was first discovered, was referred to as the "50 meV problem," since the unwanted partial ordering observed in optoelectronic devices reduced the bandgap by about 50 meV [7], or increased wavelength by about 17 nm. Electron diffraction and high-resolution TEM have subsequently shown that the ordered alloy consists of alternate

planes of the group-III sublattice enriched with Ga, In, Ga, In, etc., oriented on the $1\bar{1}1$ or $\bar{1}11$ directions, as shown in Fig. 6 - 1 for an ideal fully-ordered structure. It is typical for one of these two $\{111\}_B$ variants to be present in much larger portions than the other variant when growing with the off-axis substrates used in our growths [8].

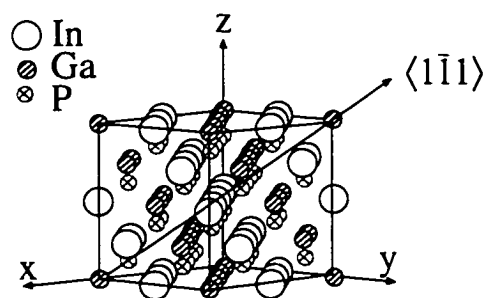


Fig. 6 - 1: Drawing of ideal ordered lattice, viewed nearly along the $[110]$ direction (after ref. [9]). Alternate group III planes along the $\langle 111 \rangle$ are made of Ga and In respectively. The order parameter of the lattice shown is 1: i.e., a perfectly-ordered lattice is depicted.

(These numbers are given for low-temperature, 2K.) The room temperature bandgap of the random alloy is blue-shifted by 85 meV or 28 nm as the ambient temperature is increased, for fully random alloy, and by 65 meV or 24 nm for the somewhat more ordered random alloys found in typical device growths [12], for reasons which are well described by Ernst et al. [13].) Due to this bandgap drop, ordered InGaP makes infrared lasers, rather than the desired red lasers.

In addition to objections in principle to the use of ordered alloys, there are practical considerations also driving us toward a selection of the random alloy. In practice, alloys with an ordering parameter greater than 0.55-0.6 have not been observed [14], and the ordered GaInP which has been grown has a high density of unwanted anti-phase boundaries (APBs) [15]. Three models of inhomogeneity in GaInP are shown schematically in Fig. 6 - 2. The "concrete" model is clearly not correct for materials where ordering has intentionally been enhanced, and recent results have largely discredited it [16]. Intentionally-ordered material generally has large ordered domains [17], with boundary walls which can be shown to be infinitesimally thin using stereographic projections of TEM images [18]. (It should

On paper, at least, a perfectly ordered alloy would have superior gain characteristics to the perfectly random InGaP alloy, due to the reduced density of states in the valence band [10]. In practice, there are a number of problems with alloy ordering. First, alloy ordering causes a significant drop in bandgap: perfectly random $\text{In}_{.48}\text{Ga}_{.52}\text{P}$ has a bandgap of 2.005 (618 nm), while perfectly ordered InGaP_2 theoretically has a bandgap of only 1.534 (808 nm) [11].

be noted that Ernst et al. found many samples had much thicker boundary walls [17]). As we shall discuss later, the piezoelectric strain and phase separation in ordered alloys are believed to cause spatial separation of electrons and holes, leading to weaker, spatially-indirect recombination.

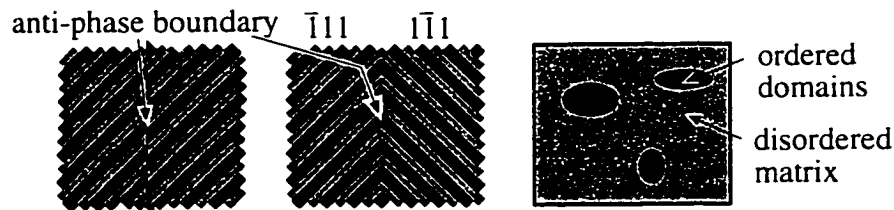


Fig. 6 - 2: Schematic views of inhomogeneity in partially-ordered GaInP. Anti-phase boundaries between same-orientation planes (left) or different orientation planes (center) represent intersections between ordered domains. Gray and black lines represent alternating Ga-rich and In-rich planes. "Concrete" model is shown right, with (more) ordered domains embedded in a disordered matrix.

In material which supports two ordering directions (i.e., nearly 001-oriented substrates), small platelets or "lamellae," of ordered alloy are observed. The lamellae are ~1-2 nm thick. Rows of lamella form domains on the order of 20x200 nm across in one report [19]. A cross-sectional TEM image of an ordered growth is shown in Fig. 6 - 3.

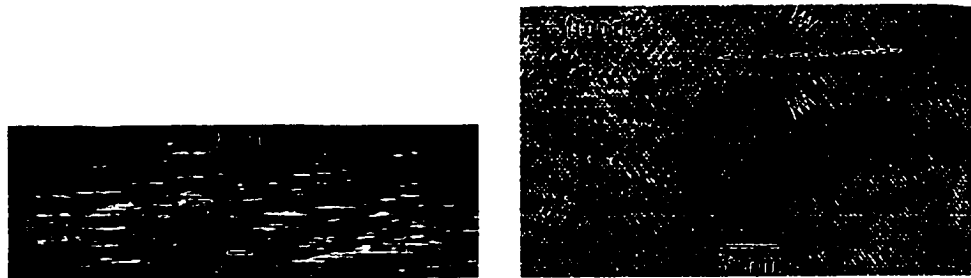


Fig. 6 - 3: A cross-sectional Dark-field TEM image (left) of ordered InGaP grown on a 001 wafer at 675° is shown. The orientation and size of the domains can be estimated from this image; the dotted line shows the ~12° angle the anti-phase boundaries follow in this sample. A lattice image is shown to the right, where the two alternating $1\bar{1}1$ and $11\bar{1}$ directions for ordering are indicated by arrows, along with the boundary between the domains. (after ref. [19])

As a result of these small domains of irregular size, with distinct crystal boundaries between one another, the photoluminescence characteristics of ordered alloys show weaker PL, and significantly broader full-width half-maxima (FWHMs) than those of the random alloy, and show little laser gain with standard growth

techniques [10]. In short, the ordered alloys which have been grown have been far from ideal, and are not suitable for use in lasers.

Larger ordered domains are observed at higher growth temperatures, but have reduced ordering parameter [10]; such work has generally used off-axis substrates oriented toward the $\langle 111 \rangle_B$ which promote ordering in a single direction. The dimensions of these lamellae are smaller for AlGaInP than for GaInP [10].

6.1.3.2 Summary of previous work in structural and luminescence characterization of ordered alloys.

In photoluminescence experiments, the weakly-ordered alloy behaves as one would expect, with the bandgap (as determined by PLE) at about the same wavelength as the luminescence peak [13, 20]. By contrast, in the ordered alloy, the PL luminescence peak occurs at wavelengths substantially below that of the bandgap measured by PLE [13, 20]. This is consistent with spatially-indirect recombination being responsible for the low-energy tail of the luminescence signature. Further evidence of spatially-indirect luminescence has included time-resolved PL, which has shown that the low energy peak has a decay time more than three orders of magnitude slower than the normal, spatially-direct luminescence [20, 21]. Finally, while the wavelength of the direct recombination peak does not change as a function of excitation intensity, the spatially indirect recombination peak blue-shifts with increasing excitation intensity, due to the fact the limited number of low-energy indirect states quickly become saturated, leaving only higher energy states available [13, 20, 21].

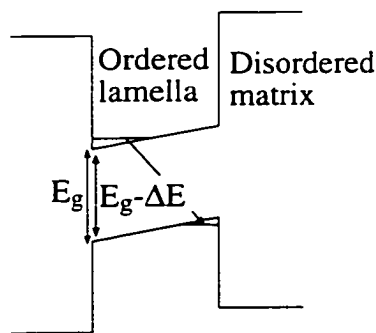


Fig. 6 - 4: Band-diagram of spatially-indirect recombination in ordered domains.

While the details of the spatially-indirect recombination are still not fully understood, the most recent evidence supports a picture like that shown in Fig. 6 - 4. A type I (straddling) band lineup is believed to be present from recent field-dependent measurements [22], rather than the type II lineup which had been widely expected earlier [13]. Piezoelectric charges on the ordered domains, due to strain, create the fields responsible for the “tilts”

shown in the band diagram [23]. However, recent electroreflectance measurements have cast some doubt on these results [24]. These fields allow a bandgap reduction " ΔE " shown in the figure, similar to that seen due to the quantum-confined stark effect (QCSE) [25].



Fig. 6 - 5: TEM Image of $\langle 113 \rangle A$ sample, taken in cross section, showing spinodal-like phase separation and columnar structure (after ref. [19])

Another possible source of spatially-indirect recombination is addressed only tangentially in the literature since its presence is far harder to quantify: phase separation [19]. This is where small indium-rich and gallium-rich regions alternate laterally, with a type-II band offset (indium-rich material attracting the holes, and gallium-rich material attracting the electrons). This can also not be ruled out as the cause of spatially-indirect recombination from our observations [17]. Evidence has been found that phase separation becomes more pronounced as the substrate's misorientation angle is increased [26]. Fig. 6 - 5 shows evidence for phase separation from a sample grown on a $\langle 113 \rangle A$ substrate at 775 °C: conditions nearly identical to those of the

lasers we focus on in Section 6.5 when discussing ordering.

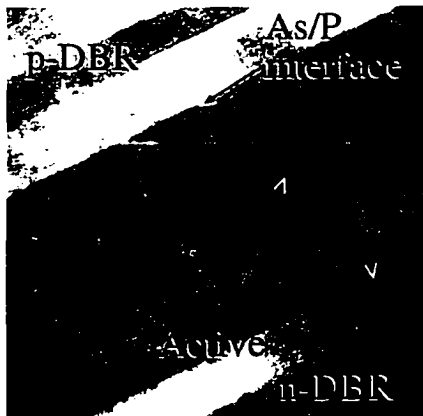


Fig. 6 - 6: TEM image of the active region of an InGaP red VCSEL, grown on a $\langle 311 \rangle A$ substrate. Note columnar microstructure (due to phase separation) in the active region. (Courtesy of Dr. Ray Twisten.)

This same columnar microstructure can be seen in TEM images of an actual VCSEL grown on a $\langle 311 \rangle A$ substrate. The image (Fig. 6 - 6) was provided by Dr. Ray Twisten of Sandia National Laboratory, and was taken using a 4-beam condition. The images shown were taken in May 1996 — the columnar microstructure was thought to be due in part to reactor turbulence, and has subsequently been reduced by changing growth conditions.

Among the parameters influencing the degree of ordering during growth are substrate orientation, III-V ratio, and growth rate and temperature. If growth temperature is too low, the atoms have insufficient mobility to move into the ordered state, while at very high temperatures, thermal energy and entropy push the atoms off the ordered sites. Ordering is highest at “intermediate” temperatures: usually about 680°C [27]. It is worth noting that essentially all growth of InGaP alloys is done by MOCVD. Orientations of 2–6° toward the $\bar{1}\bar{1}0$ (or $11\bar{1}B$) direction are used when *enhanced* ordering is desired [11]. The 15° misorientation toward the $11\bar{1}A$ direction used in our samples 1001 and 1002 is very typical among commercially-available red diode lasers. Studying samples grown at 6° and 15.6° toward the $11\bar{1}A$ (the latter also known as the $\langle 511 \rangle A$), Ahrenkiel has reported domains and columnar structure observed by dark-field TEM, contrary to previous simplifications that such wafers always provided a near featureless growth [28].

The degree of order can be calculated for lattice matched GaInP by noting that perfectly random alloys have a 2K bandgap of 2.005 eV (618 nm), and that (theoretically, at least) perfectly ordered alloy has a bandgap about 0.471 eV lower (808 nm). The formula given by Murata et al. for calculating the order parameter S is: [11]

$$S = \sqrt{\frac{2.005 - E}{0.471}}$$

where E is the 2K bandgap energy of the InGaP being studied, in eV. Other researchers prefer the symbol “ η ” to denote the order parameter: it is calculated with the formula shown above, and is identical to “ S .” The definition of the order parameter is that the enrichment of alternating layers of the lattice is given by $\text{Ga}_{0.5(1+\eta)}\text{In}_{0.5(1-\eta)}\text{P} / \text{Ga}_{0.5(1-\eta)}\text{In}_{0.5(1+\eta)}\text{P}$ [10]. Because quantum confinement effects cause a blue shift, as discussed in Appendix F, we add 10 nm to the wavelength, or subtract 28 meV from the energy observed, to obtain the equivalent bulk energy for use in the above formula. The bandgap is also reduced by 79 meV by the increased In mole fraction in our compressively strained $\text{Ga}_{.46}\text{In}_{.54}\text{P}$ QWs; thus we must add this amount to the observed photon energy before using Murata’s formula [29, 30].

6.2 Description of laser structure



Fig. 6 - 7: TEM of layer structure of a red VCSEL from Sandia National Labs. (Courtesy of Dr. Ray Twisten.)

The three red VCSEL laser wafers studied were obtained from the Honeywell Technology Center. The layer structure is very similar to that perfected earlier at Sandia National Labs [2, 31], and DARPA technology transfer programs have assisted the development of red VCSELs at Honeywell [32] and Xerox [1], through cooperation with Sandia. The DBR mirrors are made from quarter-wave stacks of $\text{Al}_x\text{Ga}_{1-x}\text{As}$ / AlAs (49/52 nm), with 33 pairs (3.3 μm) in the p-DBR, and 55-1/2 pairs (5.6 μm) in the n-DBR. Grading and pulse

doping is used to reduce the mirror resistance [32]. The central confining region, which makes a one-wavelength cavity (0.22 μm), is undoped, and made of various $(\text{Al}_x\text{Ga}_{1-x})_5\text{In}_5\text{P}$ alloys. Three compressively-strained 10-nm-wide $\text{Ga}_{0.46}\text{In}_{0.54}\text{P}$ quantum wells provide gain. As with virtually all production of AlGaInP alloys, MOCVD was used. Growth was performed in an Aixtron 200/4, at a temperature of 750-775°C. At Sandia, similar structures were grown at 80-110 mBar (a lower pressure than the 200 mBar used to grow 850 nm VCSELs) [32]. The V-III ratio is important to both controlling device lifetime, and reducing unwanted ordering; a ratio of approximately 140 is used at Sandia [5], along with a higher growth temperature of 800 °C. A TEM image of the layer structure, provided by Dr. Ray Twisten of Sandia National Laboratories, is shown in Fig. 6 - 7. (Note that Sandia used 4 or 5 thin (6 nm) QWs, rather than 3 thicker (10 nm) QWs like Honeywell).

The processing of the device structure is similar to that of the 850 nm VCSELs, although the device is smaller: a 15 μm -diameter proton implant is used, with a 10 μm aperture opening. This smaller device size, the greater number of DBR pairs, and the greater thermal resistivity of $\text{Al}_x\text{Ga}_{1-x}\text{As}$ relative to $\text{Al}_{16}\text{Ga}_{84}\text{As}$ [33], all combine to give the red VCSEL a higher thermal resistance (1.2 °C/mW)

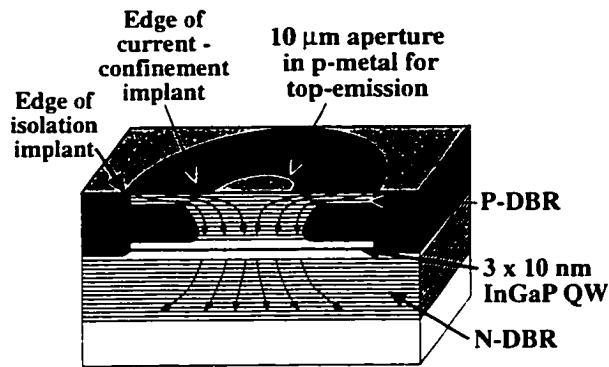


Fig. 6 - 8: Schematic of red VCSEL structure studied.

than their 850 nm counterparts ($0.8\text{ }^{\circ}\text{C/mW}$). Further, output power from red lasers generally rolls over more rapidly than from equivalent infrared lasers, due to limitations in electron confinement which can be obtained in the AlGaInP alloy system [29, 30]. The structure is shown schematically in Fig. 6 - 8.

As mentioned earlier, three wafers were studied. Two of the wafers, #1001 and #1002, were grown on substrates oriented 15° -off from the 100 toward the $\langle 111 \rangle$ A. The third wafer, #999B, was grown on a $\langle 311 \rangle$ A-oriented substrate (i.e., 26.8° toward the 111 A). Again, this orientation, like the 15° -off orientation, tends to reduce both alloy ordering and oxygen incorporation. Growth conditions had to be significantly modified between the different substrates, due to differences in dopant incorporation and growth nucleation between the two orientations. Substantial differences were observed between the 15° -off wafers and the $\langle 311 \rangle$ A-orientation wafer. VCSELs on the two 15° -off wafers showed lower initial performance than the VCSELs on $\langle 311 \rangle$ A wafer 999B, (0.7 mW peak, vs. >1.2 mW peak), but the devices on the 15° -off wafers could be improved by operation at high current (as discussed in section 6.4), which was not observed in wafer 999B. Further, differences in the cross-sectional CL data were observed between the $\langle 311 \rangle$ A wafer (which followed the familiar pattern observed in 850 nm VCSELs as shown in Chapter 4) and the 15° -off wafers (which showed substantially different CL images than those expected). Finally, substantial differences in spatially-indirect recombination were observed between the VCSELs on the $\langle 311 \rangle$ A wafer and those on the 15° -off wafers, as can be seen by comparing the CL data in sections 6.4 and 6.5.

6.2.1 Stain etching of red VCSELs

The true depth and width of the proton implants can be verified using stain etching, of the sort seen earlier in Chapter 3. As discussed earlier, the p-type material etches significantly more rapidly than n-type or implanted material. The stain etch boundaries thus show where the boundaries of the proton implantation are. However, the tails of the implant, which can significantly affect the material properties, etch more like unimplanted material, and thus cannot be easily detected using this technique. Scanning Capacitance Microscopy, or other 2-D dopant profiling techniques of the sort discussed in Chapter 9 are needed. This limitation should be kept in mind when examining the images.

6.2.1.1 Images from 15°-off wafer (1001)

The same sample used for cross-sectional electroluminescence and EBIC was later stained with an A-B etch [34] and imaged. These images are shown in Fig. 6 - 9. The differences between the aged and unaged devices, if any, are not obvious.

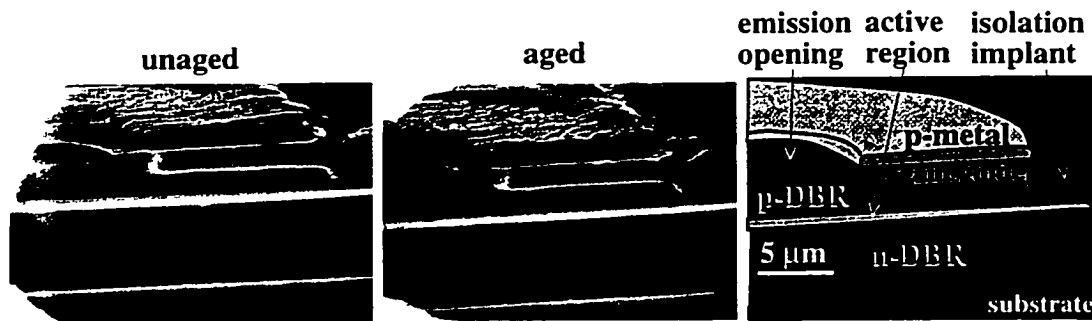


Fig. 6 - 9: Stained cross-sections from wafer 1001.

6.2.1.2 Images from (311)A wafer (999B)

Similar stain-etched samples were created from wafer 999B using the cross-sectional CL sample. For reasons that were not understood, the etch rate seemed considerably lower on this sample than the preceding one. One parameter that was difficult to control was the intensity of the incident light during the A-B etch, although it is not known how greatly that affects etch rate. In addition, the device was stained about an hour and a half after the sample from wafer 1001 was. It is not known how quickly the A-B etch loses its strength. Finally, the etching plane is

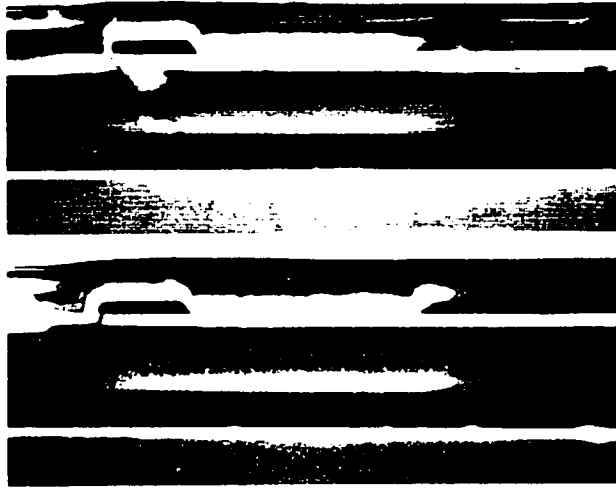


Fig. 6 - 10: Stained cross-sections from wafer 999B: undegraded sample R2 (top); degraded sample A4 (bottom).

not the same between sample types, which could also possibly affect the results. It should be noted that while the isolation implant in the 15° -off wafer clearly goes through the active region, the isolation implant in the $\langle 311 \rangle$ A wafer appears to stop shy of the active region. This may partially explain some of the differences in device behavior which we will discuss in the following sections, which possibly are not solely dependent on the difference in substrate orientation.

6.3 General observations in degraded red VCSELs

6.3.1 Top-emitting electroluminescence

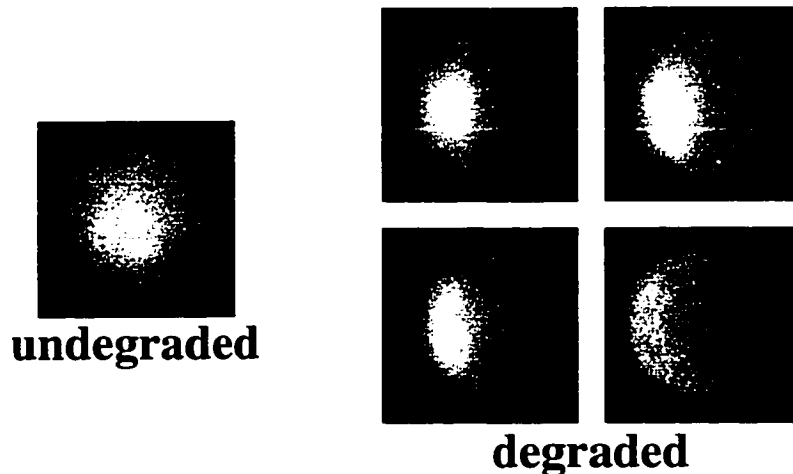


Fig. 6 - 11: Spectrally-filtered electroluminescence images of undegraded and degraded VCSELs.

Spectrally-filtered electroluminescence images were collected on undegraded and degraded VCSELs from 15°-off wafer 1002, and are shown in Fig. 6 - 11. Since no sample preparation was used, the aperture blocks us from seeing light outside the central region. Note that the degraded VCSELs show the same diffuse darkening observed in 850 nm VCSELs. The darkening always appears to come from the right, which may be due to a slight misalignment between the aperture and the proton implant. Note the absence of dark-line defects, which can be clearly observed, when they are present, using the filtered EL technique.

6.3.2 Cross-sectional electroluminescence

Electroluminescence (EL) images were taken from the edge of a 15°-off VCSEL array which was polished down to the centerline of the devices. The array first had several lasers aged over the course of a few days, and one laser was bias-annealed, as will be discussed later in the chapter. After aging, the sample was protected with a removable glass cover bonded with cyanoacrylate glue, then polished down to the centerline. The resulting cross-sectional sample had EL images with fairly uniform luminescence profiles, even from degraded devices, which had been aged to total failure. This was different than had been seen in some 850 nm VCSELs, where the central area was almost totally dark in EL.



Fig. 6 - 12: Cross-sectional electroluminescence image and optical image from a degraded red VCSEL on a 15°-off wafer. To the left is a high-contrast version; to the right is a version with higher exposure and lower contrast. The p-metal contacts can be seen at top, and provide a scale for the image.

6.3.3 Cross-sectional EBIC

The same sample from 15°-off array 1001 described in the above section (6.3.2) was examined using current-collection imaging (also known as electron beam induced current, or EBIC, imaging). A 15 keV beam in a Hitachi S-2400 scanning electron microscope (SEM) was used; a Keithley 428 current amplifier was used to amplify the collected current, and its output was fed into the auxiliary input of the microscope. Secondary emission images and electron beam images were

collected separately, and later superimposed using the layers feature in Photoshop, along with the “Screen” mode. The results are shown in Fig. 6 - 13. Even though

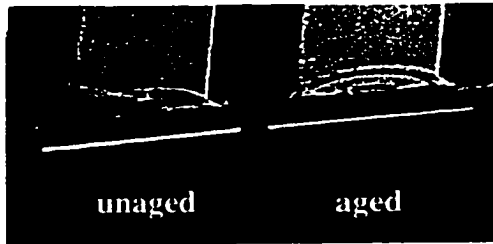


Fig. 6 - 13: Cross-sectional EBIC images of unaged and aged red VCSELs show little difference as a result of aging.

the aged device was degraded to total failure, only a modest reduction in collected current was observed when compared with its unaged neighbor. This small difference was not considered significant, given that the 10% reduction in efficiency was within the 10% range of device-to-device variation between neighboring unaged devices.

6.4 Observation of bias-annealing effects in 15°-off red VCSELs

6.4.1 Thermal impedance of red VCSELs

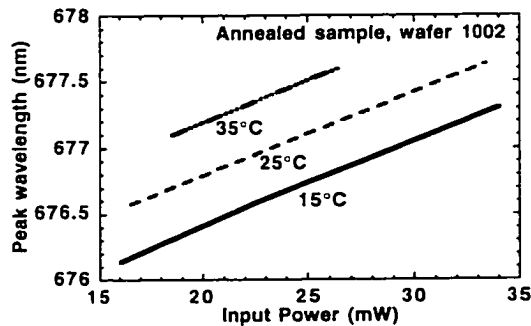


Fig. 6 - 14: Peak wavelength as a function of drive current and stage temperature.

The bias-annealing phenomenon reported here is actually dependent on both photon *and* thermal energy, so estimations of device junction temperature are important to understanding the annealing process. Surprisingly, I was not able to find measurements of the thermal impedance of red VCSELs in the literature, so I

measured it independently, using the spectral-shift techniques described earlier [35, 36]. The measured wavelength shift as a function of temperature was $0.44 \text{ \AA/}^\circ\text{C}$. The wavelength shift as a function of input power was 0.53 \AA/mW . Therefore, the resulting thermal impedance was $1.20 \text{ }^\circ\text{C/mW}$. There is an uncertainty of $\pm 20\%$ in this value, based on lateral mode-hopping and other experimental issues. A summary of the spectral measurements taken can be seen in Fig. 6 - 14. Another adjustment can be made to account for the fact that the temperature measured by

these spectral measurements is essentially the *average* temperature of the cavity, which extends more than a micron above and below the cavity, given the average mirror penetration depth. The peak temperature at the quantum well, which is what we are truly concerned with, is at least 5% higher than the “average cavity temperature.” While this can be neglected under ordinary operation, it is important for the bias-annealing we will discuss later.

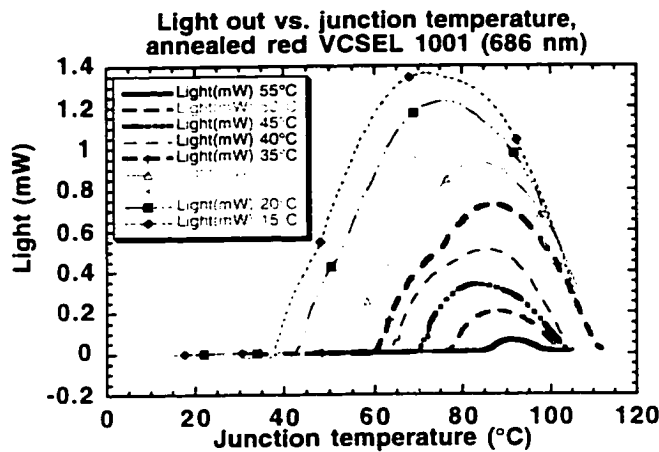


Fig. 6 - 15: Light out plotted against junction temperature, which rises with drive current. Stage temperature is shown in the insets; junction temperature was calculated using the input power minus output power times the thermal resistance (i.e., $T_j = (P_i - P_o)R_{th}$).

Estimated junction temperatures as a function of output power are shown in Fig. 6 - 15, which will be useful for estimating thermal stresses present, and acceleration factors, during accelerated aging. For 850 nm VCSELs peak temperatures are typically over 120 °C, and maximum lasing temperatures are around 200 °C. Due to lower electron confinement present

in red VCSELs, roll-over occurs at significantly lower temperatures, as can be seen here.

6.4.2 Improvement in device efficiency in annealed 15°-off samples.

Initially we set out to study degradation under accelerated aging conditions, and a surprising effect was observed. The L-I curves taken during the aging sequence are shown in Fig. 6 - 16, showing *increasing* output power as the device is aged at 14 mA and above.

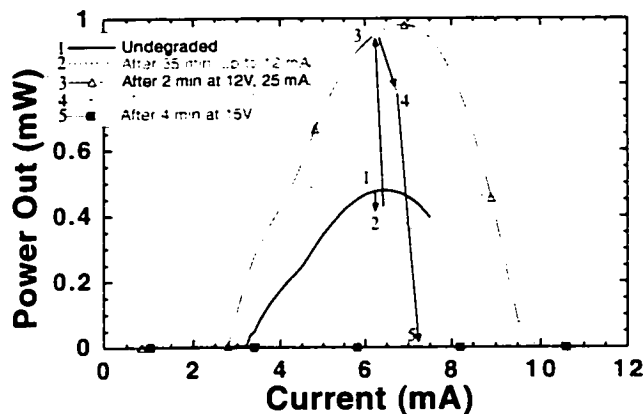


Fig. 6 - 16: L-I curves of VCSEL from wafer 1002 change as a function of stress. Peak power falls during initial aging at reasonable currents (2), but under higher current stress, peak power actually *rises* to exceed the peak power of the undegraded device (3), by a factor of 2 (!). Further increase in the stress degrades the device (4), and eventually eliminates lasing (5).

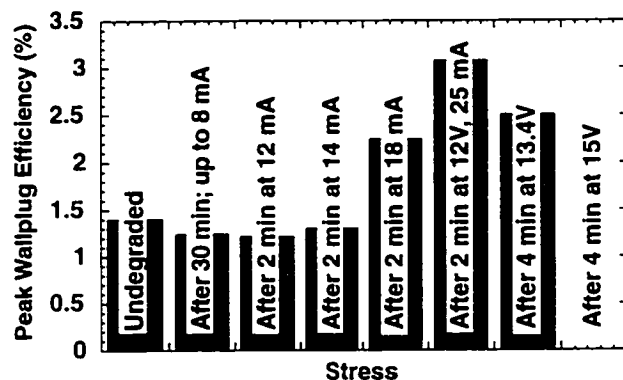


Fig. 6 - 17: History of wallplug efficiency from device with steadily increasing current stress applied. Note that a range of current stress conditions will actually improve the device efficiency.

Initially, slow degradation was observed when aging the device at currents just past device roll-over. Currents were increased to speed up device degradation. In 850 nm VCSELs, degradation increases monotonically with increasing drive current. However, in the red 15°-off wafers (1001 and 1002), the device degradation rate increases with increasing current until ~8 mA is reached.

As current is increased to 12 mA, little degradation is observed. Between 12-20 mA, device performance will actually *improve*(!) As current is further increased, above 20 mA, the device degradation rate starts to increase again. The history of the device shown in Fig. 6 - 16 is typical, and is summarized in Fig. 6 - 17.

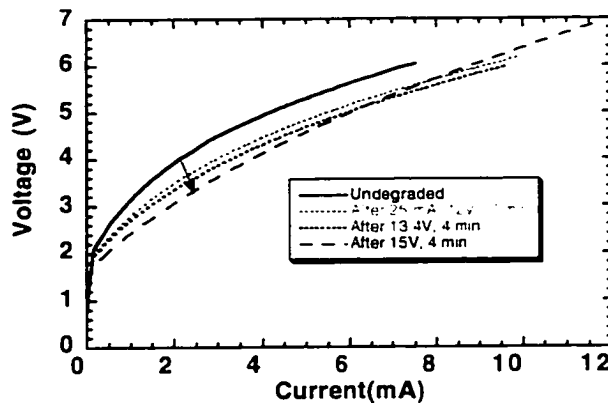


Fig. 6 - 18: I-V curves show drop in turn on voltage as device is bias-annealed.

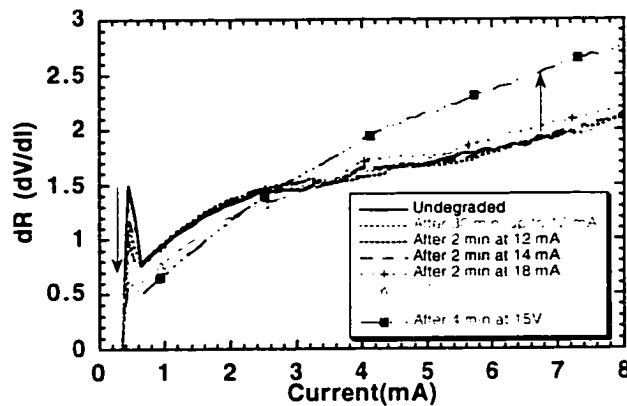


Fig. 6 - 19: Differential resistance curves show increase in differential resistance as device is bias-annealed.

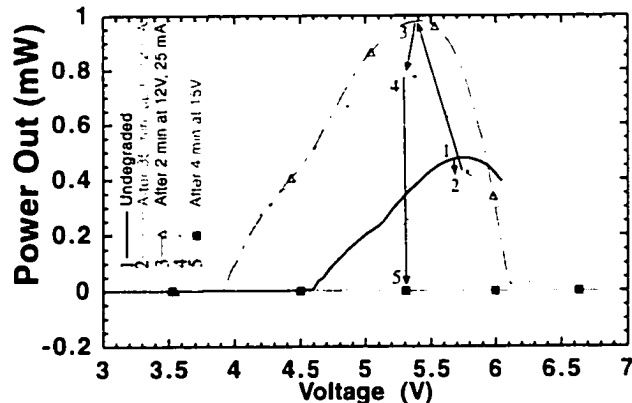


Fig. 6 - 20: L-V curves change as a function of stress, from device previously shown in Fig. 6 - 16. Note significant reduction in threshold and operating voltages after the device has been bias-annealed (curve 3).

Further study of device characteristics shows that, similar to 850 nm VCSELs (although much more dramatic in magnitude), the turn-on voltage drops, and series resistance increases in devices. These effects can be seen in the I-V curves (Fig. 6 - 18), and its derivative dR curves (Fig. 6 - 19).

The drop in turn-on voltage appears to be important: it significantly reduces threshold voltage, and thus device heating. This drop in threshold voltage can be seen in Fig. 6 - 20. Note that initially, threshold voltage increases (during reasonable annealing), due to the significant increase in threshold current for degraded VCSELs, along with the minimal changes in I-V characteristics for normal (modest) degradation currents. As the stress is increased into the "annealing" current range, where "anomalous degradation" (read "improvement") takes place, the drop in turn-on voltage is significant, and thus threshold voltage drops.

6.4.3 Improvement in lifetime in annealed 15°-off samples

A major enhancement in reliability was obtained in red VCSELs by annealing devices before they were aged. Typical results for devices from each of the two 15°-off wafers are shown in Fig. 6 - 21. In both cases, the lasers were aged at currents near peak output power (i.e., ~7 mA). The decline in peak power is less useful than the change in power at the (lower) operating bias. If a laser is operated at a fixed current, even a relatively small drop in peak power (combined with the increase in threshold which accompanies it) will terminate lasing. Thus, for fixed current bias, the lifetime enhancement obtained by bias-annealing devices is in excess of 10x.

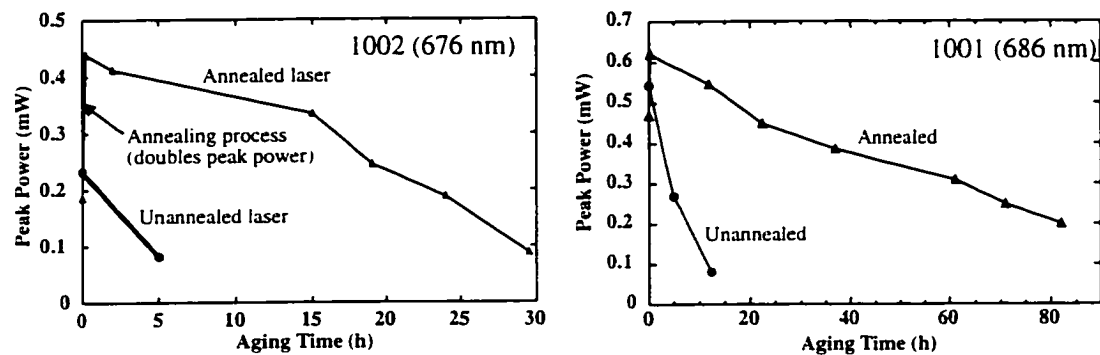


Fig. 6 - 21: Peak power versus aging time for two typical annealed and unannealed red VCSELs. Note how much longer the annealed device is able to operate.

6.4.4 Improvement in high-temperature operation in 15°-off samples

6.4.4.1 Improvement in T_0

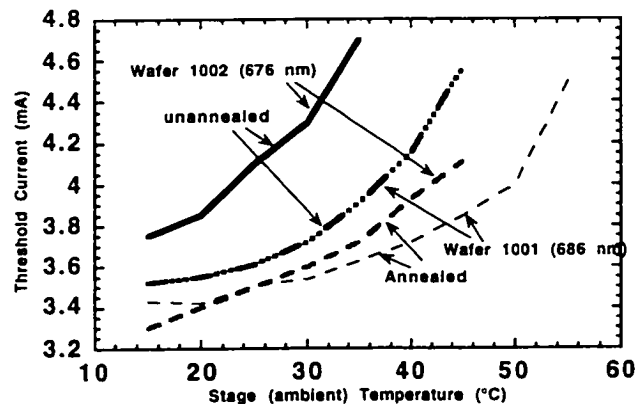


Fig. 6 - 22: Threshold current as a function of temperature.

Red VCSELs from the two 15°-off wafers 1001 (686 nm) and 1002 (676 nm) were characterized for both spectra and L-I-V curves before and after bias-annealing. We used a thermoelectric-cooler-controlled stage, with a starting temperature of 15°C, and temperature increments of 5 °C, increasing until lasing was no longer

observed. As can be seen in Fig. 6 - 22, annealing the red VCSELs provided a reduction in threshold current. More importantly, perhaps, it increased the range of available operating temperature by 10 °C, and improved T_0 . T_0 is defined by the relation $I_{th} \propto e^{T/T_0}$, and is calculated using the formula $T_0 = (T_2 - T_1) / [\ln(I_2/I_1)]$, where T_2 is the upper temperature under consideration, I_2 is its corresponding threshold current, and T_1 and I_1 are the respective stage temperature and threshold current at the lower end of interest [37]. For the two sample types tested, we compared the T_0 of the bias-annealed and unannealed VCSELs. We expect the shorter wavelength sample (1002, with 676 nm emission wavelength) to be more temperature-sensitive due to lower electron confinement (since the Fermi level has to rise closer to the barrier level when the emission energy is increased). The T_0 of wafer 1002 is 108 °C before annealing and 167° after. For sample 1001, with 686 nm emission, T_0 was 191°C before annealing, and 331° after annealing. Note also that these T_0 's are substantially better than the values observed for ordinary red stripe lasers, where T_0 would typically be on the order of 70°C (although better values have been obtained recently [38]). The high T_0 values of the red VCSEL are an advantage of the VCSEL design [35, 39], and follows from the fact only a single longitudinal wavelength can be supported during lasing. The further improvement in T_0 after annealing may come from the increased wallplug efficiency and reduced threshold voltage lowering device heating during operation. In addition, electron confinement improvements, discussed in the following section, may be partly responsible for the improvement in T_0 .

6.4.4.2 Possible improvement in roll-over temperature

Analysis of the peak output power and the junction temperature at which the peak occurs, are shown in Fig. 6 - 24. As expected, the temperature at which roll-over occurs is approximately constant, even though the input power and currents densities that these temperatures are obtained at vary considerably. The highest point shown is the one at 1.35 mW out, where the high junction temperature was obtained by high pumping intensity and a low stage temperature. The current and power densities at the peak power were 3.9 kA/cm², or 23.5 kW/cm², respectively. By contrast, on the lowest points on the graph, the temperature was reached more by

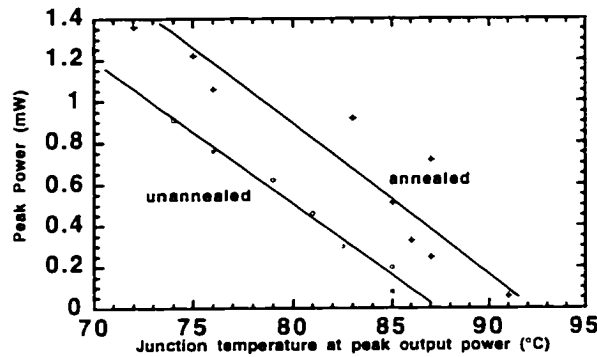


Fig. 6 - 24: Peak output power versus calculated junction temperature at peak power for sample 1001. Note apparent increase in roll-over temperature for bias-annealed VCSEL.

increase appears to be on the order of 7 °C. This increase would not necessarily be expected solely on the basis of improved conversion efficiency due to reduced non-radiative centers. With improved efficiency, a reduction in junction temperature for a given output power would be expected, but not an increase in the roll-over temperature. One possible explanation for this behavior would be similar to that discussed in the recent paper by Floyd and Treat [38]. In this paper, they observe improved T_0 and external efficiency after rapid thermal annealing of their GaInP lasers at 400-550 °C. Floyd and Treat attribute this improvement to increased

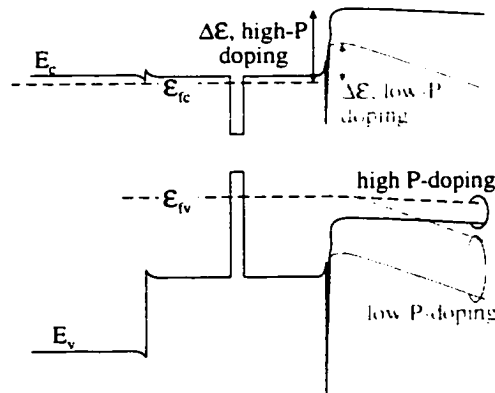


Fig. 6 - 23: Schematic diagram of electron leakage for a simplified flat-band condition. The electron confinement is increased, and the leakage current is decreased, when high hole concentrations are present (after ref. [30]).

heating from the stage, with a lower pumping intensity of 2.83 kA/cm², and 14.2 kW/cm² for the lowest point on the annealed curve.

Examining Fig. 6 - 24, we see what appears to be a systematic increase in the temperature which can be obtained before roll-over occurs for the bias-annealed VCSELs. This

electron confinement, due to removal of hydrogen which may be passivating the acceptors, thereby reducing electron confinement energy, as shown in Fig. 6 - 23. Although our estimated junction temperatures are far lower during our bias-annealing (230 °C) than the temperatures used by Floyd and Treat, the presence of minority carrier recombination supplies the majority of the energy needed for the annealing process [40]. While a reduction in non-radiative centers seems to be a certain consequence of the annealing process,

further analysis will need to be done to determine whether improved carrier confinement is also being obtained in the process. This hypothesis could be verified using two-dimensional scans of doping profiles in bias-annealed and unannealed red VCSELs. See chapter 9 for more information on techniques for profiling carrier concentrations in two dimensions and on small devices.

6.4.5 Removal of proton implant damage by bias-annealing: observations using cross-sectional cathodoluminescence

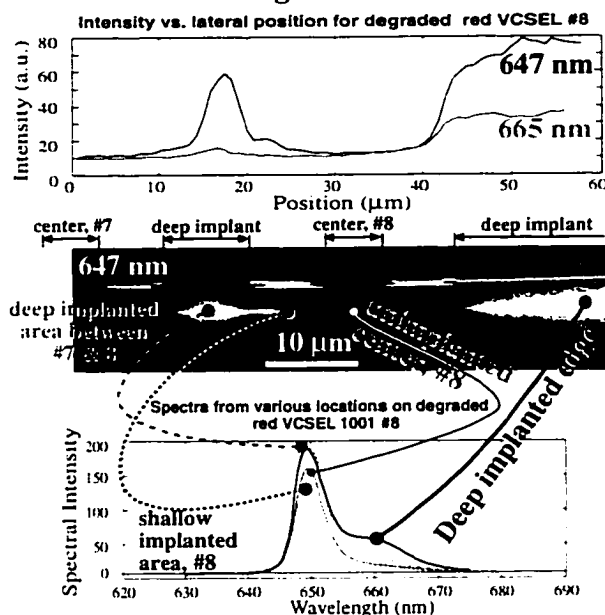


Fig. 6 - 25: Intensity profiles (top; background level ~ 6 counts), monochromatic image (center), and spectra from red VCSEL sample #8 (15°-off wafer 1001).

One of the most dramatic differences between the bias-annealed and unannealed VCSELs comes from comparing cross-sectional cathodoluminescence in annealed and unannealed red VCSELs. For reasons which are not clear, in the samples grown on 15°-off substrates, luminescence appears brightest in the areas which have been deep implanted, even for undegraded devices which have had no chance for implant annealing to take place. This was surprising, since the deep implant always kills luminescence

efficiency in other samples, either totally (as in the case of the 850 nm VCSELs) or almost totally (as in the case of the red VCSEL samples from the (311)A wafer 999B). Possibly the deep implant is not so deep as to fully penetrate the material. However, the stain-etched images shown in section 6.2 seem to refute this explanation, since the implantation does appear to go through the active region.

A device from the 15°-off wafer 1001 was selected with a few VCSEL arrays on it. Two VCSELs, #6 and #8, were aged overnight at 8 and 10 mA respectively. In addition, a third VCSEL (#2) was bias-annealed for 2 minutes at 18 mA. A glass coverslip was then bonded to the top of the array, and the sample was polished

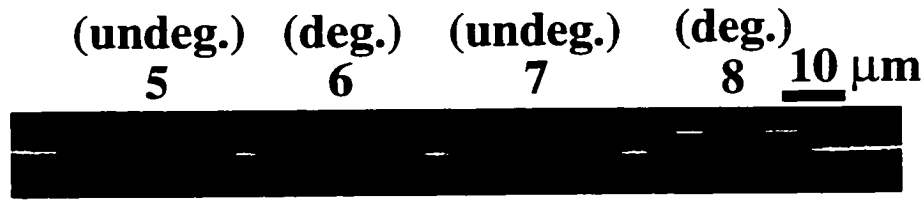


Fig. 6 - 26: Monochromatic image of degraded and undegraded VCSELs, taken at 650 nm (direct peak). This sample was normally-aged.

down to the centerline of the devices to allow the cross section to be examined by cathodoluminescence (CL). Data was then taken in a number of different ways: first, monochromatic images at a few wavelengths of interest were taken. Next, the linescan mode was used to scan along the length of the quantum well, and quantitative data on CL intensity vs. lateral position was acquired. Finally, spectra were taken. Although the opposite data acquisition sequence would have been preferable to allow better selection of the wavelengths, artifacts with sample contamination during spectral scans or linescans have previously affected monochromatic images (as discussed in Appendix E), so the image data was always acquired first to avoid potential problems. The resulting CL data, from a typical

degraded device, is shown in Fig. 6 - 25.

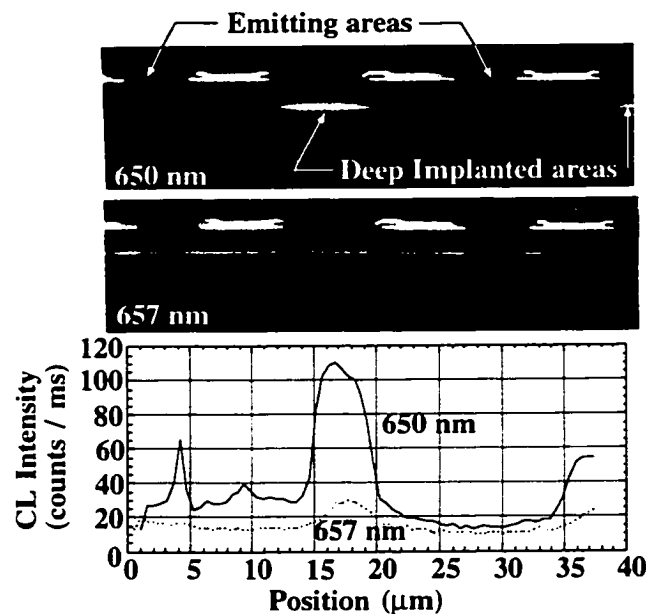


Fig. 6 - 27: Comparison of monochromatic image of an aged device taken at 650 nm (direct peak) and 657 nm (between direct and indirect peaks). Image at indirect peak (662 nm) is similar to that obtained at 650 nm.

When doing monochromatic imaging, at most wavelengths, the 15°-off samples are brightest in the deep-implanted regions. This can be seen in the image and accompanying linescans from degraded device #8 1001 (Fig. 6 - 25). Note the tail extending from the deep implant (just left of #8) toward it. This may be due to an annealing process which occurs during aging. Other than this subtle “tail,” and

the darkening evident at 654 nm, adjacent undegraded devices appeared almost identical to their degraded neighbors, as can be seen in the lower-magnification image of devices 5–8 (Fig. 6 - 26). The deep implant, and bright CL luminescence, extend well beyond the edges of the image. The “shoulder” to the long-wavelength side (662 nm) of the main peak (650 nm) is (we believe) due to spatially-indirect recombination from ordered alloy domains or inhomogeneous regions from phase separation, as we shall discuss at some length in section 6.5. Unfortunately, since the $\text{Al}_{0.5}\text{Ga}_{0.5}\text{As}$ / AlAs DBRs have an indirect bandgap throughout, they cannot be imaged by CL. Therefore, we are unable to know whether any mirror degradation, of the sort discussed in Chapter 4, is taking place in the red VCSELs.

As mentioned earlier, for these samples, CL efficiency (both at 650 and 662 nm) is highest in the deep implanted regions. At the wavelengths between the direct and indirect peaks (i.e., 653–658 nm), however, the samples appear to have nearly uniform brightness across the entire sample. A comparison of these two wavelengths is shown in Fig. 6 - 27. This wavelength range is clearly identified with a third peak in the PL spectrum (Section 6.5.2), although the third peak is not distinguishable in the CL data.

Now compare the CL image of the normally-aged array in Fig. 6 - 26 to that of the bias-annealed array from the same sample (Fig. 6 - 28). The contrast due to the deep proton implant has been largely removed during the anneal. Since only device #2 was bias-annealed, and no other lasers in this array were operated, we conclude that the effects of the anneal extend on the order of 50–100 μm laterally. The optical excitation is presumably more important in this process than the heat, although both trail off as one gets further away from the annealed device.

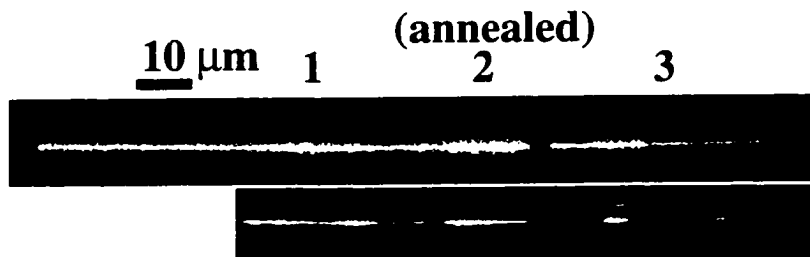


Fig. 6 - 28: Monochromatic image of an array containing a single bias-annealed red VCSEL, taken at 647 nm. Note the removal of the proton implant boundaries seen in unannealed samples. Strong thresholding is used in the lower image to show more detail of the luminescence.

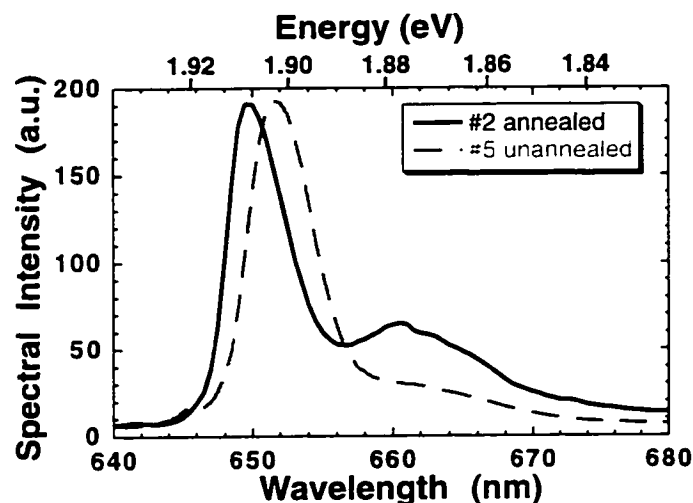


Fig. 6 - 29: Comparison of spectra from center of unaged, and bias-annealed VCSELs.

A comparison of the spectra from the bias-annealed and unannealed VCSELs is shown in Fig. 6 - 29. Note that as expected, the peak of the annealed sample is blue-shifted by roughly 6 meV due to a slight decrease in the order parameter due to disordering (or intermixing), as will be discussed in section 6.5.

However, the increase of the spatially-indirect peak in the annealed sample is totally unexpected, and we have no real explanation for this, since there is no reason we are aware of that antiphase boundary density (which is believed to be the most likely cause of the indirect peak at 662 nm) should increase in an annealed sample. This phenomenon would be better investigated by plan-view CL on similarly annealed samples, where cross-contamination between adjacent areas would not be able to influence the results. The microscopic processes at work during the annealing process are obviously quite complex. TEM characterization will likely be needed to determine how the microstructure of the device is changing.

In closing this cross-sectional CL section, we should note that similar cross-sectional cathodoluminescence experiments were performed on unaged, degraded, and bias-annealed VCSELs from wafer 1002 (which lased 10 nm shorter due to a reduction in the peak DBR reflectivity wavelength, but had a nearly identical active region and CL spectrum). Wafer 1002, which like 1001 was also grown on a 15°-off-100 substrate, showed nearly identical results. However, the results were very different than those we will show later from (311)A wafer 999B.

6.4.6 Improvement in current collection efficiency observed by cross-sectional EBIC.

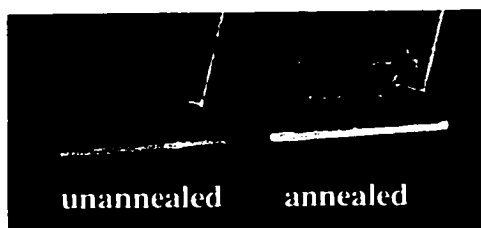


Fig. 6 - 30: Cross-sectional EBIC image of red VCSELs shows dramatic ($>2\times$) improvement in current-collection efficiency in bias-annealed VCSEL when compared to neighboring unannealed control.

The EBIC sample described earlier in section 6.3.3 also included a bias-annealed VCSEL, which was compared to the neighboring unannealed VCSELs. A very dramatic increase in current collection efficiency was observed ($\sim 2-4\times$), as is seen in Fig. 6 - 30. It seems likely that such a large enhancement can only be explained by a reduction in non-radiative centers in the cladding layers, in addition to annealing in the active region itself.

6.4.7 Discussion of bias-annealing in red VCSELs: 15° -off vs. $\langle 311 \rangle$ A samples

Improvement in device efficiency, particularly among proton-implanted lasers, is not a new observation. Indeed, it has been widely reported for 850 nm VCSELs during their early phase of aging [41, 42]. Further, Lang and Kimerling have earlier studied recombination-enhanced annealing of irradiated devices, and the annealing and improvement during operation [40]. Zhou et al. have observed a two-order-of-magnitude drop in hole trap concentration of devices with ideal stoichiometry after device operation (devices with non-ideal stoichiometry, however, showed a large increase in trap concentration) [43]. The improvement in 850 nm VCSEL efficiency early in the aging process has been attributed to a number of different causes, but primarily to annealing of proton implant damage, thereby reducing contact resistance and driving off hydrogen from dopant sites. This also has been thought to increase the effective diameter of the VCSEL. However, the behavior of the 15° -off red VCSELs differs substantially from the annealing reported earlier in 850 nm VCSELs (or for that matter, from the behavior seen in the 311-oriented sample #999B).

First, in all samples previously studied, operation past device roll-over resulted in rapidly increasing degradation rates as current was increased. The rise was particularly dramatic at currents above where the L-I curve had rolled over to

totally suppress lasing output. The VCSELs on (311)A wafer 999B follow this same expected behavior, with monotonically increasing degradation rate as a function of increasing drive current, as seen in Fig. 6 - 31. Lines through the data points are only as a guide to the eye. By contrast with the VCSELs from wafer 999B, the VCSELs from 15°-off wafer 1001 and 1002, show anomalous (negative) degradation rates from approximately 12 to 25 mA. This non-monotonic behavior is the first unusual observation unique to “bias-annealable” VCSELs.

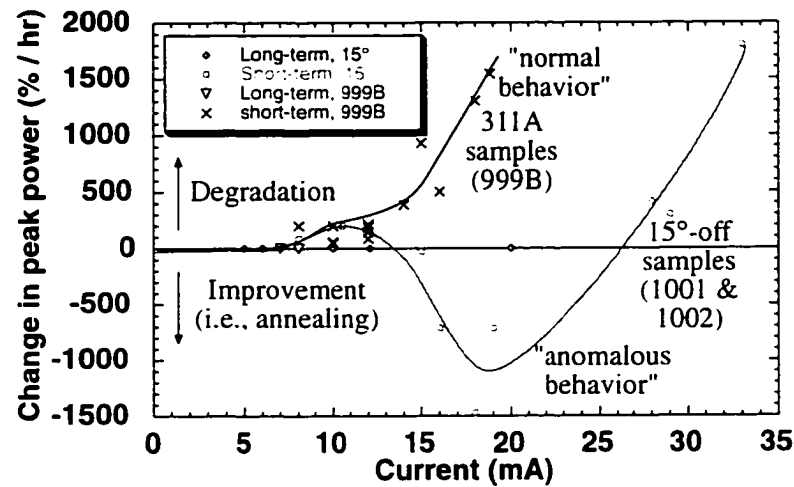


Fig. 6 - 31: Degradation rate as a function of drive current, measured using the formula $\{100\% \times P_{\max}(\text{after}) / (P_{\max}(\text{before}) \times \text{degradation time})\}$. Note the anomalous dependence of the 15°-off samples, which actually improve at higher currents.

The large scatter in the data of Fig. 6 - 31, it should be noted, is due to the different period over which the tests were made. Degradation (or annealing) was remarkably fast early on (the point at -1474% was only taken for 1 minute, while the point to its upper right at -720% was averaged over 5 minutes). Annealing or degradation slowed markedly after the initial “burn-in” phase, consistent with observations in edge-emitting lasers.

The second difference between the “annealing” in red VCSELs and that in other proton-implanted VCSELs is that, while some initial improvement in performance is observed when annealing, such improvements (if expected) should be observed across a range of operating conditions and not be strongly dependent on operation condition. However, no improvement in device characteristics is observed by operating at normal currents for red VCSELs. In addition, for 850 nm VCSELs,

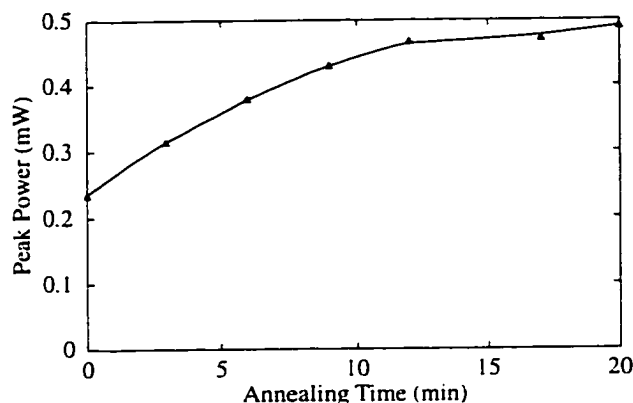


Fig. 6 - 32: Improvement in peak power for 673 nm red VCSEL using an 18 mA, 10V anneal. Improvement saturates after 10 minutes, asymptotically approaching 0.5 mW.

initial improvement in device characteristics, if rapid, is followed by equally rapid degradation. But in the red VCSELs, after the improvement from the anneal is observed, device improvement saturates after ~10 minutes at 18 mA, and no degradation is then observed, even after aging the device at 18 mA for hours. This saturation behavior is shown in Fig. 6 - 32.

Further, operation of a device at 12 mA results in a degradation rate nearly three times slower than degradation at 10 mA — also inconsistent with the behavior seen in 850 nm VCSELs. Again, while initial annealing might occur more rapidly in 850 nm VCSELs, the subsequent degradation would also be accelerated by a similar amount: this is not observed on the 15°-off red VCSELs.

Third, VCSELs which have been aged until they no longer lase (e.g., 8 mA overnight) have actually been “brought back from the dead” by annealing at (the usual annealing condition) 18 mA for 2 minutes (Fig. 6 - 33). We have never observed a similar recovery of a dead 850 nm VCSEL to lasing status.

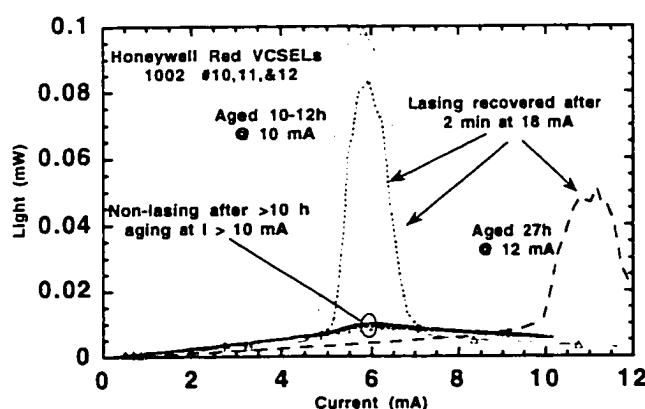


Fig. 6 - 33: VCSELs, which have been aged to non-lasing, recover lasing after bias-annealing treatment.

Fourth, and most obviously, no extension of the device lifetime through bias-annealing has been reported in the literature. We believe our bias-annealing is annihilating point defect clusters (as described by Zhou [43]). Since point defects are *required* for degradation (see Chapter 2), this

reduction in defects in turn lowers the degradation rate.

Substantial additional work will need to be done to understand why the changes described above take place, and why they are observed in 15°-off red VCSELs, but not in the 311-oriented VCSEL. It seems likely that both the very high junction temperature reached during annealing ($\sim 230^\circ\text{C}$), and the high photon intensity, are both needed to obtain the annealing effect.

It has generally been observed that for AlGaAs materials, about 2 eV is needed for migration of point defects to take place. The majority of that energy is supplied by a non-radiative recombination band-to-band, while the remainder requires a multi-phonon event [40, 44, 45]. Likewise for the annealing in the red VCSELs, both photons (or some other means of minority carrier injection) and phonons are needed to obtain the changes observed. It should be noted that thermal annealing alone is not sufficient to create the changes seen: thermal annealing to over 400°C for ~ 20 seconds or more is typically used to anneal the ohmic contacts, so the device has presumably already seen thermal exposures far in excess of those encountered in our 18 mA bias-anneal of 2 minutes at a 230°C junction temperature. Further, the light alone from the active region is also insufficient, as the maximum internal intensities of light are obtained at currents not far past roll-over, and no annealing is observed at these currents. Due to the problems with red lasers have

with electron confinement, at temperatures over 70 - 100°C (depending on the details of the structure), carrier leakage becomes the dominant path for additional injected electrons, and no further increase in intensity can be obtained [46]. Thus,

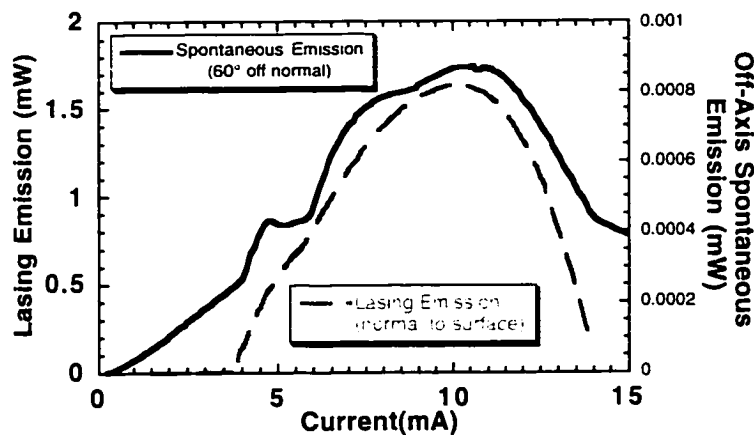


Fig. 6 - 34: Spontaneous emission from red VCSEL, as collected 60° off from emission axis (solid line). Lasing output (gray dashed line) is also provided from the same device for comparison.

photon intensity at the 18 mA bias-annealing condition is lower than the photon flux at 10 mA, where no annealing is observed. We measured spontaneous emission 60 degrees from normal (a large enough angle to not collect any lasing light): the L-I curve of the spontaneous emission is shown in Fig. 6 - 34. While spontaneous emission continues to rise well past rollover on 850 nm VCSELs, as shown in Chapter 5, it rolls over not far from where the lasing output starts to drop.

6.5 Aging-induced changes in red VCSEL cathodoluminescence spectra for $\langle 311 \rangle A$ samples

6.5.1 Previous observations of disordering and intermixing in GaInP and AlGaInP alloys.

Numerous authors have observed intermixing or disordering taking place in GaInP alloys, where the ordered alloy is converted to a random alloy. One method of alloy disordering uses implantation of non-doping ions (e.g., N^+ [14, 47] or Ar^+ [48]), followed by rapid thermal annealing (RTA) to temperatures of 700-800°C for 1 minute [48]. The implantation greatly enhances the point defect concentration, and thus the diffusion coefficient. The rapid thermal annealing then provides the driving force for the intermixing to take place. However, intermixing can be made to take place *without* ion implantation, by using higher RTA temperatures of >850°C for 1 min. [48, 49]. TEM imaging has been used to show the contrast of the partially-ordered lamellae after intermixing [14, 47]. The dynamics of this AlGaInP / GaInP intermixing appear to be quite different than that observed in GaAs / AlGaAs samples, where in the latter, interdiffusion between the quantum well and barrier take place, thereby raising the energy of the quantum states, and lowering barrier energy [50], as discussed briefly in section 3.5.3. By contrast, with the AlGaInP / GaInP samples, even under very substantially increased anneal temperatures of 1000 °C, no further energy shifts are observed in the quantum well beyond those which took place due to the initial alloy disordering [48]. In this respect, Hämisch et al. refer to the alloy disordering as a “bulk” effect, since the mechanism driving the shift in thin GaInP quantum wells is the same as the shift in thick GaInP bulk layers, and

intermixing of well and barrier layers does not appear to take place even under extreme conditions.

Electron beams have also been used to disorder GaInP alloy. Noda and Takeda did a thorough study of this phenomenon, measuring the intermixing rate as a function of temperature, dose rate (i.e., electron beam flux intensity), and beam energy [9, 51]. They found (somewhat surprisingly) no dependence of the intermixing rate on sample temperature across the range 150 to 300K (although it did drop by 50% at 20K); the expected linear dependence on beam intensity; and a beam energy threshold of 150 keV. With regard to the third point, it should be pointed out that the beam energy used for our studies was 120 keV; since Noda and Takeda observed no beam-dependent disordering at all until voltages above 150 keV, we would not expect to have difficulties with our sample disordering as we acquired the CL data at the accelerating voltages used.

Finally, and perhaps most relevantly, a high-power laser has been used to promote disordering of ordered GaInP alloy by McIlvaney et al., in a phenomenon they call “photoabsorption induced disordering (PAID)” [52]. A 30 meV shift was observed in the photoluminescence peak of a 670 nm GaInP-AlGaInP laser structure by focusing a 5 W Ar⁺ laser onto the sample. Obviously, this is a rather extreme amount of power, but in our samples, the presence of proton implants from device processing, or point defects from device aging, would greatly decrease the photon flux required for alloy disordering to take place. Furthermore, it should be kept in mind that the intracavity flux in VCSELs are expected to be two to three orders-of-magnitude higher than those being emitted, given the very high reflectivities of the DBR mirrors used, and would thus peak at roughly 10^6 W/cm² — high by any standard.

We observe that ordering is present in our samples, and study how the spectra change as the device is aged. The amount of disordering observed due to aging in our samples is relatively small (~6 meV), relative to the substantial changes (>40 meV) possible. However, substantial changes are observed in the CL efficiency of red VCSELs after aging. Much larger changes take place in the direct recombination peak (from the bulk of the material) than from the spatially-indirect recombination (perhaps from anti-phase boundary edges or columnar microstructure

due to phase separation). Ion implantation also affects the shape of the observed spectrum.

6.5.2 Intensity dependent photoluminescence on $\langle 311 \rangle$ A sample.

Previous researchers have made extensive use of intensity-dependent photoluminescence [13, 16, 21, 53, 54] to prove that their spectra contain spatially-indirect peaks, which come from ordered or phase-separated regions adjacent to one another [16, 22, 23]. To verify the peak assignments we made in interpreting our cathodoluminescence data, we did intensity-dependent PL on a plan-view sample where we had removed the substrate and n-DBR. An Ar^+ laser, with a 514 nm line, was used to pump the device, and the measurements were taken at approximately 10 K using a cryostat with liquid He cooling. Beam size was thought to be 40 μm in diameter, but the true intensity of the pump beam was not calibrated. Neutral density filters were used to attenuate the beam, and beam power was varied over two orders of magnitude. The beam is assumed to fall on an area with deep proton implantation, since over 99.8% of the area of the device is deep implanted in the area examined.

The resulting spectra are seen in Fig. 6 - 35. The results are consistent with those published elsewhere, and clearly show that the high-energy (1.914 eV) peak dominates the spectrum at high pump power, while at low power, the low-energy (indirect) peak (1.87 eV) is the most prominent spectral feature. An excellent fit can be obtained with three gaussians: the high- and low-energy peaks just mentioned, and a third at intermediate energy (1.897 eV). A fourth peak at 680 nm (1.82 eV) can be clearly seen, but accounts for only a few percent of the energy, and follows the intensity dependence of the low energy peak. As we shall see later, each of the three peaks give a distinct cathodoluminescence image when using monochromatic imaging. The significance of having three, rather than just two peaks, is not fully known. Others have reported nearly identical triple-peak spectra in the past [55], and even the simple-twin peak spectra often require a third gaussian to obtain an adequate fit due to intermediate energy luminescence being present in the spectra [16, 53]. One possible interpretation is that the two (lower-energy) spatially-indirect

components correspond to two separate effects—for example, the columnar structure of phase separation and piezoelectric charge of adjacent domains.

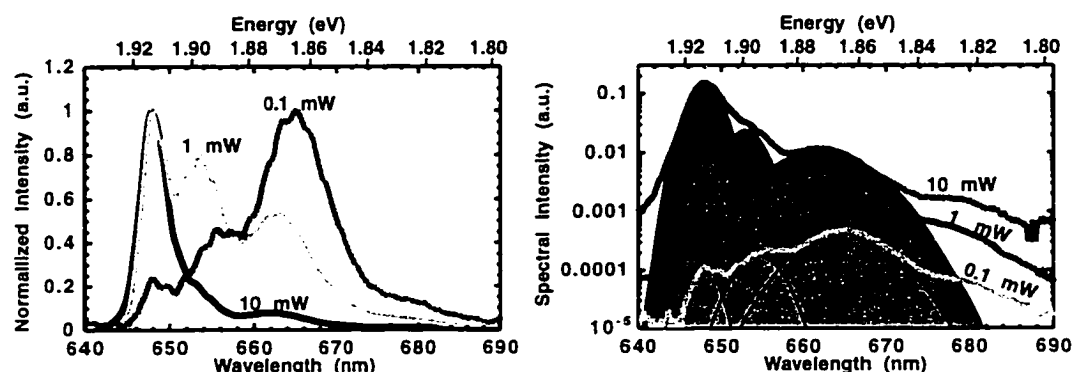


Fig. 6 - 35: Low-temperature (10 K) intensity-dependent PL spectra, normalized (left), and on a log plot (right). An excellent fit can be obtained with three gaussians, which are shown in the right plot.

The data from the triple-gaussian fit is summarized in the table of Fig. 6 - 36. Note that the wavelength of the peaks is almost unchanging as a function of incident power. The larger wavelength shifts, as expected [13], come from the spatially-indirect components. This may be due to the lowest energy states filling up first, and leaving only higher energy states available, or to a reduction in the importance of the piezoelectric field of domains in the presence of carrier screening [22, 23].

The area under the gaussians was integrated to obtain relative amounts of power: the results are summarized in the table, and plotted in Fig. 6 - 37. The behavior expected from a normal, non-ordered (e.g. GaAs) quantum well is observed from the high-energy (direct) peak: the luminescence from the direct peak increases more rapidly than the pumping power (1,670× increase with the 100× increase in intensity), as the non-radiative losses present at low pumping intensities are swamped out at higher intensities. Consistent with previous observations in multi-peak spectra, the low-energy peaks do not increase nearly as rapidly (113× for the medium energy peak, and only 26× for the low-energy peak as pump intensity is increased 100×). Presumably, the number of states available at the boundaries of the spatially-indirect structures is very limited, and thus the indirect luminescence easily saturates. This intensity-dependent PL data supports our interpretation of the CL spectra presented elsewhere in this chapter.

	0.1 mW	1.0 mW	10.0 mW
High λ	648 nm	648 nm	648 nm
High energy	1.914 eV	1.914 eV	1.914 eV
Area, H.E. peak	651	32	0.39
Medium λ	653 nm	653.2 nm	654.5 nm
Medium Energy	1.899 eV	1.898 eV	1.895
Area, M.E. peak	125	42	1.1
Low λ	662 nm	662.5 nm	665 nm
High energy	1.873 eV	1.872 eV	1.865 eV
Area, L.E. peak	144	63	5.5

Fig. 6 - 36: Summary of intensity-dependent PL results, obtained by 3-gaussian best fit. "High-energy peak" is the band-to-band recombination; the medium and low-energy peaks are spatially-indirect recombination, as discussed in the text.

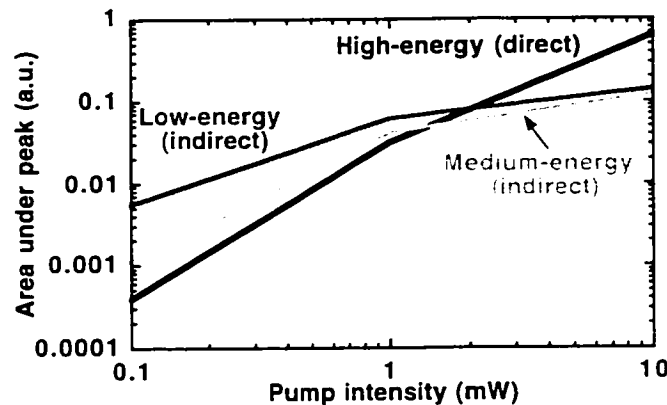


Fig. 6 - 37: Integrated area under peak vs. pump intensity. Note that direct peak scales with pump intensity, while indirect peaks saturate, as expected.

6.5.3 Observation of aging-induced changes in red VCSEL cathodoluminescence.

6.5.3.1 Plan-view cathodoluminescence spectra from $\langle 311 \rangle A$ oriented sample (#999B).

We start by comparing the spectra on degraded and undegraded red VCSELs. This comparison shows how the aging process causes the strength of the direct-recombination peak to significantly increase, and the spatially-indirect peak to slightly drop. The device shown in the following sequence was aged for three days, first at 7 mA, then at 8 mA (still below the 9 mA current that the peak output power

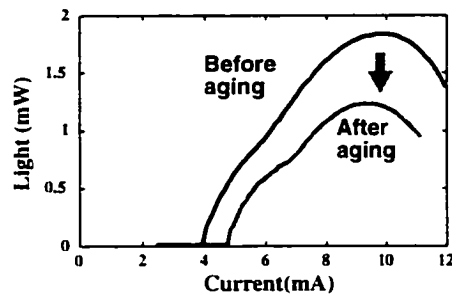


Fig. 6 - 38: L-I curve of red VCSEL studied, before and after aging.

of 1.7 mW was obtained). After aging, peak output power declined by about 35% (1.7–1.12mW), and threshold increased from 4.0 mA to 4.9 mA (Fig. 6 - 38). Other aged and unaged devices showed very similar CL characteristics, and will thus not be discussed separately. After L-I characterization, the device top was photographed, and then bonded face-down to a small piece of AlN (which was

chosen for its high thermal conductivity, good match of thermal-expansion coefficient, and stiffness). The VCSEL's GaAs substrate was removed by lapping followed by spray etching. The n-DBR was then selectively removed by leaving the sample in pure HF for about 1 minute. When the rough surface became smooth, and device stopped "fizzing," it was inspected to verify that the $\text{Al}_5\text{Ga}_5\text{As}$ / AlAs n-DBR had been completely removed, and that the AlGaInP layers (which appeared red as opposed to the "gray" AlGaAs layers) were exposed. The preparation steps are shown in Fig. 6 - 39. Further details on sample preparation can be found in Appendix B.

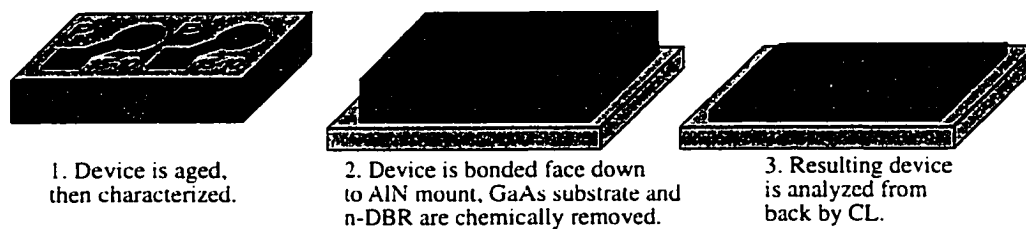


Fig. 6 - 39: Plan-view CL sample is created by bonding device face down, then etching away the substrate and n-DBR, leaving the active region, p-DBR, and p-metals intact.

This method of sample preparation has the twin advantages of being relatively simple, and of leaving intact the p-metal patterns which can be used to locate particular degraded and undegraded areas on the device. In addition, since the devices are in the same plane, very close to one another ($\sim 600 \mu\text{m}$ apart), and data was collected in the same run, the spectra can be compared directly to one another. Consistent results were obtained when comparing spectra of unaged devices to one another, or devices which had been aged under similar conditions.

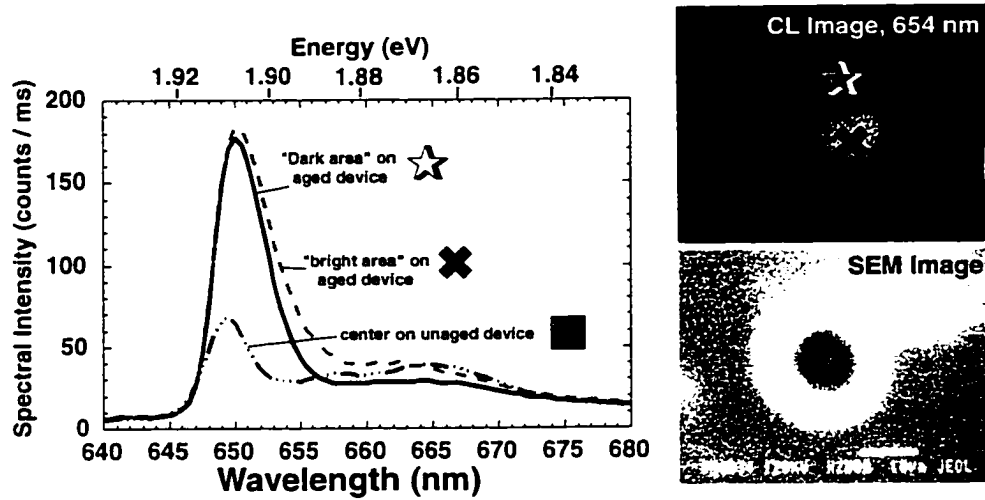


Fig. 6 - 40: Plan-view CL spectra from the center of degraded and undegraded red VCSELs.

The first spectra we examine were taken from the unimplanted center of degraded and undegraded devices, shown in Fig. 6 - 40. In the degraded device, a monochromatic (654 nm) CL scan (seen at the top right of Fig. 6 - 40) showed darkening near the top of the device, possibly due to device degradation. This is the area marked by the star on the monochromatic image. A separate spectrum was taken in the bright, lower area of the device, marked by the "x." Finally, a spectrum from the center of an undegraded device was taken, as marked by the gray square shown on the secondary emission (SEM) image on the lower right. The undegraded spectrum is expected to be very close to the as-grown material quality, since the center of the device is the only region on the wafer where ion implants don't come close to the active region.

Examining the spectra, we see two effects taking place. First, the bias-induced annealing discussed previously seems to be taking place, as judged by the dramatic increase in the height of the CL peak at 650 nm (we attribute this peak to spatially-direct recombination from the bulk of the alloy). Perhaps part of this improvement in CL efficiency is presumably due to a reduction in non-radiative centers, as discussed earlier for the bias annealed devices. Second, some reduction in the height of the peak at 662 nm appears to be taking place, which indicates it is possible that some disordering of the sort discussed in the section 6.5.1 may be taking place.

However, in spite of the improvement in CL efficiency after aging, no enhancement in actual device operating efficiency was observed on aged VCSELs from wafer 999B. Possibly, the radiative efficiency of the active region is improving, but current is not delivered as efficiently to the center of the device, as we have discussed with the 850 nm VCSELs in Chapter 3. We will analyze these spectra in greater detail in the following section.

Next, we look at the portion of the device under the p-metal. This region has a shallow (current confinement) gain-guide implant directly above it, evidently with some penetration of the implant tails into the active region, as we deduce from the spectral changes we shall discuss. This region also is quite close to the central region where lasing is taking place, and thus will receive strong photo-pumping, affecting defect annealing processes which might be photosensitive. It is not likely to degrade to the extent the center of the device will, since it is more than one diffusion length (where diffusion lengths usually don't exceed a few microns) outside the main current flow path. The lateral dependence of active region degradation is shown nicely by the cross-sectional TEM images of the active region taken by Michael Cheng [56], and reproduced in Section 4.1.

The spectra taken under the p-metal are shown in Fig. 6 - 41. The area for which the spectra were collected is indicated by the gray square on the accompanying SEM image. Note that the degraded VCSEL has a blue-shift of the (short-wavelength) direct peak, indicating more through disordering, and a lower order parameter, than that observed in other regions of the aged or unaged devices. However, this is a relatively small shift (only a few nanometers), indicating not much disordering is taking place. Note also that as before, the luminescence efficiency from the aged VCSEL is somewhat larger, indicating possible bias-annealing, and again, the intensity of the indirect peak has been slightly reduced, possibly due to increased efficiency of direct recombination reducing the carrier population available at antiphase boundaries.

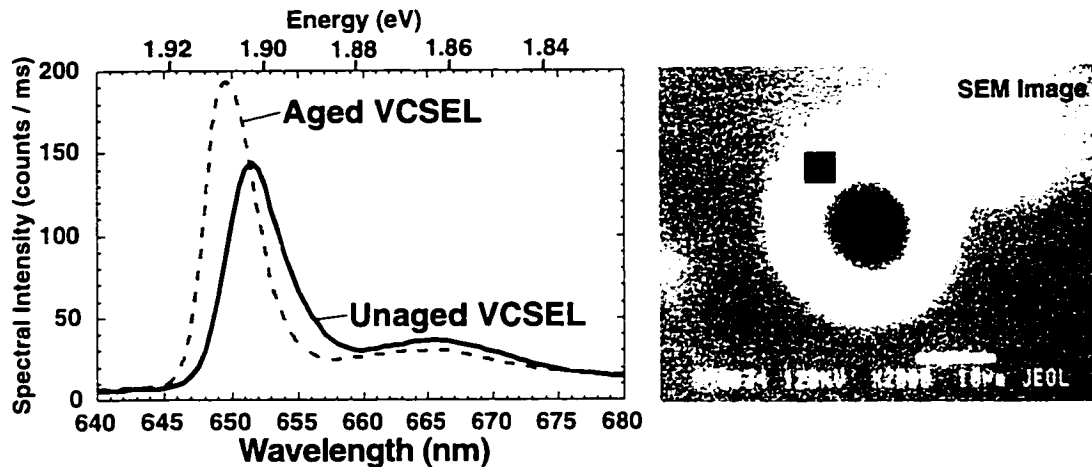


Fig. 6 - 41: Plan-view CL spectra taken under the metal of degraded and undegraded red VCSELs.

Finally, proceeding still further out, we examine spectra taken from the deep-implanted region outside the p-metal ring (Fig. 6 - 42). Note that these spectra in both aged and unaged devices are notably dimmer than those shown above, as would be expected from the loss of radiative efficiency caused by the deep implant. Not surprisingly, the spectrum taken near the edge of the device shows more annealing than that taken far away, since the annealing affects would be expected to fall off rapidly as one got further from the pumped core of the device.

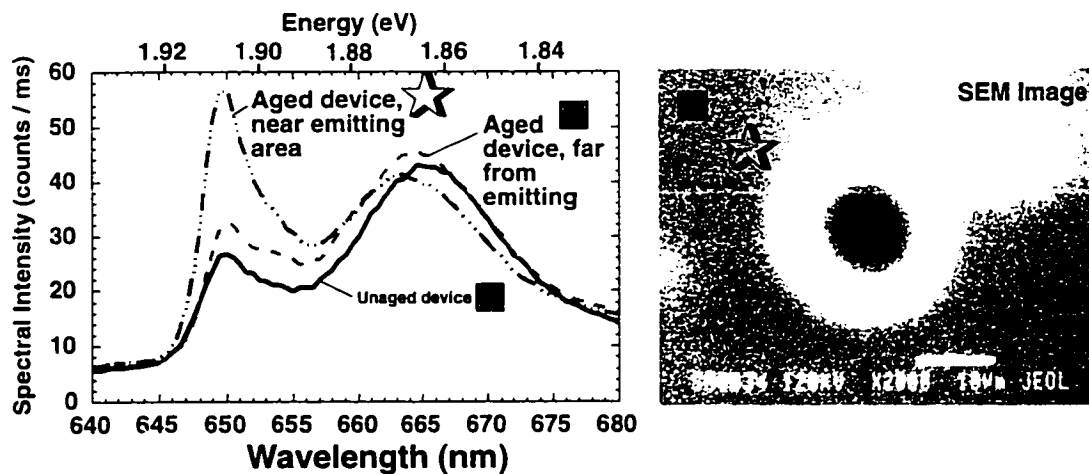


Fig. 6 - 42: Plan-view CL spectra taken outside from the deep-implanted edges of degraded and undegraded red VCSELs.

6.5.3.2 CL monochromatic images from plan-view $\langle 311 \rangle$ A-oriented wafer (#999B)

We took monochromatic images of the sample at various wavelengths, as shown in Fig. 6 - 43. Large irregularities, (such one region appearing shifted in wavelength) as well as small (micron-sized) patches were noted in the images. Linescans from these samples are seen in Fig. 6 - 44.

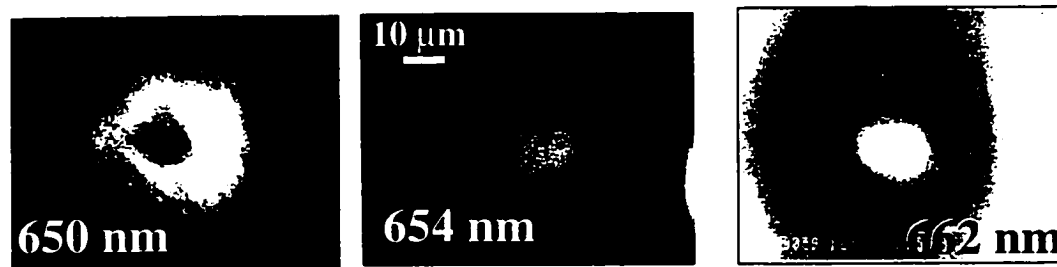


Fig. 6 - 43: Monochromatic images of degraded plan-view $\langle 311 \rangle$ A-oriented sample PB-7 (#999B). Note that the 650 nm image roughly corresponds to the shallow-implanted region; the 654 nm image shows the unimplanted center (although the top is dark, perhaps from degradation); and the 662 nm image shows both the center and deep-implanted outer regions as being bright.

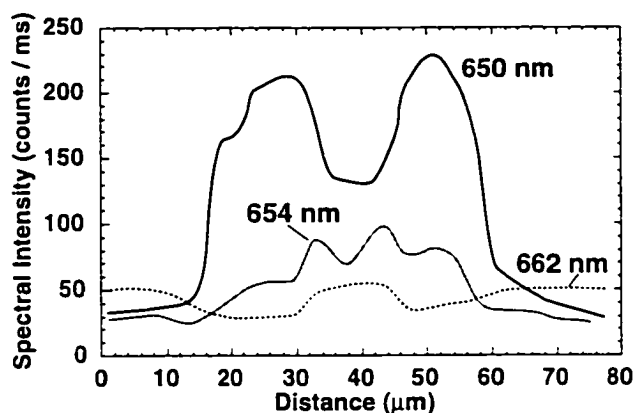


Fig. 6 - 44: Linescans showing intensity versus lateral position, for wavelengths corresponding to the direct recombination (650 nm); the spatially-indirect recombination (662 nm); and an in-between wavelength (654 nm).

Images from the undegraded VCSELs did not show broad-area darkening of the sort seen in the 654 nm image above, but still showed other non-uniformities at the edges of the p-metal contacts which appeared stain related, and inexplicable

wavelength shifts of a few nanometers in some regions which appeared to be related to growth inhomogeneity.

6.5.3.3 Analysis of plan-view CL data from $\langle 311 \rangle A$ -oriented wafer (#999B)

We can analyze the spectral data by first subtracting off the background signal, and then attempting to fit the spectra with two gaussians. Except in the wavelength range between the two peaks, we are able to achieve a remarkably good fit, as is shown in Fig. 6 - 45. These twin-peak spectra are similar in nature to those described by Ernst et al., (who refer to these as “type III” samples) [13]. They attribute the higher-energy peak to the true bandgap of the material, and the lower-energy peak to spatially-indirect recombination, possibly coming from anti-phase boundaries or phase-separated columnar microstructure, as discussed in section 6.5.1.

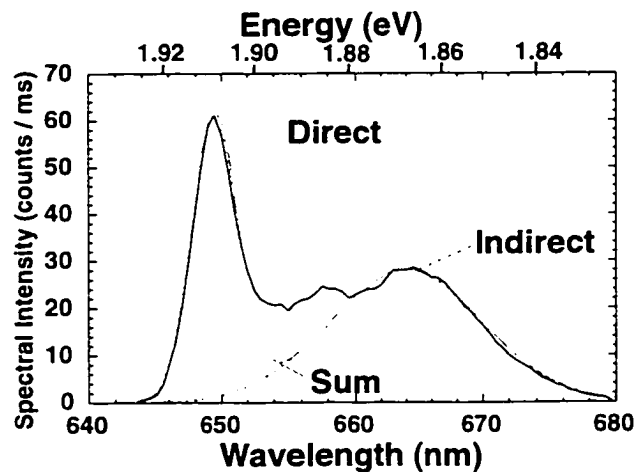


Fig. 6 - 45: The spectrum from the center of the unaged sample is shown, along with the two gaussians which were adjusted to create the best fit. Note that the sum of the two gaussians fits the measured data (solid black line) fairly well, except between the two peaks, from 653-659 nm.

We perform similar curve-fitting on the spectra of degraded and undegraded devices, at different locations. We integrate the area under the curves and determine the wavelength giving the best fit to the spectra. The results are summarized in the table shown in Fig. 6 - 46. Order parameters were calculated using the previously mentioned formula from Murata et al., after subtracting 29 meV from their energy to account for the blue shift from quantum confinement

effects [11], and adding 79 meV to account for the reduction in bandgap which occurs from using compressively-strained $\text{Ga}_{0.46}\text{In}_{0.54}\text{P}$ quantum wells [29, 30]. Areas were normalized to the areas from the spectra taken at the center of the unaged device.

Note that only minor differences in the peak positions (~ 6 meV) are observed, which may perhaps be taken as a sign that relatively little alloy disordering is taking place in the bulk of the alloy: substantial spectral shifts (>40 meV) are possible when intentional disordering is being done [48]. However, it is possible more disordering or intermixing is taking place in the immediate vicinity of the domain boundary walls, which may account for the reductions in the indirect recombination for the aged devices. Also, the changes in the area under the spatially-indirect peak are relatively small, when compared to the very large ($2.5\text{--}3\times$) increases observed in the area under the direct peaks. These increases in band-to-band recombination are probably due to a reduction in point defects and non-radiative centers, similar to the annealing described earlier in section 6.4. In addition, reduced recombination near domain boundary walls may also leave an increased carrier population available for direct recombination.

	Direct Peak (nm)	Indirect Peak (nm)	Indirect Peak (nm)	Area Direct (arb. units)	Area Indirect (arb. units)
Unaged center	649.5	.308	664	1.0	1.0
Unaged metal	651.5	.328	665	2.42	0.89
Unaged edge	650	.314	665	0.29	1.09
Aged center	650.2	.316	662	3.09	1.14
Aged degraded center	650	.314	664	2.84	0.64
Aged metal	649.5	.308	664.5	2.97	0.70
Aged near edge	649.7	.310	663.5	0.78	1.11
Aged far edge	650	.314	664	0.37	1.25

Fig. 6 - 46: Table summarizing analysis of gaussian fitting of plan-view spectra.

6.5.3.4 Cross-sectional CL from $\langle 311 \rangle$ A-oriented sample (#999B).

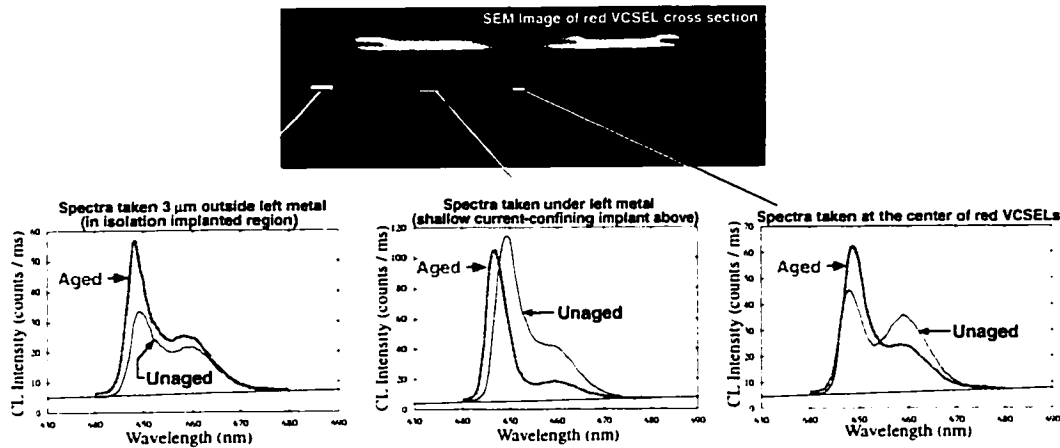


Fig. 6 - 47: Cross-sectional CL spectra from $\langle 311 \rangle$ A-oriented wafer (#999B), before and after degradation, in each of three regions. Note that the scales differ between each of the three plots.

While the plan-view samples probably are able to give the most accurate data, it is difficult to correlate the images with the relative position of the contact metal, as can be easily done for cross-sectional samples. Further, there are potential concerns about possible artifacts from the mirror reflectivity spectrum, which strongly influences the room-temperature plan-view spectrum, as discussed in Appendix E. However, the data from the cross-sectional samples is largely unaffected by the mirror's reflectivity spectrum since they are collected from the side. Thus, the cross-sectional data, which was taken prior to the plan-view data, is included as a cross-check. The cross-sectional CL spectra, shown before and after

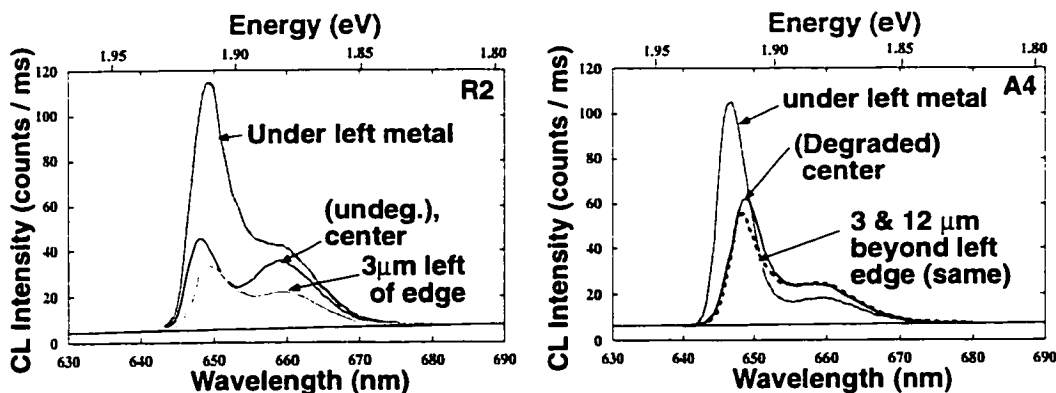


Fig. 6 - 48: Cross-sectional CL spectra from $\langle 311 \rangle$ A-oriented wafer (#999B), for undegraded sample (left) and degraded sample (right). Each plot shows spectra taken at different regions within the given device.

degradation for each of the three regions, are seen in Fig. 6 - 47. In addition, the spectra from different regions of a single device are compared in Fig. 6 - 48, which allows easier comparison for a particular device.

By comparing the cross-sectional spectra seen here with those seen earlier in the plan-view data, we see there is general agreement on the trends observed, and the spectral shapes are similar. It appears the entire plan-view spectrum of interest is within the stop-band of the DBR at low temperature, which is necessary to avoid unwanted effects of the sort seen in Appendix E. The same broad trends discussed earlier are seen here: an increase in the height of the direct peak in the shallow-implant region relative to the unimplanted center, as well as an increase in the height of the direct peak in all spectra after device aging. It should be noted that the cross-sectional samples have some unwanted experimental artifacts of their own, including for example contamination of the spectrum of the device center by luminescence from implanted regions below it, due to the deep ($R_p \sim 12 \mu\text{m}$) penetration of the electron beam. It is for these reasons we have focused our analysis on the plan-view samples, where luminescence from a single region can be easily isolated.

We also examine the linescans and images from this cross-sectional device in Fig. 6 - 49. The undegraded device shows the expected reduction in luminescence in the deep implanted regions outside the p-metal contact, with relatively uniform luminescence within the central region, while the degraded sample shows inhomogeneities which are presumably correlated with the (small) spectral shifts which take place during the aging process. Careful comparison of the images and linescans with the spectra shown earlier reveals what appear to be inconsistencies (i.e., the direct peak on the undegraded sample is far stronger in the shallow implanted region under the metal than in the center, so the 646 nm linescan and 647 nm image should not appear uniformly bright in both of the two regions). These inconsistencies, we believe, are solely related to the spectral shifts; examining the changes in the spectra appears to be more useful in this regard, since the areas under the peaks can be integrated, and the analysis is not disturbed by small spectral shifts the way the monochromatic images have been.

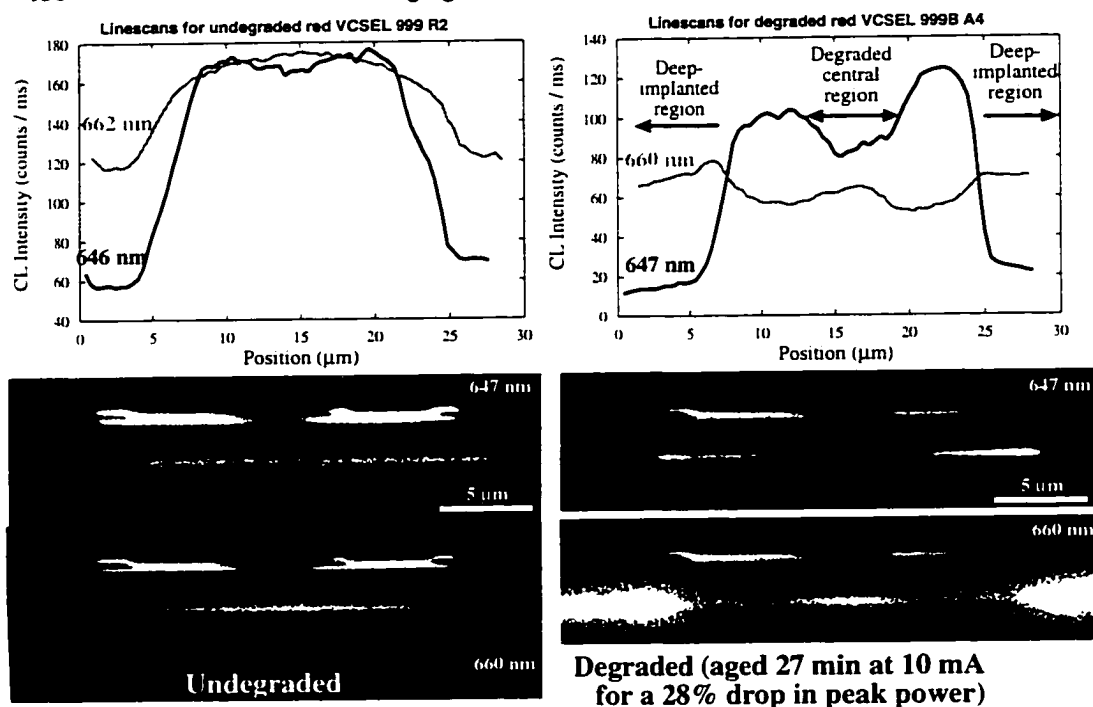


Fig. 6 - 49: Monochromatic images and linescans from (311)A -oriented wafer (#999B), taken in cross section, on undegraded (left) and degraded (right) samples.

6.6 Discussion and Conclusions

It appears that for red VCSELs as for 850 nm VCSELs, that the “current shunting” failure mechanism discussed in Chapter 3 is the primary cause of failure in the red GaInP VCSELs studied. This conclusion is supported by the observations that even deeply degraded VCSELs had little evidence of degradation in their active region, as shown both by uniform cross-sectional EBIC profiles and the *increase* in CL efficiency after aging. (In fact, I’ve intentionally used the term “aging” rather than “degradation” throughout this chapter, since the latter generally implies something getting worse, which is not the case for the annealed devices which were aged under high currents.) Ultimately, it appears the first task to improving the lifetime of red VCSELs might well be the same as is needed to improve the lifetime of proton-implanted VCSELs generally. Due to the indirect-gap DBRs, we were unable use CL to examine the DBRs for dislocation growth of the type discussed in chapter 4. It is not known whether the improvement in lifetime due to annealing is directly combating the “current shunting,” or whether it is merely a large enough

effect to partially offset the reduction in efficiency from the shunting. The former explanation seems more likely, though, given the way the annealing has been able to remove non-radiative centers, as seen by cross-sectional EBIC.

It is evident, from the improvement observed by annealing the two different 15°-off samples (1001 & 1002), that some non-radiative centers remained in the sample after processing, and were only driven out by the annealing. Possibly RTA of the wafers before processing in a manner similar to Ko et al. could be used [57]; laser annealing is also used in industry for applications where RTA does supply enough energy to overcome the potential barriers encountered. The >10-fold improvement in lifetime from the annealing could thus be obtained without the expense of individually bias-annealing each device. The annealed 15°-off samples showed considerably better lifetime than the $\langle 311 \rangle$ A samples tested. However, Mary Crawford's best (>3,000 h) reliability results were obtained on $\langle 311 \rangle$ A substrates, using no annealing [5].

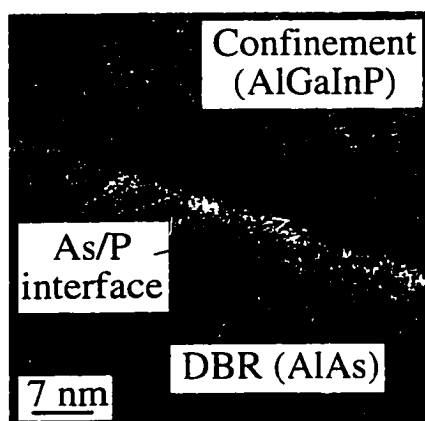


Fig. 6 - 50: High-magnification TEM of the arsenide / phosphide interface in a Sandia red VCSEL. (Courtesy of Dr. Ray Twisten.)

In these (early prototype) red VCSELs, the operating voltages of 5–6 V were higher than the best values reported in the literature [1, 58] — improvement in this category could cut the heat load by nearly 50%. The $\text{Al}_x\text{Ga}_{1-x}\text{As}$ layers are difficult to p-dope, and require different growth conditions than are used for the 850 nm VCSEL DBR mirrors [5]. Band discontinuities at the AlGaInP / AlAs interfaces are another potential problem with red VCSELs, and the aluminum content of the AlGaInP is reportedly tapered off before the transition is made to the AlAs layers in

the DBRs. Excess voltage drop at the Phosphide / Arsenide interface has been a long-running problem with stripe lasers; reducing this drop by grading is discussed by Foulger et al. [46]. A lattice-image of the interface of a red VCSEL grown on a $\langle 311 \rangle$ A substrate, is shown in Fig. 6 - 50. The arsenide / phosphide interface can be clearly observed. In spite of the visible disruption at the interface, the Sandia VCSELs shown have long had very low threshold voltages [4, 31].

References for Chapter 6:

- [1] R. L. Thornton, "Vertical Cavity Lasers and their Application to Laser Printing," *Proceedings of SPIE (Vertical-Cavity Surface Emitting Lasers II)*, vol. 3003, pp. 112-119, 1997.
- [2] J. A. Lehman, R. A. Morgan, D. Carlson, M. H. Crawford, and K. D. Choquette, "High-frequency modulation characteristics of red VCSELs," *Electronics Letters*, vol. 33, pp. 298-300, 1997.
- [3] J. A. Lott, J. R.P. Schneider, K. D. Choquette, and S. P. Kilcoyne, "Room-temperature continuous-wave operation of red vertical-cavity surface-emitting laser diodes," *Electronics Letters*, vol. 29, pp. 1693-1694, 1993.
- [4] R. P. Schneider, J. A. Lott, M. Hagerott-Crawford, and K. D. Choquette, "Epitaxial design and performance of AlGaInP red (650-690 nm) VCSELs," *International Journal of High Speed Electronics and Systems*, vol. 5, pp. 625-666, 1994.
- [5] Personal communication with Mary Crawford of Sandia National Labs
- [6] T. Kajimura, "Degradation mechanisms of $\text{Ga}_{1-x}\text{Al}_x\text{As}$ visible diode lasers," *Journal of Applied Physics*, vol. 51, pp. 908-13, 1980.
- [7] T. Suzuki and A. Gomyo, "Strong ordering in GaInP alloy semiconductors: Formation mechanism for the ordered phase," *Journal of Crystal Growth*, vol. 93, pp. 396-405, 1988.
- [8] T.-Y. Seong, J. H. Kim, Y. S. Chun, and G. B. Stringfellow, "Effects of V/III ratio on ordering and antiphase boundaries in GaInP layers," *Applied Physics Letters*, vol. 70, pp. 3137-3139, 1997.
- [9] N. Noda and S. Takeda, "Disordering of natural superlattice in (Ga,In)P induced by electron irradiation," *Physical Review B*, vol. 53, pp. 7197-7203, 1996.
- [10] C. Geng, A. Moritz, S. Heppel, A. Mühe, J. Kuhn, P. Ernst, H. Schweizer, F. Phillipp, A. Hangleiter, and F. Scholz, "Influence of order-domain size on the optical gain of AlGaInP laser structures," *Journal of Crystal Growth*, vol. 170, pp. 418-423, 1997.
- [11] H. Murata, I. H. Ho, Y. Hosokawa, and G. B. Stringfellow, "Surface photoabsorption study of the effect of substrate misorientation on ordering in GaInP," *Applied Physics Letters*, vol. 68, pp. 2237-2239, 1996.
- [12] Y. Ishitani, S. Minagawa, and T. Tanaka, "Temperature dependence of the band-gap energy of disordered GaInP," *Journal of Applied Physics*, vol. 75, pp. 5326-5331, 1994.
- [13] P. Ernst, C. Geng, F. Scholz, and H. Schweizer, "Ordering in GaInP_2 Studied by Optical Spectroscopy," *Physica Status Solidi B*, vol. 193, pp. 213-229, 1996.
- [14] M. Burkard, C. Geng, F. Mühe, F. Scholz, H. Schweizer, and F. Phillipp, "Transmission electron microscopy observation of lateral order/disorder structures in (Al)GaInP," *Applied Physics Letters*, vol. 70, pp. 1290-1292, 1997.
- [15] Baxter, Stobbs, and Wilkie, *Journal of Crystal Growth*, vol. 112, pp. 373, 1991.
- [16] E. D. Jones, R. P. J. Schneider, and A. Mascarenhas, "Magnetoluminescence Studies in Ordered InGaP_2 ," *Materials Research Society Symposium Proceedings*, vol. 417, pp. 73-78, 1996.
- [17] P. Ernst, C. Geng, G. Hahn, F. Scholz, H. Schweizer, F. Phillipp, and A. Mascarenhas, "Influence of domain size on optical properties of ordered GaInP_2 ," *Journal of Applied Physics*, vol. 79, pp. 2633-2639, 1996.

- [18] R. Wirth, C. Geng, F. Scholz, and A. Hangleiter, "Determination of Ordering Induced Birefringence in (Al)GaInP," presented at 39th Annual Electronic Materials Conference, Fort Collins, CO, 1997.
- [19] D. M. Follstaedt, R. P. Schneider, Jr., and E. D. Jones, "Microstructures of (In,Ga)P alloys grown on GaAs by metalorganic vapor-phase epitaxy," *Journal of Applied Physics*, vol. 77, pp. 3077-3087, 1995.
- [20] J. E. Fouquet, M. S. Minsky, and S. J. Rosner, "Photoluminescence excitation spectroscopy yields bandgap of $\text{Ga}_{0.5}\text{In}_{0.5}\text{P}$ containing relatively ordered domains," *Applied Physics Letters*, vol. 63, pp. 3212-3214, 1993.
- [21] M. C. DeLong, W. D. Ohlsen, I. Viohl, P. C. Taylor, and J. M. Olson, "Evidence for spatially indirect recombination in $\text{Ga}_{0.52}\text{In}_{0.48}\text{P}$," *Journal of Applied Physics*, vol. 70, pp. 2780-2787, 1991.
- [22] P. Ernst, C. Geng, M. Burkard, F. Scholz, and H. Schweizer, "Evidence for strong internal electric fields in ordered GaInP," presented at 23rd International Conference on The Physics of Semiconductors (ICPS-23), Berlin, Germany, 1996.
- [23] S. Froyen, A. Zunger, and A. Mascarenhas, "Polarization fields and band offsets in GaInP/GaAs and ordered/disordered GaInP superlattices," *Applied Physics Letters*, vol. 68, pp. 2852-2854, 1996.
- [24] J. D. Perkins, H. M. Cheong, Y. Zhang, A. Mascarenhas, J. F. Geisz, W. E. McMahon, and J. M. Olson, "Electroreflectance Measurements of Intrinsic Electric Fields in Spontaneously-Ordered GaInP₂," presented at 39th Annual Electronic Materials Conference, Fort Collins, CO, 1997.
- [25] D. A. B. Miller, D. S. Chemla, T. C. Damen, and A. C. Gossard, "Electric field dependence of optical absorption near the band gap of quantum-well structures," *Physical Review B*, vol. 32, pp. 1043-1060, 1985.
- [26] A. Diéguez, F. Peiró, A. Cornet, J. R. Morante, F. Alsina, and J. Pascual, "Competitive evolution of the fine contrast modulation and CuPt ordering in InGaP/GaAs layers," *Journal of Applied Physics*, vol. 80, pp. 3798-3803, 1996.
- [27] R. P. Schneider, E. D. Jones, J. A. Lott, and R. P. Bryan, "Photoluminescence linewidths in metalorganic vapor phase epitaxially grown ordered and disordered InAlGaP alloys," *Journal of Applied Physics*, vol. 72, pp. 5397-5400, 1992.
- [28] S. P. Ahrenkiel, Y. Zhang, A. Mascarenhas, D. J. Friedman, and J. M. Olson, "Microstructure of Double-Variant Ordered GaInP Films," presented at 39th Annual Electronic Materials Conference, Fort Collins, CO, 1997.
- [29] A. T. Meney, A. D. Prins, A. F. Phillips, J. L. Sly, E. P. O'Reilly, D. J. Dunstan, A. R. Adams, and A. Valster, "Determination of the Band Structure of Disordered AlGaInP and its Influence on Visible-Laser Characteristics," *IEEE Journal of Selected Topics on Quantum Electronics*, vol. 1, pp. 697-706, 1995.
- [30] D. P. Bour, R. S. Geels, D. W. Treat, T. L. Paoli, F. Ponce, R. L. Thornton, B. S. Krusor, R. D. Bringans, and D. F. Welch, "Strained $\text{Ga}_x\text{In}_{1-x}\text{P}/(\text{AlGa})_{0.5}\text{In}_{0.5}\text{P}$ Heterostructures and Quantum-Well Laser Diodes," *IEEE Journal of Quantum Electronics*, vol. 30, pp. 593-606, 1994.
- [31] M. Hagerott-Crawford, R. P. Schneider, K. D. Choquette, and K. L. Lear, "Temperature dependent characteristics and singlemode performance of AlGaInP-based 670-690nm vertical cavity surface-emitting lasers," *IEEE Photonics Technology Letters*, vol. 7, pp. 724-726, 1995.
- [32] M. K. Hibbs-Brenner, R. P. Schneider, Jr., R. A. Morgan, R. A. Walterson, J. A. Lehman, E. L. Kalweit, J. A. Lott, K. L. Lear, K. D. Choquette, and H. Juergensen, "Metalorganic

- vapour-phase epitaxial growth of red and infrared vertical-cavity surface-emitting laser diodes," *Microelectronics Journal*, vol. 25, pp. 747-55, 1994.
- [33] S. Adachi, "GaAs, AlAs, and $\text{Al}_x\text{Ga}_{1-x}\text{As}$: Material parameters for use in research and device applications," *Journal of Applied Physics*, vol. 58, pp. R1-29, 1985.
- [34] G. H. Olsen and M. Ettenberg, "Universal stain/etchant for interfaces in III-V compounds," *Journal of Applied Physics*, vol. 45, pp. 5112-5114, 1974.
- [35] D. B. Young, J. W. Scott, F. H. Peters, M. G. Peters, M. L. Majewski, B. J. Thibeault, S. W. Corzine, and L. A. Coldren, "Enhanced Performance of offset-gain high-barrier vertical-cavity surface-emitting lasers," *IEEE Journal of Quantum Electronics*, vol. 29, pp. 2013-2022, 1993.
- [36] J. M. Catchmark, R. A. Morgan, K. Kojima, R. E. Leibenguth, M. T. Asom, G. D. Guth, M. W. Focht, L. C. Luther, G. P. Przybylek, T. Mullally, and D. N. Christodoulides, "Extended temperature and wavelength performance of vertical cavity top surface emitting lasers," *Applied Physics Letters*, vol. 63, pp. 3122-4, 1993.
- [37] L. A. Coldren and S. W. Corzine, "Section 4.6.7, "Dependence on Well Width, Doping, and Temperature"," in *Diode Lasers and Photonic Integrated Circuits*. New York, NY: John Wiley - Interscience, 1995, pp. 174-178.
- [38] P. D. Floyd and D. W. Treat, "Improved performance of laterally oxidized GaInP/AlGaInP lasers by thermal annealing," *Applied Physics Letters*, vol. 70, pp. 2493-2495, 1997.
- [39] T. Wipiejewski, D. B. Young, M. G. Peters, B. J. Thibeault, and L. A. Coldren, "High performance vertical-cavity surface-emitting laser diodes with a Au-plated heat spreading layer," *45th Electronic Components and Technology Conference 1995 Proceedings.*, pp. 401-5, 1995.
- [40] D. V. Lang, L. C. Kimerling, and S. Y. Leung, "Recombination-enhanced annealing of the E1 and E2 defect levels in 1-MeV-electron-irradiated n-GaAs," *Journal of Applied Physics*, vol. 47, pp. 3587-3591, 1976.
- [41] D. Vakhshoori, R. A. Novotny, R. E. Leibenguth, and J. D. Wynn, "Low-threshold reliable vertical-cavity surface-emitting laser arrays for system applications," presented at Vertical-Cavity Surface-Emitting Laser Arrays, Los Angeles, CA, USA, 1994.
- [42] J. K. Guenter, R. A. Hawthorne, D. N. Granville, M. K. Hibbs-Brenner, and R. A. Morgan, "Reliability of proton-implanted VCSELs for data communications," *Proc. of SPIE (Fabrication, Testing, and Reliability of Semiconductor Lasers)*, vol. 2683, pp. 102-13, 1996.
- [43] J. Zhou, Q. Zhan, Z. Fu, D. Lü, L. Guan, and H. Chen, "Behavior of types A and B hole traps in n-type GaAs during long-period operation," *Solid-State Electronics*, vol. 35, pp. 1325-1329, 1992.
- [44] J. Salzman, Y. L. Khait, and R. Beserman, "Material evolution and gradual degradation in semiconductor lasers and light emitting diodes," *Electronics Letters*, vol. 25, pp. 244-6, 1989.
- [45] Y. L. Khait, J. Salzman, and R. Beserman, "Kinetic model for gradual degradation in semiconductor lasers and light-emitting diodes," *Applied Physics Letters*, vol. 53, pp. 2135-7, 1988.
- [46] D. L. Foulger, P. M. Smowton, P. Blood, and P. A. Mawby, "Self-consistent simulation of (AlGa)InP/GaInP visible lasers," *IEE Proc.-Optoelectron.*, vol. 144, pp. 23-29, 1997.
- [47] M. Burkard, A. Englert, C. Geng, A. Mühe, F. Scholz, H. Schweizer, and F. Phillipp, "Implantation-induced disordering of CuPt_B -ordered GaInP," *Journal of Applied Physics*, vol. 82, pp. 1042-1052, 1997.
- [48] Y. Hämisch, R. Steffen, P. Röntgen, and A. Forchel, "Implantation-Induced Order-Disorder Transition in $\text{Ga}_{0.52}\text{In}_{0.48}\text{P}/(\text{Al}_{0.35}\text{Ga}_{0.65})_{0.5}\text{In}_{0.5}\text{P}$ Heterostructures," *Japanese Journal of Applied Physics*, vol. 32, pp. L1492-1495, 1993.

- [49] Y. Hämisch, R. Steffen, A. Forchel, and P. Röntgen, "Rapid thermal annealing induced order-disorder transition in $\text{Ga}_{0.52}\text{In}_{0.48}\text{P}/(\text{Al}_{0.35}\text{Ga}_{0.65})_{0.5}\text{In}_{0.5}\text{P}$ heterostructures," *Applied Physics Letters*, vol. 62, pp. 3007-3009, 1993.
- [50] G. F. Redinbo, H. G. Craighead, and J. M. Hong, "Proton implantation intermixing of GaAs / AlGaAs quantum wells," *Journal of Applied Physics*, vol. 74, pp. 3099-3102, 1993.
- [51] N. Noda and S. Takeda, "Disordering of CuPt-type ordered structure in GaInP under electron irradiation," *Proceedings of the IOP: Microscopy of Semiconducting Materials 1995*, vol. 105, pp. 245-248, 1995.
- [52] K. McIlvaney, A. McKee, A. C. Bryce, and J. H. March, "Feasibility of monolithic device integration in GaInP/AlGaInP using photoabsorption induced disordering," *Proc. Integ. Photonics Research 1996*, vol. 6, pp. 232-234, 1996.
- [53] E. D. Jones, D. H. Follstaedt, H. Lee, and J. S. Nelson, "Observation of excitonic and band-to-band behaviour in ordered InGaP₂ alloys," *Proc. of the 22nd Intl. Conf. Phys. Semiconductors*, vol. 1, pp. 293-296, 1995.
- [54] M. C. DeLong, D. J. Mowbray, R. A. Hogg, M. S. Skolnick, M. Hopkinson, J. P. R. David, P. C. Taylor, S. Kurtz, R., and J. M. Olson, "Photoluminescence, photoluminescence excitation, and resonant Raman spectroscopy of disordered and ordered $\text{Ga}_{0.52}\text{In}_{0.48}\text{P}$," *Journal of Applied Physics*, vol. 73, pp. 5163-5172, 1993.
- [55] C. E. Inglefield, M. C. DeLong, P. C. Taylor, Y. S. Chun, I. H. Ho, and G. B. Stringfellow, "Characterization of unicompositional GaInP₂ ordering," presented at 39th Electronic Materials Conference, Ft. Collins, CO, 1997.
- [56] Y. M. Cheng, R. W. Herrick, P. M. Petroff, M. K. Hibbs-Brenner, and R. A. Morgan, "Degradation mechanisms of vertical cavity surface emitting lasers," *34th Annual Proceedings of International Reliability Physics Symposium*, pp. 211-13, 1996.
- [57] J. Ko, M. J. Mondry, D. B. Young, S. Y. Hu, L. A. Coldren, and A. C. Gossard, "Threshold reduction by rapid thermal annealing in MBE-grown AlInGaAs multi-quantum well lasers on GaAs," *Electronics Letters*, vol. 32, pp. 351-352, 1996.
- [58] M. H. Crawford, K. D. Choquette, R. J. Hickman, and K. M. Geib, "Low threshold and high temperature performance of selectively oxidized visible VCSELs," *Proceedings of the Conf. on Lasers and Electro-Optics (CLEO-97)*, pp. 290, 1997.

Chapter 7: Degradation in other types of gain-guided VCSELs

So far, we have dealt with failure modes in production VCSELs in Chapters 3, 4, and 5; in addition, we have shown that the primary failure mechanism (“current shunting”) is also responsible for the failure of red VCSELs. In this chapter we extend our view over a much wider range of VCSELs. We start by looking at other “standard design” proton-implanted VCSELs which are nominally identical to those discussed earlier. The fact they fail in very different ways shows how important small differences in design and fabrication can be to reliability. We also deal briefly with “dielectric-mirror” gain guided VCSELs. While none of the VCSELs featured in this chapter are representative of production devices, the results shown here illustrate the large variety of different failure modes. In addition, the results in this chapter show the value of the spectrally-filtered electroluminescence technique discussed briefly in Chapter 3, and in greater detail in Appendix F.

7.1 Degradation in non-production “standard Design” 850 nm Proton-Implanted VCSELs

The “standard design” proton implanted VCSEL is the GaAs-QW, 850 nm design described in detail in Chapter 3. It has been widely used in data links by a number of companies. The same, nearly identical design, was demonstrated at Bell Labs in the early 90’s, and has been the subject of experimentation by nearly a dozen companies, several universities, and government labs worldwide. We have had the good fortune to collaborate with a number of different sources, and to obtain devices at various states of development to examine. The lasers shown in this section were generally degraded elsewhere, at ambient temperatures of 70–90°C, currents of 15–30 mA, and for 48–3,000 hours. The VCSELs were examined at currents well below threshold to avoid modal behavior affecting the results.

Spectrally-filtered electroluminescence [1, 2] was performed, with 10 nm FWHM bandpass filters being used to allow just the spontaneous emission escaping from the (generally 770–790 nm) reflectivity nulls to affect the image. However, we also include images taken either without filters, or with 830–850 nm filters, to show just how little defect contrast is obtained with standard (unfiltered) electroluminescence imaging.

7.1.1 MBE-grown VCSELs

A typical image after aging from one batch of VCSELs is seen in Fig. 7- 1. Note the relatively small (2–5 μm) dark patches present after aging (the luminescence before aging was extremely uniform).



Fig. 7- 1: MBE grown VCSELs after 72-hour, 30 mA burn-in. Note that the features observed at 780 nm (left) could be observed across all wavelengths from 750 - 790 nm. Little contrast is obtainable at 850 nm (right). (The white line is from video system; the dot on upper part of right image is a dust spot.)

Two devices which had been aged for a few thousand hours at 70 °C are shown in Fig. 7- 2 and Fig. 7- 3. Note that for all three MBE VCSELs shown, the "current shunting" failure mechanism discussed in Chapter 3 is probably *not* the cause of failure. Rather, the most likely failure mechanism (on the basis of the EL imaging shown) is probably the generation of a dense dislocation network in the active region, of the sort shown in Chapter 4.

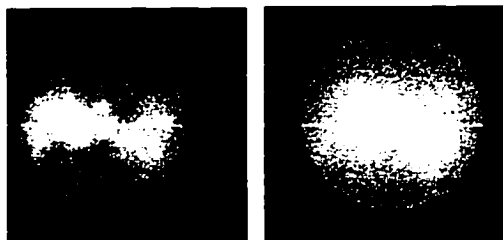


Fig. 7- 2: MBE VCSEL after aging for thousands of hours. 780 nm image (left) shows dark areas with "sharp peaks" at top and bottom. Unfiltered image (right) shows little contrast.



Fig. 7- 3: MBE VCSEL after aging for thousands of hours. 780 nm image (left) shows a dark "band" across the center with two especially dark areas in it. Unfiltered image (right) shows little contrast, as before.

7.1.2 MOCVD-grown VCSELs

The two MOCVD-grown VCSEL shown in this section appeared to fail due to true dark-line defects, probably in the active region. We distinguish "DLDs," by which we mean sharply-defined lines, from the broad, patchy "dislocation

networks” or “dark spots” seen in the previous section. The device shown in Fig. 7- 4 failed after $\sim 1,000$ hours. The device shown in Fig. 7- 5 failed quickly due to DLDs (10’s of hours). Wenbin Jiang has reported DLDs (both $\langle 110 \rangle$ and $\langle 100 \rangle$) as being the primary failure mechanism observed in Motorola VCSELs [3].

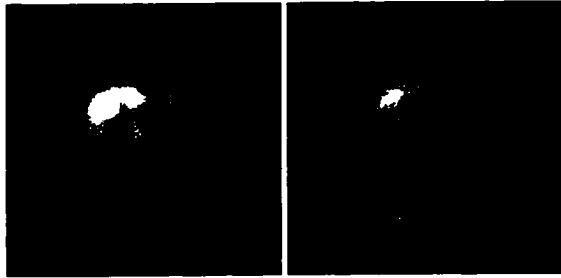


Fig. 7- 4: Aged MOCVD VCSEL with dark-line defects. 780 nm image (left) shows DLDs clearly. Unfiltered image (right) shows less contrast, but still has higher contrast than the images shown earlier in this chapter.

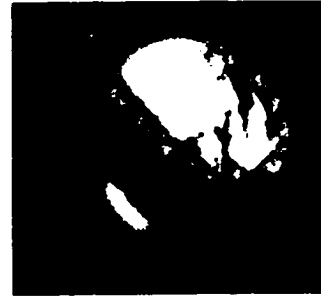


Fig. 7- 5: Large device which failed quickly due to DLDs. Too little luminescence was emitted to allow the use of optical filters with our camera; thus, this is an unfiltered image.

7.2 Dielectric Mirror VCSELs

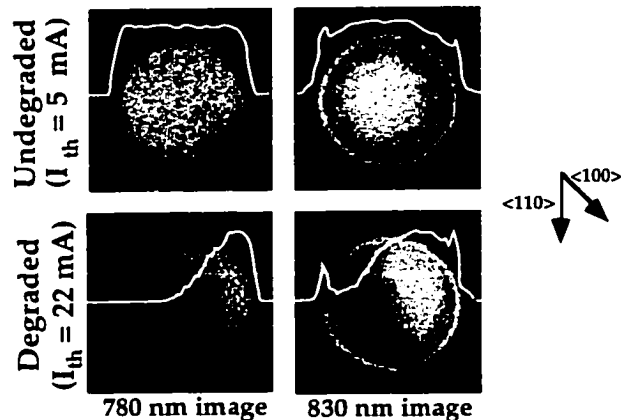


Fig. 7- 6: Dielectric mirror VCSEL before and after rapid aging. Image before aging is very uniform; after aging a $\langle 100 \rangle$ DLD network through the active region has terminated lasing. Linescans in white indicate intensity vs. lateral position through the center of the image.

A number of promising designs using intracavity contacts and dielectric mirrors with oxide apertures have produced record-low threshold gain-guided VCSELs [4]. However, the strain from the dielectric mirrors is known to be problematic. Hybrid designs also exist, where several (e.g., 6) epitaxial mirror pairs are grown in the p-DBR, and the dielectric mirror layers are deposited on top to achieve the desired reflectivity of $>99.7\%$ [5].

We studied how such dielectric mirror devices age under extreme current. We found some devices extremely reliable, indicating no inherent problems with the design.

However, some devices quickly failed due to growth of dark-line defects, as shown in Fig. 7- 6 and Fig. 7- 7.

Before aging, contrast enhancement could be used to detect non-uniformity in some devices, as seen in a large (25- μm -aperture device) Fig. 7- 8. Addressing the source of this non-uniformity might allow for the majority of devices to be improved to the (excellent) standard of the best devices.



Fig. 7- 7: Dielectric mirror VCSEL after rapid aging. 780 nm image is seen at left; unlike previous devices from this chapter, independent image contrast is seen in the 830 nm image (right), showing what appear to be $\langle 110 \rangle$ DLD networks growing from the left of the device toward the right.



Fig. 7- 8: Filtered EL of dielectric mirror device. Image contrast has been enhanced. 780 nm image (left); 830 nm image (right).

References for Chapter 7:

- [1] R. W. Herrick, Y. M. Cheng, P. M. Petroff, M. K. Hibbs-Brenner, and R. A. Morgan, "Spectrally-filtered electroluminescence of vertical-cavity surface-emitting lasers," *IEEE Photonics Technology Letters*, vol. 7, pp. 1107-9, 1995.
- [2] R. W. Herrick, Y. M. Cheng, J. M. Beck, P. M. Petroff, J. W. Scott, M. G. Peters, G. D. Robinson, L. A. Coldren, R. A. Morgan, and M. K. Hibbs-Brenner, "Analysis of VCSEL degradation modes," *Proc. of the SPIE (Fabrication, Testing, and Reliability of Semiconductor Lasers)*, vol. 2683, pp. 123-33, 1996.
- [3] C. A. Gaw, W. Jiang, M. Lebby, P. A. Kiely, and P. R. Claisse, "Characteristics of VCSELs and VCSEL arrays for optical data links," *Proc. of SPIE*, vol. 3004 (Fabrication, Testing, and Reliability of Semiconductor Lasers II), pp. 122-133, 1997.
- [4] D. L. Huffaker, L. A. Graham, H. Deng, and D. G. Deppe, "Sub-40 μA Continuous-Wave Lasing in an Oxidized Vertical-Cavity Surface-Emitting Laser with Dielectric Mirrors," *IEEE Photon. Technol. Lett.*, vol. 8, pp. 974-976, 1996.
- [5] R. A. Morgan, M. K. Hibbs-Brenner, J. A. Lehman, E. L. Kalweit, R. A. Walterson, T. M. Marta, and T. Akinwande, "Hybrid dielectric/AlGaAs mirror spatially filtered vertical cavity top-surface emitting laser," *Applied Physics Letters*, vol. 66, pp. 1157-9, 1995.

Chapter 8: Degradation in index-guided VCSELs

Index-guided VCSELs have a number of advantages over the gain-guided VCSELs which have been the primary focus of our work. While gain-guided lasers count on a thermal lensing to create an index guide, such lensing is unstable and chaotic [1]. Index-guided lasers have more stable beam divergence characteristics, and more predictable modulation response, which is valuable for high speed switching. Index-guided lasers also allow for higher-power single-mode operation [2]. On the down side, index-guided lasers are generally more difficult to produce, and have more potential reliability problems than gain-guided lasers. In particular, the methods used to create an index step also generally subject the device to mechanical stress which may promote $\langle 110 \rangle$ DLD growth. As we shall see, $\langle 110 \rangle$ DLD growth is indeed the primary failure mechanism for index-guided VCSELs.

8.1. 980 nm UCSB Pillar VCSELs

8.1.1 Description of structure

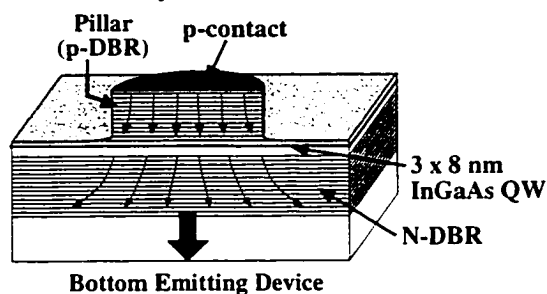


Fig. 8 - 1: Schematic drawing of bottom-emitting, 980 nm pillar VCSEL. The arrows show the current flow path.

The UCSB pillar VCSELs are grown by MBE, and have three 8-nm-wide $\text{In}_{0.18}\text{Ga}_{0.82}\text{As}$ quantum wells, which lase at ~ 980 nm. The p-DBRs are made of $\text{Al}_{0.67}\text{Ga}_{0.33}\text{As}$ / GaAs , while the n-DBRs are AlAs / GaAs stacks. Processing involves etching a pillar through the p-DBR, and putting down a

dielectric insulator which only allows current to flow through the pillar; laser emission is through the substrate, and out a window in the n-metal. The devices then had indium bumps evaporated on the pillars, and were flip-chip bonded. The resulting devices have index guided modes, with high side-mode suppression ratios. The p-down mounting, and excellent heat sinking, allowed record CW powers to be obtained for a variety of sizes [3]. A schematic drawing of the structure is shown in Fig. 8 - 1.

8.1.2 Filtered electroluminescence in degraded etched-pillar VCSELs

We examined flip-chip bonded pillar VCSELs using filtered EL. While some smaller diameter pillar VCSELs have proven very robust, most larger diameter pillars have shown dislocations even before they've been operated, and degrade quickly. With the assistance of filtered EL, we have been able to show that cracks are present. As with our discussion in Chapter 7, the use of spectral filters is useful to isolate spontaneous emission outside the mirror stop band. The filtered images from one device before and after aging are seen in Fig. 8 - 2. The pillar VCSELs studied were produced by Matt Peters, and packaged by Gerry Robinson. Unpackaged devices were also studied, and also showed cracks. Several additional undegraded devices are seen in Fig. 8 - 3.

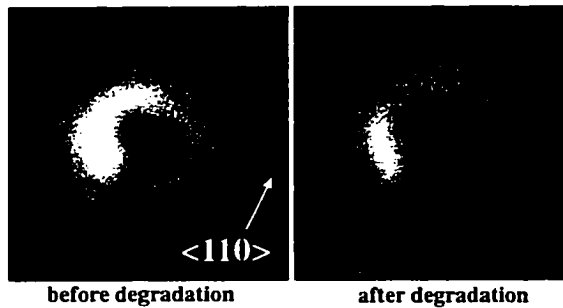


Fig. 8 - 2: Filtered EL images (taken using a short-pass filter with $\lambda \leq 920$ nm) show cracks due to strain from thick indium solder bumps in 12 μm -diameter pillar VCSELs. Cracks do not lengthen as device is aged (right), but they do get wider, possibly due to $\langle 110 \rangle$ DLDs growing out of the crack.

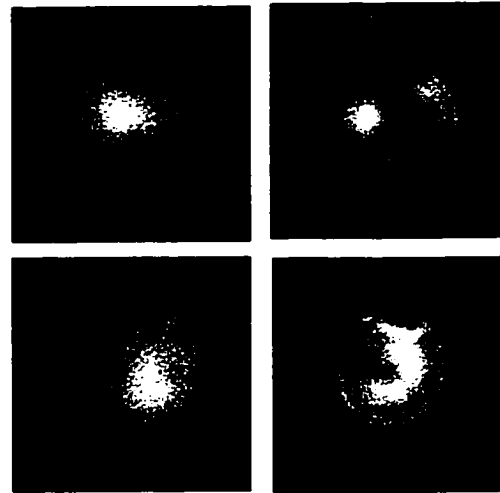


Fig. 8 - 3: Additional filtered EL images of undegraded pillar VCSELs show cracks before aging.

From these images, we conclude that the high stress induced by the thick indium dots evaporated on the pillars may exceed the pillar's yield strength, thereby forming micro-cracks or dislocations in the pillar. We will show in the next section that by using a lower stress technique to form metal bumps (such as plating porous gold bumps), or avoiding placing bumps on the pillars, these stresses can be avoided, and pillar VCSEL lifetime can be greatly extended (Fig. 8 - 4). The InGaAs active region used is known to be inherently very resistant to degradation,

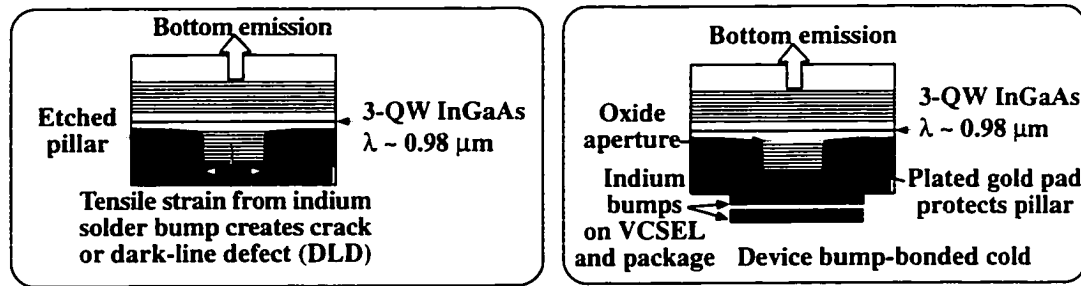


Fig. 8 - 4: Packaging for original UCSB pillar VCSELs (left) allowed indium to apply strain directly to pillars, resulting in cracks in larger ($> 10 \mu\text{m}$) devices. For UCSB oxide-aperture devices (right) porous gold protected pillar from indium bumps.

as discussed in Chapter 2 and Appendix C, which gives these devices good potential for reliable operation. The reliability of the best of the devices tested also gives reason for encouragement that the pillar design is not inherently unreliable. An index guided “ridge waveguide” design has been used by Motorola, with lifetimes of $>10^6$ h being obtained [4].

8.2. 980 nm UCSB oxide-aperture VCSELs

8.2.1 Advantages of oxide aperture VCSELs

While many of the advantages of index-guided lasers can be obtained using a simple pillar design such as that shown in the previous chapter, such a design has a number of disadvantages. First of all, a large fraction of the drive current is being delivered to the edges of the device where it has little chance of contributing to stimulated emission. Second, a great deal of optical scattering can take place at the sidewalls of the pillar waveguides. Both these issues are dealt with in oxide-aperture VCSELs.

Oxide aperture VCSELs are formed by etching a mesa to expose an “oxidation layer” with a high aluminum mole fraction, and then laterally oxidizing the layer in a wet-oxidation furnace. Current is then forced to go through the unoxidized center, improving the efficiency of current delivery [5]. More importantly, perhaps, the oxide has a lower index of refraction than is present in the unoxidized center. Thus an optical “waveguide” is formed, where diffraction loss is offset by the lensing effect from the aperture [6].

Thanks to these improvements, oxide aperture VCSELs have provided the lowest lasing threshold ($<40 \mu\text{A}$) [7], the highest power conversion efficiency at low powers ($>50\%$ p.c.e. at 2 mA) [8], and the highest modulation current efficiency ($>14 \text{ GHz}/\sqrt{\text{mA}}$) with $>15 \text{ GHz}$ for $I < 2 \text{ mA}$ [9, 10].

8.2.2 Background on oxidation and hydrolysis of AlAs and aluminum-rich AlGaAs alloys.

The oxidation technique used for making the oxide-aperture VCSELs has an interesting history [11]. Prof. Nick Holonyak (Univ. of Illinois) noted that over a period of several years, many of the epitaxial growths produced with high aluminum fraction were unstable. In samples with $\text{Al}_x\text{Ga}_{1-x}\text{As}$ layers having $x > 0.85$, he observed delamination due to an undesired hydrolysis reaction which turned the layers into Al_2O_3 . Layer thickness also influenced the speed of the hydrolysis process, with very thin layers (i.e., hundreds of angstroms) much less likely to hydrolyze than thicker ones. His group was able to accelerate the hydrolysis process by using both wet and dry oxidation in furnaces. Eventually, this process was used to produce oxide apertures in laser diodes.

Given that the technique used to produce the oxide apertures originated as a method of testing degradation, it is natural to worry about the stability of oxide-aperture VCSELs after they have been fabricated. However, it has been demonstrated that the proper oxidation technique can leave the outer surface of the VCSEL pillar sealed so that if the device is subsequently re-introduced into the furnace, no additional oxidation takes place [12]. In fact, intentional oxidation may well prevent the unwanted hydrolysis discussed in Chapter 1 [11].

In addition, there was a great deal of concern about the stress resulting from the very high change in lattice constant between the AlAs that was the starting compound, and the Al_2O_3 which is created during hydrolysis (Note that the As is thought to be removed from the device by reacting with the hydrogen from the water vapor to form AsH_3 gas which diffuses out of the device.) . The theoretical linear shrinkage is 20%, with a measured linear shrinkage of $>12\%$ [13]. At Sandia National Laboratories, the devices with the AlAs apertures have proven to have poor lifetime, and the VCSELs pillars easily de-laminate. However, by using

$\text{Al}_{0.98}\text{Ga}_{0.02}\text{As}$, with a lower 6.7% shrinkage [14] and better mechanical properties, both problems are eliminated [15]. Much of the strain problem may well be eliminated by the formation of pores in the oxide which take up much of the shrinkage, and also allow the waste products to escape, and fresh reagent to reach the aperture tip. The oxide aperture VCSELs have shown reliability of 2–3,000 hours at 125°C ambient [16], and thus appear reliable enough for implementation in many commercial systems. Nevertheless, as we shall see, the oxide aperture still appears to be the primary site for nucleation of degradation, so concern about the effects of oxide stress cannot be totally dismissed, even if their effect is more benign than had been anticipated.

One additional reliability consideration has been uncovered from TEM and carrier luminescence studies: defects extend up to 30 nm from the oxide tip. Therefore, it appears advisable to not place the oxide aperture too close to the active region, since these defects could easily nucleate dislocation formation. It also appears to be valuable to minimize the aperture thickness, not only to minimize stress and the degradation it can cause [15], but also to improve device performance by reducing diffraction losses [6].

8.2.3 Description of 980 nm oxide aperture VCSEL Structure

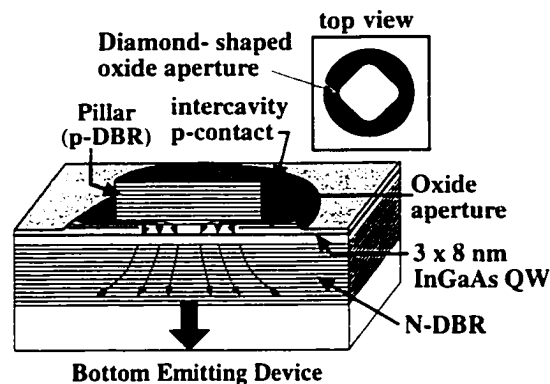


Fig. 8 - 5: Schematic drawing of 980 nm UCSB oxide aperture VCSEL structure

The InGaAs QW VCSELs with oxide apertures were produced and packaged by Brian Thibeault. They use a with the addition of a 30-nm-thick oxide aperture 0.14 μm above the active region to provide both current confinement, and index guiding of the optical wave. Note that although placing the oxide aperture

very close to the active region lowers unwanted current spreading [5], defects visibly extend at least 15 nm above and below the aperture [17], and would be expected to accelerate degradation. These devices can be modulated at up to 15 GHz

with only 2.1 mA of current. Details of the structure, and its performance, can be found elsewhere [10]. A schematic of the structure is shown in Fig. 8 - 5. As discussed in Section 8.1, these devices had porous gold bumps plated on the mesas to provide thermal contact and protect the mesas from bonding stress. Indium was then evaporated on the gold bumps, and the device was bump-bonded at room temperature to a submount, as shown earlier in Fig. 8 - 4.

8.2.4 Filtered electroluminescence of 980 nm oxide aperture VCSELs

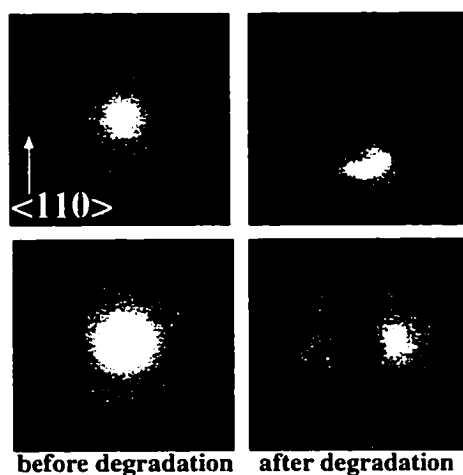


Fig. 8 - 6: Filtered EL shows uniform emission before aging, and $\langle 110 \rangle$ DLDs growing from corners of the oxide apertures after aging.

Filtered electroluminescence was performed as before (with a short pass filter, $\lambda \leq 920$ nm). Typical results from two devices are shown in Fig. 8 - 6. A drawing of the possible degradation process is shown in Fig. 8 - 7. The devices have proven quite robust, and very high currents and junction temperatures are required to obtain any measurable degradation for most well-made oxide aperture VCSELs [16].

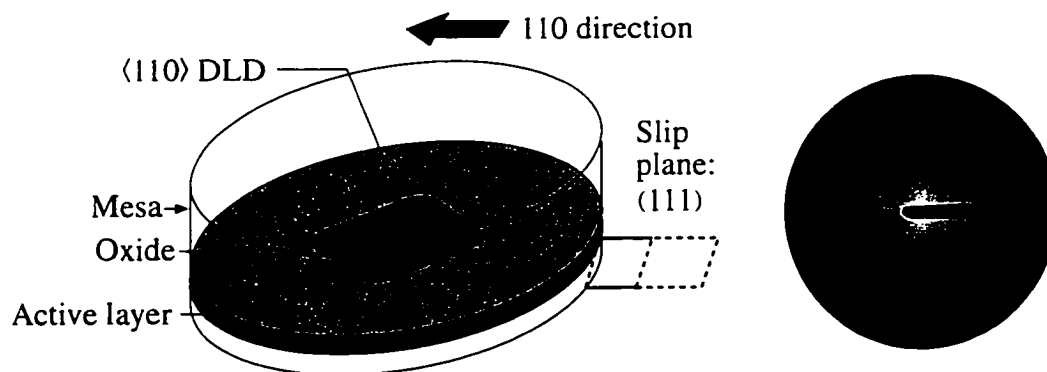


Fig. 8 - 7: Drawing of the suspected nucleation and growth of $\langle 110 \rangle$ DLDs from the 980 nm oxide aperture devices.

8.3. 850 nm GaAs QW Sandia top-emitting oxide aperture VCSELs

8.3.1 Description of 850 nm oxide-aperture structure

850 nm GaAs-QW oxide-aperture VCSELs were obtained from Kent Choquette and Hong Hou of Sandia National Laboratories. The devices in question had “heavily-doped” n-DBRs ($2 \times 10^{18} \text{ cm}^{-3}$ of Si) rather than the usual lower (1×10^{18}) doping. No other changes to the structure had been made, and yet degradation was much more rapid in these devices with heavily doped n-DBR than in the normal structure. Since this was unexpected, Dr. Hou asked me if I would be interested in looking at their devices. It should be noted that Geib et al. (also of Sandia) studied the effects of doping on loss, and observed much larger increases in loss than would be expected from free carrier absorption alone [18]. Some have suggested that this may be due to morphology problems which are correlated with the high doping levels [19].

The layer structure is relatively similar to the Honeywell VCSELs described earlier, with 5 8-nm-thick GaAs QWs, and top emission. However, the DBRs are made of $\text{Al}_{15}\text{Ga}_{85}\text{As}$ / $\text{Al}_{92}\text{Ga}_{08}\text{As}$, with AlAs not being used in the DBRs. The oxide aperture layer was ~45 nm thick, and placed ~0.10 μm above the QWs. The aperture was made of $\text{Al}_{98}\text{Ga}_{02}\text{As}$: the additional few percent gallium greatly reduced the stress from the aperture, and improved the lifetime [15].

Relatively large mesas (>50 μm) are created by dry etching. A 5–10- μm -wide ring contact is used to contact the p-DBR. The devices are top emitting. However, since the oxide aperture extends in by ~15 μm from the mesa edge, the ring contact does not block the EL, and a complete picture of the EL can be obtained without needing any special sample preparation.

Some of the most interesting results came from the comparison of square and round mesa devices: equal numbers of each shape, in a variety of sizes, were contained on the sample. The round-mesa devices gave a diamond-shaped aperture, due to crystallographic-axis dependence of oxidation rates. The square mesa, however, gave a square aperture. As we shall see, the degradation modes observed were quite different for the two shapes.

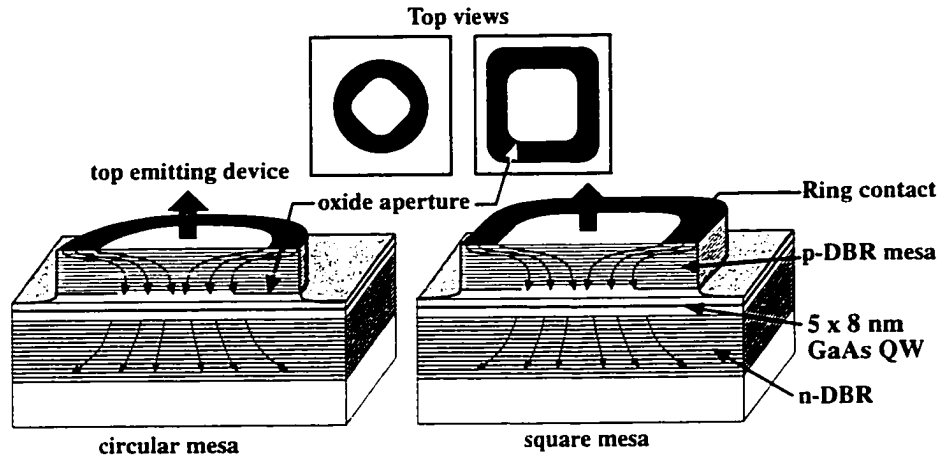


Fig. 8 - 8: Schematic drawing of 850 nm Sandia oxide aperture VCSELs. Both circular and square mesas were investigated, with the former having diamond-shaped apertures, and the latter having square-shaped apertures.

8.3.2 Filtered electroluminescence from 850 nm oxide aperture devices

Filtered electroluminescence was performed using various bandpass filters. As before, the 780 nm filters gave excellent defect contrast, while the unfiltered images showed little contrast. The images were all very uniform before degradation. The images after degradation are shown in Fig. 8 - 9.

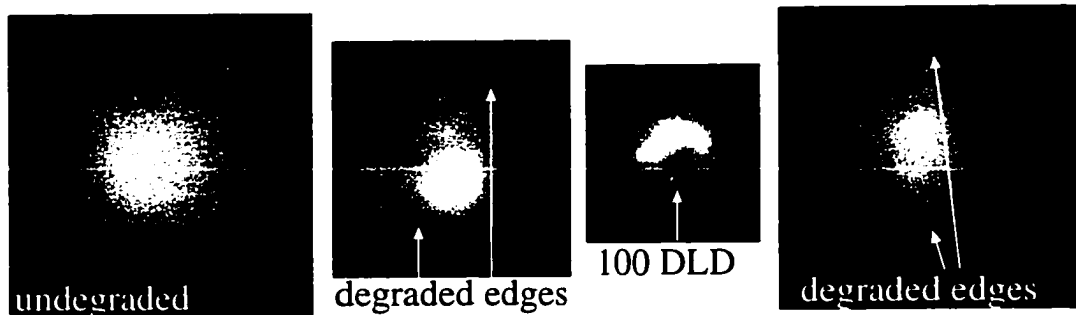


Fig. 8 - 9: Filtered EL images of undegraded (far left) devices were uniform. Degraded square VCSELs (center left and far right) degraded along top and bottom edges. Degraded circular VCSEL (center right) showed $\langle 100 \rangle$ DLD nucleating from bottom corner of aperture.

For the square-mesa VCSELs, darkening started along the top and bottom aperture edges. Little aging appeared to start from the right or left, so the EL image gradually became a rectangle with the square's original width, but reduced height. Relatively high currents past peak output power were required to obtain degradation for the devices shown.

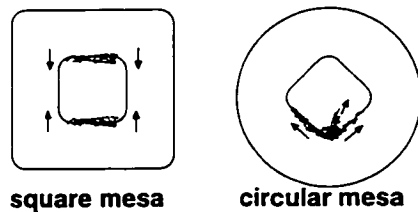


Fig. 8 - 10: Drawing of the propagation of damage in aged square-mesa and circular-mesa devices.

By contrast, the circular-aperture mesa device studied degraded almost immediately at a very modest current. A $\langle 100 \rangle$ DLD appeared to nucleate from the bottom corner of the oxide aperture. We did not study a large enough number of devices to determine whether square- or circular-mesa VCSELs had better reliability.

However, from an intuitive standpoint, we would expect that the very different strain configurations in the two types would lead one of the two designs to have better reliability. I believe this is a promising topic for future investigation.

The anisotropy of the degradation in the square-mesa devices originally seemed surprising. However, there is a substantial body of evidence that 110 and $1\bar{1}0$ DLDs should not be expected to grow at equal rates [20-22].

8.3.3 Cross-sectional CL from 850 nm oxide aperture devices

Cross-sectional cathodoluminescence was performed on an array of square-mesa VCSELs, which included both aged and unaged devices. The results from an unaged device are shown in Fig. 8 - 11. Note that the p-contact appeared to blue-shift the luminescence directly under the contact ring. This appeared to be strain-related, rather than due to doping, since additional doping would be expected to result in a red shift (appendix F). No dislocations were observed in the p-DBR after aging, as were seen in proton-implanted devices (Chapter 4).

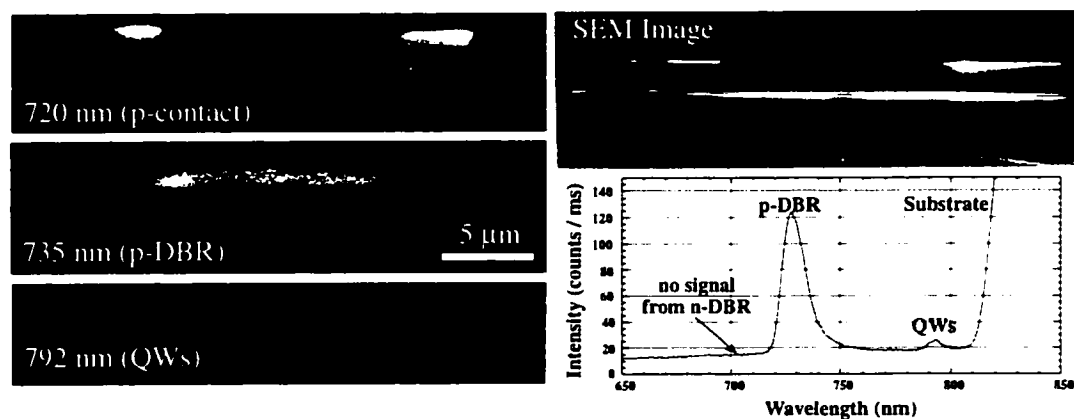


Fig. 8 - 11: Monochromatic CL images (left), SEM image (top right), and CL spectrum (bottom right) for an unaged oxide aperture device.

The CL observations of the “overdoped” Sandia VCSELs were very unusual relative to what had been observed earlier from the Honeywell VCSELs. The results tend to confirm the belief that the n-DBR doping was at fault for the poor reliability of these VCSELs. These were the only devices we have studied for which *no* n-DBR luminescence could be detected in the spectrum. No monochromatic image of the n-DBR could be formed either. Perhaps a high density of non-radiative centers were present in the n-DBR due to non-ideal growth conditions. Furthermore, no luminescence from *any* part of the quantum well could be detected after aging. While it might be expected that the central portion of the active region would be dark after aging (as seen in Ch. 4), there is no reason why that darkening should extend the entire width of the mesa for every aged device. However, if a degradation process originating from uniformly distributed defects in the n-DBR were responsible, this might help to explain why no luminescence could be detected from the active region in any aged device.

Shifting our focus to observations on n-DBRs in proton-implanted VCSELs, we have seen dramatic ($>3\times$) inconsistency between the n-DBR efficiency between various VCSELs (Fig. 4-4), even from the same devices from the same wafer. Except for some indications of precipitates at the n-DBR interfaces using TEM (at the end of Appendix B), we have little indication of what sort of degradation might be taking place. We have never seen spatially-resolvable structures in the n-DBR using CL. Very careful quantitative CL measurements, using known (unaged) reference samples to calibrate at every data run, would be needed to make progress in this area. Studying the effect of the n-DBR on VCSEL degradation is an area we have hardly touched on, but which is promising for future work.

References for Chapter 8:

- [1] K. L. Lear, R. P. Schneider, Jr., K. D. Choquette, and S. P. Kilcoyne, “Index Guiding Dependent Effects in Implant and Oxide Confined Vertical-Cavity Lasers,” *IEEE Photonics Technology Letters*, vol. 8, pp. 740-742, 1996.
- [2] K. D. Choquette, H. Q. Hou, G. R. Hadley, K. M. Geib, D. Mathes, and R. Hull, “High Power Single Transverse Mode Selectively Oxidized VCSELs,” *Proc. of '97 LEOS Summer Topicals*, pp. 73-74, 1997.
- [3] F. H. Peters, M. G. Peters, D. B. Young, J. W. Scott, and L. A. Coldren, “High-power vertical-cavity surface-emitting lasers,” *Electronics Letters*, vol. 29, pp. 200-201, 1993.

- [4] C. A. Gaw, W. Jiang, M. Lebby, P. A. Kiely, and P. R. Claisse, "Characteristics of VCSELs and VCSEL arrays for optical data links," *Proc. of SPIE*, vol. 3004 (Fabrication, Testing, and Reliability of Semiconductor Lasers II), pp. 122-133, 1997.
- [5] E. R. Hegblom, N. M. Margalit, B. J. Thibeault, L. A. Coldren, and J. E. Bowers, "Current Spreading in Apertured Vertical Cavity Lasers," *Proceedings of SPIE, "Vertical Cavity Lasers II"*, vol. 3002, 1997.
- [6] E. R. Hegblom, D. I. Babic, B. J. Thibeault, and L. A. Coldren, "Scattering Losses from Dielectric Apertures in Vertical Cavity Lasers," *Journal of Selected Topics in Quantum Electronics*, vol. 3, pp. 379-389, 1997.
- [7] D. L. Huffaker, L. A. Graham, H. Deng, and D. G. Deppe, "Sub-40 μ A Continuous-Wave Lasing in an Oxidized Vertical-Cavity Surface-Emitting Laser with Dielectric Mirrors," *IEEE Photon. Technol. Lett.*, vol. 8, pp. 974-976, 1996.
- [8] K. L. Lear, K. D. Choquette, R. P. Schneider, Jr., S. P. Kilcoyne, and K. M. Geib, "Selectively oxidised vertical cavity surface emitting lasers with 50% power conversion efficiency," *Electronics Letters*, vol. 31, pp. 208-9, 1995.
- [9] K. L. Lear, V. M. Hietala, H. Q. Hou, J. Banas, B. E. Hammons, J. Zolper, and S. P. Kilcoyne, "Small and large signal modulation of 850 nm oxide-confined VCSELs," *CLEO '97*, pp. 193-194, 1997.
- [10] B. J. Thibeault, K. Bertilsson, E. R. Hegblom, E. Strzelecka, P. D. Floyd, R. Naone, and L. A. Coldren, "High-Speed Characteristics of Low-Optical Loss Oxide-Apertured Vertical-Cavity Lasers," *IEEE Photonics Technology Letters*, vol. 9, pp. 11-13, 1997.
- [11] R. D. Dupuis, "III-V Compound Semiconductor Native Oxides — The Newest of the Semiconductor Device Materials," *Compound Semiconductor*, vol. 3 #1, pp. 32-34, 1997.
- [12] D. L. Huffaker, D. G. Deppe, C. Lei, and L. A. Hodge, "Sealing AlAs against oxidative decomposition and its use in device fabrication," *Applied Physics Letters*, vol. 68, pp. 1948-50, 1996.
- [13] M. H. MacDougal, H. Zhao, P. D. Dapkus, and M. Ziari, "Wide-bandwidth distributed Bragg reflectors using oxide/GaAs multilayers," *Electronics Letters*, vol. 30, pp. 1147-9, 1994.
- [14] R. D. Twisten, D. M. Follstaedt, K. D. Choquette, and R. P. Schneider, "Microstructure of laterally oxidized $\text{Al}_x\text{Ga}_{1-x}\text{As}$ layers in vertical-cavity lasers," *Applied Physics Letters*, vol. 69, pp. 19-21, 1996.
- [15] K. D. Choquette, K. M. Geib, H. C. Chui, B. E. Hammons, H. Q. Hou, T. J. Drummond, and R. Hull, "Selective oxidation of buried AlGaAs versus AlAs layers," *Applied Physics Letters*, vol. 69, pp. 1385-7, 1996.
- [16] K. L. Lear, "Oxide-Confined VCSELs: a Reality Check," *Proc. of SPIE*, vol. Reliability, Fabrication, and Testing III, 1998.
- [17] S. S. Shi, E. L. Hu, J. P. Zhang, Y. L. Chang, P. Parikh, and U. Mishra, "Photoluminescence study of hydrogenated aluminum oxide-semiconductor interface," *Applied Physics Letters*, vol. 70, pp. 1293-1295, 1997.
- [18] K. M. Geib, K. D. Choquette, H. C. Chui, and H. Hou, "Mirror reflectivity and doping considerations for high-performance oxide-confined vertical-cavity lasers," *Proc. of CLEO-96*, pp. 422-423, 1996.
- [19] Personal communication with Eric Hegblom
- [20] D. B. Holt, "Device Effects of Dislocations," *Journal de Physique*, vol. 40, pp. C6-189-199, 1979.
- [21] E. Depaetère, D. Vignaud, J. L. Farvacque, B. Sieber, and A. Lefebvre, "The photoplastic effect in GaAs, a model for device degradation phenomena," *Philosophical Magazine A*, vol. 61, pp. 893-907, 1990.

- [22] D. B. Holt, E. Napchan, L. Lazzarini, M. Urchulutegui, and G. Salviati, "Quantitative studies of beam-induced defects in III-V compounds by cathodoluminescence and transmission electron microscopy," *Materials Science and Engineering B*, vol. 24, pp. 130-134, 1994.

9. Conclusions and Suggested Future Work.

9.1 Brief summary of findings

By now, hopefully the reader has grasped just how complex VCSEL degradation is, and the large variety of different failure modes which exist in aged VCSELs. The one which appears to be the most important is the “current shunting” mechanism discussed in Chapter 3, which also appears to be the cause of failure for red InGaP VCSELs. We have shown that this mechanism is the sole cause of failure for rapidly-degraded proton implanted VCSELs. Other mechanisms, which were not accelerated by as large a factor during rapid aging, may also be important under actual operation. To resolve this uncertainty, we recommend doing more work on gradually degraded devices. To ease the analysis process, we suggest specially aging arrays of devices, as we detail in the next section.

Failure mechanisms involving dislocation growth, of many different types, were shown in Chapters 4, 7, and 8. In fact, this would have been the failure mechanism one would expect to dominate the aging process, if one had to predict on the basis of stripe laser results. The assumption that rapidly-aged and gradually-aged VCSELs fail in the same manner is probably valid for the VCSELs of Chapters 7 and 8, where DLDs in the active region appears to be the sole failure mechanism. However, more work would be needed to verify this conclusion.

Perhaps the main point to doing failure analysis is being able to make suggestions which improve the lifetime of the devices. We have come up with a few of our own. General suggestions are contained in Chapters 2 and 4 and Appendix C. We also discussed a “wide-gap-mirror” idea in Chapter 5 which reduced the early failure rate in early tests. Suggestions specific to red VCSELs and index-guided VCSELs are contained in Chapters 6 and 8 respectively. The annealing procedure for red InGaP devices particularly stands out as being potentially useful for improving the lifetime of the devices studied.

9.2 Future work.

9.2.1 Failure Analysis on 850 nm VCSELs

A great deal of evidence has been accumulated showing that VCSELs which are rapidly aged fail solely due to the “current shunting” mechanism discussed in Chapter 3. In addition, there is evidence to suggest that this is the dominant mechanism for VCSELs which are aged at normal currents in year-long accelerated life tests. While no dislocation growth takes place in rapidly-degraded VCSELs, dislocations *do* grow in VCSELs aged more gradually. With this observation having been made, it seems worthwhile to concentrate on studying gradually-degraded devices, which are expected to be more indicative of the true failure mode. The only reason such devices haven’t been studied more thoroughly up until now is the degree of difficulty doing sample preparation on tiny (400- μm square) die.

9.2.1.1 Recommended Aging Procedures for Future Samples

The ideal sample for failure analysis would be a chip approximately 2x3 mm in dimension (or larger), to allow polishing without edge effects dominating, or to allow cross sectioning for TEM. It would have at least 8 devices in a row along the same line, to allow easy examination of more than a single device. The devices would be far enough apart to not directly affect one another during aging, but close enough together that multiple devices could be observed in TEM (pitch $\leq 250\ \mu\text{m}$). This having been said, even a number of devices on a sparser 600 μm pitch (used for packagable VCSELs) would be an improvement over the current state of affairs.

Such an array could be aged using normal, single-VCSEL mounts and current supplies by connecting up to 8 devices in parallel using either separate wire bonds or a stitch bonding technique, and a standard header. Aging over a minimum of 2,000 hours, at moderate currents ($\sim 20\ \text{mA}$ per device), and temperatures which allowed the device to still lase would all be ideal; however, such conditions may not sufficiently accelerate the aging process with VCSELs which have improved reliability.

Mounting of the array should be focused on simplifying demounting for ease of failure analysis. Devices should be mounted using a soluble cement (e.g., cyanoacrylate, or “Krazy Glue” which dissolves in acetone). This is, of course, non conductive. A thin strand of silver epoxy, or better yet, silver paint, can be used to provide electrical continuity between the header and the n-side of the device. Note

that silver paint would not, by itself, have sufficient adhesion to permit subsequent wire bonding. Cyanoacrylate glues, however, *do* have sufficient strength to allow wire bonding of devices. At least a dozen arrays should be aged, to allow for a variety of destructive techniques to be used, and to account for yield losses in sample preparation.

Thus prepared, gradually-aged arrays of devices would allow easy observation by a variety of different techniques, and give greater confidence that the results were reflective of what would be observed under actual aging conditions.

9.2.1.2 Investigation of doping profiles

Clearly one of the key findings of this work is that degradation, at least in its early stages, is attributable not to degradation of the device in the usual sense of non-radiative centers, but due to modification of the current path taken. Our evidence of this is indirect: we can show that CL and EBIC (which don't depend on current flow paths) give perfectly uniform profiles, while EL (which *is* sensitive to current flow) changes after aging. However, *direct* evidence of dopant passivation would be valuable. Two techniques to quantify the changes in activated doping are suggested, and are discussed briefly in the following sections.

9.2.1.2.1 Etch-dependent techniques

Two-dimensional doping profiles have been studied in silicon devices by cleaving or polishing a device cross section, and then using a doping selective etch, which etches highly-doped material more rapidly than lightly-doped material. The device can then be examined by TEM [1], SEM [2], or atomic force microscopy (AFM)[3]. Provided it is available, AFM appears to be the most useful method, since the quantitative data of etch depth versus x and y is easily extracted, and the sample preparation is much simpler than for TEM. The doping selective etches have better depth contrast for highly doped regions (e.g., comparing 10^{19} cm^{-3} vs. 10^{20} cm^{-3}), and much less accuracy for low-doped regions (e.g. 10^{15} cm^{-3} vs. 10^{16} cm^{-3}). This is clearly evident in the doping calibration curve (Fig. 2a) shown in Barrett et al [3]. In this respect the doping-dependent etch techniques are complementary to scanning capacitance microscopy (SCM), which is excellent for distinguishing low doping levels, but has less accuracy in highly-doped areas.

9.2.1.2.2 Scanning Capacitance Microscopy (SCM)

Scanning capacitance microscopy measures the capacitance between a conductive AFM tip and the sample (usually at 915 MHz). Heavily doped regions generally have high capacitance, while lightly-doped regions have lower capacitance. SCM can measure doping levels down to 10^{14} cm^{-3} , with 20 nm spatial resolution [4]. For additional details, a nice discussion is present at Digital Instrument's web site (www.di.com) under the applications note section.

9.2.1.3 Humidity and Electrostatic Discharge (ESD) Failures

As the devices are improved to provide very low early failure rates across the full operating temperature range, the focus will turn to failure modes other than those caused by aging itself. As discussed in Chapter 1, hydrolysis threatens to put a "reliability roof" over any device which is not properly packaged or otherwise sealed. Electrostatic Discharge (ESD) is also an ever-present threat, with failure levels typically being $< 1000 \text{ V}$ [5]. While Honeywell sent devices of both types to look at, I have not done any analysis of note on either type of failure mechanism.

9.2.1.4 Looking for DLDs using *in-situ* cross-sectional scanning tunneling microscopy (STM)

Cross-sectional STM should in principle easily be able to detect the presence of dark-line defects in the vicinity of the scanning probe. It might be able to map out such defects in a manner similar to the cross-sectional TEM shown in Chapter 4, with much simpler sample preparation. There is even some hope the results might be able to give us quantitative information on the electrical properties of dislocations — something that has been in short supply.

9.2.1.5 Spectral measurements of increased cavity loss as device degrades

If spatially-resolved ($\sim 10 \mu\text{m}$) reflectivity spectra could be taken of VCSELs before and after degradation, we might be able to see the effects of increased mirror loss. The full-width half-maximum (FWHM) of the reflectivity null is proportional to the cavity loss. If DLDs in the cavity were adding to the loss, we would expect to be able to observe an increase in the width of the reflectivity null.

9.2.2 Failure Analysis on Other Structures

9.2.2.1 Red VCSELs

Further work to understand the annealing process would be obvious. More fundamental experiments, using variable temperature and externally-applied (laser)

irradiation intensity could be used. Methods which allowed quantitative measurement of trap density (e.g., by DLTS) would also be potentially useful.

We propose an experiment to verify whether current-shunting is present in red VCSELs, and whether dopant passivation is taking place in the n- or p-DBR. This takes advantage of our ability to selectively remove the DBR mirrors by wet etching. In this experiment, two identical arrays are aged by identical amounts. On one sample, the p-metals are polished off, and the p-DBR is removed with HF, leaving the cladding layers, the active region, the n-DBR, and the substrate. A semitransparent contact is then deposited, allowing electroluminescence observations to be made. The other sample is bonded epi-side down to a conductive mount using a small amount of silver epoxy, and being careful to avoid shorting around the edges. The edges of the device are protected with photoresist, and a hole is opened in the n-metal using a strong HF/HNO₃ etch. The substrate is then removed by spray etching, and the n-DBR is removed with HF. A semitransparent contact is then made to the n-side that remains.

Both samples are then imaged using filtered EL. By examining the patterns observed in the two samples, we can determine whether degradation has occurred in the active region (in which case it should cause darkening in both samples); whether passivation of the p-DBR has occurred (in which case do dark central spot should be observed after the p-DBR has been removed), or if passivation of the n-DBR has occurred. Anticipated images are shown in Fig. 9-1. We assume, given the very different behaviors of the n- and p-DBR in degradation, that if dopant passivation is indeed a culprit, it will occur much more rapidly in one DBR than in the other.

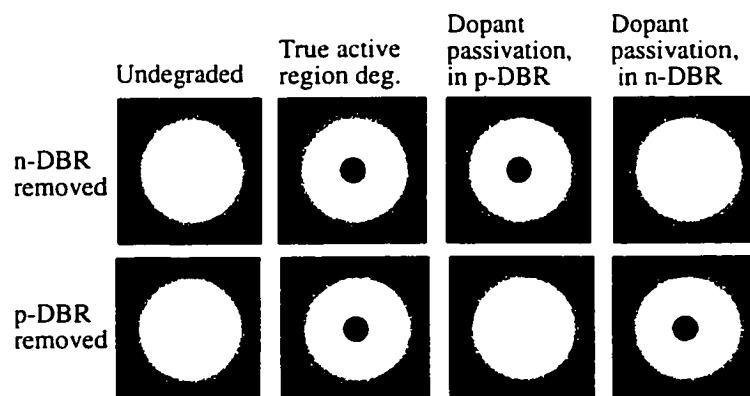


Fig. 9 - 1: Anticipated images from specially-prepared arrays.

9.2.2.2 Oxide Aperture VCSELs

Only very preliminary studies were performed on oxide-aperture devices. A number of the newer design recommendations which are being made, placing the aperture extremely close to the active region, seem particularly problematic for reliability, given that obvious damage can be seen as far as 15 nm below the tip.

9.2.2.3 Fused VCSELs

Excellent 1.3 and 1.55 μm VCSELs have been produced by fusing GaAs-based mirrors with InP-based active regions [6]. It is logical to expect the failure mechanism in these VCSELs to differ from the failure mechanisms seen in the GaAs QW devices we studied. Of course, the fused junction itself is an area of potential concern, since the area immediately surrounding it has locally high strain, and areas with recombination centers. I provided some minor assistance for Near Margalit to start with life testing on these lasers — the initial results look surprisingly good, especially since no design optimization has been made to specifically address reliability concerns. Failure analysis on these VCSELs would be a worthwhile project.

9.2.2.4 GaN lasers

GaN or InGaN lasers, with lasing wavelengths in the violet, are of great interest for data storage. While early devices showed very poor lifetime (<1 second at room temperature), they are rapidly improving. The material is quite amazing, since even with very high dislocation densities ($>10^{10} \text{ cm}^{-2}$), device performance is fairly good. Further, the dislocations do not appear to strongly affect device degradation — contact resistance, and contact degradation, are the limiting factors. In other III-V materials, both performance and reliability are adversely affected by dislocation concentrations above 10^4 cm^{-2} . Understanding what is important in GaN reliability would be of interest.

9.2.3 Fundamental Work

Historically, work on device degradation has been quickly dropped once a device has achieved the desired (low) failure rates for the applications envisioned. The field of failure analysis has thus never matured to the level other fields have achieved, and has what seem to me to be an inordinate number of unanswered questions. However, this must also stem from the fact that degradation is not

repeatable — it is by its nature chaotic and involving fractal growth; the dislocations which are its fundamental unit are quite hard to measure since they are only one atomic row wide, and it is impossible to observe the fundamental reactions taking place, since point defect flow cannot be observed.

9.2.3.1 Understanding how active region strain and growth conditions affect dislocation growth

For traditional stripe lasers, perfecting the active region (using the optimizations we shall discuss below) is the primary focus of efforts to improve reliability. Studying *why* compressively strained active regions give better reliability would help to shed light on debates which have gone unresolved for decades, and which are important to predicting which new materials systems will give the best reliability. My original plan for my Ph.D. studies also was to investigate how growth conditions affect reliability in a more quantitative manner than the purely empirical unpublished studies which have taken place to date. The discovery of a large number of previously unreported VCSEL failure mechanisms changed the focus of my research. However, once these novel mechanisms have been eliminated, perfecting the active region, (e.g., QW strain, growth conditions, etc.), will also be perhaps the primary focus in VCSEL improvement efforts.

9.2.3.2 Understanding how dopants selected affect degradation

As illustrated by the very poor lifetime of the Sandia VCSELs with heavy silicon doping in their n-DBR, doping can have a strong affect on lifetime. The cause-effect relationship has not been well-explored. How high can we go with doping? How far from the active region should we stop to maximize device lifetime? What growth conditions optimize dopant incorporation? As discussed in chapter 4, dopant segregation often causes a pile-up of dopants at the inverted interface (i.e., where AlAs is tapered down to AlGaAs). Dopants may be accompanied by an elevated point defect concentration, which may contribute to defect formation. Optimizing dopant profile to give low resistance, without excessive concentrations, would seem prudent. Further, since dopants differ in the ways they incorporate in the lattice (i.e., substitutional vs. interstitial), and in how mobile they are (e.g., Zn vs. C), we might be able to improve device lifetime by experimenting with different species of dopants. Stability is also affected by growth

conditions, with substitutional dopants being far more stable than ones which incorporate at interstitial sites. Finally, the p-n junction is usually not exactly placed in the active region: it usually is displaced to one side or another, leaving a “virtual anode” or “virtual cathode,” which has an effect on reliability [7]. These aspects would be interesting to study further.

9.2.3.3 Growth technique

In chapter 4, we mentioned SIMS studies which have shown that oxygen can incorporate at the inverted interface in the DBRs, presumably due to oxygen gettering by the AlAs. This has not been observed in LPE or MOCVD [8], perhaps due to the presence of hydrogen, which is able to reduce oxides and remove them from the growth chamber before they are incorporated in the lattice. Outstanding stripe laser reliability has been demonstrated in both MBE and MOCVD structures (albeit with lower aluminum mole fraction, and far fewer interfaces than are used in VCSELs). It would be interesting to see if any systematic difference in reliability was observed when comparing structures which have identical design and processing, with growth technique being the only variable. Comparing fundamental properties, such as point defect concentrations, carrier lifetimes, and doping profiles with each growth method would also be valuable.

9.2.3.4 Active layer thickness

Judging from the difference in the character of DLD growth seen in devices with different well widths (refer to Chapter 2), there appear to be fundamental changes in how DLD propagation takes place as well width is changed. Understanding why this happens, and how the dislocations grow, might allow us to better control dislocation growth. More generally, developing fractal models which are able to mimic the observed behavior of dislocations would also improve our understanding of dislocation growth, and make reliability models of arrays more accurate by predicting how reliability of neighboring elements can affect other array emitters.

9.2.3.5 Structural strain

Many of the early oxide-aperture VCSELs had very poor lifetime. This was probably due to two effects: first, as has been shown by Sandia, the oxidation of pure AlAs layers creates both poor p-mirror adhesion, high strain, and low device

lifetimes. Further, many of the early oxide-aperture VCSELs had highly-strained dielectric mirrors. As discussed in Chapter 2, it has been shown that elastic strain accelerates the growth of $\langle 110 \rangle$ DLDs.

Even for the less-vulnerable gain-guided lasers, strain from dielectrics and contact metals can drive degradation. With additional work, dielectrics such as Si_3N_4 can be deposited with very low stress, although for most applications, simply minimizing the dielectric thickness is enough to avert problems. Keeping metals to reasonable thickness, and using deposition techniques which minimize strain, is also helpful.

9.2.3.6 Optimal metallization

Given that the evidence in section 4.3.2 appears to indicate that the p-contacts are a source of nucleation for the dislocations, it would be useful to study whether alternate p-metal layers would be less likely to nucleate such dislocations.

9.2.3.7 Laser induced degradation

As a study in fundamental materials properties and device physics, a high-power laser (either Ar^+ or Ti: Sapphire) can be focused on the sample, and induce dislocations. Samples grown with different conditions, different doping levels, or different layer structures could be rapidly compared. Further, the effects of proton implantation, interfaces, and different metallization recipes could be compared.

9.2.3.8 Electrical properties of dislocations

Little quantitative information is known about the fundamental properties of dislocations in GaAs, either electrical or optical. Ballistic electron emission microscopy (BEEM) has been used to measure the electrical properties of misfit dislocations in InGaAs [9]. Similar measurements of degraded active regions in GaAs would be useful in understanding how carriers recombine in active regions after some degradation has taken place. This could prove helpful in modeling devices and systems that were robust even after they had aged through most of their life. Designing an experiment to measure the optical absorption cross-section of dislocated material would also be of interest.

References for Chapter 9

- [1] R. Alvis, S. Luning, L. Thompson, R. Sinclair, and P. Griffin, "Physical characterization of two-dimensional doping profiles for process modeling," *Journal of Vacuum Science and Technology B*, vol. 14, pp. 231-235, 1996.
- [2] D. Venables and D. M. Maher, "Quantitative two-dimensional dopant profiles obtained directly from secondary electron images," *Journal of Vacuum Science and Technology B*, vol. 14, pp. 421-425, 1996.
- [3] M. Barrett, M. Dennis, D. Tiffin, Y. Li, and C. K. Shih, "Two-dimensional dopant profiling of very large scale integrated devices using selective etching and atomic force microscopy," *Journal of Vacuum Science and Technology B*, vol. 14, pp. 447-451, 1996.
- [4] G. Neubauer, A. Erickson, C. C. Williams, J. J. Kopanski, M. Rodgers, and D. Adderton, "Two-dimensional scanning capacitance microscopy measurements of cross-sectioned very large scale integration test structures," *Journal of Vacuum Science and Technology B*, vol. 14, pp. 426-432, 1996.
- [5] M. Lebby, C. A. Gaw, J. Wenbin, P. A. Kiely, S. Chan Long, P. R. Claisse, J. Ramdani, D. H. Hartman, D. B. Schwartz, and J. Grula, "Use of VCSEL arrays for parallel optical interconnects," *Proc. of SPIE*, vol. 2683 (Fabrication, Testing, and Reliability of Semiconductor Lasers), pp. 81-91, 1996.
- [6] N. M. Margalit, J. Piprek, S. Zhang, D. I. Babic, K. Streubel, R. P. Mirin, J. R. Wesselmann, J. E. Bowers, and E. L. Hu, "64 °C Continuous-wave Operation of 1.5- μ m Vertical-Cavity Lasers," *IEEE Journal of Selected Topics in Quantum Electronics*, vol. 3, pp. 359-365, 1997.
- [7] R. B. Martins, P. Henoc, B. Akamatsu, and J. F. Palmier, "A model for the degradation of Ga(Al)As single-quantum-well lasers," *Journal of Applied Physics*, vol. 70, pp. 554-61, 1991.
- [8] T. Achnich, G. Burri, and M. Illegems, "Study of oxygen incorporation in AlGaAs layers growth by molecular-beam epitaxy," *Journal of Vacuum Science & Technology A (Vacuum, Surfaces, and Films)*, vol. 7, pp. 2537-41, 1989.
- [9] E. Y. Lee, S. Bhargava, M. A. Chin, and V. Narayanamurti, "Observation of misfit dislocations in InGaAs/GaAs interface by ballistic electron emission microscopy," *Applied Physics Letters*, vol. 69, pp. 940-2, 1996.

Appendix A: Scanning Probe Microscopy Experiments.

A.1. Near-field scanning optical microscopy (NSOM)

A.1.1 Background on NSOM, and advantages of technique

One of the key issues to understanding the device degradation has been understanding what causes dislocation formation in the p-DBR. Since we believe this is driven by minority carriers in the $\text{Al}_{16}\text{Ga}_{84}\text{As}$ layers of the DBRs, it would be valuable to definitively prove that there is indeed a significant minority carrier population present in the AlGaAs layers during normal (electrically-pumped) device operation. This should be quite simple given the unique spectral signature from the p-DBRs, peaking at 790 nm, as shown in Chapter 5. Unfortunately, the complex mirror reflectivity spectrum of the DBR (also shown in Chapter 5) has reflectivity nulls which result in spectral peaks at the same wavelength. These can be attributed to spontaneous emission from the active region escaping through the mirror reflectivity. Further, no direct 790 nm peaks were observed from the side-on spectra of the cleaved VCSELs either. Thus, it appeared it would be quite valuable to be able to take spatially-resolved spectra, from both the p-DBR, and from the active region, and show that 790 nm luminescence was originating from the p-DBR itself.

Near-field Scanning Optical Microscopy (NSOM) is well suited to this task, having better than diffraction-limited spatial resolution, which is controlled by the diameter of the aperture tip (generally 0.1 μm for these experiments). While the signal picked up is generally controlled by evanescent coupling, and falls off rapidly below the surface (as the wave expands into 2π steradians), our experiments were complicated by waveguiding effects from the VCSEL layers. Nonetheless, we were able to obtain unambiguous evidence of luminescence from the p-DBR in normal VCSEL samples — luminescence which we did not see from the n-DBR side, or from samples with higher aluminum mole fraction mirrors. While the evidence still requires some understanding of many complicated effects at play, I regard these results as most direct proof that optical pumping from the active region is injecting minority carriers into the DBRs, and in particular, into the p-DBR. The NSOM experiments were done on cross-sectioned samples I prepared and mounted to allow

electrical operation under normal lasing conditions, while observing luminescence being emitted from the side. The measurements and analysis were done by Jessie DeAro and Kenneth Weston of Prof. Steven Buratto's group, in the UCSB Chemistry Department. I am deeply indebted to them for their collaboration in this work.

A.1.2 Experimental Configurations

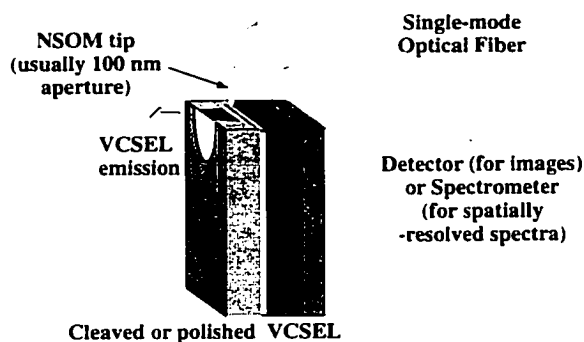


Fig. A - 1: Schematic diagram of NSOM experimental configuration.

The experimental apparatus used for the NSOM is shown schematically in Fig. A - 1. The configuration shown is one of four that were used. Electroluminescence mapping is depicted, where a sinusoidal current is sent into the VCSEL, and the light generated by the laser is detected by a sensitive

detector which is routed into a lock-in amplifier. The tip is rastered across the sample, and a map is created of the signal vs. x and y . It should be noted that while the spatial resolution of the NSOM tips exceeds the diffraction limit, the throughput of the tips is only 10^{-6} . (i.e., for every 10^6 photons impinging on the tip, only 1 will be detected at the other end of the fiber.) Thus, very sensitive detectors are needed.

The second experimental configuration was spatially resolved electroluminescence spectra. Scans were taken with $0.1\ \mu\text{m}$ transverse spacing, from a few microns below the active region (in the n-DBR), to a few microns above the active region (in the p-DBR). Peak voltages of 1.8V were used. The data sets were collected using a spectrometer with a cooled Si CCD array. These scans were later analyzed extensively by Jessie DeAro (to be published).

The third configuration used collected spatially-resolved photoluminescence spectra. In this configuration, light from a He-Ne (633 nm) laser is coupled through the tip to excite the sample (including layers which would not be expected to luminesce under forward bias). Again, spectra were taken at $0.1\ \mu\text{m}$ steps. A beam

splitter was used to allow the simultaneous injection of pump photons, and collection of signal photons. PL mapping was also performed.

The fourth and final configuration was for photocurrent. In this configuration, the electrical leads of the laser were connected to the lock-in amplifier, and He-Ne light is coupled into the VCSEL. This is somewhat similar to cross-sectional EBIC: if carriers are generated in or near the depletion region, they will be collected and create a photo-current. Carriers generated outside the depletion region recombine without contributing to photo-current. This technique has been used to find problems with buried laser regrowth in the past [1].

A.1.3 Results with normal VCSEL (with $\text{Al}_{.16}\text{Ga}_{.84}\text{As}$ layers in DBRs).

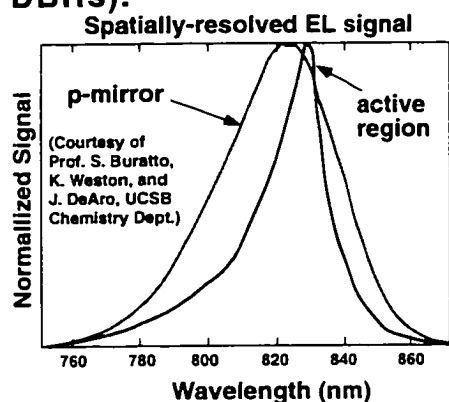


Fig. A - 2: Spatially-resolved electroluminescence spectra.

The spectra from two spots, one at the active region, and one at the p-mirror near the active region, are shown in Fig. A - 2. These spectra show clear differences, with a much greater contribution from 790 nm light originating from the $\text{Al}_{.16}\text{Ga}_{.84}\text{As}$ layers in the p-DBR. This is not an experimental artifact, since it is not seen in the n-DBRs (which have at least a 3-fold reduction in absorption of spontaneous emission), nor is it seen in VCSELs with wider-bandgap mirrors, as discussed in the next section.

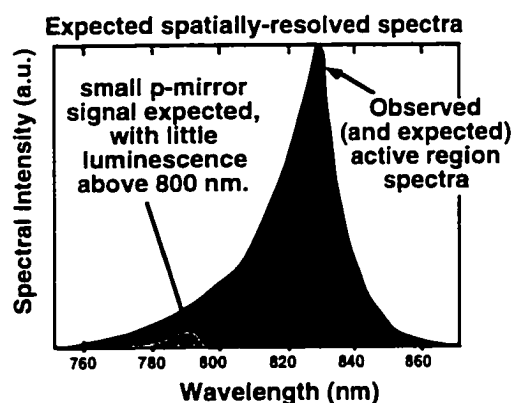


Fig. A - 3: Data expected from ideal (thin) sample in the absence of waveguiding effects.

The spectra we expected to see were more similar to those shown in Fig. A - 3, with relatively little luminescence from the active region wavelengths being observed when the tip was over the p-DBR. However, in reality, light from the active region several microns below the cleaved surface is able to successfully couple into the NSOM tips by way of waveguiding

(i.e., multiple reflections) off DBR layers. In the absence of such photon scattering, very little light from deeper in the structure would be expected to couple into the NSOM tip, since the intensity of the light falls off very rapidly with increasing distance from the tip. In theory, a thin sample could be made which would avoid these undesired waveguiding effects, and give clearer data, as shown in Fig. A - 4. However, such a sample would be both difficult to make, and difficult to inject current into. The evidence presented in this chapter 5, coupled with common sense, was seen as all the evidence needed that minority carriers are indeed being injected into the DBR layers, so we did not pursue fabrication of such a sample.

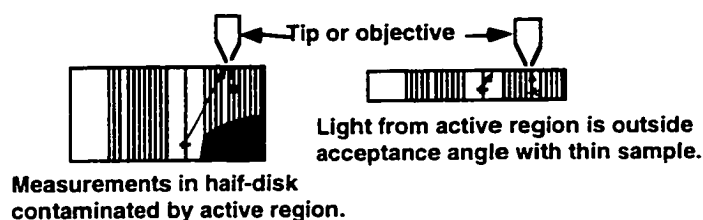


Fig. A - 4: Comparison of collection effects from thin and thick samples.

For more detail on the NSOM results taken on the normal VCSEL samples, refer to the paper by DeAro, Weston, Buratto, Herrick, and Petroff [2].

A.1.4 Results with modified VCSELs (with $\text{Al}_{.24}\text{Ga}_{.76}\text{As}$ layers in DBRs).

As was discussed in Chapter 5, by increasing the aluminum mole fraction used in the AlGaAs layers of the DBR, the bandgap increases from 1.58 eV to 1.67 eV, and the absorption of the mirrors is calculated to fall by approximately a factor of 20 (i.e., to be reduced by 95%). Thus, by making VCSELs with this design modification, we expect to essentially eliminate absorption and thus also eliminate the resultant minority carrier injection and the luminescence observed from the mirror layers.

Three types of NSOM analysis (described earlier) are shown below in Fig. A - 6. While the photocurrent image gives the signal expected, both the EL and PL images show unexpected results. The EL image shows brighter luminescence coming from the substrate than from the active region itself. Of course, the design does not call for the substrate to be emitting light, so this was a surprise. However, we have observed this in conventional EL as well (see Fig. A - 8 later in this chapter). We believe spontaneous emission which is able to get through the

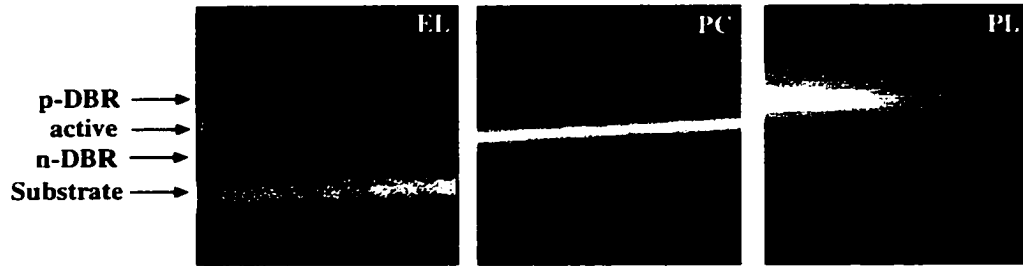


Fig. A - 6: Spatially-resolved electroluminescence (EL), photocurrent (PC), and photoluminescence (PL) maps for an ordinary wide-bandgap VCSEL. (Courtesy of Jessie DeAro.)

reflectivity nulls in the n-DBR is able to optically pump the substrate, and as the carriers recombine, they give off 870 nm luminescence. This can be confirmed with the spatially-resolved EL spectral scans which were taken. This effect (of the spontaneous emission optically pumping the substrate) appears to modify the thermal profile of the device, as we discuss in the section on scanning thermal microscopy (SThM) results later in this chapter. The proton implant can be clearly seen in the PL image, and is similar to that seen with CL (as seen in chapter 4). The weakness of the n-DBR relative to the p-DBR in this image is believed to be a function of the plane-fitting routine used, since the spectral intensity of the n-DBR was only slightly lower than that of the p-DBR.

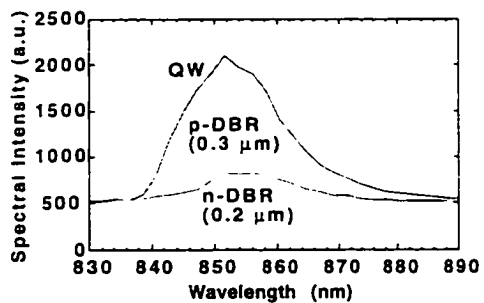


Fig. A - 5: Spatially-resolved spectra taken from the active region, the p-DBR, and the n-DBR, in a wide-bandgap DBR sample. Note that unlike the conventional sample (Fig. A - 2), there is little difference between the spectra. (Spectra courtesy of Jessie DeAro)

As expected, the wide gap mirror samples eliminate both the presence of the 790 nm peak which was previously observed due to $\text{Al}_{16}\text{Ga}_{84}\text{As}$ luminescence, and the shift of the spectrum as a function of position. Three spectra (including two taken at the same positions as the spectra shown earlier in Fig. A - 2) are shown below in Fig. A - 5. Note that they are essentially the same, as would be expected in the absence of a spectral contribution from the p-DBR.

A.2. Scanning Thermal Microscopy (SThM) for thermal profiles

A.2.1 Experimental Goals and Background on SThM.

Past investigations of dislocation properties have generally focused on what *doesn't* happen in the vicinity of a dislocation (e.g., reduced luminescence, shorter carrier lifetime, etc.), rather than what does happen. To the best of my knowledge, no one has ever shown *direct* evidence of non-radiative recombination taking place at a dislocation core. Indeed, it is a matter of some controversy as to whether the dislocation core itself is electrically active, or whether traps and impurities which surround the dislocation are responsible for the changes we observe, as was discussed in Chapter 2. By studying the thermal image of a cross-sectioned VCSEL, we hoped to get the first *direct* image of the heat being generated at the dislocation cores. It was also hoped that spots where hot carriers were present (namely, those with undesired barriers in the conduction or valance bands) would be seen in the thermal image. As a side benefit, we would also get the first experimental thermal map of a VCSEL.

These measurements would be taken using Scanning Thermal Microscopy, a newly-invented technique utilizing a custom-made Atomic Force Microscopy (AFM) tip on a standard AFM microscope. This tip is essentially a tiny thermocouple with a very small radius. SThM has a resolution of as little as 10 nm (i.e., 0.01 μm), and phonons are able to tunnel directly into the thermocouple with no scattering. As with the NSOM measurements, the tip is rastered across the sample, and an image of thermal voltage versus x and y is stored to a computer file, to be analyzed and plotted. More detail can be found in paper's published by Prof. Majumdar's group [3, 4]. The VCSEL measurements were taken by Ke Luo, a postdoctoral assistant working in Prof. Arun Majumdar's lab in the Mechanical Engineering Department at UCSB.

The sample preparation is identical to that used for NSOM, and is discussed in Appendix B in more detail. It was unfortunate that to date, we've never had a good sample and a good tip existing simultaneously. Both sample and tip making were difficult enough, and given the ease of damaging the tip or the sample, neither could be expected to last indefinitely. Thus, the full goals of the work (namely high-

resolution thermal imaging of dislocation cores) has not been realized. The initial results were taken with an excellent tip, but the sample had unwanted topography due to the use of a Syton polish at the end of the process. Syton, a KOH-containing solution of colloidal silica, provides a modest chemical attack for silicon, and even works well (albeit slowly) for GaAs devices with modest Al-mole-fraction. However, it evidently etches AlAs fairly aggressively, and left “fins” on our sample. While the resolution of the tip was quite good, the thermal images obtained were perfectly correlated with surface topography. Measured temperature rose every time the tip went into a valley (and was thus being heated both from the end and the sides of the tip); measured temperature fell where the tip was on a ridge. Hence, we wanted to repeat the measurement with a sample which had minimal topographic variation. Unfortunately, the tips tested on this improved sample all had poor resolution. Prof. Majumdar moved to Berkeley at the start of 1997, and is currently working on training new students.

The results which we did obtain, where we examined the thermal map with a resolution lower than that of the DBR stacks, are discussed below, and have been the subject of two publications [5, 6].

A.2.2 SThM results

While several models [5-14] have addressed the anticipated thermal profile of VCSELs, we believe this is the first experimental measurement of that profile. One of the findings of our work has been that it shows the need for including a more accurate heat source model than most work includes. Specifically, most models assume all of the heat is generated at the active region. However, it should be pointed out that the majority of carrier recombination contributes to spontaneous emission, which results in photons being emitted from the active region; a smaller fraction contributes directly to non-radiative recombination, which generates heat directly. The dominance of spontaneous emission can be seen through simple rate analysis [15, 16]. The photons emitted through spontaneous emission can be a) emitted from the device (only a 4% probability given the small cone angle within Snell’s window that can escape); b) reabsorbed by the active region after being reflected back, or c) absorbed by the substrate. We are particularly interested in the last possibility, which has been widely ignored in modeling in the literature, with

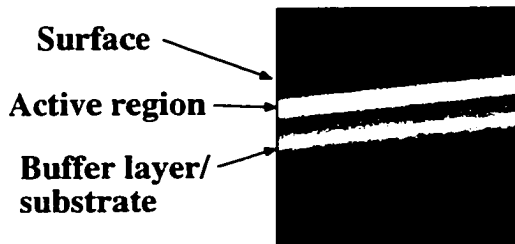


Fig. A - 8: Electroluminescence image from cross-sectioned VCSEL with wide-bandgap mirrors, showing bright luminescence from substrate.

only a few exceptions [7, 8]. The effect of the spontaneous emission carrying energy from the active region into the substrate has been dubbed “radiative transfer” by Newman et al [8]. In their paper, they note that this effect cuts the calculated thermal resistance of the device in half: it is not an insignificant effect. In VCSELs, this effect would be expected to

play a less important role, since the highly-reflective lower mirror would prevent the majority of the spontaneous emission (namely that fraction within the stop-band) from reaching the substrate. Nonetheless, the broad spectral profile of spontaneous emission allows a significant fraction to reach the substrate, and thus substrate luminescence is observed both in NSOM and conventional EL images of cross-sectioned devices, as seen in Fig. A - 8.

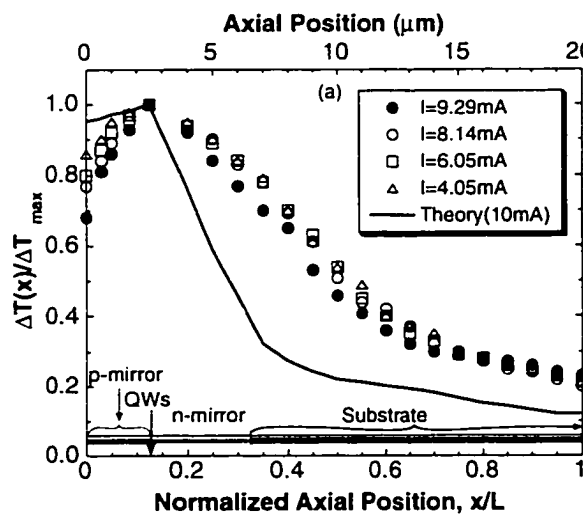


Fig. A - 7: A comparison of the predicted and measured thermal profile in the axial direction (i.e., normal to the surface) (after [5, 6]).

The results of this “radiative transfer” (i.e., substrate heating by spontaneous emission) are readily seen in comparing the results of a model which does not include radiative transfer [14], and the experimental results obtained [5, 6] (Fig. A - 7). Note that the axial profile obtained shows far more heating at the substrate than predicted by the model. The radial profile, which is not strongly dependent on this effect, was in fairly close agreement with that predicted in theory [5, 6].

References for Appendix A:

- [1] S. K. Buratto, J. W. P. Hsu, E. Betzig, J. K. Trautman, R. B. Bylisma, C. C. Bahr, and M. J. Cardillo, "Near-field photoconductivity: Application to carrier transport in InGaAsP," *Applied Physic Letters*, vol. 65, pp. 2654-6, 1994.
- [2] J. DeAro, K. Weston, S. Buratto, R. W. Herrick, and P. M. Petroff, "Near-field scanning microscopy on cleaved vertical cavity lasers," *Submitted to Journal of Applied Physics*, 1997.
- [3] A. Majumdar, K. Luo, Z. Shi, and J. Varesi, "Scanning thermal microscopy at nonometer scales: a new frontier in experimental heat transfer," *Experimental Heat Transfer*, vol. 9, pp. 83-103, 1996.
- [4] K. Luo, Z. Shi, J. Varesi, and A. Majumdar, "Sensor nanofabrication, performance, and conduction mechanisms in scanning thermal microscopy," *J. Vac. Sci. Tech. B*, vol. 15, pp. 349-360, 1997.
- [5] K. Luo, R. W. Herrick, A. Majumdar, and P. Petroff, "Internal temperature distribution of a vertical-cavity surface-emitting laser measured by scanning thermal microscopy," presented at ASME International Mechanical Engineering Congress and Exposition, Atlanta Georgia, Nov. 17-22, 1996.
- [6] K. Luo, R. W. Herrick, A. Majumdar, and P. Petroff, "Scanning thermal microscopy of a vertical-cavity surface-emitting laser," *Accepted for publication in Applied Physics Letters*, 1997.
- [7] R. G. Plumb and A. Jeziorska, "Electrostatic discharge damage to pump lasers while operating," presented at Fabrication, Testing, and Reliability of Semiconductor Lasers, San Jose, CA, 1997.
- [8] D. H. Newman, D. J. Bond, and J. Stefani, "Thermal-resistance models for proton-isolated double-heterostructure lasers," *IEEE Solid-State and Electron Devices*, vol. 2, pp. 41-46, 1978.
- [9] T. Wipiejewski, M. G. Peters, D. B. Young, B. J. Thibeault, G. A. Fish, and L. A. Coldren, "Thermal resistance of etched-pillar vertical-cavity surface-emitting laser diodes," *Proc. of SPIE*, vol. 2691, pp. 171-182, 1996.
- [10] T. Wipiejewski, M. G. Peters, B. J. Thibeault, D. B. Young, and L. A. Coldren, "Size-Dependent Output Power Saturation of Vertical-Cavity Surface-Emitting Laser Diodes," *IEEE Photonics Technology Letters*, vol. 8, pp. 10-12, 1996.
- [11] G. R. Hadley, K. L. Lear, M. E. Warren, K. D. Choquette, J. W. Scott, and S. W. Corzine, "Comprehensive numerical modeling of vertical-cavity surface-emitting lasers," *IEEE Journal of Quantum Electronics*, vol. 32, pp. 607-16, 1996.
- [12] L. Yung-Cheng, S. E. Swirhun, W. S. Fu, T. M. Keyser, J. L. Jewell, and W. E. Quinn, "Thermal management of VCSEL-based optoelectronic modules," *IEEE Trans. on Components, Packaging and Manufacturing Technology, Part B: Adv. Packaging*, vol. 19, pp. 540-7, 1996.
- [13] Y. C. Lee, S. E. Swirhun, W. S. Fu, T. A. Keyser, J. L. Jewell, and W. E. Quinn, "Thermal management of VCSEL-based optoelectronic modules," *Proceedings. 45th Electronic Components and Technology Conference*, Las Vegas, NV, USA, 1995.
- [14] G. Chen, "A comparative study on the thermal characteristics of vertical-cavity surface-emitting lasers," *Journal of Applied Physics*, vol. 77, pp. 4251-8, 1995.
- [15] L. A. Coldren and S. W. Corzine, in *Diode Lasers and Photonic Integrated Circuits*, Wiley Series in Microwave and Optical Engineering. New York, NY: John Wiley - Interscience, 1995, pp. 198, 199.
- [16] G. P. Agrawal, "Fast-Fourier-transform based beam-propagation model for stripe-geometry semiconductor lasers: Inclusion of axial effect," *Journal of Applied Physics*, vol. 56, pp. 3100-3108, 1984.

Appendix B: Sample Preparation Techniques

The sample preparation techniques were essential to getting inside the devices, and seeing what the aging process had done to them. They are also what set our work apart from the simpler, less detailed failure analyses generally done in industry. Development of sample preparation techniques and complicated preparation of samples easily consumed the majority of my time in this research. I do not recommend that you try to read this very long appendix in its entirety: it is divided into sections covering various types of sample preparation. Read only the sections that are relevant to the type of research you are interested in doing. Cross references to other sections of the Appendix, where appropriate, are made.

With something like the appendix that follows, I certainly could have saved much of the time spent developing sample preparation techniques. Nonetheless, readers should be under no illusion that it would be straightforward to replicate these results — any one of the CL analyses, for example, should easily be assumed to take at least a week, providing that those performing the analyses have prior experience in sample preparation. Those knowledgeable about TEM shouldn't need this caution at any rate, as the difficulties involved in sample preparation are only too obvious.

If I had it to do over again, I would try to be far less ambitious, as I spent many months without success trying to make TEM samples. The difficulties with TEM sample preparation are discussed below. The requirements for analysis techniques other than TEM (e.g. CL or EBIC) are far easier - I would have been better off doing such an analysis first, and I would advise the reader to do the same. TEM gives unparalleled depth of information, but it also exacts a heavy price, which the reader should be aware of. It also doesn't show everything that's happening: the "current-shunting" failure mechanism of Chapter 3 would likely not show up at all in TEM. While it's not often done, I will frequently discuss in this appendix what I tried that *didn't* work, in the hopes that it will help others avoid repeating the same mistakes.

B.1. Cross-sectional sample preparation techniques for arrays

I assume in this section that the reader has seen others performing wedge sample preparation, and has access to a variable speed grinding wheel and a lightweight aluminum tripod. If this is not the case, I recommend reading one of the papers by the inventors of the tripod polishers [1], and contacting one of the many firms that sell TEM sample preparation supplies for more basic background information than we will present here [2].

B.1.1 Rapid aging technique.

Devices were first characterized, taking LIV data, and then rapidly aged at 10-20 times threshold (i.e., 40-80 mA) for several minutes, until threshold increased by 20-400%. We frequently would age various devices in the array by varying amounts, to allow devices at different stages of the degradation process to be examined. For more detail, see Chapter 3.

B.1.2 Preparing the array for cross-sectioning.

It was clear that the mechanical stresses associated with material removal were near the adhesion limits of the M-Bond 610 glue used, since delamination of the device was not uncommon, particularly for TEM samples. Any unwanted residue on the top device surface or on the glass prior to bonding would likely compromise the bond strength, so devices and the glass cover slips were carefully cleaned in solvents, using acetone followed by methanol. They were then bonded together using one of two epoxies. The M-Bond 610, mentioned above, is widely used for TEM sample preparation. This glue is mixed and then refrigerated. It has strict limitations on thermal ramp-rate, and placing the sample directly on a hot plate after bonding it with the cover slip will result in a high bond void content, which not only means a weaker bond, but also leaves space for coarse trapped grit particles, which later dislodge and put scratches in your sample. Thus the M-Bond must be slowly warmed, and cured at relatively high temperatures ($>150^{\circ}\text{C}$) for at least an hour. The Allied 110 epoxy [3], while not reputed to be as strong, is superior in almost every other manner. It has no limitation on its ramp rate, so samples can be placed directly on a hot plate. It requires less than a minute at 120°C to cure. It changes color, to a deep red, when cured, so it is clearly evident when the curing

cycle has been completed, unlike the M-Bond. The only other disadvantage of Allied 110 is a poor shelf life. It lasts less than one week after mixing under refrigeration, though it will last several months if frozen.

B.1.3 Tripod polishing procedures

While several instruction sheets have been prepared to discuss the methods used for TEM sample preparation[1, 2], all of them leave out numerous details which are crucial to obtaining successful results. The following account still may not be all-inclusive, but I will mention a several details previous accounts have failed to mention.

B.1.3.1 Sample mounting.

The first order of business is the matter of mounting the sample on the stub. We will assume for the moment that the sample is reasonably sized. If this is not the case, the sample will first need to be cut or rough ground to reasonable starting dimensions. These optional steps, along with the rest of the process are shown in Fig. B- 1.

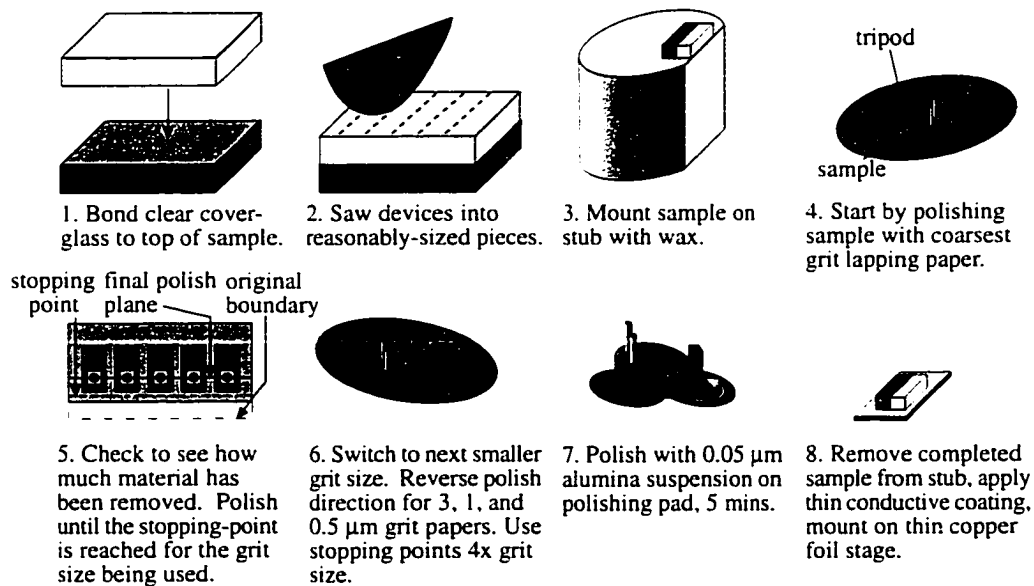


Fig. B- 1: Steps of cross-sectional sample preparation.

The sample is next mounted to the stub with wax or soluble glue. Wax is usually preferable, in that it easily comes off by melting it on a hot plate. Make sure to heat the sample to a reasonably high temperature ($>120^{\circ}\text{C}$), so that the wax bond

is thin. The hot plate temperature can then be lowered, and more wax can be built up around the sides of the sample to strengthen the mechanical connection between the die and the stub. I lost a significant number of samples (20-40%), where either the sample was knocked off the stub, or the glass was ripped off the sample. In the former case, the sample usually washed down the drain, and in the latter case, there was no opportunity to recover the sample. These problems frequently develop later in grinding, as you switch to finer-grit disks. The coarse grit disks (15 and 6 μm) rarely present a problem, since only a few points of grit are making physical contact. The fine grit disks have much higher drag force on the sample, and can rip the tripod out of your hand in the leading edge configuration (to be defined and discussed below). Don't be afraid to build up extra wax, which may even extend up over the top of the sample — you'll reduce the excess in the next step. For the wax to have high enough viscosity to hold its shape, hot plate temperature needs to be fairly low ($\sim 90^\circ\text{C}$), otherwise the wax will simply run down the sides, and fail to build up substantial reinforcement along the sides.

After a billet of wax has been built up around the edges of the sample, the excess should be removed by using a cotton swab (Q-Tip) which is damp (not

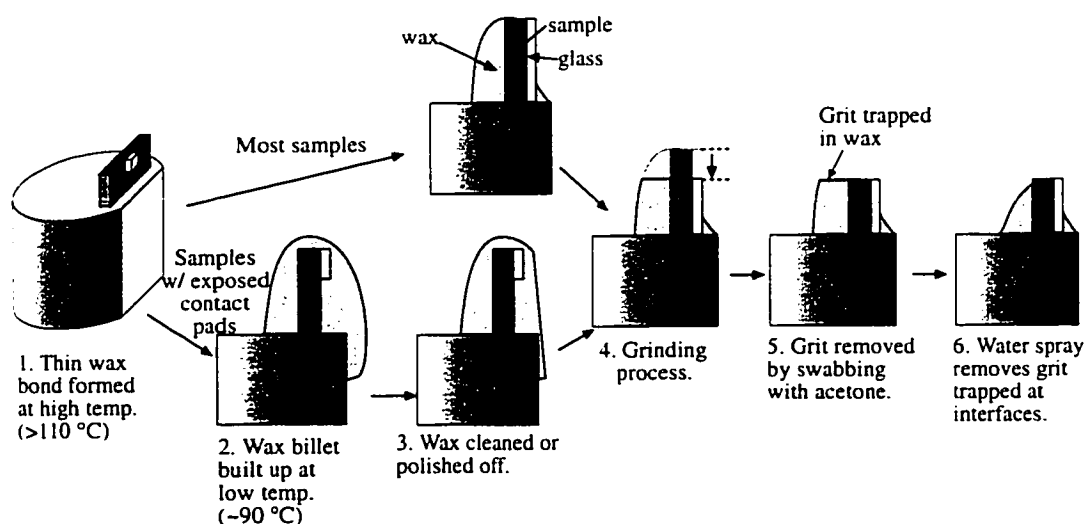


Fig. B- 2: Wax reinforcement of the sample, and removal of excess wax and grit at each succeeding step. Upper branch is for standard fully-encapsulated sample. Lower branch is for sample which has contact pads which remain exposed, while encapsulating the device itself with a small piece of coverslip glass.

soaked) with acetone. This was done by first wetting the swab with an acetone squeeze bottle, then blowing or dabbing the excess off. The purpose of this step is to eliminate the possibility of wax trapping grit from previous steps, which will then become liberated as the grinding proceeds. The coarse grit from early steps will then end up causing scratches as the fine grinding proceeds. The removal of wax and trapped abrasive grit will likely need to be repeated each time grit is changed, as shown in Fig. B- 2. Excess wax does not need to be removed before the first grinding step, however, as no prior trapped grit is present before starting.

Now, with the sample securely mounted on the stub, we wish to level the tripod. To do so we use a bubble level. First verify that the test surface is level (many work tables are not). Place the tripod sample-down, as it will be used on the grinding wheel, and place the bubble level on top of the tripod, being careful that it does not rest on the Pyrex step in the center. Now adjust the tripod legs until the bubble is centered. If you already know how much material will be removed from the sample, you can adjust the legs so that the bubble will be level when you are finished by rotating the micrometer screws counter-clockwise by that amount. Each tick on the micrometer screw is 10 μm ; “10” on the micrometer really means 100 μm ; and one full revolution of the micrometer is 250 μm . If you don’t know how much material you will be removing, you can adjust the plane of polish later, when you get closer to your stopping point (e.g., when you’re using the 3 μm grit). The purpose of this step is to give you a polish plane that is nearly perpendicular with the sample, so that the cross section remains rectangular, and does not become a trapezoidal cross section.

B.1.3.2 Starting Grinding

Now, you are *finally* ready to start grinding (!) Get out a clean mylar-based diamond-grit disc. If you don’t already have any, I recommend buying an assortment [4] including 15, 6, 3, 1, and 0.5 μm grits, which is the sequence I invariably use. Assuming you have over 100 μm of material to remove, start with the brown 15 μm -grit disc. Feel free to write disc size, your name, and other stuff on the back of the disc in permanent marker — it’s easy to get confused which disc has which grit size, and making a mistake risks ruining your sample with a larger grit disc than you’d intended. Put a little water on the glass wheel, and spread it

around. Place the disc on the wheel, and use the squeegee to force out remaining water. Turn the wheel up to its maximum speed, and force out the remaining water by centripetal action. At this point, the disc should be quite difficult to push sideways. Test it by trying to push the disc laterally. If it is possible to slide the disc sideways, remove the disc, and clean the disc and the wheel with soap — grease or oil contamination is a frequent cause of poor adhesion between the wheel and mylar disc. The other possible cause of problems is that some discs have an unusual texture on their back. Such discs need to have exceedingly small amounts of water on the wheel. By putting just two drops of water on a tissue, and barely wetting the glass wheel (Newton rings will be clearly visible), good bonding should be obtainable in such cases.

Turn the wheel on at 90-140 rpm rotation, and turn on the “wheel wash” water jet slowly. Too little water will make for excessive drag force and an excessive material removal rate, and allow debris to build up. Conversely, use of too much water will allow excess water to get under the edges of the disc, and the disc may come loose from the wheel.

Mylar polishing discs normally require no pre-treatment. However, some manufacturers recommend treating new sheets with the white plastic “kitchen scrubbers” used for cleaning Teflon pans. By rubbing the new mylar polishing disc with the scrubbing pad, agglomerates can be removed. Some users have reported getting large scratches from 0.5 μm grit discs which had not been through this pre-treatment step: again it only needs to be done before the first use of a new pad.

Get a box of small wipes (we use Kimwipes which are about 1/3 the size of an ordinary Kleenex), and fold them into a 5-cm square. I also recommend wearing gloves to prevent absorption of GaAs through the skin, as well as to prevent contamination of the sample by finger oils. Hold the folded wipe against the wheel, and allow it to become soaked with water. This step also cleans any residual contamination off the discs. If you feel any “bumps” through the wiper, turn off the water, stop the wheel, and find where the bumps are coming from. Usually, it is from polishing debris trapped between the glass and the mylar disc.

Now touch the legs of the tripod on the rotating polishing wheel. Again, if you feel any “thumping” due to debris trapped under the disc, stop the wheel and

clean the disc. If no bumps are evident, you can slowly lower the sample onto the disc to start grinding.

B.1.3.3 Tripod orientation.

The tripod can be held in three different ways: with the sample facing into the direction of rotation; sample cross-wise to the direction of rotation; and sample facing away from the direction of rotation, as shown in Fig. B- 3.

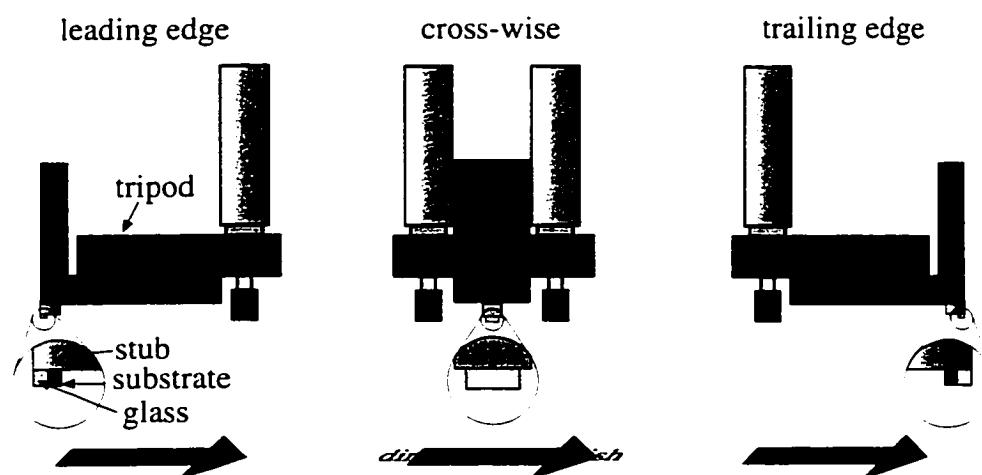


Fig. B- 3: Three directions of tripod orientation.

The first orientation (namely sample facing into the direction of rotation) is the direction I normally start with on the 15 and 6 μm grit layers. The advantage to orienting the tripod in this direction is that the brittle glass layer on top of the device will not form chip-outs as it will when the glass is on the trailing edge. The material removal rate is also substantially (up to 3x) faster in the leading-edge configuration. The sample is almost never held sideways, since a single scratch along the direction of the epitaxy could ruin the entire sample, a vertical scratch (obtained in the leading or trailing edge orientation) would only damage a very small portion of the sample. Also, sideways grinding is also much more likely to trap grit in the glue bond between the sample and the glass.

After switching to the 3 μm or smaller grits, the tripod is switched to the "trailing edge" orientation, where grit passes the legs before the sample. In this orientation, there is notably lower force applied by the grit to the sample. The sample can "float" (possibly hydroplaning) on the water layer in this orientation,

reducing the drag force and the potential for sample damage. Others have also noted this affect, and dubbed it “the trailing edge effect.” While the trailing edge is more susceptible to chip outs with the initial large grits, it also gives a better polish [5]. Surface polish quality becomes far more crucial as we get close to our stopping point, while any chips which may now form in the cover glass are small enough to be innocuous. Others have also noted that in the “trailing edge” orientation, grit is much less likely to get trapped at the glue line [6], possibly due to the fact the sample “floats” more effectively this way.

B.1.3.4 Continuing grinding

Hold the sample either into the direction of rotation (“leading edge orientation” 15 and 6 μm grits) or away from the direction of rotation (“trailing edge orientation” 3 μm grit onward). Hold the tripod with one hand (do *not* apply downward pressure on the sample, as this will introduce cracks in the sample), and hold the Kimwipe in the other hand, pushing down on the “sample track.” By “sample track,” I mean the dark line of GaAs dust that is generated as the disc wears the sample away. This will be very evident with the coarse discs, and progressively less obvious as you switch to finer-grit discs. The wiper is used to keep the paper clean, and remove sanding debris, but it also allows you at a glance to know how quickly material is being removed. While this takes some experience, if the Kimwipe quickly becomes very dark from a polishing track, check the sample very frequently in the microscope to ensure that material isn’t being removed too quickly. Conversely, if no track is being formed during grinding, it’s a safe bet that material isn’t being removed. There are a number of possible reasons for this. Most likely, you have attached too much other material (usually glass or wax) to the sample, which increases the contact area, thereby reducing the pressure per square millimeter being applied. On other occasions, I had tried to polish samples which were bonded to headers, or bonded with alumina pads. All of these wear very slowly, if at all, and are not recommended.

From time to time, you will need to stop grinding, and inspect the sample to see how much material remains from the edge of the sample to your desired polishing plane. You will need to do this frequently when you are a novice. As you gain experience, you will gain a better feel for what the material removal rate is likely

to be, and will only need to check a few times for each grit. When you are prepared to stop, remove the sample from the wheel, and turn off the water flow, but leave the wheel rotating. If you leave the water on, or stop the rotation, water can get under the disc, causing disc adhesion problems.

Before inspecting progress under the microscope, it is often helpful to clean the grit off the top of the sample to allow a clear view of progress. You can use a Q-tip or a high-pressure water spray for this purpose. I used an air brush filled with de-ionized water, which was very effective at removing left-over grit. I then blew the sample dry, and inspected it. When inspecting the sample, you must either have features of known size, or have a microscope with a calibrated reticule to allow measurement of the thickness remaining to the desired polish plane.

One makes note of the material removed since the last check, and compares the remaining material thickness to the desired disc change-over point. While a number of factors can affect the change-over point, for GaAs, 4-times the grit size is a good rule of thumb. Thus, when using 15 μm discs, one should leave a minimum of 60 μm of material before changing to the 6 μm disc. One should then leave a minimum of 24 μm of material before changing over to the 3 μm disc, and so on. It's better to change over too soon, than to take off too much material, and risk introducing sub-surface damage. The purpose for this factor of 4 is that there are some abrasives on the polishing disc larger than their nominal size, and further, there is a sub-surface damage layer which also goes deeper than the nominal grit size.

Each time the discs are changed, the sample should be thoroughly cleaned to prevent contamination of the fine discs with coarse grits which would otherwise remain on the sample. The sample is thoroughly cleaned with a water spray to remove all remaining grit, and then blasted dry. If cross contamination problems remain, ultrasonic or Q-tip cleaning may be necessary. The sample should be inspected under the microscope, and excess wax surrounding the sample should be removed with a Q-tip and acetone, as discussed earlier.

Finally, the disc should be given a final cleaning with the Kimwipe used earlier, and that Kimwipe should then be discarded to prevent cross-contamination. Next, the wheel should be turned up to its maximum speed (600 rpm), to allow

centrifugal action to spin off excess water. Then, the disc is dried with paper toweling.

B.1.3.5 Finishing the sample

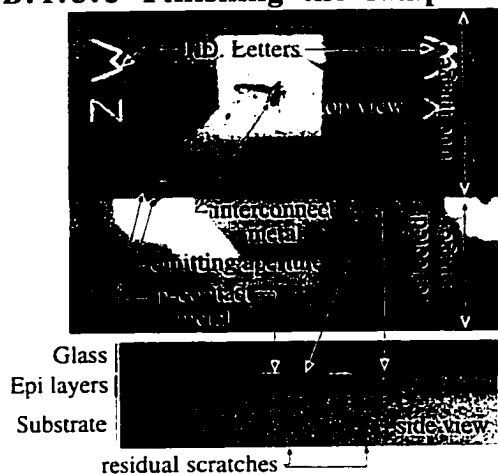


Fig. B- 4: Top and side view of cross-section.

As we get to the 1 and 0.5 μm grit stages, we inspect the sample both from the top, and from the side, as shown in Fig. B-4. Any scratches or damage in the cross section, which were concealed during previous steps, should now become evident. If extra grinding is needed to polish these out, it can be done before the polishing step is started. Final adjustments to the plane of polish should be made, so it runs through the center of all the apertures. When the 0.5 μm grit step is finished, you should be very close to your desired polish

plane, as only a fraction of a micron of material is removed during the polishing step. I do *not* recommend using 0.1 μm grit paper under any circumstances, as it is too easily contaminated with debris, and almost always leaves large scratches in your sample.

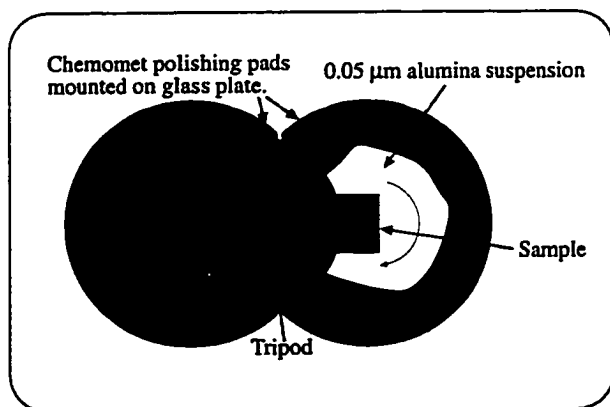


Fig. B- 5: Equipment used for final polishing.

The final polish, for reasons we will discuss below, is a purely mechanical one using a special Baikowski 0.05 μm grit [7], and a Buehler Chemomet pad [8]. I found that even this very fine polishing generated enough debris to cause significant scratches. To minimize waste, I eventually dispensed with the use

of full 8" pads for this step, and used hand polishing instead of the polishing wheel. Two 10-cm squares of the Chemomet pad were cut out (or flats were cut along two 2-7/8" pad), as shown in Fig. B- 5.

These pads were bonded with their self-adhesive backing to a glass plate, with one pad serving merely to hold the legs of the tripod to the same height as the sample, and the pad under the sample doing the polishing. I would start with 5 minutes of gentle circles in one direction or the other, and the sample resting in 3 ml of Baikalex suspension. Periodically, an additional 1 ml would be applied to keep the sample wet. After 5 minutes of polishing, the pad was discarded, and the glass cleaned and dried. A new pad and fresh polishing solution were applied, and an additional half-minute to minute of polishing were done. This final step eliminates scratches from debris that had built up toward the end of the first 5 minutes of polishing. At this point, the sample should be thoroughly cleaned and inspected in a Nomarski microscope. The cross-sectional sample face should be smooth and scratch-free. The sample was coated with ~3 nm of gold (enough to be barely visible), both to reduce charging problems, as well as to seal the surface against hydrolysis of AIAs. The sample is now ready for CL, NSOM, SThM, cross-sectional EBIC, or a number of other cross-sectional techniques. Or, you can go on and make this a TEM sample by polishing away most of the back side of the sample.

B.1.3.6 Difficulties with using chemical polishing agents: unequal AIAs and AlGaAs etch rates.

Another property of AIAs that the reader should be aware of is its susceptibility to rapid etching in the high-pH colloidal-silica polishes (e.g., "Syton") which are widely used in TEM sample preparation. While these KOH-based solutions are ideal for polishing silicon, due to the balance between mechanical action and chemical polishing, better results can be obtained for simple GaAs devices by using solutions with higher etch rates on GaAs, such as clorox (sodium hypochlorite) solutions, as noted in the Buehler Dialog applications note [9], although this solution etches AIAs at such a different rate that it is used as a stain-etch (i.e., it has the same basic high-selectivity problem as the KOH-based solutions). The chemical polishing rate of the KOH is so slow that approximately 30-minutes of polishing is needed to polish out all the damage from the 0.5 μ m

mechanical grinding that precedes it. Without at least 30-minutes in the polish, notably reduced CL intensity is observed [10].

VCSELs which were prepared for cross-sectioning using the standard polish showed significant etching of the AlAs (i.e., $>1\text{ }\mu\text{m}$), particularly in the p-doped area which had not been proton implanted. The GaAs, by contrast, etched much more slowly. The protruding “shelves” of remaining GaAs then broke off in chunks during polishing, leaving an unusable sample. We shall discuss our investigation of non-selective etches in the following section: no ideal etch was found, as all etches added substantial amounts of topography. We thus used purely mechanical polishing for all cross-section preparation.

Several days were expended in an attempt to find low-selectivity chemical etches which would remove the surface damage layer, without leaving undesired topography. An extensive literature search was first performed. The primary outcome of this was the realization that finding good etch rate data is fairly difficult. Peroxide-base solutions (most typically $\text{NH}_4\text{OH}:\text{H}_2\text{O}_2$) were reputed to be “tunable” to etch AlAs faster than GaAs at one pH range, and GaAs faster than AlAs elsewhere in the pH range. In theory, by finding just the right pH, the two components could be exactly balanced. However, the literature I uncovered did not show any evidence to support this, and focused exclusively on tuning the pH to give maximum selectivity [11, 12], the opposite of the unity selectivity coefficient we wanted.

The literature search did uncover a very dilute citric acid-peroxide (100:1) etch which was reputed to have an etch rate $2\text{--}3\text{ }\text{\AA}/\text{sec.}$, nearly independent of Al-fraction from $x=0$ all the way up to 60% [13]. However, the SThM sample that was prepared this way appeared to have some 25 nm of topography after nominally removing 100 nm of material, while gently agitating the sample across a Chemomet pad. A dilute (1:250) Br:methanol solution gave better results, with 10 nm topography. However, this was still unacceptable for our SThM scanning, as *any* topography results in correlated variations in temperature distribution, preventing artifact-free results from being obtained.

B.1.3.7 Protect samples from atmospheric moisture.

It is very important to know that over 40% of the thickness of epitaxy in the Honeywell devices is pure AlAs. AlAs quickly hydrolyzes in the presence of water or water vapor, and is converted to Al_2O_3 , eliminating the lattice features of the AlAs layer. After a few days of atmospheric exposure, unprotected NSOM samples showed so much topography that they were unusable. Thus samples were subsequently stored in a desiccator after they were polished to the middle, to prevent hydrolyzation in the presence of atmospheric moisture. There may be some value to doing the final polishing with oil-based (rather than water-based) polishing compounds — this point has not been explored to date.

B.1.3.8 TEM sample preparation

I do not wish to mislead the reader, so I should state that while I spent several months working on this problem, I have relatively little experience in the end of the process. I generally was trying to prepare single die, which have a number of their own problems, and never got all the way to making a good sample of my own for reasons which will be described in Section B.3.

The side of the sample which was just polished should be bonded to a grid with M-Bond 610 or Allied 110 [3], and cured. Great care should be taken to use no more glue than absolutely necessary, as excess glue can wick across from the sample and cover the interface you later desire to inspect with TEM (Fig. B- 6). This excess glue will prevent the device from being electron transparent, and cannot be removed once the glue is cured. However, if one realizes the sample has been compromised with glue contamination *before* the glue has been cured, it can be removed with acetone.



Fig. B- 6: Sample being bonded to TEM grid (left). If excess glue is used (center), a meniscus forms with glue across the center of the sample (which will subsequently prevent the sample from being electron transparent). A thin bond-line is needed (right) to prevent this.

Wide-slot grids are best when they can be used. Smaller-opening grids often prevent the sample from being ion milled at low angles, and result in copper deposition on the

sample, by way of sputter knock-on reactions. After the glue has cured, the grid is mounted to a Pyrex stub with crystal-bond wax. Before mounting the grid to the stub, turn it grid-side-up, and fill the opening in the grid with wax. Put plenty of wax on the stub, too. This wax must fully support the sample when it is thin, so there must not be any voids in it - check this by looking through the Pyrex stub from the back under a microscope.

Now mount the stub in its slot in the tripod, and retract one of the legs a full turn. This will provide a wedge. By using a calibrated focus stage on a microscope, measure the thickness of the sample. Polish it as described earlier, and change grits according to the sample thickness remaining. Since the wedge angle should result in a thickness of approximately $10\text{ }\mu\text{m}$ at the edge, and $<0.1\text{ }\mu\text{m}$ in the center of the grid, you should stop using $3\text{ }\mu\text{m}$ grit when you start to see the copper grid itself getting polished. The legs will need to be advanced or retracted to have the plane of polish advance so that both sides of the wedge are polished away equally. After the polishing is finished on the second side, brief ion milling should be all that's needed. After verification that the sample is electron transparent, it should be coated in a thin conductive layer to eliminate damage from hydrolyzation of the AIs, and prevent charge buildup on the glass layer.

B.1.4 Sample preparation for NSOM and SThM samples.

While most sample are static, and do not need electrical contact to the sample pads, the NSOM and SThM samples are exceptions, since the data is taken while the device is operating normally. This adds quite a few additional steps to the sample preparation process. The original approach I took involved mounting the device on a submount with wire bonds, and gluing contact wires to standoff pads: this elaborate and difficult packaging approach took most of a week from start to finish, and is not recommended. Below, I discuss a simplified approach which did not involve wire bonding at all.

The sample is first prepared for cross sectioning as discussed above, with one exception: rather than using a thick (1 mm) glass slide on top of the devices to provide edge protection, a sliver of cover-slip glass (0.17 mm thickness) was carefully bonded on, to cover the apertures, but not the bond pads a few tenths of a millimeter away. During the first several attempts, since the bonded area of the glass

is much smaller than would be the case for a normal sample, the glass was ripped off the sample during the final polishing stages. Subsequently, additional support for the glass was provided by fully encapsulating the sample in wax, as shown earlier in the bottom branch of Fig. B- 2. After sample preparation was complete, the sample was encapsulated in very thin (~ 3 nm) gold or e-beam deposited dielectric to prevent hydrolysis. Note that 20 nm of PECVD-deposited Si_3N_4 was also tried; however, consistent with what I was told by those who study dielectric film nucleation, thin PECVD nitride is not actually a continuous film, but rather is made up of isolated platelets. The sample which was encapsulated with thin nitride thus failed quickly due to hydrolysis, as would be expected of an unencapsulated sample.

After encapsulation, the sample is mounted to a small (<1 cm) insulator (microscope slide glass was cleaved into small pieces and used for this purpose). Small-gauge wires (e.g., 34-gauge wire-wrap leads) are also bonded to the edges of the glass mount. Krazy Glue does not work well for bonding wires, particularly with wires having Teflon insulation: they easily pulled off in subsequent handling. A small amount of Krazy Glue was used to set the position of the wires and sample. Then, five-minute epoxy was used to build up the billet around the sample, and was heaped over the top of the wires to provide strain-relief. Be sure *not* to cover the ends of the wires, since these need to be contacted with silver epoxy in the subsequent steps. A larger mount allows greater contact area and thus better strain-relief for the wires. However, large mounts won't fit in many types of AFMs, so check on size and weight restrictions before making the sample.

Next, positive and negative traces are drawn with silver epoxy, using a sharpened stick. The traces are drawn to the exposed ends of the wire (which does not need to be stripped, as long as metal can be seen at the end). The negative trace is quite easy to draw: it should go from the n-metal on the bottom of the device to the black lead. The positive trace requires a good, void-free billet of non conductive glue around the sample (to prevent short circuits), and a somewhat steady hand. Roughening the metal pad beforehand with a sharp probe is probably advisable, since there may be an insulating epoxy residue left over from when the glass slide was bonded onto the sample. A drawing of the sample is shown in Fig. B- 7. The silver epoxy is cured according to the directions (20 minutes at 120°C in our case).

The sample should then be tested. Light should come out of the sample at the standard threshold voltage. If it does not, either a short or open exists, and the problem can usually be diagnosed and fixed using an assembly microscope and a curve tracer..

B.1.5 Sample preparation for cross-sectional EBIC samples

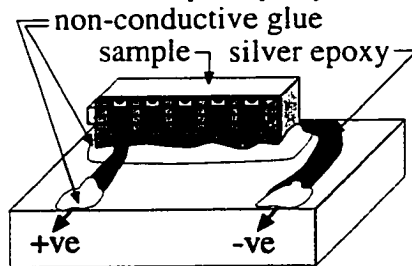


Fig. B- 7: NSOM / SThM sample is mounted edge-up on an insulating mount, with silver epoxy painted between device contacts and contact wires.

Three types of EBIC samples were examined. One type began as an array, in which many devices in many rows were rapidly degraded. The substrate was then thinned to $\sim 100 \mu\text{m}$, and we attempted to cleave devices along their centerline. Sample results are seen in section 3.4: one drawback to this approach is that the cleaves are usually not smooth, and show stair-stepping [14]. However, since we aged several rows, we have multiple chances to get a good cleave.

A second type of sample was also aged as an array, and polished into a cross-section using standard techniques. Slide glass was bonded to the top using acetone-soluble cyanoacrylate ("Sally Mann Nail Glue," which has better solubility than "Krazy Glue.") While it should go without saying that we were careful not to use acetone to remove excess wax (as suggested earlier in many cases), we still had the glass rip off the top of the sample near the end of the process. This would normally prevent use of the sample; fortunately, we were able to salvage the sample. At the end, the glass cover was removed with acetone, and contact could be made to the bond pads. While this proved good enough for our needs (results are contained in Figs 6-12, -13, and -30) I would still recommend something more akin to the NSOM sample preparation for future work (i.e., epoxy bonding a cover slip which left access to the bond pads).

The third type of sample for cross-sectional EBIC was the normally-degraded device mounted on a header. A very small cover glass slip ($< 300 \mu\text{m}$ square) was bonded to the top of the device using epoxy, without disturbing the existing wirebond. After curing, the device was encapsulated in a few large drops

of Allied 110 epoxy. Flats were carefully cut on the package, at an angle which would allow the positive lead to be unaffected by subsequent cross-sectioning steps. Standard cross-sectioning techniques were then used. Difficulty with low material removal rates were encountered (due to the large area of the header preventing quick grinding). Excess header material should also be removed by sectioning saw. The encapsulant often pulled off (the subsequent headers were cleaned in solvents to promote adhesion and remove flux residues). Grit became trapped between the glass coverslip and the sample, breaking the contact in one case. These samples required great care in handling. Only one was prepared which functioned electrically, while another was adequate only for CL.

B.2. Plan-view sample preparation

Cross-sectional sample preparation is essential if one is to unambiguously show which layers the defects were in. But cross sections are only a small portion ($<0.5\%$) of the sample as a whole, encompassing what may have occurred in only a few percent of the area. Cross sections may even miss the dislocations in the device altogether. For these reasons, we also need top (or bottom) views of the device which we call “plan view” images. In such images, by using spectral filtering, we can see the entire active layer, and see where degradation has occurred.

B.2.1 Plan view sample preparation for red InGaP VCSEL samples

We start with a description of the preparation of red VCSEL plan view samples, since this is the easiest type of sample to prepare, due to chemical selectivity between the arsenides and the phosphides. The sample preparation was detailed in chapter 6, and we show the basic steps again for the reader's convenience in Fig. B- 8.

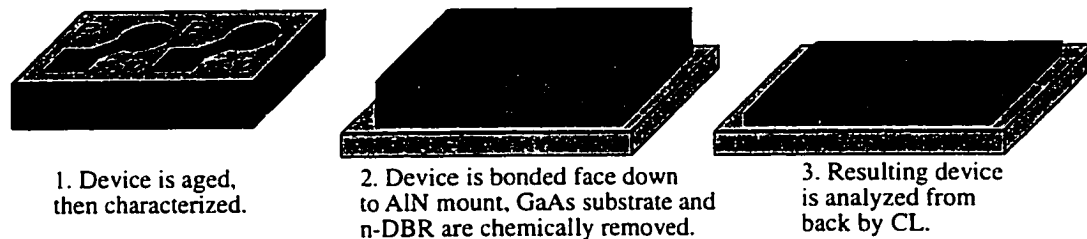


Fig. B- 8: Steps for sample preparation of plan view sample from red InGaP VCSEL.

After aging and characterization, the device is photographed, then bonded face down to an AlN submount using Allied 110 epoxy [3]. Most of the substrate was removed using standard abrasive polishing techniques, leaving $<100\text{ }\mu\text{m}$ of substrate material. A bead of photoresist was carefully painted around the perimeter of the sample with a very fine 0000 brush. The photoresist was then soft baked to drive off solvents. The purpose of the photoresist ring was to prevent lateral undercutting of the sample in subsequent steps.

The remaining substrate was removed using spray etching [12, 15]. The etch solution used was 8 ml of NH_4OH to 240 ml H_2O_2 , with the hydrogen peroxide being the standard 30% strength. The etch rate was on the order of $2\text{ }\mu\text{m}$ per minute [15], so the remaining substrate removal took less than half an hour. (Many people don't like to mechanically thin the sample back, and are willing to wait a few hours for the spray etching to remove the entire substrate thickness. However, you need to use abrasives to remove the n-metal anyway in our case, so it's not very difficult to remove much of the substrate while you're at it.)

While it is in theory necessary to check your sample fairly frequently during spray etching, due to the relatively low 100:1 selectivity (i.e., the AlAs has a non-negligible 20 nm per minute rate), checking every ten minutes is probably acceptable, given that we're going to remove the n-DBR anyway. It is quite obvious when the etch is finished, since the sample appears red due to the mirror's reflectivity spectrum.

The sample was then immersed in undiluted HF to remove the DBR. As shall be discussed below, HF is able to remove $\text{Al}_x\text{Ga}_{1-x}\text{As}$ with $x>0.5$ [16]. However, we assumed (correctly, as it turned out) that it would not etch AlGaInP. The DBR etching takes about two minutes, and the sample gives off bubbles ("fizzes") while the etch is taking place. The sample appears extremely rough while etching is proceeding. When the AlGaInP layer is reached, a mirror-like red surface appears, and the bubbling stops. Remove the sample from the HF etch, rinse, and inspect. If the entire surface of interest is smooth, use acetone to remove the photoresist ring, and rinse the sample. Photograph the sample, with backlighting if desired. The metal contacts on the top of the sample can be seen through the p-DBR even if the sample has been bonded to an opaque mount.

Very concentrated solutions of sulfuric acid (e.g., 3:1:1 $\text{H}_2\text{SO}_4:\text{H}_2\text{O}_2:\text{H}_2\text{O}$) are purported to selectively etch arsenides (GaAs or AlGaAs) while not etching phosphides (GaInP or AlGaInP) [17]. This sulfuric etch was used to prepare the sample for intensity-dependent PL. However, the results were not very satisfactory, with a great deal of lateral underetching, a non-negligible etch rate of phosphide alloys, and slow etching parts of the DBR (due possibly to the formation of unetchable aluminum oxides). Thus, the more laborious process discussed earlier is recommended over this simple chemical etch. If different chemical etches are to be tried, testing the etches on trial samples before committing to an aged sample would be prudent.

B.2.2 Plan view sample preparation for 850 nm VCSELs

We made 850 nm plan view samples similar to those described in the previous section for the red VCSELs. However, because we did not have an analogous selective etch which would remove the DBRs, and stop at the confinement layers, sample preparation required far more skill. The same (non-selective) abrasive techniques described earlier were used to polish away the substrate. A chemo-mechanical polish was used to remove the n-DBR. Details are discussed below.

B.2.2.1 Array mounting

We start by bonding our aged array to a submount for mechanical support. Our first sample was bonded to a 1-mm-thick piece of glass cut from a microscope slide. One advantage to using glass was that after the substrate had been removed, the sample could be photographed from the front and the back, allowing us to clearly see where individual VCSELs lined up relative to the sample edges. As it turned out, it would prove far easier than anticipated to identify which VCSEL was being examined, since the 120 keV beam had sufficient penetration that the ID letters on each device were easily readable through several microns of epitaxy (!). There was also a disadvantage to using a glass mount: the epitaxy in the scanned areas cracked after prolonged observation, perhaps due to thermal mismatch, or temperature gradients associated with the poor conductivity of the glass.

The next samples were bonded face down to an AlN submount using Allied Epoxy 110. No further sample cracking was observed. The AlN has good thermal

conductivity (more than an order of magnitude better than glass), and a thermal expansion coefficient (CTE) very close to that of GaAs. It is also rigid, strong, and translucent, while allowed for back-illumination of thinned samples where ID letters could be seen through the device.

B.2.2.2 Substrate removal

The sample and its stage can be measured for thickness using either a dial gauge or a calibrated microscope. Rough material removal then starts, using any method desired (Buehler Minimet or standard tripod polishing, for example). Grits are changed in accordance with the 4x-grit-size rule discussed in section 1.3.4. Adjustments must be made to keep the sample planar during this process: we measured the thickness of each of the sample's corners, and adjusted the tripod legs to keep the polish plane parallel to the AlN submount. When we have removed most of the substrate, 0.5 μm grit paper should be in use to remove the last few microns of GaAs, since the fine grit minimizes the depth of the damage layer. Rings will clearly be visible when the n-DBR has been reached, and fine adjustments will be needed at this point to adjust the plane of polish.

An alternate approach would have been to spray etch the substrate off as described above for red InGaP VCSELs. A protective rim of photoresist around the edge probably would not be needed for the spray etching of this sample, and would interfere with the polishing steps to follow.

In the first sample, we went to the Br:Meth polish directly after the n-DBR had been reached, but had very bad edge-rounding problems with the Br:Meth polish, getting only 3 devices (out of over 20) which had the desired n-DBR thickness remaining. In subsequent samples, a Chemomet pad with a 0.3 μm alumina suspension was used to remove the bottom couple of microns of the n-DBR (i.e., the part of the n-DBR first encountered), and 0.05 μm was used for removing the next micron of the n-DBR. A very brief polish with the Br:Meth was used to chemically remove the surface damage layer as the final step. We desired to leave 5-10 DBR periods of the n-DBR for CL analyses, and fewer for EBIC and other types of work. Since this process leaves "rings" of exposed AlAs, and since the sample would suffer from charge build-up anyway, we coat the samples with a thin, transparent conductive layer of gold (≈ 5 nm thick). The finished sample is

photographed with back lighting, and by comparing the image with the original photo from the top, we are able to establish where aged devices are, and how many layers are left for each device.

When checking the device for progress, be careful not to be confused by surface topography. The rings which were present at the first inspection oxidized, and briefly acted as a mask before being polished away. Rinsing in methanol rather than water helps to reduce this "masking action." Due to the "masking," the ring pattern seen in the first inspection was present during subsequent inspections, leaving the impression that no etching was taking place. Careful examination under a standard microscope (not the Nomarski microscope used) would have revealed the true situation, where material *was* being removed. It is worthwhile to "push down" on the sample when first starting polishing to break through any surface oxides, and then to reduce pressure during the remaining 15 seconds of polishing, since reducing pressure reduces the unwanted edge rounding. The sample should then be examined again under the microscope for progress.

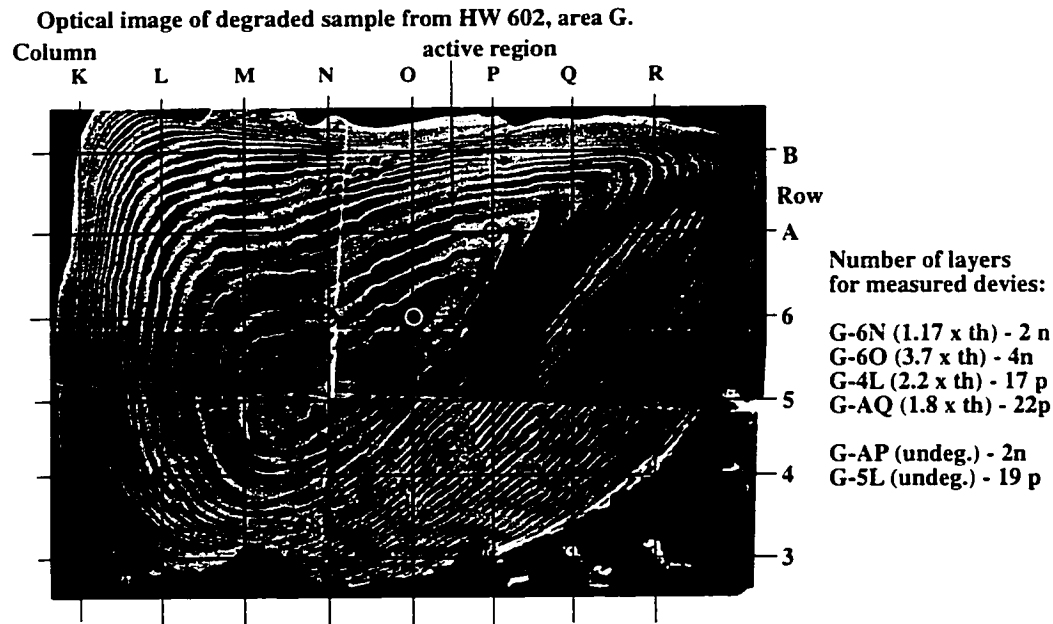


Fig. B- 9: Photo of plan-view CL sample after polishing off substrate and most of n-DBR.

B.2.3 Preparation of plan-view samples by wet chemical etching.

B.2.3.1 Selective layer etching

The ultimate goal in plan-view sample preparation was to develop a technique which allows plan-view TEM samples to be made. The mechanical polishing technique for 850 nm VCSELs had at best a precision of 0.1 μm , and even that only applied to a fairly small area of the sample. TEM samples have far tighter tolerances — a selective etch technique which was able to remove the p- and n-DBRs along, with the $\text{Al}_x\text{Ga}_{1-x}\text{As}$ confinement layers, would be ideal. The three quantum well layers (7 nm each) and two barrier layers between them (10 nm each) would have a total thickness of 41 nm — well within the ideal TEM sample thickness of <100 nm.

VCSEL samples similar to ours, except without graded interfaces, have proven easy to etch layer-by-layer [18]. HF-based etches etch aluminum fractions higher than 60% quickly, although they don't etch fractions less than 50% at all, as shown in Fig. B- 10 [16]. Low-aluminum-fraction layers can be etched with various citric-peroxide solutions. These etches are selective because they will etch Ga_2O_3 , but not Al_2O_3 which forms an unetchable layer. However, citric:peroxide etches will only etch up to 30 or 40% aluminum fraction [19-21]. If abrupt interfaces are present, and both DBR compositions avoid the "dead range" between 30 and 60% Al-fraction, clean etching results would be expected, and have been observed in past work.

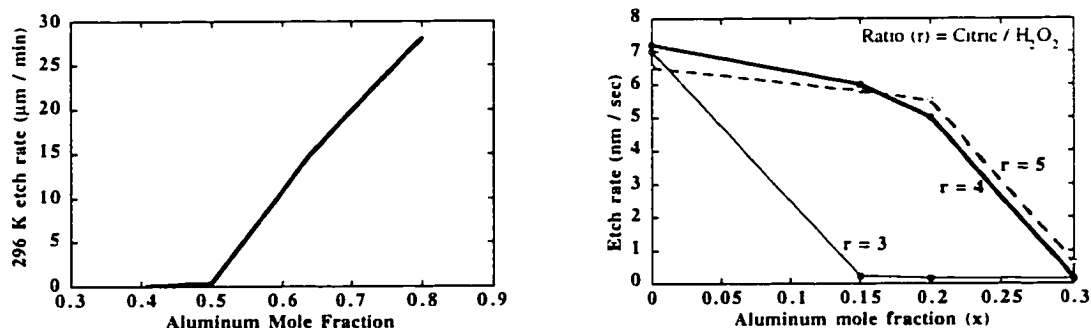


Fig. B- 10: HF-based etches (left) [16] allow selective removal of high-aluminum-fraction layers, while citric acid based etches (right) [20] allow selective removal of low-aluminum-fraction layers.

The difficulty comes in with the graded layers which are required to obtain low-resistance in the mirrors. In these graded layers, the composition is gradually

increased or decreased across a distance of about 20 nm, from $\text{Al}_{16}\text{Ga}_{84}\text{As}$ to AlAs . In the midst of this grading, from $\text{Al}_3\text{Ga}_7\text{As}$ to $\text{Al}_6\text{Ga}_4\text{As}$, is an “unetchable” layer some 5 nm thick. To be more exact, it is unetchable by both the HF and the citric acid solutions. However, it is etchable by solutions with lower selectivity, such as (for example) 1:2:17 $\text{H}_3\text{PO}_4\text{:H}_2\text{O}_2\text{:H}_2\text{O}$. A three step procedure was used, first etching the $\text{Al}_{16}\text{Ga}_{84}\text{As}$ layer in 1:4 $\text{H}_2\text{O}_2\text{:Citric}$ (50% by weight) for 10 seconds, stopping at the “unetchable part” of the graded layer. The sample was rinsed to reduce cross-contamination, then the graded layer was etched for a few seconds in a non-selective etch such as the phosphoric etch mentioned above. The sample was again rinsed, then etched in 1:1 (or even 1:100) HF:DI (concentration doesn’t really matter, it etches AlAs almost infinitely fast - the etch rate is microns per second) until the graded layer is again reached. Finally, the sample was rinsed and the sample was briefly etched in the non-selective etch again. This cycle was repeated the number of times needed to remove the number of mirror periods the sample had. This procedure is shown in Fig. B- 11. Unfortunately, this etch built up sufficient roughness after a few cycles to make the sample unusable. We were unable to discover the cause of this roughness.

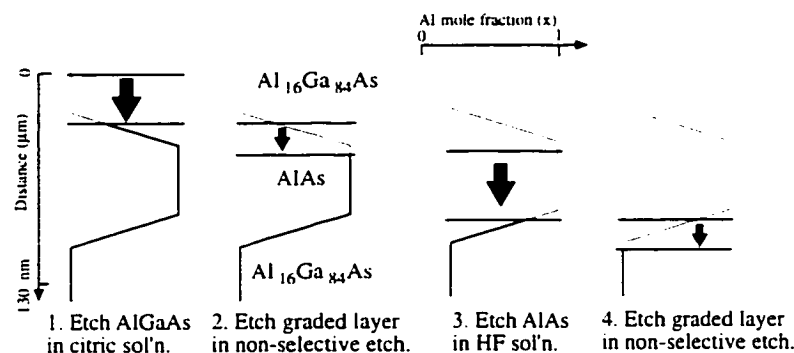


Fig. B- 11: Etching procedure for selective etching of DBR.

In theory, if the etch builds up any roughness due to “micropatterning” (i.e., slow-etching areas due to oxides or contamination which are unevenly distributed), the interface where etching stops will allow the slower-etching areas to catch up to the more rapidly etched areas, and give a perfectly smooth surface. In practice, a rough surface was always obtained in this etching after several etch cycles had been repeated. Some reduction could be made by thoroughly cleaning the sample in strong bases to remove surface oxides. Others etching DBR samples with graded

interfaces have reported similar difficulties [22], while those etching samples with narrower graded regions using digital alloys have reported good results [23]. After several unsuccessful attempts at varying this procedure, monitoring it more carefully using a microscope during etching, and using longer non-selective etch times, I came to the conclusion that this "cyclical selective etching procedure" might better be used for removing just the last few periods in a sample where the majority of the DBR had been removed by a non-selective chemical or mechanical polishing. Perhaps mechanical polishing *during* one or more of the steps in the cycle would help to reduce etch roughness due to micro-patterning: if contamination deposits thin unetchable layers, rubbing the sample across a polishing pad should rub these contaminants off. A great improvement was observed by polishing during the etch when using Br:Meth, as discussed later.

We subsequently found a paper on succinic acid selective etching [24], which can be adjusted to etch 0–60% mole fraction, theoretically eliminating the problem that graded interfaces are not etched in the 30–50% mole fraction band. This approach would allow for a simpler 2-step cycle and possibly eliminate the problems we encountered with roughening.

By contrast, plan-view sample preparation for an in-plane laser is generally trivial, with a monotonic decrease in aluminum fraction as one approaches the active region, allowing a single selective etch to be used.

B.2.3.2 Non-selective etching

Many of the problems with selective etches which might come up due to difficulties etching the graded interfaces can in principle be eliminated by using non-selective wet etches. Dozens of different solutions were characterized. Many did an excellent job on my samples if I only wanted to remove half a micron of material, but built up roughness quickly after a couple of microns of material had been etched. Since the p-DBR is just over 3 μm thick, and the n-DBR is just over 4 μm thick, this roughness build-up was unacceptable.

In the end, it was found that the only etch which gave a smooth surface after several microns of material removal was a dilute Bromine:Methanol (hereafter Br:Meth) solution with a mechanical polishing action being applied as the etch was taking place. Dropping a sample directly in the solution without applying a

polishing action resulted in the same unacceptable roughness build up observed in other etches. Presumably the mechanical action rubs off the oxides or contamination that “mask off” some areas of the sample, and cause roughness build-up. I did not re-evaluate other etching solutions with simultaneous polishing, but would not be surprised if they also gave smooth etches.

Strong Br:Meth solutions are reputed to give a rougher surface, and at any rate have too high an etch rate to allow controlled etching. Solutions of 1:250 and 1:1000 were used. The solution was placed in a bottle with an eyedropper, and one eyedropper full at a time was all that was needed to wet the Chemomet polishing pad bonded to a glass plate. Note that the methanol dissolves the adhesive on the back of the pad, causing it to curl up. The sample, mounted to a tripod polisher or stainless steel stage, was then moved in a gentle circular motion, with little downward pressure. While this etch induces no subsurface damage the way the mechanical polishes do, it causes a disturbing amount of edge rounding. Even a large 1-cm-square sample will be left without a flat center, as will be seen later in Fig. B- 9. Thus, one should remove all but the last 0.5 μm or so with purely mechanical means, and not call on the Br:Meth solution to do any more than clean up the thin surface damage layer.

The reproducibility of the etch was not as good as I would have hoped: at times I would polish the sample on the pad moistened with solution, and nothing would happen (as if the surface oxide layer had not been penetrated); then I would apply pressure to the sample and polish for another 30 seconds, and microns of material had been removed. There appears to be an initial “breakthrough” which is needed, followed by much faster material removal.

My first success with Br:Meth showed another interesting feature: I rinsed the sample in water after etching, and inspected it under the microscope. Due to the substantial edge rounding described earlier, a number of rings were observed as the contours of AlGaAs and AlAs showed more material removal closer to the edges. The AlAs showed the usual green or brown oxide on top. Further etching removed material from most parts of the samples, but left mesas everywhere the aluminum oxide (from the AlAs areas) had been. Evidently, the aluminum oxide forms an un-

etchable mask. In the future, I rinsed the sample with methanol rather than water, which seemed to reduce the problems.

Finally, a few words of caution are in order. First, when using the dilute solution for chemo-mechanical polishing, use it in a vented flow bench, since bromine solutions give off an irritating, chlorine-like odor. When mixing the solution, you will need to pour pure bromine out of a bottle, which emits a strong brown smoke from the bottle. This smoke can cause respiratory distress - be sure to do this from outside a flow bench with the shield as far down as you can get it. Wear heavy rubber gloves when pouring solutions. The bromine has high surface tension, will wick down the side of the bottle, and if the bottle is more than half full, will get on your gloves. If wearing the standard clear PVC glove, it is able to diffuse through pores in the PVC (or etch the pores large enough to get through — this was not evident). I found bromine had soaked onto my fingers the first time I was mixing this solution. Accurate safety data is hard to come by, but fortunately I can report no burns or irritation in spite of over 5 minutes of un-noticed contact. Needless to say, I wore heavy rubber glove from that point out.

B.2.4 Removing p-metal without removing much semiconductor material

B.2.4.1 Polishing p-metal off

The best method for removing p-metal from a sample without removing more than 0.1 μm of the p-DBR involves using an alumina polishing suspension [7]. This was the method used to prepare the samples with semi-transparent contacts (Section 3.6), as well as those where metal interdiffusion was studied (Section 4.4). As before, the sample is generally mounted to a stub, and placed in a tripod polisher which is leveled with a bubble level. However, excellent results can also be obtained using automated polishers such as the Buehler Minimet, which also hold the sample mount level. While I would continue to check level when using the tripod polisher, and make adjustments as necessary, leveling with a polishing pad was far less critical than when using a mylar disc, since the Buehler Chemomet pad [8] had some “give” to it, and thus was able to apply pressure across the entire sample, not just to the highest point on the sample as with the diamond paper. Edge rounding was significant, but not a serious problem on larger samples. On a 1-cm-square sample, one could expect to lose the VCSELs closest to the edge, but those

located a couple of mm away from the edge did not have significantly more material removed than those in the center ($<0.2 \mu\text{m}$ thickness differential). Edge rounding could be further reduced by building up a protective wax “moat” around the sample edges, then pressing it flat with a glass slide while it was still warm.

Initially, a $0.05 \mu\text{m}$ alumina suspension was used to remove the interconnect metal, the oxide, and the p-contact. This could take several hours on large samples, though. Later, a larger $0.3 \mu\text{m}$ grit was used to speed the initial material removal, and I switched to $0.05 \mu\text{m}$ grit when we got closer to the finishing point. As before, I recommend using the Baikolox “CR” (non-agglomerated) suspension [7], and using a new polishing pad for the last few minutes of polishing to remove debris from earlier steps.

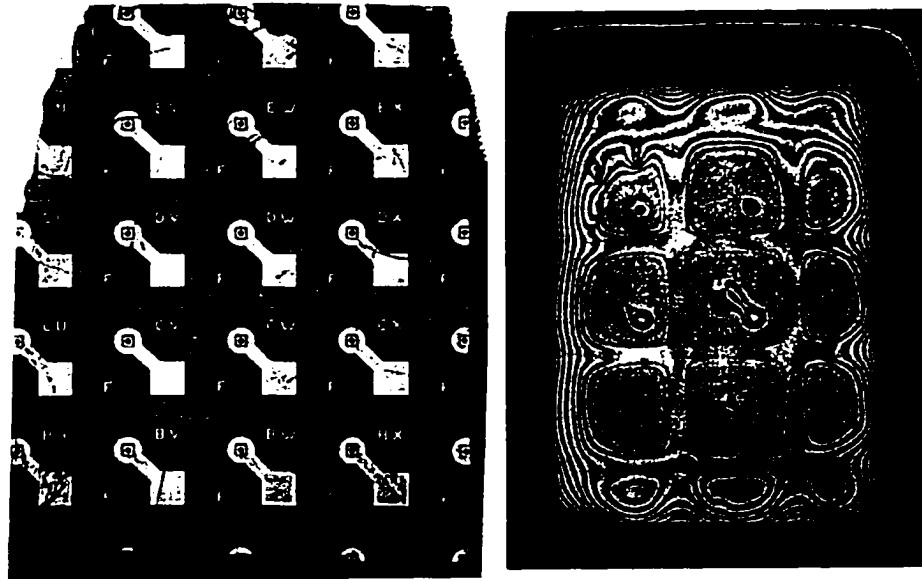


Fig. B- 12: Image of array before (left) and after (right) polishing p-metals off. Note that a small amount of metal remains in the center of the device, and DBR rings are present at the edges, due to edge rounding effects.

B.2.4.2 Deposition of semi-transparent metal.

If desired, after removal of the p-metals, the polished sample can be coated in semi-transparent indium tin oxide to allow electroluminescence, as shown in Chapter 3. The ideal method of applying a semitransparent contact is to reactively sputter using an indium tin oxide (ITO) target in an oxygen atmosphere. We unfortunately did not have this target available. We had access to a thermal evaporator, with indium and indium tin oxide sources. Indium tin oxide (91% In_2O_3 ,

+ 9% SnO_2) [25] is a yellow, ceramic-like powder with big chunks which must be ground into a fine powder before it can be evaporated. Before deposition, we painted on a ring of photoresist around the edges of the sample to prevent a short circuit from forming around the edges of the device.

Straightforward evaporation of indium tin oxide left a rough layer which did not have good electrical characteristics or transparency. This is perhaps not too surprising, given that good stoichiometry is very difficult to obtain: the oxygen outgasses early in the evaporation, leaving an poor quality (opaque) indium-rich deposition.

We next tried depositing pure indium was deposited, and subsequently annealed it in air on a hot plate in an attempt to oxidize it into In_2O_3 . It ended up beading into large indium droplets. Even depositing a thin (5 nm) “sticking” layer of titanium before the indium deposition resulted in the same beading after annealing.

The method which proved successful was to first deposit $<0.05 \mu\text{m}$ of indium as a contact layer. Upon annealing, it was hoped this would interdiffuse with the semiconductor to improve electrical contact. Then, a layer of ITO of undetermined thickness ($<0.1 \mu\text{m}$?) was deposited. This layer was intended to serve as a surfactant layer for the indium above, providing a template during the annealing process, to avoid beading. Finally, $\sim 0.4 \mu\text{m}$ of indium was deposited on top. The photoresist ring was stripped off the top (careful: the indium is soft and can get scratched during this stage — forego the usual ultrasonic bath for this liftoff step). The sample could then be annealed on a hot plate at $\sim 250^\circ\text{C}$ for 30 minutes or longer. The indium oxidized during the anneal. The device was periodically checked to see if the desired transparency had been obtained. For our purposes, not very much light transmission was needed: just a few percent would allow us to image our sample. The sample did not appear transparent after annealing, as it should with a good ITO deposition. Nonetheless, it allowed us to obtain EL images of aged devices after the p-metals had been polished away. Probe contact could be made directly with the semi-transparent contact, with no need for metal pads.

B.2.4.3 Wet Etching p-metals

Given the evidence that glide dislocations originated at the p-contact interface, a technique which allowed us to remove the metal (without disturbing the

semiconductor beneath it) would be very valuable. It would allow, among other things, plan-view examination of the contact layers of aged VCSELs. We thus attempted to develop a method for wet etching the p-contacts off. While we were ultimately unsuccessful, and were not able to develop anything better than the polishing technique discussed above, I believe a discussion of the difficulties involved in developing a contact etch would be valuable to the reader.

While the metals used in Honeywell's VCSEL are proprietary, the metals typically used for p-contacts are: a) a "sticking" layer (usually Cr or Ti), b) a doping layer (optional; often Zn or Be); c) a barrier layer to keep gold out (often Pt); and finally d) a gold layer which allows good wire bonding and won't oxidize. The gold can be easily removed using a ferro-cyanide etch (the more common KI etch will vigorously attack the epitaxy through pinholes in the oxide). Likewise, etches exist which will etch the sticking and doping layers without attacking the semiconductor. However, very few solutions will etch the platinum barrier layer.

In general, strong acids and bases will not etch the $\text{Al}_{16}\text{Ga}_{84}\text{As}$ contact layer without an oxidizer such as H_2O_2 . The acid or base is not capable of etching the semiconductor itself, only the oxide of the semiconductor. Thus the oxidizer forms a thin surface layer of oxide with the semiconductor, which is dissolved and removed by the acid or base, exposing fresh semiconductor to the oxidizer, which then forms a thin surface oxide on it, allowing etching to proceed.

There are two plans of attack that could be hoped to meet with success. First, the straightforward method would be to remove the gold, exposing the hard-to-etch platinum barrier layer. Then, identify a solution which will etch the platinum without attacking any of the exposed areas of the sample. I tried a number of strong acids, and left the sample in them as long as 30 minutes. However, only solutions containing nitric acid (a strong oxidizer) appeared to etch the platinum. Unfortunately, these solutions with nitric acids also quickly etched the entire sample away as well. Even solutions without an oxidizer got through pinholes in the growth, and quickly undermined the sample by etching the AlAs layers. Many strong acids, including HCl and HF, which could be hoped to etch Pt, will also rapidly etch AlAs.

The second plan of attack would be to leave the platinum barrier layer in place, and attempt to undercut it laterally (from the sides) by etching the sticking and/or doping layers beneath the platinum. This was also tried. A number of methods were used to expose the edges of the p-contact, including mechanical polishing of the interconnect metals, and removing the interconnect metals by bonding a plastic sheet with strong epoxy, and ripping the interconnect metal and oxide off. The p-contact would then need to be undercut by about 15 μm laterally. It was left in strong etching solutions for up to 7 hours, with no progress (e.g., peeling of the edges) observed.

Chemical removal of the p-metals could possibly be done by wet etching the gold, then ion milling the barrier layer, and then wet etching the sticking layer. With data about etch rates of various metals was contradictory and hard to come by, we dropped this line of work in favor of the following purely mechanical technique, which yielded surprisingly good results.

B.3. Sample prep for Single Die

As if preparing VCSEL *arrays* for TEM was not already difficult enough, most VCSELs are presently sold as individual devices - cubes that are only 400 – 600 μm on a side. A number of different techniques were attempted to allow these die to be examined by CL and TEM. While virtually all the techniques were successful for making CL cross sections, none of the approaches worked for TEM sample preparation of individual devices.

The common difficulties with the conventional approaches were essentially mechanical issues. Arrays are large enough to be mounted on the large-aperture grids directly, while single die VCSELs must have pieces glued on to increase their dimensions if they are to be handled and mounted. Even after being bonded into such a matrix of spacer pieces, the sample die would frequently be ripped out of the matrix during final polishing stages, or the glue around the device would be ion milled away. We were not able to find any report in the literature of researchers being able to prepare a pre-specified on die of this size, without resorting to FIB techniques.

B.3.1 Encapsulants

The procedure that I will later describe for making thin sections is fairly tedious, requiring a day to demount the die, carefully build up the glass on all sides of the die, and go through a number of gluing, clamping, curing, and cutting operations. I had originally hoped that it would be possible to leave the die mounted on the header, and encapsulate it in epoxy. (The device *must* be encapsulated in some sort of material to protect the edges from chipping damage during the polishing steps, since GaAs is a brittle material.)

The clear encapsulants tried (5-minute epoxy, as well as harder specialty epoxies), worked fairly well for a simple CL and EBIC cross sections. However, they all broke apart when I tried to thin the sample into a wedge and got sections down on the order of 10-30 μm thick. (I was subsequently told that this brittleness is a well-known limitation of these epoxies, and that such encapsulants are thus never used for making TEM samples.)

For samples where one is only interested in making good CL cross sections (where only one side of the package needs to be ground away), embedding the device in clear epoxy is probably the ideal approach, since this approach is far less tedious than the methods which will be described later. But be warned that it will prevent subsequent examination with TEM.

B.3.1.1 Opaque encapsulants

Where precision is not required in placing the cross sectioning plane, the device can be embedded in a high-temperature, high-pressure mold of bakelite. (Since bakelite is opaque, it allows only $\pm 3 \mu\text{m}$ precision of the sectioning plane, as opposed to $\pm 0.5 \mu\text{m}$ precision for the VCSELs mounted in glass. The majority of VCSELs could be studied with either technique; only a few VCSELs with small epitaxial defects require sub-micron precision of the sectioning plane.) Care must be taken to keep the pressure of the mold relatively low to avoid breakage (nominal casting pressure is $\sim 4,200$ psi). The casting process is relatively fast compared with the process of going through the multiple gluing, clamping, and curing operations to sandwich the device between glass spacers. The biggest drawbacks to bakelite are that the opacity prevents one from telling how much further polishing needs to go, and for smaller die, bakelite's hold can be insecure.

A pair of die were bonded together, cast in bakelite, ground to the center on one side, and then dimpled on the other to less than 5- μm thickness. Red light was visible through the VCSEL layers (presumably due to transmission through the AlAs layers), although the GaAs substrate was still thick enough to be opaque. The sample was ion milled, and then placed in the transmission electron microscope (TEM) for inspection. It was still too thick to be imaged. Upon removal from the TEM, it was noted that the sample had fallen out of the bakelite. In hindsight, it might be prudent to glue a larger piece of GaAs to the back of the sample in the future; this piece could anchor the sample in a thicker part of the bakelite.

It is important to note that in the absence of a method to directly monitor progress from the top (e.g., by being able to look through a transparent cover slip which has been bonded on top for edge protection), some other means of monitoring progress must be made. In the case described above, the metal pattern had distinctive letters which could be seen in cross section, allowing us to estimate how far from the desired stopping point we were. Without such a pattern, one could place special scribing patterns in the top of the device, for example a scribed letter "V." By monitoring how far apart the trenches are from one another in cross section, and comparing with a photo taken from the top, one could determine how much material had been removed from the cross section.

B.3.2 On-the-header preparation

After failing to find a technique with better than 50% yield in die de-mounting, I worked on a technique to prepare die while they were still mounted to their original headers. This involved first gluing a piece of glass no larger than the die on top to protect the die from chipping. Then, both sides of the package were sawn away with a low-speed sample preparation saw. Next, the sample (and the header) were polished to the middle of the VCSEL aperture, then mounted on a grid to polish the other side down to a wedge. When the sample got down to a 10- μm -thick section, the silver epoxy bond failed, and the device came un-mounted from the header. Mounting to a fine-mesh grid which directly supported the device would have prevented this problem, but would preclude the desired low-angle ion milling in the next steps. Fortunately, further work allowed the development of a high-yield de-mounting technique.

B.3.3 Demounting procedure

While the die-attach epoxy used by HP is extremely strong, I was nevertheless able to develop a technique for removing VCSEL die with 100% yield. Note that the usual methods of removing die, by dissolving the epoxy in strong solvents such as Urasol or Dynasol, are said to attack die with greater than 50% Aluminum in the AlGaAs epitaxial layers. (We had a 100% Al mole-fraction in every other layer of the DBRs, which clearly rules out these solvents.)

While I will attempt to carefully describe the die removal technique, it requires an hour or two of practice to develop the skills - don't try this on valuable die before you've proven to yourself you can remove several test die in a row without breaking one! Small die (e.g., 300x400 μm for a single VCSEL) are easier to remove; larger die (e.g., 700 μm -square with twin VCSELs) are quite hard to remove without breakage until one has mastered the de-mounting technique.

One starts by decapping the header, and sticking the leads through a ceramic block with holes drilled through it. Then one places the device and block on a hot plate set to 300-325°C, for 15-30 minutes or longer. (Actual device temperature is probably considerably lower than the hot plate, given that the laser was "insulated" from the hot plate by the ceramic block.) The thermal exposure causes the epoxy to decompose. 5 or 10 minute exposures proved inadequate, and resulted in die breakage; the decomposition process evidently is not instantaneous. On the other hand, excessive thermal exposure should be avoided, since annealing of proton implantation may significantly change the device before you've had a chance to make your observations of it. If desired, die attach stations could be used to heat the header (or even maybe something jury-rigged with a soldering iron) in place of the hot plate.

While the header is still on the hot plate, an assembly (low-power, stereoscopic) microscope is moved into place, and excess silver epoxy is scraped off the header with an x-acto knife, all the way to the sides of the device. Then the x-acto knife is used to cut a trench in the header. The trench runs alongside the die. (Fig. B- 13) This requires a "sawing" motion, with a fair amount of pressure.

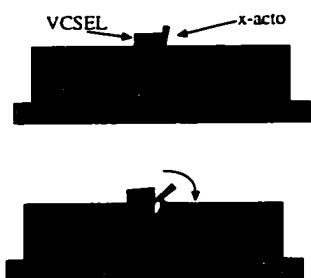


Fig. B- 13 a) sawing trench alongside die; b) rotating knife to lift die.

Finally, the most difficult part of the operation (or perhaps just the moment of truth): the knife is rotated, lifting the die off the header. (Fig. B- 13b) If *any* resistance is felt during this motion, the die is not ready to come off - do not proceed! (Cut the trench deeper and closer to the die, and give the epoxy more time to weaken before trying again.) Do not actually remove the die from the header; just angle one side up, then let it back down, and remove the header and ceramic block from the hot

plate. At this point the de-mounted die is ready to be cleaned with solvents, and either glued into a glass sandwich, or cast in bakelite.

Fortunately, the epoxy used by Honeywell was far easier to remove, and 10 minutes on a hot plate at 250°C weakened its bond enough to push it off the header with tweezers; the aforementioned procedure with an x-acto knife was unnecessary. I always removed the wire bond with an x-acto knife before this step, while the die was still held by the header. After demounting the die, there is a very good chance of losing it. Take every precaution possible, including using only good tweezers with low spring force (allowing you to feel the force applied to the die), carrying the die in appropriate boxes, and not walking around while carrying the die in tweezers, etc. If you do lose the die despite these precautions, it is of little use looking for it. I have lost about half a dozen die in the course of this thesis, and spent about 15 minutes looking for them in each case, using both a flashlight held along a darkened floor, and wet cloths which pick up particulates on the floor. In no case have I ever recovered a dropped die. However, once the die has been embedded or encapsulated, the resulting assembly is so much larger that the chances of finding it when dropped are fairly good.

B.3.4 Encapsulating a removed die in a solid matrix

While the following procedure is very tedious, if I were to spend further time attempting to prepare a TEM sample by mechanical means, it is still the method I would use. By embedding the die in a solid matrix, it receives better support than is possible with castable embedding media mentioned above; further, progress can be directly monitored by examining the sample through glass on the top.

After the die have been removed from the header, time should be spent removing any remaining silver epoxy on the die. This should be easy, as the epoxy will likely be brittle from the heat treatment it has just received. If epoxy remains on the sidewalls of the die, it may be necessary to heat it on a hot plate at 250°C or higher, and scrape the sides *while* the device is hot. (The epoxy is much weaker and more fluid at high temperature than after it cools down.) The importance of cleaning the sides of the die cannot be overstated, as residual silver epoxy will prevent a thin, strong bond to the adjacent embedding pieces, and expose the die to possible attack during ion milling, as discussed in the next section. The die and spacer pieces should be cleaned with solvents prior to the following steps.

Using either M-Bond 610 or Allied Epoxy 110 [3], bond the die to a piece of (1-mm-thick) microscope slide-glass 1 cm square. This is best done by spreading a thin layer of glue on a slide, and smearing it thinly. The top-surface of the die is then gently dipped in the thin glue. If glue is directly painted on the top of the die, excess will smear out, and build a fillet of hardened glue around the edges after curing, which will prevent the spacer pieces from forming a thin glue line with the sides of the die in subsequent steps. This is shown in Fig. B- 14.

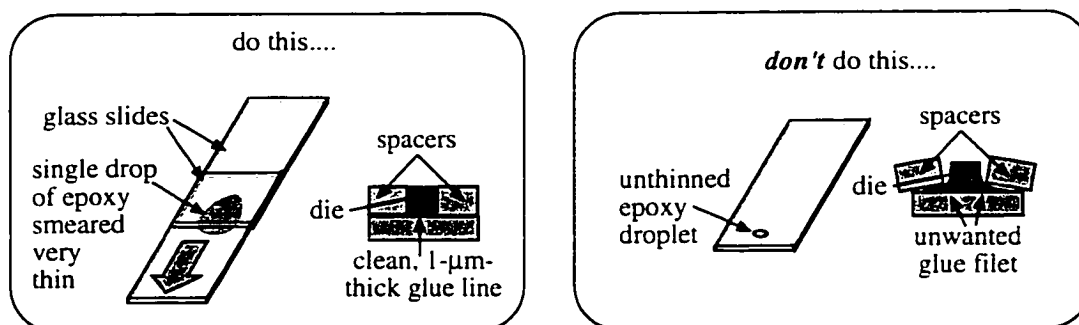


Fig. B- 14: Dip die in glue which has been spread thin (left). Dipping die directly in epoxy, or applying epoxy directly, will leave meniscus of glue which will subsequently prevent spacers from being properly applied.

A small vise or clamping fixture should be prepared. The important features of this vise are: a) it should be built in such a way as to assure that its jaws remain parallel to one another as the jaws are brought together, and b) it should have a smooth enough advancing action to allow one to feel when the jaws have made contact with the die. Overtightening, as could easily happen on a large vise, or one without a smooth advance motion, will quickly crush the small brittle die — I know

— I've done it before! The jaws should be wrapped in Teflon tape, so that excess glue will bond to the easily-removed Teflon tape, and not directly to the jaw faces. If bonding to the jaw faces occurs, it will definitely ruin the sample, and may even ruin the vise.

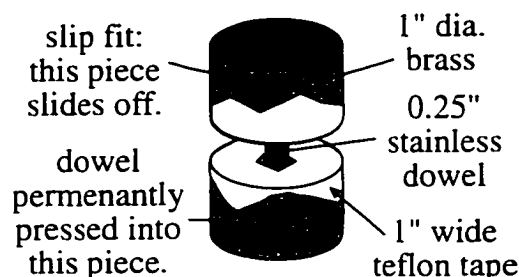


Fig. B- 15: Clamping fixture used for sample preparation.

Alternately, we had special clamping fixtures made with a precision dowel which was press fit into a brass, with the top brass piece being a (tight) slip fit along the dowel. The weight of the upper brass piece provided clamping force. The fit of the upper piece was tight enough to assure that the jaw faces were

parallel. The clamping fixture is shown in Fig. B- 15.

After curing the glue according to directions, remove the vise from the hot plate, and allow it to cool before removing the sample. Next, using small spacer pieces of GaAs or glass, paint epoxy on both sides of the die, as well as on the glass, as shown in Fig. B- 16, step 2. Clamp in a vise, and cure the glue. If you are wondering whether it would be possible to have done this at the same time as step 1, the answer is that it would not be possible to apply clamping pressure to both the die and the spacers at the same time: one will surely stick up above the other. Now polish the sample until the sample and side pieces are level with one another. To do this, I usually use a tripod polisher and 15 μm grit paper to grind the sample

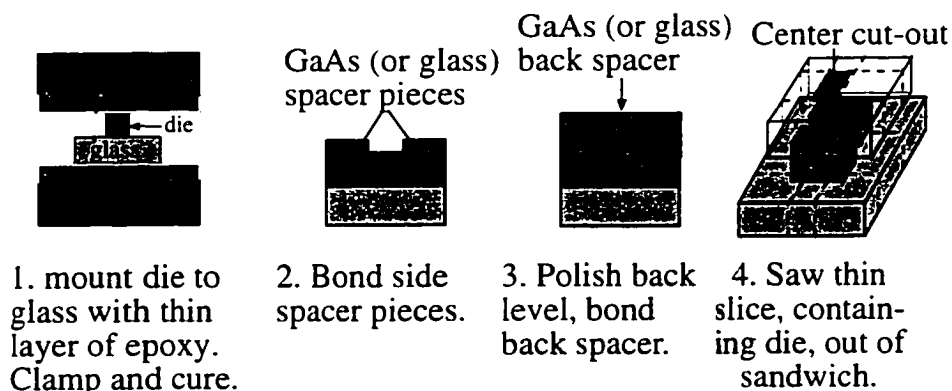


Fig. B- 16: Steps for embedding a single die in a solid matrix.

until it is clear that the side spacer pieces are level with the die. A quick polish with 3 μm paper following this gives a smooth surface on the back, which the final embedding piece can be bonded to. Glue GaAs to the back, clamp, and cure (step 3). Finally, saw the excess material off the sides, as shown in step 4.

The sample is now ready for polishing, and the procedure is essentially identical to that described in section B.1. With some skill the entire procedure outlined above can be done in a day, but is obviously far more tedious than epoxy embedding would be. Nonetheless, the solid glass surrounding the device is far less brittle than epoxy, and holds a much better chance of giving useful results.

B.3.5 Get sample very thin before trying to ion mill

One final caution in making such samples: both the die I have prepared to the final stage (where you could see through the die, they hadn't been ripped out of the embedding matrix, scratched, pulled off the stub, etc.) fell out of the matrix during ion milling. (Ion milling is needed to remove the polishing damage layer.) This problem of glue bonds failing can't happen with an array, since the array is a single piece of material. However, with small die, the glue which bonds the die to the adjacent embedding pieces etches much more rapidly than either the die or the surrounding pieces. If you ion mill for too long, the glue gets milled away and there's nothing left holding the die, which then falls out of its grid. I tried to eliminate ion milling using a low-selectivity wet chemical etch to replace the ion milling, as described in Section 1.3.6. However, such a non-selective etch proved elusive, as all etches added unwanted surface topography. It may well be that the etches would prove "good enough" (i.e., that the 10% thickness contrast provided would not ruin the TEM image), but I did not go to the trouble of preparing a full TEM sample and imaging it to prove or disprove this. This having been said, there are two things one should do: a) keep the glue line as thin as possible, and b) make the sample quite thin (2 μm) before beginning ion milling, so that milling time will be minimal.

B.3.6 FIB machining approach

While the mechanical sample preparation methods work well for large arrays, the procedures outlined above in Section B-3.1 - 3.5 proved extremely time-consuming, and have a steep learning curve. Even the easier array preparation taxed

the skill of the best undergraduate assistants, requiring a prolonged apprenticeship before good samples were produced. As mentioned, the only way to reliably prepare small die for TEM imaging is with focused-ion beam FIB machining [26-28]. These FIB systems, often utilizing a beam of argon which can be focused into a 10-nm-wide spot, are able to ion mill away selected areas of material. The procedure for preparation involves demounting the die, thinning it to within 10–40 μm of the desired imaging plane on both sides, and then mounting it on a cut-back grid. A top-view, showing which parts are to be milled away, is shown in Fig. B-17. A three-dimensional view of a die mounted on a cut-back grid, after FIB removal of material, is shown in Fig. B-18.

FIB sample preparation has been widely described in the literature, with widely varying results having been reported. Some parties have obtained excellent results [26, 28], while others have published TEM photos from FIB samples with relatively poor spatial resolution [27].

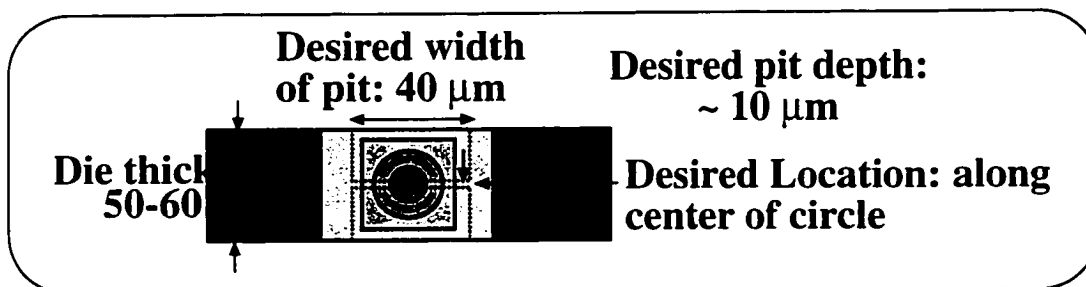


Fig. B- 17: Top-view of die prepared for FIB sample preparation.

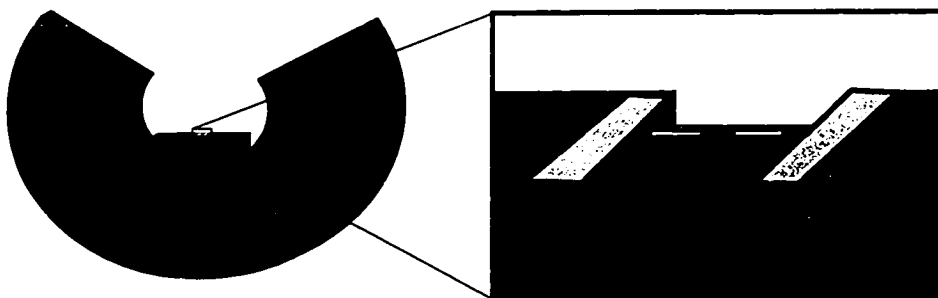


Fig. B- 18: Three-dimensional view of mounted FIB sample on cutback grid. Closeup is shown in inset to right.

The sample is then sent to a vendor, who coats the top of the die with a protective metal layer, to prevent the “wings” of the beam from attacking the top of

the cross-section. The sample is placed in the FIB, and material is rapidly removed from the edges with relatively large-diameter, high-current beams. Successively smaller beams are used to take slower cuts as the machine gets closer to the desired cross section. The sample can be tilted with respect to the beam if necessary to maintain uniform cross-section thickness from top to bottom. Etch rate, in one reported case, was $1 \mu\text{m}^3/\text{nA}/\text{min.}$, with a 4 nA maximum current being reported [26]. Thus, if the sample is mechanically thinned to within $10 \mu\text{m}$ of the active region on each side (which is quite a challenge to come this close), and the trench milled is $10 \mu\text{m}$ deep and $40 \mu\text{m}$ across, rough machining will take about 40 minutes. If the initial mechanical thinning is less aggressive and we only come within $30\text{--}40 \mu\text{m}$ of the desired cross section, the trench volume increases dramatically, and with it the rough machining time. Our first vendor, FIB Applied Semiconductor Technologies, didn't ask for much in the way of mechanical thinning, so we sent a $60 \mu\text{m}$ thick sample to them. But they cut corners by not machining the sample as deep as we'd asked - only $3\text{--}4 \mu\text{m}$ deep rather than the $10 \mu\text{m}$ we requested. This prevented us from seeing the active region. The next vendor we used, Phillips Materials Analysis Group, asked for much more aggressive mechanical thinning, and we sent a $20 \mu\text{m}$ thick sample to them.

B.3.6.1 Sample preparation for FIB machining.

The mechanical thinning of samples in preparation for FIB has a few unique challenges. First, no coverslip can be permanently bonded to the top, so the lack of edge protection is potentially problematic. It is a general rule of thumb that GaAs samples cannot be successfully prepared without some sort of bonded layer, and yet we need a clean top layer to allow good adhesion of protective metal before FIB is started. Second, without an embedment, the potential pressure applied to the small die is enormous. Third, the contact area with the sample stub is very small, and the sample is quite likely to get knocked off the stub during the sample preparation process.

The second and third problems were dealt with by covering the sample in relatively large pieces of wax, which left a wax "blob" some 5-mm (or greater) in diameter to help spread the force applied by the weight of the tripod. This "blob," similar to that shown in Fig. B- 2, also braces the die against the shear forces being

applied by the grinding disks. This wax embedment requires the use of a lower temperature hot plate $\sim 90^\circ\text{C}$. Higher temperatures, while excellent for creating thin bonding layers, lower the wax viscosity too low to maintain the desired "droplet" shape.

The first problem discussed above, the lack of edge protection, and the great potential for chipouts, was dealt with in two ways. In the first trials (all with dummy devices), I faced the sample into the direction of the wheel. Chipouts are much more likely to be a problem on the trailing edge of the sample than on its leading edge. While it was necessary to change to finer grits earlier than had been the case before, due to higher material removal rates, chip-outs were avoided. In one instance, when the second side was thinned to within $10\text{ }\mu\text{m}$ of the sample, a large chunk came out of the top of the laser. To provide additional edge protection, I bonded glass coverslips on top of subsequent samples with a cyanoacrylate glue. This "nail" glue (e.g., Sally Mann nail glue, available in Pharmacies) is similar to "Krazy Glue," but has a residue which is more easily removed in acetone. After the samples were thinned to within about $10\text{ }\mu\text{m}$ of the center of the device the sample was bonded to the cut-back grid using Allied Epoxy 110 [3], cured, and then soaked in acetone to remove the glass coverslip. It was shipped to the FIB vendor in a membrane case.

B.3.6.2 Results from normally-degraded VCSEL prepared for TEM by FIB Machining.

The results were disappointing: the strain from the remaining metal (both protective and p-contact metal) caused the sample to corrugate, with ripples of micron-periodicity that prevented serious twin-beam analysis from being undertaken. Slip dislocations appeared in a cross-hatch pattern, and were likely artifacts from p-metal stress. A few large precipitates appeared in isolated locations of the final sample, and may have been due to a high milling rate. The sample is shown in Fig. B- 19.

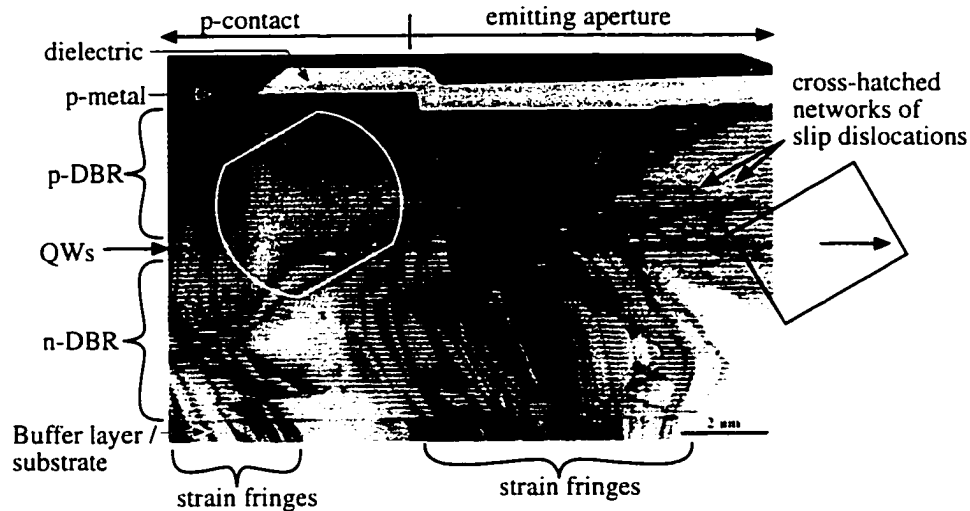


Fig. B- 19: TEM image of normally degraded VCSEL after cross sectioning by FIB. Cross hatches are thought to be an artifact. Box to the right shows size and height of TEM from Fig. B- 20 (actual area was to the right of this image). Circular area to the left shows approximate size and height of the TEM from Fig. B- 21.

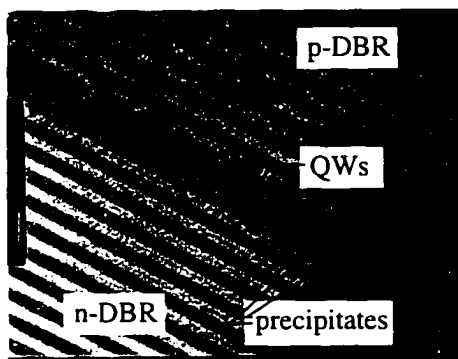


Fig. B- 20: TEM image of normally degraded VCSEL cross section, showing precipitates in the AlAs layer of the n-DBR next to the $\text{Al}_x\text{Ga}_{1-x}\text{As}$ n-confinement layer.

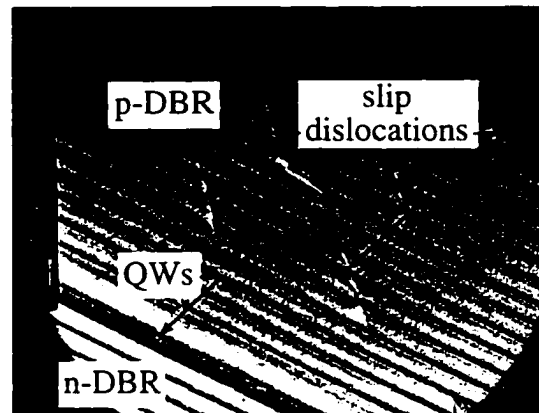


Fig. B- 21: Slip dislocations in p-DBR of a normally-degraded VCSEL.

Two images which were taken at UCSB may actually reflect real degradation. The first which is very likely a real effect has also been seen on previous rapidly degraded VCSELs: precipitates in the n-DBR. In this case, they were observed only in the first layer of the n-DBR (Fig. B- 20), something which would be nearly impossible to explain away as a sample preparation artifact. Because of the sample limitations discussed earlier, we were not able to map out

exactly where these precipitates were concentrated laterally, which would be necessary to establishing their cause.

Slip dislocations in the p-DBR were also observed (Fig. B- 21), beyond the cross-hatch network mentioned earlier. Without further work, it is impossible to determine whether these dislocations are real, or if they are merely artifacts.

References for Appendix B:

- [1] J. Benedict, R. Anderson, and S. J. Klepeis, "Recent developments in the use of the Tripod Polisher for TEM specimen preparation," *Proc. of the Mat. Res. Soc., (Specimen Preparation for Transmission Electron Microscopy of Materials - III)*, vol. 254, pp. 121-40, 1991.
- [2] South Bay Technology, "Technical Manual for Tripod Polisher Model 590," . San Clemente, CA, 1989.
- [3] Epoxy-Bond 110 was purchased from Allied High-Tech products, 2376 E. Pacifica Place, Rancho Dominguez, CA 90220, (800) 675-1118.
- [4] Assortment of mylar-backed diamond polishing discs were purchased from Allied High-Tech products, 2376 E. Pacifica Place, Rancho Dominguez, CA 90220, (800) 675-1118.
- [5] P. Kaszuba, "A technique for achieving ultra-smooth chip cross sections," presented at 21st International Symposium for Testing and Failure Analysis, Santa Clara, California, 1995.
- [6] Grant Girolami, personal communication.
- [7] 0.05 μm alumina polishing suspension (CR85PS) was purchased from Baikowski Intl., 325 Westinghouse Dr., Charlotte, NC 28273, (704) 587-7100
- [8] Buehler Chemomet pads (#40-7918) were purchased from Buehler, Ltd., 41 Waukegan Rd., Lake Bluff, IL 60044, (800) 283-4537
- [9] I. Buehler, "Gallium Arsenide Electronic Component," . vol. Method Number 8.04. Buhler Dialog Manual: Buhler, Inc., Lake Bluff, Illinois, 1993.
- [10] R. Mann, , 1996.
- [11] K. Kenefick, "Selective etching characteristics of peroxide/ammonium-hydroxide solutions for GaAs/Al_{0.16}Ga_{0.84}As.," *Journal of the Electrochemical Society*, vol. 129, pp. 2380-2, 1982.
- [12] J. J. LePore, "An improved technique for selective etching of GaAs and Ga_{1-x}Al_xAs," *Journal of Applied Physics*, vol. 51, pp. 6441-6442, 1980.
- [13] M. Schneider, C. Colvard, K. Alavi, and E. Kohn, "Characteristics of nonselective GaAs/(Al,Ga)As heterostructure etching at very low etch rates," presented at Advanced Processing of Semiconductor Devices, Bay Point, FL, USA, 1987.
- [14] R. Ito, H. Nakashima, S. Kishino, and O. Nakada, "Degradation sources in GaAs-AlGaAs double-heterostructure lasers," *IEEE Journal of Quantum Electronics*, vol. QE-11, pp. 551-556, 1975.
- [15] D. Babic, "GaAs substrate removal," in *Double-Fused long-wavelength vertical-cavity lasers*. Ann Arbor, MI: University Microfilms, 1995, pp. 136-138.
- [16] E. Yablonovitch, "Epitaxial Lift-Off," in *Properties of GaAs*, 2nd edition, published by INSPEC, 1990.
- [17] S. J. Pearton, "Critical issues of III-V compound semiconductor processing," *Materials Science and Engineering B*, vol. 44, pp. 1-7, 1997.

- [18] K. Bacher and J. S. Harris, Jr., "A wet etching technique for accurate etching of GaAs/AlAs distributed Bragg reflectors," *Journal of the Electrochemical Society*, vol. 142, pp. 2386-8, 1995.
- [19] C. Juang, K. J. Kuhn, and R. B. Darling, "Selective etching of GaAs and $\text{Al}_{0.30}\text{Ga}_{0.70}\text{As}$ with citric acid/hydrogen peroxide solutions," *Journal of Vacuum Science & Technology B (Microelectronics Processing and Phenomena)*, vol. 8, pp. 1122-4, 1990.
- [20] H. J. Lee, M. S. Tse, K. Radhakrishnan, K. Prasad, J. Weng, S. F. Yoon, X. Zhou, H. S. Tan, S. K. Ting, and Y. C. Leong, "Selective wet etching of a $\text{GaAs}/\text{Al}_x\text{Ga}_{1-x}\text{As}$ heterostructure with citric acid-hydrogen peroxide solutions for pseudomorphic $\text{GaAs}/\text{Al}_x\text{Ga}_{1-x}\text{As}/\text{In}_y\text{Ga}_{1-y}\text{As}$ heterojunction field effect transistor fabrication," presented at First International Conference on Low Dimensional Structures and Devices, Singapore, 1995.
- [21] T. Kitano, S. Izumi, H. Minami, T. Ishikawa, K. Sato, T. Sonoda, and M. Otsubo, "Selective wet etching for highly uniform $\text{GaAs}/\text{Al}_{0.15}\text{Ga}_{0.85}\text{As}$ heterostructure field effect transistors," *Journal of Vacuum Science and Technology B*, vol. 15, pp. 167-170, 1997.
- [22] Near Margalit, personal communication.
- [23] D. Bruce Young, unpublished
- [24] S. A. Merritt and M. Dagenais, "Etch characteristics of succinic acid / ammonia / hydrogen peroxide versus aluminum mole fraction in AlGaAs," *J. Electrochemical Society*, vol. 140, pp. L138-L139, 1993.
- [25] Indium Tin Oxide (91% In_2O_3 : 9% SnO_2) (#36235) was purchased from Johnson Matthey, 30 Bond St., Ward Hill, MA 01835-8099 (800) 343-0660
- [26] R. Hull, D. Bahnck, F. A. Stevie, L. A. Koszi, and S. N. G. Chu, "Microscopic studies of semiconductor lasers utilizing a combination of transmission electron microscopy, electroluminescence imaging, and focused ion beam sputtering," *Applied Physics Letters*, vol. 62, pp. 3408-10, 1993.
- [27] J. Szot, R. Hornsey, T. Ohnishi, and S. Minagawa, "Focused ion beam micromachining for transmission electron microscopy specimen preparation of semiconductor laser diodes," *Journal of Vacuum Science & Technology B (Microelectronics Processing and Phenomena)*, vol. 10, pp. 575-9, 1992.
- [28] G. Ben Assayag, C. Vieu, J. Gierak, H. Chaabane, A. Pepin, and P. Henoc, "Localized thinning of GaAs/GaAlAs nanostructures by a combined scanning electron micrograph/focus ion beam system for high-quality cross-sectional transmission electron microscopy samples," *Journal of Vacuum Science & Technology B (Microelectronics Processing and Phenomena)*, vol. 11, pp. 531-5, 1993.

Appendix C: Use of strained-layer quantum wells for enhanced lifetime.

C.1. Experimental observations of dislocation pinning in In - containing alloys.

This appendix contains fundamental information on a subject which lies at the heart of the improvement in laser reliability, but which has been inadequately investigated. It is the direction I originally wanted to pursue as the central topic of my dissertation, before it became more oriented toward detailed failure analysis studies. The “defect pinning” observed in InGaAs devices is able to totally eliminate infant mortality, and completely prevent rapid $\langle 100 \rangle$ DLD formation [1]. Similar findings have been made at shorter wavelengths using InAlGaAs [2], and strained $\text{In}_{0.57}\text{Ga}_{0.43}\text{P}$ QWs [3]. Comparing only lasers which survive early failure, the gradual failure rate in strained QW lasers is also superior to that in conventional unstrained lasers [3-5].

For the time being, strained quantum wells have not been widely adopted for VCSELs, with the GaAs quantum well design dominating the marketplace. Pursuing a deeper understanding of *why* InAlGaAs lasers are more reliable than comparable GaAs lasers will likely be key to improving VCSEL lifetime to allow use in applications requiring higher power than data communications, such as lasers for writing CD's, high speed printing, and industrial and medical applications. Ultimately, once changes have been made to address the failure mechanisms unique to VCSELs, the degradation of the active region will remain a key limiting factor.

The leaders in this field were former co-workers of mine at McDonnell Douglas, who published the first report of defect pinning in InGaAs QW lasers [1], and were able to show that even deliberately damaged In-containing devices would not form $\langle 100 \rangle$ dark-line defects (DLDs) [3, 6]. These observations were made using electron beam induced current (EBIC) imaging. In this sort of imaging, shown earlier in Chapter 2, the beam enters the sample perpendicular to the active region, and is rastered across the entire device. Undegraded areas show a strong signal, as the carriers are collected from the electrical contacts. Near DLDs, carriers recombine quickly, and are not collected, resulting in a dark area in the EBIC image [7].

A comparison between intentionally-damaged GaAs and InGaAs lasers is shown in Fig. C - 1. The GaAs QW lasers failed quickly (usually within a day) due to $\langle 100 \rangle$ DLDs. The InGaAs QW lasers proved immune to $\langle 100 \rangle$ DLD growth, and continued to lase, even when a scribe was made *directly through* the lasing stripe itself!

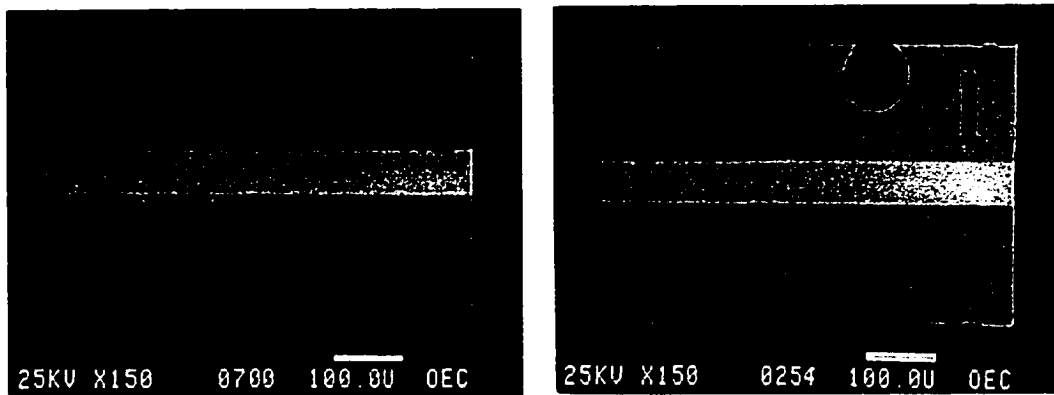


Fig. C - 1: EBIC images of intentionally-damaged GaAs (left) and InGaAs (right) QW lasers after aging (after [6]).

No growth of $\langle 100 \rangle$ DLDs was observed in InGaAs QW lasers with more than 5% In in the quantum well. [6]. However, other researchers have found that $\langle 110 \rangle$ DLDs continue to grow in InGaAs QW lasers, albeit 100 times slower than the $\langle 100 \rangle$ DLD growth rate in GaAs QW lasers [5].

C.2. Analysis of dislocation pinning.

C.2.1 Lattice-hardening explanations.

Papers which report "dislocation pinning" in strained layer lasers often cite a paper by Paul Kirkby [8]. This paper was originally intended to address observations of dislocation pinning in thick, LPE grown detector samples. In the paper, he proposes that In atoms, which are larger than the Al or Ga atoms, migrate into areas next to dislocations where tensile strain is present, and are able to prevent dislocation propagation. An analogy is drawn to the use of carbon to work-harden steel by pinning dislocations. While the explanations make sense for the samples they discuss, it is not clear that the same theories can be used to explain samples grown by techniques where there is far less mobility in the crystal constituents than for the melts deposited by LPE. Indeed, I am not aware of any evidence in cross-

sectional TEM which shows preferential migration of indium into areas near the dislocation networks to allow dislocation pinning. Further, it is not clear why $\langle 110 \rangle$ DLDs are free to propagate (only $\langle 100 \rangle$ DLDs are “pinned”) if a true pinning mechanism exists.

C.2.2 Indium and Aluminum “Voodoo.”

In this section, I will attempt to address the simplification that has become common knowledge: that any laser can be improved by adding indium to it, or by taking aluminum away. While these conclusions appear to be generally justified, one can do far better by understanding *why* these generalities often hold.

The late Dr. Robert Waters, who was one of the world’s leading authorities on laser diode reliability, was profoundly uncomfortable with the conventional wisdom that the *stress* of the indium was responsible for dislocation pinning. As discussed in Chapter 2, stress generally is a bad thing, promoting the growth of glide dislocations (which also spawn climb dislocations)[9]. Stress provides strain energy to propel dislocation growth [10-13]. Dr. Waters believed that indium enhanced device reliability *in spite of* its stress, and not because of it; specifically, he believed chemical properties of indium were responsible for its usefulness, and not its lattice mismatch. One key piece of evidence he pointed to was InGaAsP lasers which were lattice matched to their GaAs substrate, and had reliability which was greatly improved over conventional GaAs QW lasers [3, 14]. In this case, the *strain* from the indium can’t be given the credit for improvement, since the active region is nominally unstrained. Unfortunately, this result relies heavily on the accuracy of the lattice matching for its validity. While some early papers suggested that indium could be used as an “isoelectronic” dopant, where even small amounts of indium would provide dislocation pinning, more rigorous studies have shown that substantial amounts of indium (>5%) are needed for dislocation pinning [6]. Wang et al. show calculations which explain this in terms of the strain force being able to overcome the osmotic force for dislocation growth. Their predictions lead to the conclusions that: 1) n-doped material will be longer lived (consistent with experimental observations), and 2) that tensile-strained quantum wells will have poorer reliability than unstrained QWs [15]. The later claim has not been tested independently of material bandgap, although experiments current being conducted

by Professor Eugene Fitzgerald of the Materials Department at MIT may fill this gap. He has perfected the ability to grow templates of arbitrary lattice constant, upon which similar quantum wells could be grown with tensile or compressive strain. This would allow the relationship between stress and indium mole fraction to be separated. Both tensile and compressively strained devices, with the same indium mole fraction, will be able to be fabricated. Far more research on this topic is needed if we are to optimize device lifetimes, particularly in new materials systems.

C.2.3 Radiative Transfer.

Another reason why InGaAs (though not InAlGaAs) QW lasers would be expected to outlast their GaAs QW counterparts is simply due to “radiative transfer” effect described in Appendix A [16, 17]. The GaAs substrate is transparent to emission at 980 nm, while it strongly absorbs at 850 nm. Thus, the spontaneous emission of a GaAs QW laser would be strongly absorbed just a few microns below the active region, creating an additional heat source, while with a InGaAs QW laser, the spontaneous emission could be transmitted through the entire substrate, and perhaps even escape from the chip, without generating heat. Newman et al. estimated radiative transfer could reduce thermal resistance by a factor of 2 [16], even for absorbing substrate lasers — transparent substrate lasers would be expected to experience an even larger improvement.

C.3. Implementation difficulties of InAlGaAs QW lasers

It should be pointed out that while it is fairly straightforward to add indium to a GaAs QW and make InGaAs QW lasers, this has the generally undesired effect of increasing device wavelength. For most of the lasers studied, data communications standards forced them to have a wavelength below 860 nm, so that they could use inexpensive GaAs and Si detectors. One can add indium, *and* keep the emission wavelength below 860 nm by also adding aluminum to the quantum well [4]. However, this system is notoriously difficult to grow well, since the indium require low growth temperatures to prevent indium evaporation, while the aluminum requires high growth temperatures to obtain high-quality growth with minimal oxygen incorporation. Worse yet, while seemingly acceptable lasers can be grown with a certain range of growth temperatures, the tolerance for truly reliable

lasers is much narrower, and potential reliability cannot easily be established at time zero. This narrow tolerance window, which is only $\sim 20^\circ\text{C}$ wide, has been briefly discussed by Baumann et al. [18, 19], and prevented numerous well-equipped groups working on InAlGaAs in the late 80's from succeeding at wavelengths shorter than 860 nm. 850 nm VCSELs with InAlGaAs QWs have only recently been produced [20, 21], even though they have been the subject of research for nearly five years.

References for Appendix C:

- [1] R. G. Waters, D. P. Bour, S. L. Yellen, and N. F. Ruggieri, "Inhibited dark-line defect formation in strained InGaAs/AlGaAs quantum well lasers," *IEEE Photonics Technology Letters*, vol. 2, pp. 531-3, 1990.
- [2] R. G. Waters, R. J. Dalby, J. A. Baumann, J. L. De Sanctis, and A. H. Shepard, "Dark-line-resistant diode laser at 0.8 μm comprising InAlGaAs strained quantum well," *IEEE Photonics Technology Letters*, vol. 3, pp. 409-11, 1991.
- [3] S. L. Yellen, A. H. Shepard, R. J. Dalby, J. A. Baumann, H. B. Serreze, T. S. Guido, R. Soltz, K. J. Bystrom, C. M. Harding, and R. G. Waters, "Reliability of GaAs-based semiconductor diode lasers: 0.6-1.1 μm ," *IEEE Journal of Quantum Electronics*, vol. 29, pp. 2058-67, 1993.
- [4] S. L. Yellen, R. G. Waters, A. H. Shepard, J. A. Baumann, and R. J. Dalby, "Reliability of InAlGaAs strained-quantum-well lasers operating at 0.81 μm ," *IEEE Photonics Technology Letters*, vol. 4, pp. 829-31, 1992.
- [5] K. Fukagai, S. Ishikawa, K. Endo, and T. Yuasa, "Current density dependence for dark-line defect growth velocity in strained InGaAs/AlGaAs quantum well laser diodes," *Japanese Journal of Applied Physics, Part 2 (Letters)*, vol. 30, pp. L371-3, 1991.
- [6] R. G. Waters, "Diode laser degradation mechanisms: a review," *Progress in Quantum Electronics*, vol. 15, pp. 153-74, 1991.
- [7] R. G. Waters and R. K. Bertaska, "Dark-line observations in failed quantum well lasers," *Applied Physics Letters*, vol. 52, pp. 1347-8, 1988.
- [8] P. A. Kirkby, "Dislocation pinning in GaAs by the deliberate introduction of impurities," presented at 1974 International Semiconductor Laser Conference, Atlanta, GA, USA, 1974.
- [9] T. Kamejima, K. Ishida, and J. Matsui, "Injection-enhanced dislocation glide under uniaxial stress in GaAs-(GaAl)As double heterostructure laser," *Japanese Journal of Applied Physics*, vol. 16, pp. 233-40, 1977.
- [10] P. W. Epperlein, A. Fried, and A. Jakubowicz, "Stress-induced defects in GaAs quantum well lasers," presented at Proceedings of the Seventeenth International Symposium, Jersey, UK, 1990.
- [11] I. Rechenberg, G. Beister, F. Bugge, G. Erbert, S. Gramlich, A. Klein, J. Maege, M. Pilatzek, U. Richter, S. S. Ruvimov, H. Treptow, and M. Weyers, "Potential sources of degradation in InGaAs/GaAs laser diodes," *Mater. Sci. Eng. B, Solid-State*, vol. B28, pp. 310-13, 1994.
- [12] S. Ruvimov, A. Klein, U. Richter, I. Rechenberg, K. Scheerschmidt, and J. Heydenreich, "TEM study of the rapid degradation of pump laser diodes," *Physica Status Solidi A*, vol. 146, pp. 415-24, 1994.

- [13] A. Jakubowicz, "Material and fabrication-related limitations to high-power operation of GaAs/AlGaAs and InGaAs/AlGaAs laser diodes," *Materials Science and Engineering B*, vol. 44, pp. 359-363, 1997.
- [14] S. L. Yellen, A. H. Shepard, C. M. Harding, J. A. Baumann, R. G. Waters, D. Z. Garbuzov, V. Pjataev, V. Kochergin, and P. S. Zory, "Dark-line-resistant, aluminum-free diode laser at 0.8 μm ," *IEEE Photonics Technology Letters*, vol. 4, pp. 1328-30, 1992.
- [15] H. Wang, A. A. Hopgood, and G. I. Ng, "Analysis of dark-line defect growth suppression in $\text{In}_x\text{Ga}_{1-x}\text{As/GaAs}$ strained heterostructures," *Journal of Applied Physics*, vol. 81, pp. 3117-3123, 1997.
- [16] D. H. Newman, D. J. Bond, and J. Stefani, "Thermal-resistance models for proton-isolated double-heterostructure lasers," *IEEE Solid-State and Electron Devices*, vol. 2, pp. 41-46, 1978.
- [17] R. G. Plumb and A. Jeziorska, "Electrostatic discharge damage to pump lasers while operating," presented at Fabrication, Testing, and Reliability of Semiconductor Lasers, San Jose, CA, 1997.
- [18] J. Baumann, S. Yellen, R. Juhala, A. Shepard, C. Harding, R. Dalby, and R. Waters, "Strained quaternary InAlGaAs 810 nm lasers," *Proc. of SPIE*, vol. 1850 (Laser Diode Technology and Applications V), pp. 203-14, 1993.
- [19] J. A. Baumann, R. J. Dalby, R. G. Waters, S. L. Yellen, C. Harding, and A. Shepard, "Growth of InAlGaAs strained quantum well structures for reliable 0.8 μm lasers," *Journal of Electronic Materials*, vol. 23, pp. 207-16, 1994.
- [20] J. Ko, E. R. Hegblom, Y. Akulova, and B. J. Thibeault, "Low-threshold 840-nm laterally oxidized vertical-cavity lasers using AlInGaAs-AlGaAs strained active layers," *IEEE Photonics Technology Letters*, vol. 9, pp. 863-865, 1997.
- [21] J. Ko, B. J. Thibeault, Y. Akulova, E. R. Hegblom, B. D. Young, and L. A. Coldren, "MBE-grown Strained AlInGaAs/AlGaAs Vertical Cavity Lasers with Low Threshold Currents and High Output Power," *Proc. of IEEE LEOS '96*, pp. 388-389, 1996.

Appendix D: VCSEL reliability estimates

D.1. Introduction

While we will sometimes casually refer to our work as involving “VCSEL reliability,” I generally make a distinction between studying VCSEL degradation, and studying VCSEL reliability. Working on “reliability” connotes (to me at least) lifetesting extensive numbers of diodes, performing statistical analyses, and perhaps, treating the laser as a black box, where output parameters (such as light out) are affected by input parameters (such as operating current or temperature). By contrast, studying degradation (a.k.a. failure analysis) involves more knowledge of device design and operation, and attempts to pinpoint the cause of failure, and what can be done to extend it. However, it generally is unable to predict how long-lived the devices are likely to be. Our studies have been oriented exclusively toward studying the nature of degradation, and have not generally included any lifetesting involving more than a few days at a time. The one exception is a fixed-current aging rack which we have used to test the reliability of 1.55 μm VCSELs. While I believe having a full-featured lifetester at UCSB to age and test diodes would be useful, I also agree with the assessment of my professors that designing and building a lifetester (something I worked on for a few months) is probably not the best use of graduate student labor. Purchasing one, or receiving an old one as an industry gift, would probably be more attractive alternatives.

Having made my role in reliability testing clear, there is still an important relationship between reliability testing on one hand, and failure analysis on the other. The pressure on failure analysts comes directly from what is found by the people doing reliability tests. If the reliability tests are very positive, further work in failure analysis is often terminated — widespread interest in GaAs laser diode degradation ended in the mid- to late-70’s for this reason. On the other hand, if the reliability is inadequate, as with the blue-green II-VI laser diodes which last at best 100 hours, then extending the lifetime becomes the key focus in the device design process.

D.2. The importance of choosing the proper failure distributions.

One seemingly arcane aspect of reliability estimation revolves around the failure distribution shape assumed, and whether one assumes an “exponential” or “Lognormal” distribution. I have attempted here to clarify the difference between the two, and show how choosing the wrong distribution can cause one to make over-optimistic estimate.

D.2.1 Why is more than one distribution needed? How do you select the proper one to use?

We start by defining the “failure rate” $f(t)$ as the probability of failure (i.e. “death” or “cessation of function”) within a given period. Failure rate for humans is shown in Fig. D - 1, with data supplied from Henley and Kumamoto [1][2]. This shows the classical “bathtub distribution.” The left side of the tub is the high early failure rate, due to those born with congenital defects or other weaknesses, who die early in life. In product manufacturing, it is hoped that these devices can be removed from the sample by some sort of burn-in screening, so customers will not be affected by the infant mortalities. The other (right) end of the bathtub shows “wearout” failures, as the cumulative toll of long operation eventually ends life.

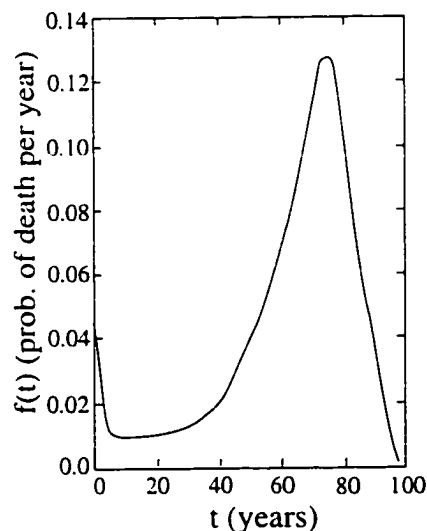


Fig. D - 1: Failure rate for humans, in percent chance of death per year (after ref. [1]).

Wearout failure is present in a wide variety of products, including light bulbs and semiconductor lasers. Note that $f(t)$ is percent chance of failure per year of the *original* population: since few of the original population survive past 80 years, the death rate falls, even though the chance of death for the few survivors continued to mount. Another parameter, “ λ ” (the hazard rate) calculates the chance of death of the *remaining* population. As would be expected, it continues to rise every year past 10 years, and does have an upper bounds.

Under different circumstances we use the “exponential distribution,” which assumes a

“constant hazard rate.” This is used when the lifetime is not limited by wearout, but rather solely by weak parts or random overstresses. Essentially, this the bathtub with the right side pushed so far out that it is no longer relevant. Examples of when to use this would include calculating how likely it is that a power transformer will be knocked out by a lightning strike, or how long some very long-lived electronic circuits will last. It appears that LEDs, with a much lower applied current density than lasers, follow the exponential distribution as well.

D.2.2 Evidence that semiconductor lasers fail due to “wearout.”

It has long been known that semiconductor lasers suffer from degradation due to coalescence of point defects into microloops, which cause gradual degradation of the active region even if other more severe forms of device degradation are not present. It is prudent to expect device failure rates to increase near the end of service life, and to perform accelerated (overstress) testing to observe this aging.

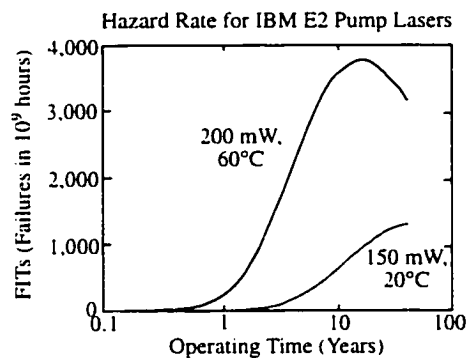


Fig. D - 2: Failure rate as a function of time for high-power laser pump diodes (after [3]).

Increasing failure rates associated with wearout are shown well in Fig. D - 2, which shows how the hazard rate increases as the device ages. These are high-power 980 nm pump lasers made by IBM laser enterprise of Switzerland, the world's leading supplier of 980 nm lasers. As expected, the lasers fail more rapidly if operating current, or operating temperature, are increased. It is by controlling these factors that we are able to accelerate

aging, and anticipate how many years a laser design is capable of lasting under normal operation, with as little as a few months of study.

The same sort of wearout failure has been observed in Honeywell VCSELs [4-6], as seen in Fig. D - 3. This has also been confirmed by work done by Boeing [7]. Given the published values of μ and σ , we can calculate $f(t)$ using the formula [2]:

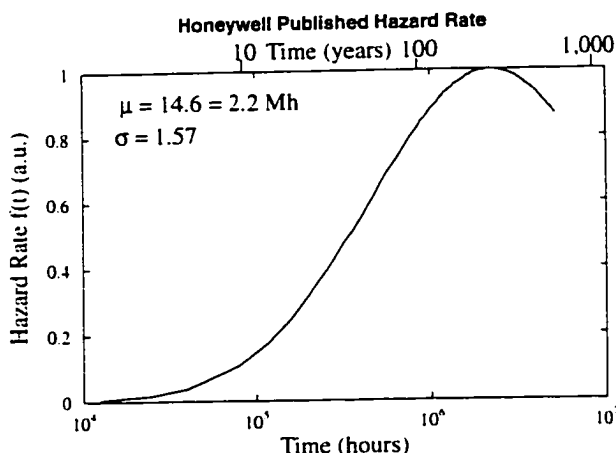


Fig. D - 3: Predicted failure rate as a function of time for Honeywell VCSELs at 40°C ambient temperature, or 52°C junction temperature, and 10 mA drive current.

$$f(t) = \frac{1}{\sigma\sqrt{2\pi}} \exp\left(-\frac{(t - \tau)^2}{2\sigma^2}\right)$$

where “ τ ” is μ , “ t ” is the natural

log (ln) of the time, and “ σ ”

describes the distribution of failures. As we mentioned before, new devices have shown a greatly

reduced $\sigma = 0.225$ [8], which

eliminates failures earlier than 10^6 hours at a 40°C ambient temperature.

D.2.3 Consequences of using the wrong failure distribution.

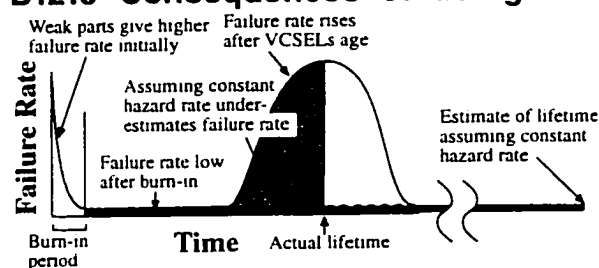


Fig. D - 4: Failure rates for VCSELs increase substantially toward the end of lifetime. Assuming a constant (non-increasing) failure rate leads to a serious overestimate of lifetime.

Failure distribution has very

important consequences to how lifestests should be done: testing a larger number of parts at a milder condition isn't a viable life-test strategy when the wearout failure mechanism is at work. Rather, degradation needs to be accelerated (preferably by increasing operating

temperature), to quickly push the devices through their normal degradation, and get into the wear-out portion of the curve where the failures occur. The failure rate then increases dramatically. For example, normal operation at 70°C will only start yielding increased degradation rates after aging devices several years. For us to assume that degradation rates will stay constant (low) would lead to a substantial overestimate of device reliability. This is shown schematically in Fig. D - 4. A similar analogy can be made with human mortality: if we (incorrectly) used observations of fatality rates only among those in early life and assumed a constant hazard rate, we would reach the conclusion that the median lifetime will be 250 years(!) What's more, among those who have made it to their 250th birthday, they

would have a 50-50 chance of living to see their 500th birthday! Clearly, ignoring wearout effects is wrong in estimating human lifetimes; I hope I have also showed it is also wrong for semiconductor lasers. More details on failure distributions are contained in Franklin Nash's MRS paper [9] and in his book [2].

D.3. Extrapolation of early degradation.

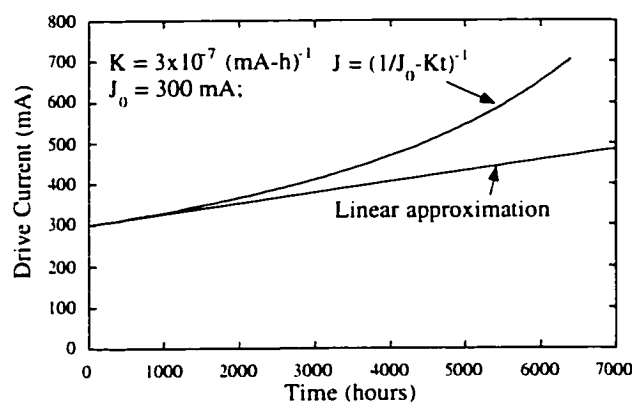


Fig. D - 5: Increase in drive current as a function of time for gradually-degrading laser diodes.

Finally, we address another common (and often misguided) practice: aging lasers under very benign conditions, observing the very small changes in output power that result, and then extrapolating what anticipated lifetime should be. For example, if our laser drops 2% in output power over one year, we assume it will take

25 years for the output power to drop 50%. Even for simple semiconductor lasers, this is a questionable practice, at least in part because the formation of dislocation networks as the device ages itself accelerates the aging rate due the additional heat, particularly where the device is being used in automatic power control (APC) mode. Empirical studies from a number of sources have shown that the current required to maintain output power followed the form: $J(t) = (1/J_0 - Kt)^{-1}$ [10]. This is true for gradual degradation: rapid degradation due to dark line defects would kill the device far more quickly. (Also not covered in this formula the ~10% initial power drop which often occurs in the first 100 hours, as the device is being "broken in.") The simple linear approximation which examines the slope early in the device's lifetime overestimates the time to current doubling by approximately a factor of 2 in the case shown in Fig. D - 5. Typical values for large stripe lasers have been inserted in the equation.

VCSELs, with their greater complexity, are even less amenable to extrapolation than other types of semiconductor lasers. With initial annealing of the

proton implant improving the device at the same time as normal degradation processes take place, degradation rates appear even lower than normal early on in the aging process; it is quite common for devices to improve initially [4].

For this reason, it is important that accelerated aging be done, and that actual device failures (as opposed to mere extrapolation to failure time) be used. This point is made clearly in James Guenter's SPIE paper [4].

References for Appendix D:

- [1] E. J. Henley and H. Kumamoto, *Reliability Engineering and Risk Assessment*. Boston, MA: Kulwer Academic Publishers, 1981.
- [2] F. R. Nash, *Estimating Device Reliability: Assessment of Credibility*. Norwell, MA: Kluwer Academic Publishers, 1993.
- [3] E.-E. Latta, A. Moser, A. Oosenbrug, C. Harder, M. Gasser, and T. Forster, "Operational limits of GaAs-based single quantum well laser diodes," *IEEE Journal of Quantum Electronics*, vol. (submitted for publication, and then withdrawn), 1991.
- [4] J. K. Guenter, R. A. Hawthorne, D. N. Granville, M. K. Hibbs-Brenner, and R. A. Morgan, "Reliability of proton-implanted VCSELs for data communications," *Proc. of SPIE (Fabrication, Testing, and Reliability of Semiconductor Lasers)*, vol. 2683, pp. 102-13, 1996.
- [5] R. A. Hawthorne, III, J. K. Guenter, D. N. Granville, M. K. Hibbs-Brenner, and R. A. Morgan, "Reliability study of 850 nm VCSELs for data communications," *34th Annual Proceedings of International Reliability Physics Symposium*, pp. 203-10, 1996.
- [6] Applications Note entitled "Reliability of Honeywell 850 nm VCSEL," by Robert Hawthorne, III, dated March 1997
- [7] H. E. Hager, E. Y. Chan, M. W. Beranek, and C. S. Hong, "VCSEL optical subassembly for avionics fiber-optic modules," presented at Fabrication, Testing, and Reliability of Semiconductor Lasers, San Jose, CA, USA, 1996.
- [8] M. K. Hibbs-Brenner, "VCSEL research, development, and applications at Honeywell," presented at '97 LEOS Summer Topicals, Montreal, Canada, 1997.
- [9] F. R. Nash, "Making reliability estimates when zero failures are seen during laboratory aging," *Proc. of the Materials Research Soc.*, vol. 184 (Degradation in III-V Compound Semiconductor Devices and Structures), pp. 3-21, 1990.
- [10] R. G. Waters and R. K. Bertaska, "Degradation phenomenology in (Al)GaAs quantum well lasers," *Applied Physics Letters*, vol. 52, pp. 179-81, 1988.

Appendix E: Introduction to Electron Beam-Induced Current (EBIC) and Cathodoluminescence (CL).

E.1. Description of Experimental Apparatus

One of our most important experimental tools was cathodoluminescence (CL) [1, 2]. For those unfamiliar with CL, an analogy can be made with the luminescence which takes place in a CRT tube: an electron beam creates electron-hole pairs in phosphors (or the sample); those electron-hole pairs give off light when they recombine. In areas where non-radiative recombination centers exist (e.g., in areas damaged by proton implantation or in areas with dislocation networks), carriers recombine non-radiatively, and the sample gives off little light. In undamaged areas, luminescence is observed. However, a few limitations exist. First, material with an indirect bandgap (e.g., AlAs or $\text{Al}_x\text{Ga}_{1-x}\text{As}$ with $x > 0.4$) will not give off cathodoluminescence, any more than it will give off photoluminescence. Second, the structure has to be appropriate for doing the analysis: it must have an escape path for light which allows the light to be captured by the CL mirror. Metal, or a highly reflective DBR mirror can prevent light from escaping from the device and being collected by the CL system. Finally, it is very important to understand how the image itself is generated: the beam is rastered across the sample, and the CL signal collected from the entire device (at the selected wavelength) is recorded point for point. The light collection apparatus has no spatial resolution in itself: the spatial resolution in the monochromatic images is indexed according to the beam position, *not* where the light escaped. Thus electron beam spread has a tremendous impact both on the spatial resolution of the collected images, and in how they should be interpreted. My co-worker Michael Cheng and I initially drew incorrect conclusions about VCSEL degradation from data sets which we will show as case studies in E.3.1.2 and E.3.3. Both careful, sceptical analysis of the collected data, along with a knowledge of possible experimental artifacts, is needed to draw correct conclusions from the data collected.

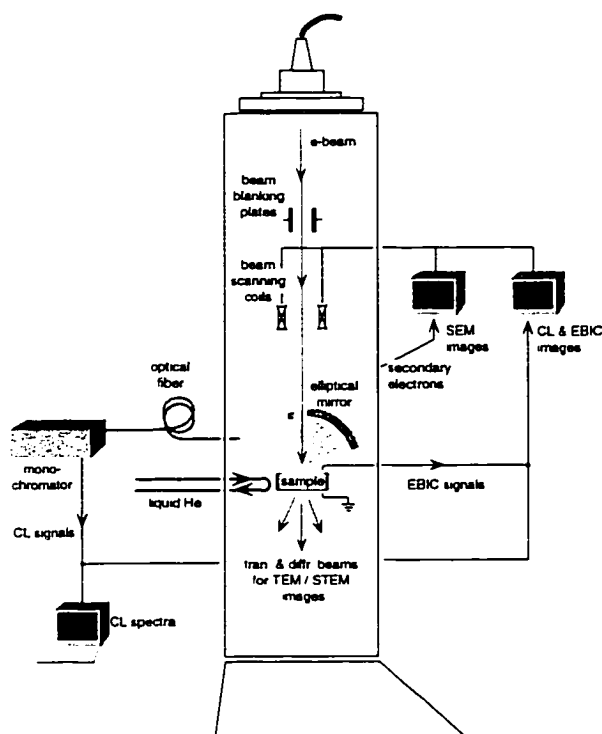


Fig. E - 1: Experimental diagram of cathodoluminescence (CL) system (Courtesy of Dr. Michael Cheng).

and good penetration depth. Experiments are performed with liquid helium cooling to increase signal-to-noise ratio, and minimize spectral broadening. Estimated sample temperature was 8K.

Cross-sectional EBIC was performed in a Hitachi S-2400, at 10–20 keV. A special stage with an isolated probe was used, and the isolated lead was connected to an electrical feedthrough. The electron beam created electron-hole pairs; those generated in the depletion region were collected through the afore-mentioned lead. (The process is similar to the generation and collection of a current in a solar cell.) The small (nano-Ampere) current was amplified by a Keithley 428 current amplifier, and then fed into the “auxiliary” input of the SEM. A number of excellent references provide more detail about electron-beam induced current (EBIC), which purists also sometime refer to as “current collection microscopy.” [1, 3-7]

Cathodoluminescence was performed in a custom-modified JEOL 1200 EX. Light was collected using a high-N.A. mirror, and focused into a large-diameter silica fiber. The experimental diagram is shown in Fig. E - 1. From there it was directed into a 0.85 m dual-grating spectrometer, and detected by a GaAs PMT. Later, we were able to improve the sensitivity of the system by replacing the large spectrometer with a smaller one (Spex/ISA Triax 180) which gave >50% throughput. A 120 kV accelerating potential was used in the microscope, giving a very narrow beam near the surface,

E.2. Electron Beam Spread in Sample.

E.2.1 Beam Spread For High-Voltage (120 keV) CL Operation

The dynamics of the electron beam scattering in the sample strongly impact the image resolution. All analyses were performed at our microscope's maximum accelerating potential: 120 keV. At this potential, electron-hole generation in GaAs peaks at $R_p \sim 12 \mu\text{m}$, and extends down to roughly $30 \mu\text{m}$, which is far deeper than thickness of the samples we are interested in examining. Our real interest is in how quickly the beam spreads in the first five microns or so. This can be roughly gauged by the 100 keV Monte Carlo simulation shown in left center of Fig. E - 2 [5].

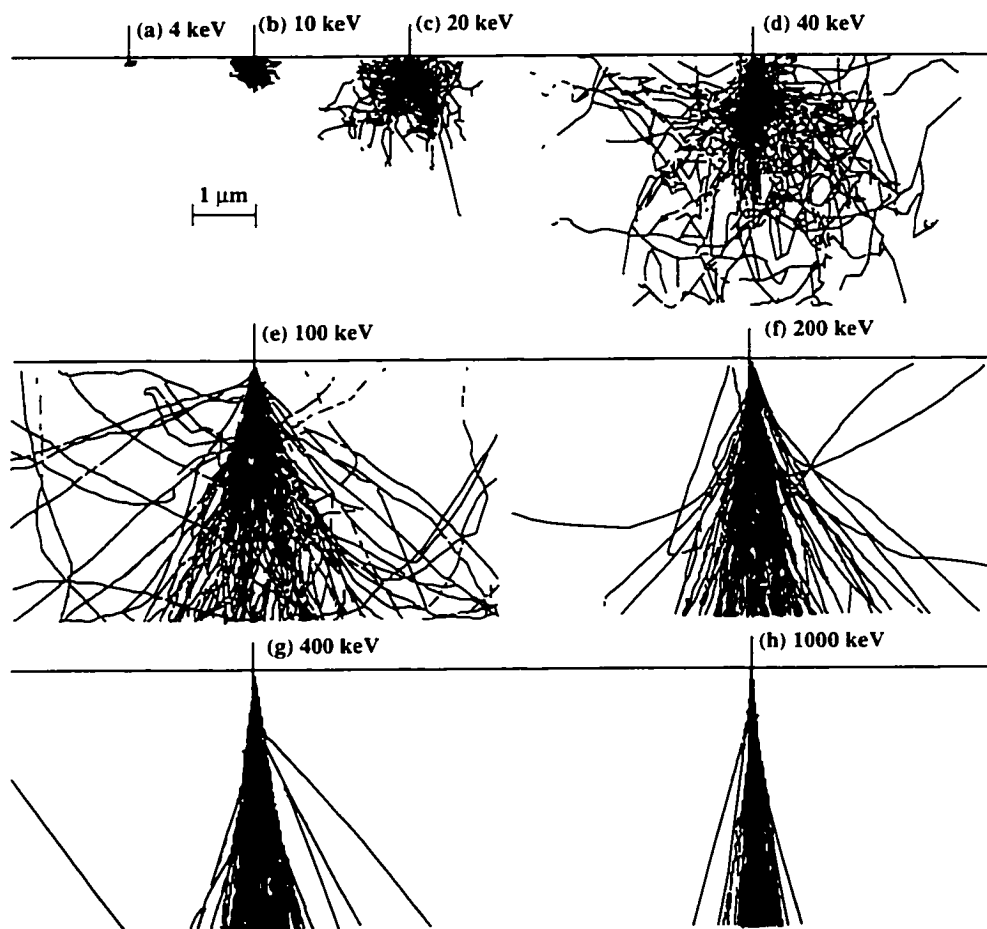


Fig. E - 2: Simulations of electron profiles in GaAs (after ref. [5])

Projected electron range is given by the formula: $R_e(E) = (2.41 \times 10^{-7} / \rho) E^{1.75}$ (in μm), where E is the incident electron energy in keV, and ρ is the material density in gm/cm^3 [5]. Typical values of ρ are 5.32 for GaAs, 3.7 for AlAs, 4.81 for InP, 5.67 for InAs, and 4.14 for GaP, 2.40 for AlP, and 2.33 for Si [8].

It should be mentioned that our CL system is essentially unique: most commercial systems are based on modifying an SEM with a maximum potential of 40 kV. In such systems, the beam spreads significantly (often to more than a micron wide) and penetrates just a few microns. While this can be advantageous for exciting the surface layer selectively without exciting the layers below, for most applications the high accelerating potential of our system is a great advantage. We also are able to do high-voltage plan-view EBIC [5] with a custom sample holder.

Using the Monte Carlo simulations shown in Fig. E - 2, and accounting for the beam spread shown due to scattering, Hwang et al. have plotted beam full-width half max. versus beam energy for a few selected depths. While the widest point in the beam increases as energy to the $^{7/4}$ power, at cross-sections close to the surface (as in the case of luminescence which is only emitted from a quantum well), beam full-width-half-max. (FWHM) drops with increasing energy, as should be clear from Fig. E - 2. This occurs due to lower scattering angles at high electron energies.

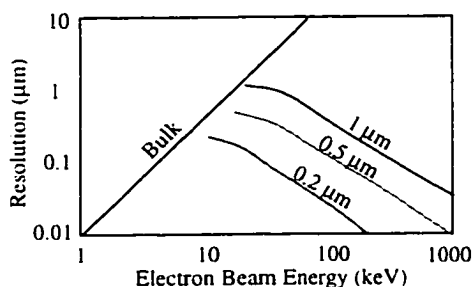


Fig. E - 3: Resolution versus beam energy for bulk sample, and for samples with quantum wells 0.2, 0.5, and 1 μm below the surface. Resolution improves as the QW is moved closer to the surface, or as beam energy is increased (after Hwang et al, ref. [5]).

The results are shown in Fig. E - 3. It should be noted that these simulations show far less backscattering than those obtained by using models provided by Dr. David Joy [3]. The additional backscattering would not be relevant for a thin film (such as a TEM sample), but it may reduce resolution in our unthinned samples.

EBIC has been implemented elsewhere with higher accelerating potential microscopes. The resolution is almost exactly

inversely proportional to the accelerating potential [5]. One observer was able to see sharply resolved DLDs in QWs beneath more than 3 μm of p-DBRs using EBIC on a 400 keV TEM, while at lower voltage (e.g., on our 120 keV machine), the resolution would be expected to be poorer than 1 μm for this sort of unthinned sample. Plan-view EBIC of degraded VCSELs was recently published [9]. We did relatively little top-emitting EBIC, since dark-line defects weren't observed in samples we examined, and p-metal apertures prevented seeing anything outside the central area. (Cross sectional EBIC is generally not useful with high voltage beams, due to excessive beam spread, and thus low-voltage EBIC for cross-sectional profiles will be addressed separately in the next section.)

E.2.2 Beam Spread for Low-Voltage (≤ 25 keV) EBIC operation

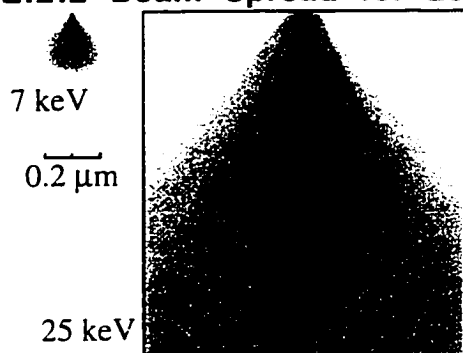


Fig. E - 4: Electron beam spread in GaAs for two different accelerating voltages. Electron-hole pair generation is proportional to the gray scale, with black occurring at the point of maximum generation.

Cross-sectional EBIC measurements

were done on devices which were degraded and then cleaved or polished along their centerline. We were thus able to look for the formation of dislocations or non-radiative centers near the active region.

A tradeoff is obtained between good signal-to-noise ratio (at high voltages) and low beam spread (at low voltages). Simulations and experimental profiles were taken by Shimizu et al. [4], and are shown in Fig. E - 4.

E.3. Limitations, and experimental artifacts observed in CL.

E.3.1 Volumetric Effects

E.3.1.1 General Observations on Beam Spread.

Beam spread, as discussed in the previous section, controls the images observed for certain types of samples. One must consider the entire volume of the sample that will be excited by the beam, and how much of that light will be collected. While a thin sample, with a small excited volume will give high spatial resolution, it also will have a relatively weak signal. By contrast, our cross sectional

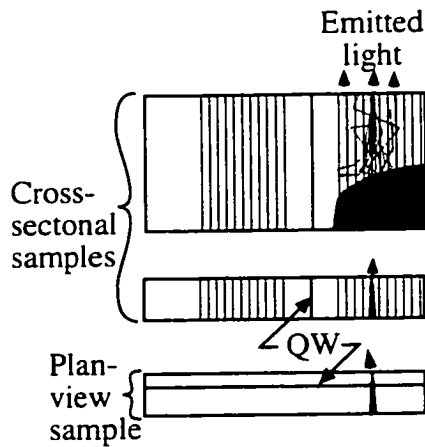


Fig. E - 5: Thick cross sectional sample (top) has luminescence spread over a large area. Thin cross-sectional sample (middle) has good resolution, but is hard to make, and has a weaker signal. Plan-view sample (bottom) has CL coming only from quantum well, and thus has good resolution.

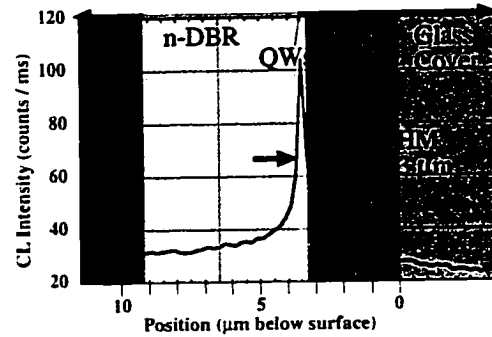


Fig. E - 6: Monochromatic line scan (650 nm) of a red InGaP-QW VCSEL cross section.

samples were easy to prepare, had very strong signals, but had sub-optimum resolution. A comparison is shown in Fig. E - 5. One disadvantage of thick samples is that

dislocation networks are generally not visible unless extremely dense. This is because CL light is generated in the dislocation-free region behind the dislocation, and washes out the contrast that would otherwise be seen in a thin sample.

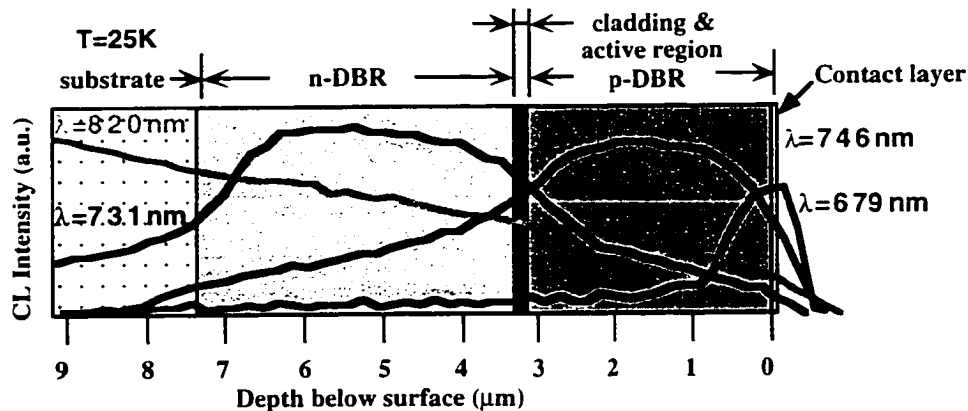


Fig. E - 7: Monochromatic profiles of cleaved VCSEL structures. Tentative peak assignments are 820 nm: substrate; 746 nm: p-DBR; 731 nm: n-DBR; and 679 nm: p-contact layer (courtesy of Dr. Michael Cheng).

The profile obtained from a red VCSEL cross sections gives an indication of the fact that a using a thick sample has compromised resolution from the InGaP quantum well to 0.3 μm FWHM, considerably wider than the $<0.005 \mu\text{m}$ beam size

at the entry point (Fig. E - 6). Bulk layers showed an even softer falloff, as seen in Fig. E - 7. However, with thresholding and contrast adjustment, a resolution of 0.1-0.2 μm was routinely obtained in CL.

E.3.1.2 Case Study: CL on Degraded Array with Tilted Polish Plane.



Fig. E - 8: Monochromatic cross-sectional CL images from devices 4 (left), 5 (center), and 6 (right) (Courtesy of Dr. Michael Cheng).

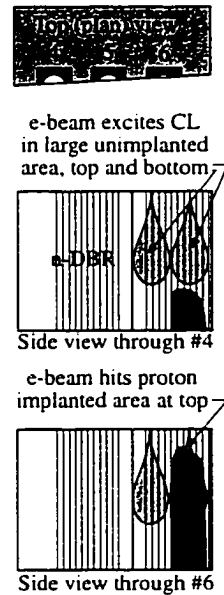


Fig. E - 9: A plan-view drawing shows how a crooked polishing plane removed more material from device 6 than from device 4 (top). A side view of device 4 (center) shows a large volume can be excited through the entire thickness of the p-DBR. Device #6 (at bottom) has reduced CL efficiency at the top of the p-DBR (which is at the right side of the drawing), due to the non-radiative centers introduced by the current-confinement implant.

The images in Fig. E - 8 were originally mis-interpreted by reading the data as if from a (straightforward) thin sample. In the original interpretation, we were trying to determine how the entire top of the p-DBR had degraded totally, from side to side, without degrading much along the bottom of the p-DBR.

However, further analysis showed that the misalignment of the polish plane had resulted in a systematic reduction in the thickness of the unimplanted p-DBR from left to right (Fig. E - 9, top). This change, and not severe degradation in the upper part of the p-DBR, was likely responsible for the differences observed. In the thicker cross-sections (e.g., device #4), a relatively large thickness of unimplanted material exists at both the top and bottom of the p-DBR. However, for thin sections, only minimal unimplanted volume is present at the top of

the DBR, resulting in the appearance of a "dark band" across the entire top of the p-DBR even where no dislocation growth has taken place.

It should be evident that much of the potential for mis-interpretation could be eliminated by using thin samples where a micron-thick-section is being examined, and the same volume of unimplanted material would be excited across the entire width of the sample. In addition, spatial resolution would likely be much higher, since only a small volume would be sampled by the beam, rather than a 30- μm -deep teardrop shape. However, such thin samples are very difficult to make, very fragile once complete, and have significantly reduced signal-to-noise ratios. With our new high-throughput spectrometer (installed in early '97), the last objection is effectively removed, and experiments with thin CL samples would be useful for future analysis, particularly to show the true boundaries of the proton implant.

E.3.2 Effects of mirror reflectivity on plan-view CL imaging.

CL has not, in our experience, proven very useful for imaging the quantum well of *unprepared* VCSEL samples. The CL signal from such samples is exceedingly weak, as can be seen from the spectrum in Figs. 3-8 & 3-9. By comparison, the signal from a prepared VCSEL is shown in Fig. 3-9, with strong luminescence from the active region. This latter sample has most of the n-DBR polished off, and we are looking (through the bottom of the sample) at a device where only a few DBR pairs stand in the way of light escaping. Thus, it is relatively easy for light to escape, relative to the situation with 22 p-DBR pairs and ~99.8% reflectivity in the unprepared VCSEL.

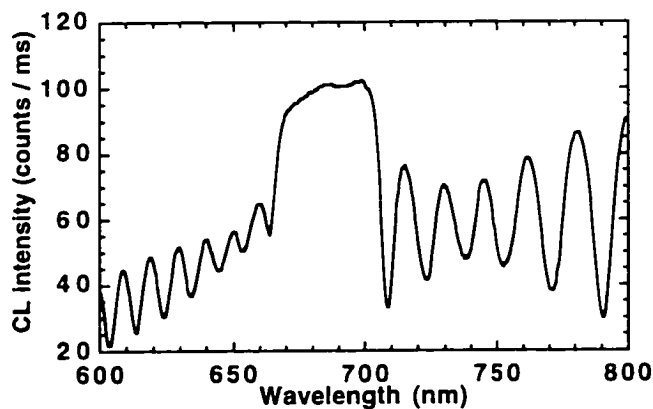


Fig. E - 10: Room-temperature plan-view CL spectrum from InGaP-QW red VCSEL. QW spectrum is broad enough that the mirror reflectivity stop band and reflectivity nulls can be clearly observed.

Another effect of the DBR reflectivity can be seen in Fig. E - 10. This sample is being viewed from the bottom, and has had the n-DBR completely removed by selective etching. What remains is the InGaP QW sandwiched in an AlGaInP confinement region, with the p-DBR below it. The room

temperature emission spectra from both the InGaP QW (which spans the range 600–750 nm) is much broader than the mirror stop-band (which spans 667–705 nm). The AlN mount and glue may also contribute some broad luminescence to the spectrum, as we shall discuss in Section E.3.4. Because the luminescence is broader than the mirror stop band, mirror reflectivity characteristics dominate the spectrum, and do not allow us to take a true room temperature CL spectrum. Fortunately, the low-temperature (<10K) CL spectrum is much narrower, and falls entirely within the stop band, and does not appear to suffer from this problem. It is also approximately two orders of magnitude stronger, and thus gives much better signal-to-noise ratio, and the ability to separate spectral peaks from various parts of the device.

E.3.3 Carbon Contamination Artifacts

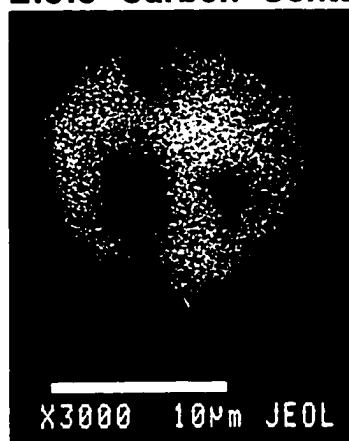


Fig. E - 11: Plan-view (i.e., top-view) image of an undegraded VCSEL after spectra were taken at three different spots. Each area where the beam dwelled appears as a "dark spot" due to deposition of a black carbon film. (Courtesy of Dr. Michael Cheng.)

Carbon contamination is a problem with all electron microscopy, particularly given the organic compounds that are used to make the conductive glues for device mounting. Fortunately, carbon contamination can be reduced in a relatively straightforward manner: cleaning the stage prior to sample mounting, and minimizing conductive cement near the area to be inspected greatly reduce the problem. Also essential is regular refilling of the liquid nitrogen trap. A great deal of experience in this matter showed that if the (JEOL 1200 EX CL) microscope were operated longer than about 2 hours, the liquid nitrogen in the cold trap would have boiled off, so the cold finger could no longer collect carbon-based vapors. After this occurred, using the microscope for even 10 seconds on any area would leave a clear indication (in the form of a thin carbon film) where the electron beam had been rastered. This could be very undesirable, as was the case for the image taken in Fig. E - 11. In this image, the cold trap was not used. The dark spots were initially

thought to be “dark-spot defects,” until it was noted that even the unaged devices quickly developed such spots after spectra were taken at multiple points. The methods of data collection were drastically changed as a result of this lesson. Monochromatic images were taken before, rather than after taking spectra. Spectra were taken from an area, rather than a single point — “spot mode” was not used in our subsequent data runs.

E.3.4 Photopumping from device submount

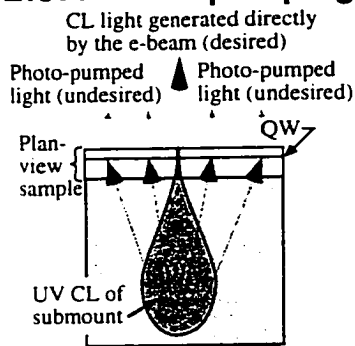


Fig. E - 12: Light is generated by the electron beam in certain types of submounts, which then optically pumps the sample.

Finally, we discuss the importance of using a submount or substrate which does not emit light with larger photon energy than the sample of interest. We preferred AlN sample mounts for the excellent CTE match to our samples, as well as their rigidity. However, as with many insulators, AlN gives off light in the UV when bombarded by e-beam radiation. The UV CL photons, which are generated over a fairly large area, then optically pump the quantum well. This effectively destroys the spatial resolution of the CL system. A plan view sample was prepared where both

the p- and n-DBR were removed, leaving only a thin InGaP film with AlGaInP confinement layers. While good spectra could be obtained, no spatially-resolved monochromatic images could be taken. I believe if a thin (but opaque) film had been deposited on the submount before the sample was bonded to it, the photopumping light could have been blocked, and this problem would have been avoided.

A similar problem was observed when taking CL spectra on a Green Nichia InGaN LED. The sapphire substrate gives off UV radiation, and while excellent spectra could be obtained, little useful monochromatic imaging could be performed. In this instance, only painstaking sample preparation to eliminate the sapphire would have allowed plan-view imaging.

References for Appendix E:

- [1] P. M. Petroff, D. V. Lang, R. A. Logan, and J. L. Strudel, "Scanning transmission electron microscopy techniques for simultaneous electronic analysis and observation of defects in semiconductors," *Scanning Electron Microscopy*, 1978, vol. 1, pp. 325-32, 1978.

- [2] P. M. Petroff, R. A. Logan, and A. Savage, "Nonradiative recombination at dislocations in III-V compound semiconductors," *Physical Review Letters*, vol. 44, pp. 287-91, 1980.
- [3] D. C. Joy, *Monte Carlo modeling for electron microscopy and microanalysis*. New York: Oxford University Press, 1995.
- [4] R. Shimizu, T. Ikuta, T. E. Everhart, and W. J. DeVore, "Experimental and theoretical study of energy dissipation profiles of keV electrons in polymethylmethacrylate," *Journal of Applied Physics*, vol. 46, pp. 1581-1584, 1975.
- [5] D. M. Hwang, L. DeChiaro, M. C. Wang, P. S. D. Lin, C. E. Zah, S. Ovadia, T. P. Lee, D. Darby, Y. A. Tkachenko, and J. C. M. Hwang, "High-voltage electron-beam-induced-current imaging of microdefects in laser diodes and MESFETs," presented at 32nd Annual (Cat. No.94CH3332-4) Proceedings of 1994 IEEE International Reliability Physics Symposium, San Jose, CA, USA, 1994.
- [6] R. B. Martins, P. Henoc, B. Akamatsu, and J. F. Palmier, "A model for the degradation of Ga(Al)As single-quantum-well lasers," *Journal of Applied Physics*, vol. 70, pp. 554-61, 1991.
- [7] J. I. Hanoka and R. O. Bell, "Electron-beam-induced currents in semiconductors," *Annual review of materials science. Vol. 11*, pp. 353-80, 1981.
- [8] V. Swaminathan and A. T. Macrander, "Section 1.5, "Tables of Materials Properties",," in *Materials aspects of GaAs and InP based structures*. Englewood Cliffs, NJ: Prentice Hall, 1991, pp. 27-28.
- [9] C. A. Gaw, W. Jiang, M. Lebby, P. A. Kiely, and P. R. Claisse, "Characteristics of VCSELs and VCSEL arrays for optical data links," *Proc. of SPIE*, vol. 3004 (Fabrication, Testing, and Reliability of Semiconductor Lasers II), pp. 122-133, 1997.

Appendix F: Material properties of AlGaAs and AlGaInP

F.1. Material properties of AlGaAs.

F.1.1 Bandgap of AlGaAs as a function of Al mole fraction and temperature.

A first step in identifying the spectral peaks observed in the CL spectrum is to obtain data on the device structure, and on the spectral properties of the materials being studied. The variation in bandgap and wavelength for $\text{Al}_x\text{Ga}_{1-x}\text{As}$ as a function of Al mole fraction is shown in Fig. F - 1.

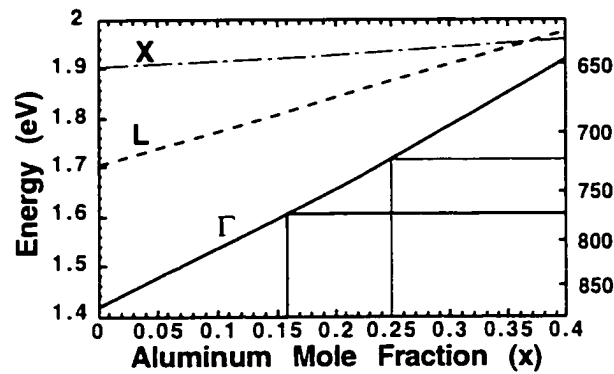


Fig. F - 1: Increase in bandgap as a function of increasing Al mole fraction.

The equations used to create Fig. F - 1 are shown below. For room temperature luminescence, we use:

$$E_g = 1.424 + 1.24x + .007x^2 \quad (\text{in eV}) \quad (\text{Eqn. F-1})$$

where "x" is the aluminum mole fraction of $\text{Al}_x\text{Ga}_{1-x}\text{As}$, 1.424 is the bandgap of GaAs, 1.24 is an empirically determined linear fitting parameter, and .007 is likewise an empirically determined bowing parameter. This bandgap is from the direct (Γ) valley. The luminescence efficiency for $x > 0.40$ becomes very weak, since AlGaAs goes indirect at mole fractions above $x \approx 0.43$. [1].

For low temperature luminescence, we obtain energies 100 meV larger, or wavelengths approximately 40 nm shorter:

$$E_g = 1.52 + 1.24x + .007x^2 \quad (\text{in eV}) \quad (\text{Eqn. F-2})$$

We can also convert from room temperature wavelengths to low temperature wavelengths using:

$$E_g(T) = E_g(0^\circ\text{K}) - (5.41 \times 10^{-4} \text{ eV/}^\circ\text{K})T^2/(T+204^\circ\text{K}) \quad (\text{in eV}) \quad (\text{Eqn. F-3})$$

These equations do not lead to fully consistent results, and are only approximate. One source of uncertainty is in doping-related shifts, as discussed below. The energies can be converted to wavelengths using the formula:

$$\lambda \text{ (nm)} = 1240 \text{ (nm-eV)} / E_g \text{ (eV)}$$

F.1.2 Quantum-confinement effects in 850 nm Honeywell VCSELs

For the 7-nm-wide GaAs QW, with $\text{Al}_{0.25}\text{Ga}_{0.75}\text{As}$ barriers, and a 60/40 split between the conduction and valence band, $\Delta E_c = 186 \text{ meV}$, and $\Delta E_v = 124 \text{ meV}$. If we assume that in the quantum well $m_e = 0.067m_0$, and $m_{hh} = 0.47m_0$, where m_e is the effective mass of the electron, m_{hh} is the effective mass of the heavy hole, and m_0 is the mass of an electron in free space ($9.11 \times 10^{-31} \text{ kg}$), we have all the information we need to do quantum confinement calculations [2]. The blue shift for the electrons as a result of confinement is 48 meV; for the heavy holes, it is 10.7 meV; thus the total blue shift is ~59 meV, or 31 nm. This is consistent with the observed low-temperature shift of 32 nm (796 nm in the GaAs QW vs. 828 nm in the GaAs substrate).

F.1.3 Absorption spectra change with doping in GaAs

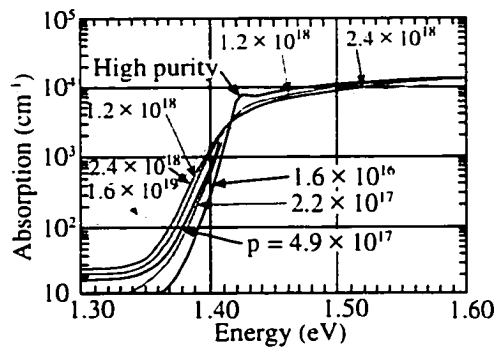


Fig. F - 2: Absorption as a function of wavelength for various levels of p-doping, at 297 K (after ref. [3]).

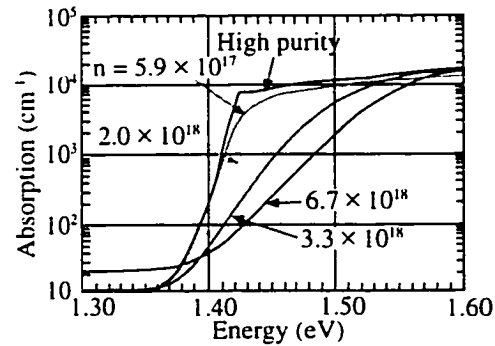


Fig. F - 3: Absorption as a function of wavelength for various levels of n-doping at 297 K (after ref. [3]).

Notable shifts in bandgap occur as a function of doping. These are a result of a number of competing factors, including bandgap renormalization, the addition

of a sub-bandgap doping tail, the unequal density of states, and a number of other factors [4]. Excellent, and widely cited, studies were done more than 20 years ago by Casey et al. The absorption spectra for n-doped and p-doped GaAs are shown in Fig. F - 3 and Fig. F - 2 [3].

As we can see, for the n-doped samples, there is relatively little change in bandgap as a result of doping until very large values of doping are used (i.e., $2 \times 10^{19} \text{ cm}^{-3}$). However, a substantial red-shift occurs as a result of p-doping, even for relatively small amounts of doping (i.e. $2.2 \times 10^{17} \text{ cm}^{-3}$). Keep in mind the doping in the bulk of our samples is nominally 1×10^{18} , and in the graded transition regions, $3\text{-}4 \times 10^{18} \text{ cm}^{-3}$ [5]. We believe that the doping-related shift is responsible for the 15 nm shift between the CL emission of the n-DBR and p-DBR (see Chapters 3 and 4 for CL results), since the composition of both mirrors is nominally identical: $\text{Al}_{16}\text{Ga}_{84}\text{As} / \text{AlAs}$.

F.2. Material Properties of AlGaInP alloys

F.2.1 Bandgap of AlGaInP

While there is still some disagreement as to the bandgap of AlGaInP alloys, and the ratio of conduction versus valence band offsets, we use the values of Meney et al. [6]. While earlier work found the direct-indirect crossover point between the Γ and X valleys to occur at $(\text{Al}_{0.7}\text{Ga}_{0.3})_{0.5}\text{In}_{0.5}\text{P}$, Meney et al. [6] believe it occurs with the lower aluminum mole fraction $(\text{Al}_{0.58}\text{Ga}_{0.42})_{0.5}\text{In}_{0.5}\text{P}$, which is also supported by recent measurements at Sandia National Laboratories [7]. The 2K values Meney et al. give for random alloy are:

$$E_g(\Gamma) = 1.985 + 0.610x \text{ (in eV)}$$

$$E_g(X) = 2.282 + 0.085x$$

where "x" is the aluminum mole fraction in $(\text{Al}_x\text{Ga}_{1-x})_{0.5}\text{In}_{0.5}\text{P}$

At room temperature, the bandgap is slightly smaller than at 2K:

$$E_g(\Gamma) = 1.900 + 0.610x \text{ (in eV)}$$

$$E_g(X) = 2.204 + 0.085x$$

Note that the bandgap increase as a function of aluminum mole fraction (i.e., $0.610x$) is not thought to change as a function of temperature, from which we can infer that the band offsets are not dependent of temperature. Ishitani et al. [8] experimentally found that for disordered alloy, the bandgap change as a function of temperature is given by:

$$E_g(T) = E_0 - E_1 \{ 1/[\exp(\theta/T)-1] + 0.5 \}$$

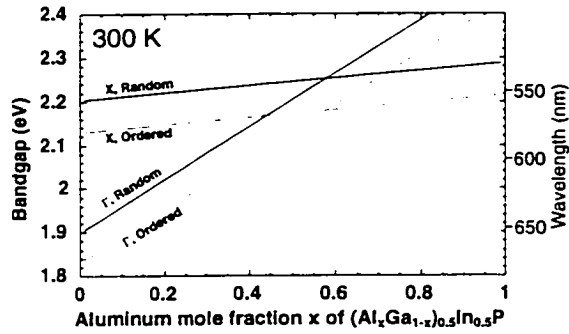


Fig. F - 4: Bandgap of $(\text{Al}_x\text{Ga}_{1-x})_{0.5}\text{In}_{0.5}\text{P}$ as a function of aluminum mole fraction x (after Fig. 1, ref. [10]).

where T is the temperature, in $^{\circ}\text{K}$; E_0 , E_1 , and θ are experimentally-determined constants, which are roughly 2.05, 0.063, and 214 $^{\circ}\text{K}$, respectively. Better fits can be obtained by using the higher-order curve fits given by Ishitani et al. [8]. Additional detail is contained in one of the recent papers by the same group [9].

Ordered alloys are thought to follow the same dependence on x , but be up to 0.1 eV lower in energy across the entire composition range. The bandgap of AlGaInP is shown in Fig. F - 4.

F.2.2 Band offsets of AlGaInP

Meney et al. give the following formulas for band offsets [6]:

$$\Delta E_c(\Gamma) = 0 + 63x - 157x^2 \text{ (in meV)}$$

$$\Delta E_c(X) = 304 + 22x - 157x^2$$

$$-\Delta E_v = 0 - 63x - 157x^2$$

The band offsets of $(\text{Al}_x\text{Ga}_{1-x})_{0.5}\text{In}_{0.5}\text{P}$ are shown in Fig. F - 5.

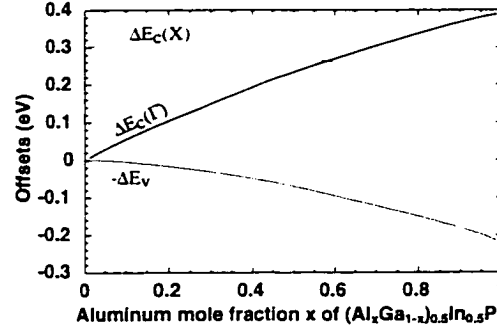


Fig. F - 5: Band offsets of $(\text{Al}_x\text{Ga}_{1-x})_{0.5}\text{In}_{0.5}\text{P}$ as a function of aluminum mole fraction x (after Fig. 4, ref. [6]).

F.2.3 Quantum confinement effects in AlGaInP / GaInP heterostructures studied.

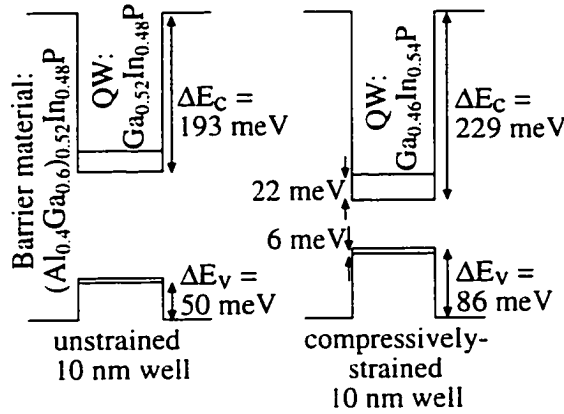


Fig. F - 6: Diagram of energy levels in unstrained and compressively-strained 10 nm GaInP quantum wells with $(\text{Al}_{0.4}\text{Ga}_{0.6})_{0.52}\text{In}_{0.48}\text{P}$ barriers.

Using the formulas for the preceding section, we investigate the size of quantum confinement effects for compressively-strained $\text{Ga}_{0.46}\text{In}_{0.54}\text{P}$ quantum wells with $(\text{Al}_{0.4}\text{Ga}_{0.6})_{0.52}\text{In}_{0.48}\text{P}$ barriers. This is the structure used in the red lasers studied. The nominal electron barrier height (ΔE_c) is 230 meV, while the barrier height for holes (ΔE_v) is 86 meV. We did the confinement calculations for both a nominally

lattice-matched (i.e., unstrained) quantum well, as well as a compressively-strained well. All samples tested had a compressively strained well. We assume $m_{hh} = 0.5m_0$, and $m_e = 0.11m_0$. Solving the finite quantum well problem, we obtain electron energy levels of 21 and 22 meV above the conduction band, respectively, for the unstrained and compressively-strained quantum wells. Holes are 5 and 6 meV below the valence band, respectively. Thus the unstrained well results in a blue-shift of 26 meV (8.4 nm), both at 2K, and at room temperature. The 10 nm well results in a 28 meV (9.8 nm) blue shift. The levels are shown in Fig. F - 6.

The bandgap for strained $\text{Ga}_x\text{In}_{1-x}\text{P}$ alloys is given by Bour [10]: $E_g = 1.351 + 0.643x + 0.786x^2$ (in eV). Comparing lattice-matched alloys ($x=0.516$, $E_g = 1.892$ eV) with our indium-rich QW devices ($x = 0.46$, $E_g = 1.813$ eV), we calculate a difference in bandgap of 79 meV, which agrees well with the our experimental difference of 83 meV after accounting for quantum confinement effects.

References for Appendix F:

- [1] D. E. Aspnes, S. M. Kelso, R. A. Logan, and R. Bhat, "Optical Properties of $\text{Al}_x\text{Ga}_{1-x}\text{As}$," *Journal of Applied Physics*, vol. 60, pp. 754-67, 1986.
- [2] L. A. Coldren and S. W. Corzine, "Appendix 1.1.2, Potential Wells and Bound Electrons," in *Diode Lasers and Photonic Integrated Circuits*, Wiley Series in Microwave and Optical Engineering. New York, NY: John Wiley - Interscience, 1995, pp. 393-399.
- [3] H. C. Casey, Jr., D. D. Sell, and K. W. Wecht, "Concentration dependence of the absorption coefficient for n- and p-type GaAs between 1.3 and 1.6 eV," *Journal of Applied Physics*, vol. 46, pp. 250-7, 1975.
- [4] K. W. Böer, "Chapter 20, Optical Absorption at Lattice Defects," in *Survey of Semiconductor Physics*, vol. 1, 1st ed. New York, NY: Van Nostrand Reinhold, 1990, pp. 491-530.
- [5] M. K. Hibbs-Brenner, R. P. Schneider, Jr., R. A. Morgan, R. A. Walterson, J. A. Lehman, E. L. Kalweit, J. A. Lott, K. L. Lear, K. D. Choquette, and H. Juergensen, "Metalorganic vapour-phase epitaxial growth of red and infrared vertical-cavity surface-emitting laser diodes," *Microelectronics Journal*, vol. 25, pp. 747-55, 1994.
- [6] A. T. Meney, A. D. Prins, A. F. Phillips, J. L. Sly, E. P. O'Reilly, D. J. Dunstan, A. R. Adams, and A. Valster, "Determination of the Band Structure of Disordered AlGaInP and its Influence on Visible-Laser Characteristics," *IEEE Journal of Selected Topics on Quantum Electronics*, vol. 1, pp. 697-706, 1995.
- [7] J. S. Nelson, E. D. Jones, S. M. Meyers, and D. M. Follstaedt, "Compositional dependence of the luminescence of $\text{In}_{0.49}(\text{Al}_y\text{Ga}_{1-y})_{0.51}\text{P}$ alloys," *Physical Review B*, vol. 53, pp. 15893-15901, 1996.
- [8] Y. Ishitani, S. Minagawa, and T. Tanaka, "Temperature dependence of the band-gap energy of disordered GaInP ," *Journal of Applied Physics*, vol. 75, pp. 5326-5331, 1994.
- [9] Y. Ishitani, S. Minagawa, H. Hamada, and T. Tanaka, "Temperature dependence of photoluminescence intensity from AlGaInP/GaInP -quantum well devices," *Journal of Applied Physics*, vol. 82, pp. 1336-1344, 1997.
- [10] D. P. Bour, R. S. Geels, D. W. Treat, T. L. Paoli, F. Ponce, R. L. Thornton, B. S. Krusor, R. D. Bringans, and D. F. Welch, "Strained $\text{Ga}_x\text{In}_{1-x}\text{P}/(\text{AlGa})_{0.5}\text{In}_{0.5}\text{P}$ Heterostructures and Quantum-Well Laser Diodes," *IEEE Journal of Quantum Electronics*, vol. 30, pp. 593-606, 1994.

Appendix G: Spectrally Filtered Electroluminescence

G.1. Device degradation, and using EL to look for dark spot defects and dislocation networks

G.1.1 Why spectral filters are necessary to get meaningful EL images

While we have shown a large number of failure analysis techniques in this thesis, most of them are only useful for research. Because the sample preparation required is so laborious, only a small number of devices can be spot checked with such techniques. Electroluminescence, however, is nearly ideal for examining failed devices. It is quick, simple, requires no sample preparation, and is non-destructive. The equipment required is extremely minimal: a useable system could be assembled for less than \$1,000. For these reasons, EL is probably the most used technique for examining degraded LEDs. With the simple addition of spectral filtering, EL is also a very useful technique for examining degradation in VCSELs.

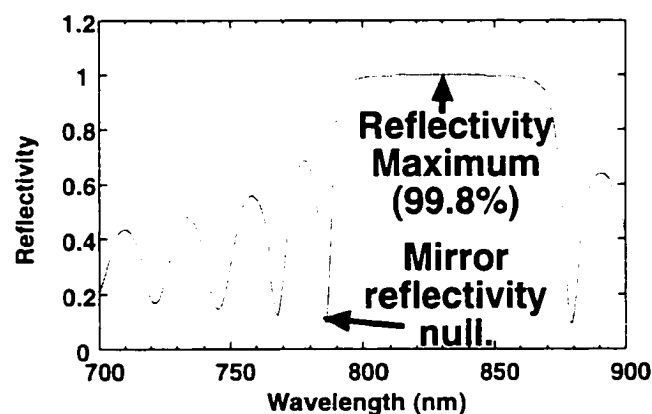


Fig. G - 1: Calculated mirror reflectivity spectrum for VCSEL with 830 nm resonance wavelength.

We start by showing the mirror reflectivity spectrum in Fig. G - 1, for a VCSEL with a 830 nm resonance wavelength. Note that the nominal emission wavelength, 850 nm, is the norm across the broad central portion of the wafer, but layer thickness falls off by a few percent toward the edges, resulting in a blue-shift of the

cavity characteristics. This was discussed in Chapter 5.

Next, consider what happens to photons which are emitted from the active region at various wavelengths, as illustrated in Fig. G - 2. We focus on the sub-threshold case, since we nearly always do our imaging at drive currents below 1 mA, while the device threshold is 4 mA. These sub-milliamp imaging currents allow us to avoid modal effects of the sort we will discuss at the end of this

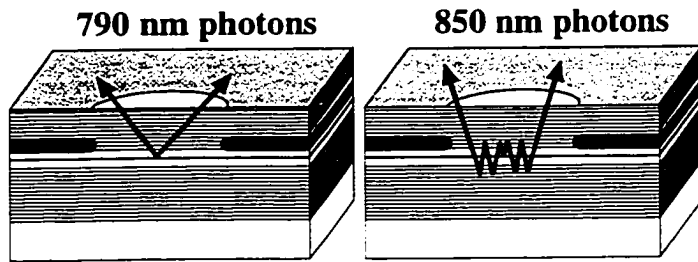


Fig. G - 2: Photons at wavelengths where mirror reflectivity is low can usually escape on the first pass (left), while at the mirror reflectivity peak, an average of 500 passes are needed before the photons can escape (right).

Appendix. Photons are not, on average, going to be emitted in a perfectly vertical direction: i.e., they are going to have some lateral k-vector. At the mirror resonance wavelength, the photon is likely to bounce up and down between the mirrors

(we have a >99.9% reflective bottom mirror, and 99.8% reflective top mirror) for hundreds of passes before it finally is emitted. Unfortunately, the photon thus is strongly affected by cavity gain, and the image ends up being homogenized. By contrast, with a reflectivity below 20% in the mirror reflectivity nulls, most photons emitted upward at the proper wavelength are able to escape without any reflection. The image at the reflectivity null thus is able to give a fairly high contrast image which accurately depicts the emission intensity map of the active region.

EL images of a rapidly degraded device are seen in Fig. G - 3. It should be noted that the device depicted here has DBRs which have a higher aluminum mole fraction (i.e., $\text{Al}_{24}\text{Ga}_{76}\text{As}$ versus the standard $\text{Al}_{16}\text{Ga}_{84}\text{As}$). As a result, the p-DBR emission (if present at all) would occur at 730 nm rather than 790 nm, and there can be no confusion about the source of the 790 nm luminescence: it is coming entirely from the active region.

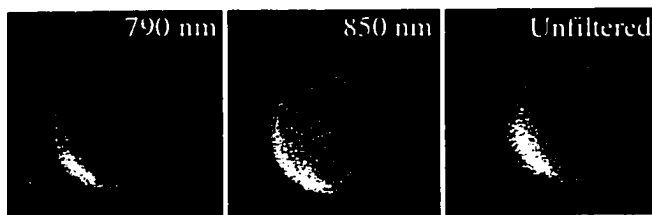


Fig. G - 3: EL images with 10-nm-FWHM bandpass filters at 790 nm (left) and 850 nm (center). Unfiltered image is shown at right.

The fact the dark circle in the 790 nm image is not centered is most likely due to misalignment between the current-confinement implant (which controls the current flow and thus where the darkening occurs) and the aperture (which

controls where we can see light). We see near-total darkening toward the right of the (790 nm) filtered EL image, due possibly to the "current shunting" failure

mechanism preventing carriers from reaching the right side of the device. At 850 nm, the gain across the entire device (including bright areas beyond the aperture edges) end up averaging over large lateral distances, and homogenizing the image. Thus, we are not able to see the dark features observed at 790 nm. At these sub-threshold currents, ~20 % of the power is contained in the 770-790 nm band, and the remaining 80% is at 830-850 nm (see Chapter 5). Thus the unfiltered image is a weighted average of the two, looking more like the 850 nm image than the 790 nm image.

G.1.2 Experimental Details

G.1.2.1 Filters Used

Ealing 10-nm-full-width-half-maximum (FWHM) bandpass filters were used to select a particular region of the spectrum [1]. The filters were 0.5" diameter round. The filters were the standard 3-cavity dielectric stack design. Over a dozen filters were purchased to allow us to look at any wavelength of interest. A custom-machined filter holder allowed us to switch between up to four filters at a time. A number of sources sell rotating filter holders for up to 8×0.5 " filters. We also tried high-pass and low-pass filters, but did not obtain results which were as good. The 3-cavity bandpass filters have a fast roll-off, and over 40 dB (10,000 \times) of suppression of wavelengths outside the pass band. By comparison, high-pass and low-pass filters have a much more gradual cut-off, and have only 20 dB (100 \times) of suppression. Standard low-pass filters thus give a lower contrast image in filtered EL than can be obtained with 3-cavity bandpass filters.

Neutral density (N.D.) filters were also purchased from Ealing to reduce the image intensity at higher drive currents. Note that the common reflective N.D. filters using a thin aluminum film are not recommended, since the light observed from VCSELs is at least partly coherent, and metal N.D. filters show intensity fringes. Absorptive N.D. filters avoid such problems. Unfortunately, the vast majority of absorptive filters are made with a type of glass manufactured by Schott, which loses neutral density quickly as wavelength increases in the infrared. The absorption of Ealing N.D. filters, by comparison, is above the specified value (i.e., ~13 \times rather than 10 \times for a 1 N.D. filter) throughout the spectral range.

G.1.2.2 Microscope Objective Tests

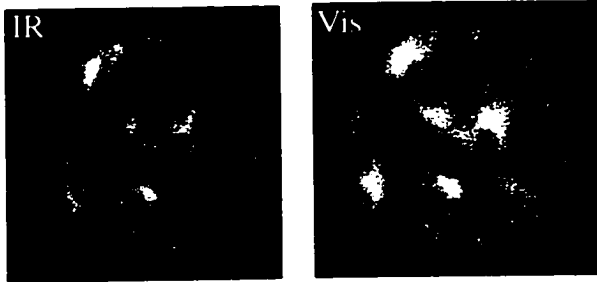


Fig. G - 4: Images from the Olympus IR Plan objective (left), and from the best visible objective (right).

Early EL results were very disappointing, since most microscope objectives are optimized for the visible, and have very poor performance in the infra-red. We performed extensive testing on a wide variety of different objective designs, and found that the Olympus IR Plan

objectives (LM594I) [2] gave by far the best results. These objectives are designed for 500–1700 nm, with special coatings also being used to optimize contrast in this wavelength range. While we did not have the facilities to do true optical bench testing, the profiling that was done indicated that the resolution of the Olympus IR objective was nearly double that of the best visible objective tested. One other “infra-red” objective from Newport, was also tested: it provided performance no better than the other visible objectives. The images from the Olympus objectives, as well as from the best visible objective, are shown in Fig. G - 4.

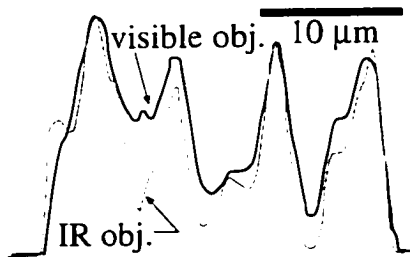


Fig. G - 5: Line scans through the images shown in Fig. G - 4. Note the improved contrast (in terms of better peak-to-valley ratio) with the IR objective.

While the images shown do not do justice to the amount of additional detail which could be seen with the better objective, it is obvious from these pictures that the IR objective has higher resolution and better contrast. The latter point can be made in a more quantitative manner by comparing line scans through the same cross section of the images, as shown in Fig. G - 5.

G.1.2.3 Camera and Frame Grabber

Both the camera and frame grabber used were considered to be excellent quality, scientific-grade components. However, normal cameras and frame grabbers are optimized for a number of criteria which are not important to those doing EL. For example, one of the key criteria is number of frames which can be acquired per second (>100 fps is available in newer boards; 0.1 frames per second would be

adequate by my standards); another benchmark is timing accuracy, which affects lateral resolution (our lateral resolution is limited solely by the optics discussed in the previous section).

While having many attributes that we don't need, the camera and frame grabbers typically used lack many important attributes for good-quality EL. First, there are a number of different brightness and contrast adjustments, both on the frame grabber, on the camera, and built into the automatic gain control (AGC) circuitry of the camera itself. While these are generally useful, they prevent accurate photometry data from being taken, since with non-linear response curves, one no longer knows what the relationship is between the actual photon intensity and the acquired image brightness. Second, while the eye is able to average frames, and see a great deal of filamentary detail in images, much of that detail is lost when capturing the image. Even the best cameras with uncooled CCDs are only able to capture 6 bits of useful information; with ours 4 bits (i.e. 16 levels) was closer to the best obtainable signal-to-noise ratio. Some improvement (which would get us closer to the 6-bit level) could have been made by frame averaging. However, this feature was not supported in our software. Finally, integration time on our camera was not adjustable. On degraded devices, we occasionally had to make large increases in currents to obtain adequate image brightness. Some work, such as PL imaging (mentioned briefly in Chapter 3) could not be done at all, since the intensity could not be further increased. In astronomical cameras, the image acquisition time can be extended to increase sensitivity to weak sources.

These shortcomings in conventional cameras could almost entirely be addressed by purchasing almost any astronomical camera with a cooled CCD and built-in frame grabber hardware. The hardware and software is optimized to allow photometry: i.e., precise, quantitative comparison of brightness from feature-to-feature. Because noise is reduced greatly by cooling the CCD with a built-in thermoelectric (TE) cooler, up to 12 bits of useful information can be gathered. Further improvement is made by the fact the digitization takes place directly from the CCD chip, without having to go through an intermediate step of being converted to a video signal. Astronomical camera software always has a wide variety of features such as frame averaging. It should go without saying that astronomical cameras

have user-controllable integration times, and are capable of picking up even the weakest images. More detail can be obtained at the helpful web site maintained by Apogee Instruments (www.apogee-ccd.com).

G.1.3 Emission from DBRs

While it is attractive to attempt to image dislocations in the p-DBR (of the sort shown in Chapter 4), this is very difficult to do conclusively using electroluminescence. In the transparent contact images shown in Chapter 3, any scratches (i.e. dislocations) at the surface created clear dark-lines in the image, so we can certainly see dark lines which are outside the active region. However, it is almost impossible to distinguish whether light is electroluminescence originating from the active region, or whether it is photoluminescence from the mirror layers which is the result of minority carrier injection. That is to say, it is very difficult to tell what plane the luminescence is originating from. It is not clear whether confocal electroluminescence would be useful: confocal microscopy allows one to view luminescence from just one particular plane, and block light originating elsewhere. Unfortunately, confocal microscopes are expensive and not widely available, so we have not had the opportunity to try this technique.

G.2. Modal dynamics, spectral narrowing, and surface roughness.

G.2.1 Basic principles: how surface roughness can create dark and bright spots.

So far in this appendix, we have talked about the dark spots we can see with filtered EL, and gone on the assumption that they are always due to dislocation networks, or some other degradation phenomenon. However, this is not always the case. VCSELs are so sensitive to mirror reflectivity that small phase shifts in a selected area can prevent lasing in that region. Above threshold, non-uniformities in the gain (either due to thermal lensing, or device degradation) can force filamentation in the lasing structure. We refer to above-threshold filamentation as “modal dynamics,” since it is unstable by its nature, and changes rapidly with drive current.

A number of tests can be used to distinguish dark areas due to degradation from those due to rough mirrors. The first test would be simple optical microscopy

of the part in question. If there is visible surface roughness or imperfection, this is likely to result in a non-uniform EL image, for reasons we will discuss at length below, and show experimentally. Second, we can use filters to look for “complimentary emission”: a dark spot at one wavelength appears to be a bright spot at another wavelength. Complimentary emission never occurs with true degradation, and is related to spoiled reflectivity through undesirable phase shifts. This complimentary emission is shown in Fig. G - 6 (not a Honeywell device). By tilting the filters off angle, we can shift the peak wavelength of the bandpass [3]. We can go from one image of G-6 to the other with as little as a 15° rotation of the filter (~ 5 nm) under certain conditions. By comparison, no change in the image over a very broad range of wavelengths is observed when dark spots are due to true degradation. Any wavelength near or outside the DBRs pass band will show a similar image of the “dark patches,” when such patches are due to true degradation rather than surface roughness.

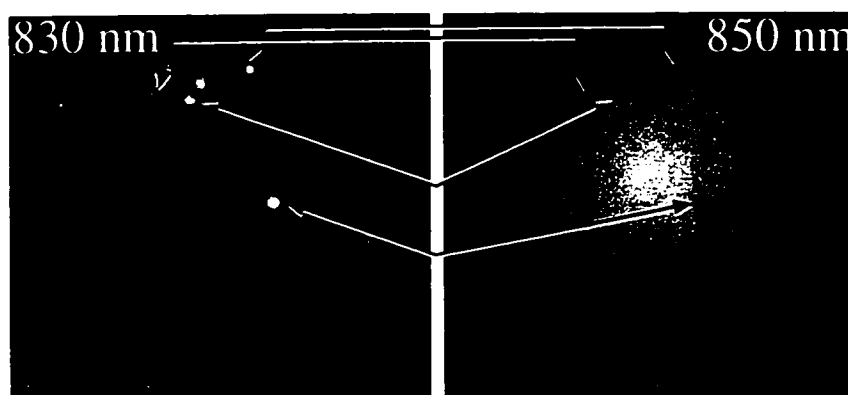


Fig. G - 6: Complimentary emission is observed in filtered EL of large VCSEL with surface defects. At lasing wavelength (right), rough spots appear dark, while off-resonance (left), the same spots appear bright. Arrows identify complimentary pairs.

The principle behind complimentary emission is shown in Fig. G - 7. Surface roughness, either in the coatings or in the epitaxial layers, creates an undesired phase shift which spoils the resonance in the rough region. The sensitivity of VCSELs to even small changes in mirror thickness was demonstrated by Dowd et al., who were able to dramatically change the modal characteristics by removing only 60–70 nm from the top using FIB machining [4]. The surface

roughness greatly reduces the efficiency of the stimulated emission needed for lasing, and thus leaves a higher carrier population under the rough spots.

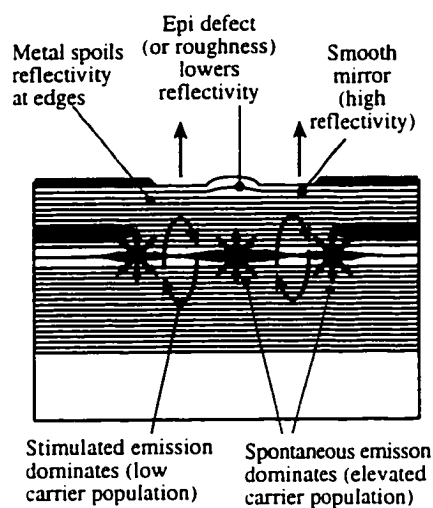


Fig. G - 7: Cross section through device shows stimulated emission lowers carrier concentration in smooth sections, while in rough sections, carrier concentration is able to build up higher.

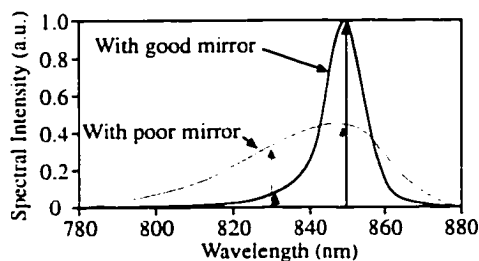


Fig. G - 8: Spectral narrowing in smooth sections gives a higher peak, but less power outside the peak.

The spectra which result can be seen schematically in Fig. G - 8. Spectral narrowing is well-understood phenomenon, and happens even below threshold (where these images were taken). At the peak resonance wavelength of the mirror (850 nm), the intensity is higher where the mirror is smooth. However, in the rough spots where stimulated emission has been spoiled, the greater spectral width makes the rough spots brighter off the resonance wavelength (e.g., at 830 nm). Similar "complimentary emission" can be observed by spatial hole burning above the lasing thresholds, as we shall show below.

If the defects of the sort shown in Fig. G - 6 are in the epitaxy (rather than the coating), they will frequently serve as nucleation sites for degradation. Thus, "rough" devices should be screened out of production lots. Using the off-resonance wavelength to image the EL seems to be the most obvious way of recognizing even small defects which might be overlooked by optical inspection.

G.2.2 Multifilamentary devices.

While the complimentary emission of the previous device in Fig. G - 6 was unintentional, intentional surface patterning can be useful for making quasi-incoherent devices. Quasi-incoherent VCSELs have advantages of both LEDs

(fewer problems with modal interference effects), and advantages of lasers (high switching speeds, high efficiency, and efficient fiber coupling). Such “multi-filamentary” or “quasi-incoherent” devices [5] have a very broad, 5 nm FWHM, as discussed earlier in Chapter 5.

Fig. G - 9 shows filtered EL from a normal 15- μm -aperture device [6]. Note the number of independent filaments, each of which is constrained enough laterally to have a significant lateral k-vector of a non-uniform size, and thus each filament lases at a slightly different wavelength. Consistent with our observations in the previous section, complimentary emission is observed.

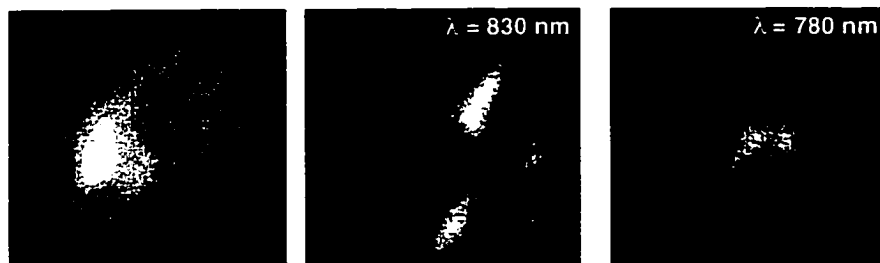


Fig. G - 9: Unfiltered image (left) looks relatively homogeneous; 830 and 780 nm images both show structure not visible without filters.

More through studies, using better optics (see section G.1.1.2) and more wavelengths, are shown in Fig. G - 10. Careful comparison was made of images at the lasing wavelength (830 nm), and other wavelengths, by overlapping images which had been assigned different colors. It was found that the 820 nm image was most nearly the opposite of the 830 nm image (i.e., spots that were bright in the 820 nm image were dark in the 830 image, and vice-versa). This is consistent with our explanation of complimentary emission due to surface roughness in the previous section. At shorter wavelengths, absorption and re-emission of luminescence by the $\text{Al}_{16}\text{Ga}_{84}\text{As}$ DBR layers tends to interfere with the simple complimentary nature of the image. Absorption and re-emission becomes more important as photon energy increases, and with it the rapid rise in the AlGaAs absorption coefficient (see Appendix F for details). Thus the 750 nm image was quite homogeneous in all devices examined, with much lower contrast than images seen at non-absorbing wavelengths.

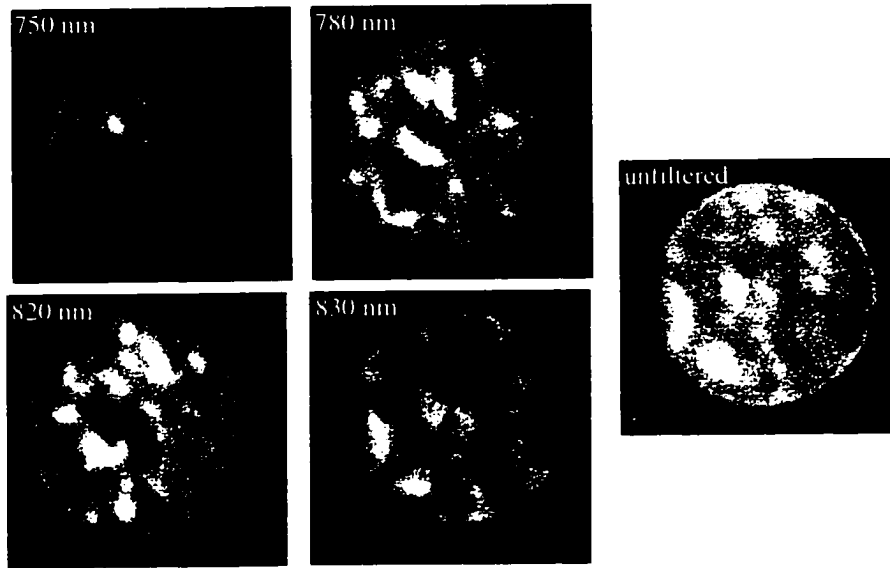


Fig. G - 10: Filtered EL images of a large (25- μm -aperture) multifilamentary VCSEL.

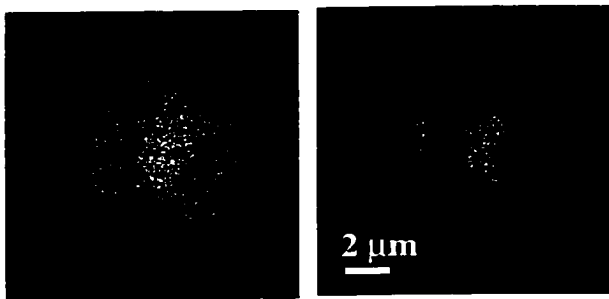


Fig. G - 11: EBIC images of 15- μm -diameter multifilamentary VCSELs show reduced current collection efficiency in smooth areas where carriers are annihilated by stimulated emission before they can be collected. Normal image is shown at left; enhanced contrast image is shown to the right.

The stimulated emission effects are very strong, even well below threshold. We had originally discounted them because we were operating at currents only a few percent of threshold current for many of these images. However, studies which have been performed on VCSELs by Raddatz et al. have shown how spectral narrowing can take place even at

very low currents [7]. This affected every observation made, including EBIC (Fig. G - 11) and cross-sectional NSOM, where the variations in carrier concentration were immediately apparent as dramatic changes in brightness coming out the sides of the sample.

G.2.3 Above threshold: modal dynamics in ordinary VCSELs



Fig. G - 12: Filtered EL of lasing VCSEL. 850 nm image (right) shows lasing filaments, concentrated at the top of the device. 780 nm image (left) shows dark areas of reduced spontaneous emission where the lasing mode has depleted the carrier population.

Finally, we show that complimentary emission is also observed in lasing devices with smooth DBR mirrors (Fig. G - 12). Thermal lensing creates filaments, where strong lasing builds up, and the carrier population is depleted. These filament areas appear dark at wavelengths off the resonance peak, consistent with the spectral narrowing model presented earlier.

References for Appendix G:

- [1] Bandpass filters were purchased from Ealing Electro-Optics, 89 Doug Brown Way, Holliston, MA, 01746, (508) 429-8370, (800) 343-4912
- [2] Olympus LM594I 80x MS plan ULWD objective was purchased from the Scientific Instrument Company, 5855 Uplander Way, Culver City, CA 90230, (310) 568-9188
- [3] c.f. p. 45 of the 1994 Corion catalog: $\lambda_\theta = \lambda_0(n_e^2 - \sin^2\theta)^{1/2}(n_e)^{-1}$, where: λ_θ = center wavelength at θ° angle of incidence; λ_0 = center wavelength at 0° angle of incidence; θ = angle of incident light from normal; and n_e = effective index; derived from the indices of the filter used; use 2.0 for most dielectric stacks.
- [4] P. Dowd, L. Raddatz, Y. Sumaila, M. Asghari, I. H. White, R. V. Penty, P. J. Heard, G. C. Allen, R. P. Schneider, M. R. T. Tan, and S. Y. Wang, "Mode Control in Vertical-Cavity Surface-Emitting Lasers by Post-Processing Using Focused Ion-Beam Etching," *IEEE Photonics Technology Letters*, vol. 9, pp. 1193-1195, 1997.
- [5] R. A. Morgan and M. K. Hibbs-Brenner, "Vertical-cavity surface-emitting laser arrays," *Proc. of SPIE*, vol. 2398 (Circular-Grating Light-Emitting Sources), pp. 65-93, 1995.
- [6] R. W. Herrick, Y. M. Cheng, P. M. Petroff, M. K. Hibbs-Brenner, and R. A. Morgan, "Spectrally-filtered electroluminescence of vertical-cavity surface-emitting lasers," *IEEE Photonics Technology Letters*, vol. 7, pp. 1107-9, 1995.
- [7] L. Raddatz, I. H. White, H. D. Summers, K. H. Hahn, M. R. Tan, and S. Y. Wang, "Measurement of guiding effects in vertical-cavity surface-emitting lasers," *IEEE Photonics Technology Letters*, vol. 8, pp. 743-5, 1996.

Appendix H: Observation of the changes in L-I, I-V, and C-V curves with degradation.

H.1. Examining how the L-I characteristics change with time.

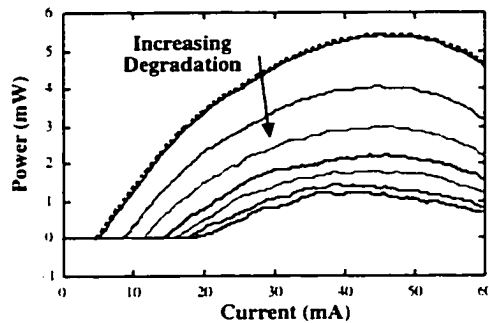


Fig. H - 1: L-I curves for a device as it is aged.

One of the major questions of our research into VCSEL degradation has been, “granted, the p-DBR degrades under some circumstances, but does mirror degradation affect device operation directly?” This is an incredibly difficult question to answer, and I have no indisputable evidence showing how mirror degradation affects device performance. It should be noted that even if there is no direct electrical or optical impact

of mirror degradation, dislocations from the p-DBR can nucleate dislocations in the active region — something which may well happen according to evidence discussed earlier in Chapter 4 [1]. One of the greatest hopes of resolving the question about the effect of mirror degradation on device performance lay with careful analysis of the light out vs. current in (L-I) characteristics. This sort of analysis is widely used on undegraded semiconductor lasers to determine gain parameters, injection efficiency, and cavity loss. It is best done with a range of different cavity lengths for stripe lasers. To simplify theory somewhat, changes in p-mirror’s reflectivity

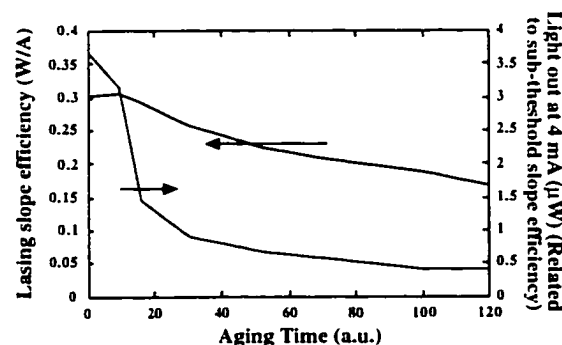


Fig. H - 2: The sub-threshold output and slope efficiency both fall as the device ages.

(e.g., due to dislocation formation) result in reduced slope efficiency, while changes in the sub-threshold efficiency should be due to changes in active region efficiency alone. While this may be reasonable for in-plane lasers (with relatively low-reflectivity mirrors), there is substantial evidence that stimulated emission is significant in VCSELs well below lasing

threshold, given the very high reflectivity of the mirrors. In Appendix G we have shown that significant spatial hole burning (which is caused by stimulated emission) occurs for currents as low as 80 μA on lasers with 4,000 μA threshold currents! This has also been shown by Raddatz et al. [2]. It is in this context that I point out that the sub-threshold efficiency data was taken near threshold (4 mA), as seen in Fig. H - 2. While the power reduction was the same at lower (e.g., 1 mA) biases, the test apparatus had significant, non-reproducible zero offsets that prevent accurate measurement of slope efficiencies in the low micro-ampere range, where stimulated emission could reasonably be neglected. We have shown L-I characteristics taken at much lower currents in Section 3.8.2, using a better test apparatus. Taking data from the side of VCSELs, provided light is able to escape from the sides, is (in principle) a better way to be able to determine the true spontaneous emission as a function of current.

The series of L-I curves taken in Fig. H - 1 have aging that is approximately equal to 10-15 years per curve at room temperature (considerably less at higher temperatures or powers). The sub-threshold characteristics, seen Fig. H - 2, fall early-on, and dramatically, providing strong evidence that the active region is indeed putting out less light, and that device degradation is not solely or primarily due to reduced reflectivity of the p-DBR.

Another possibility raised was that the generation of minority carriers in the p-DBR (i.e., the generation of electrons) by the optical pumping discussed in chapter 5, would consume a significant fraction of the injection current, and thus have a negative electrical effect on the device. However, this seems to me to be double-counting. Since an additional hole is created for each electron injected, the recombination event should have no net impact on the device's electrical characteristics.

Detailed derivations to extract changes in active region efficiency and mirror reflectivity were planned until the aging results from the red VCSELs were obtained, as discussed in Section 6.4. Remarkably, laser performance actually *improved* when VCSELs were aged at very high currents (15–20 mA for a 15 μm -diameter active region device with a 3.5 mA initial threshold). The wallplug power conversion efficiency actually doubled from 2% undegraded to 4% after aging.

Simplistic analysis of the data would have yielded the conclusion that the aging process in this case reduced mirror loss — an exceedingly unlikely event. Far more likely is an explanation of photo- or thermal annealing reducing the point defect concentration in the active region, and thus improving its efficiency. This sort of annealing has also been observed elsewhere [3].

While analysis of L-I characteristics can be valuable for extracting internal parameters where many other parameters (e.g., active region performance, mirror reflectivity) are known or at least constant, it seems of much more limited utility in an instance such as ours, where both the active region and mirror characteristics are changing simultaneously in unknown ways. Also, un-mentioned to this point is the addition of optical loss in the active region. The dislocation network is extremely dense through the entire active region (where optical flux is a maximum); on the other hand, p-DBR dislocations are much sparser and located where the standing wave intensity is quite low (near the surface). Thus, even if we could assume predictable changes occurred in the active region, we could not reasonably expect to de-convolve the joint effects of mirror loss *and* active region loss on the overall cavity loss. Perhaps the best way to measure how the mirror characteristics change is through a direct physical measurement. This is quite challenging on actual degraded devices, since the area to be measured is about 10 μm in diameter, and even a tiny change from 99.8% (the original p-DBR reflectivity) to 99.6% after degradation would double the mirror losses, yet be almost undetectable using a simple reflectivity measurement. However, with a high-resolution spectrometer, and the right optical hardware, it may be possible to combine sufficient spatial and spectral resolution to measure the cavity lifetime. The spectral width of the cavity null is proportional to cavity loss. Thus, for the change in mirror reflectivity mentioned above, even though the reflectivity has only changed by a small fraction of a percent, the width of the null would double.

In the excellent paper by C.C. Wu et al.[4], the issue of loss at the edge of the optical cavity is discussed. They note that their L-I curve becomes less “kinky” as the device degrades, implying that a larger number of modes are supported in the degraded device. Our findings are the opposite: the L-I curve becomes more kinky as the device degrades.

H.2. C-V and I-V Characterization

An array of VCSELs was aged at 60 mA (where the VCSELs were past their peak-power point, and putting out 0.5-1.0 mW at the start of device aging). Voltage was 2.8 V, for 167 mW in, and an estimated junction temperature $\approx 150^\circ\text{C}$. The devices were aged from 18–48 hours, until the threshold had measurably increased. C-V measurements were then taken at 1 MHz with an HP 4912B LCR meter, while I-V measurements were made using an HP 4145B parameter analyzer.

H.2.1 C-V characterization

C-V characterization has been used as a tool to study laser degradation nearly 25 years ago by Yang et al [5], who observed an increase in the trap density from $5 \times 10^{16} \text{ cm}^{-3}$ before aging to $1.5 \times 10^{18} \text{ cm}^{-3}$ afterward. Here, we do not deal with deep-level transient spectroscopy (DLTS), which uses temperature-dependent capacitance measurements to determine trap concentrations. Rather, we focus on the more straightforward method of using changes in the C-V profile to indicate changes in the dopant profile near the active region [5-8].

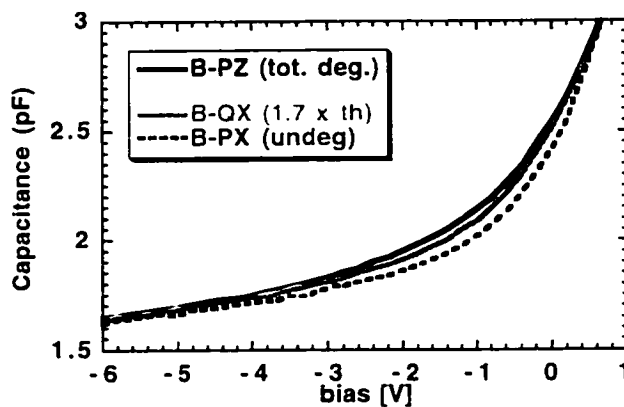


Fig. H - 3: Capacitance voltage characteristics for VCSELs in various stages of degradation.

Relatively little change in capacitance was observed after aging, with a 4-8% increase visible at -1 V (Fig. H - 3). This increase could be due to a number of causes, with the two most likely explanations being reduced depletion region width due to zinc from the p-DBR diffusing into the confinement layers, or due to lateral expansion of the

capacitor (nominally a $40 \mu\text{m}$ square) due to annealing of the proton implantation. The data were analyzed in a number of methods for extraction of additional data, including taking the derivative $d(C^2)/dV$ vs. C (or V), which then allows $N_B(x)$ vs. x_B to be plotted. The differences between devices were small enough that this data

was lost in the noise; no additional information beyond that shown here was gathered from this analysis.

This inconclusive finding is consistent with the back-of-the-envelope analysis performed a few years ago, where I ruled out DLTS analysis for VCSEL structures generally, due to low modulation of the depletion width in the highly-doped DBR layers bounding the wide undoped $1\text{-}\lambda$ region. It should be noted that most of the C-V and DLTS papers published have used special, low-doped structures to give maximum penetration of the intrinsic region under reverse bias

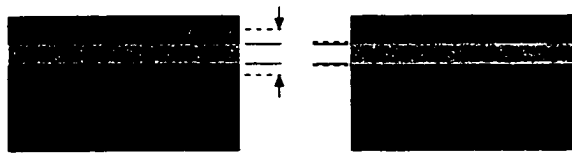


Fig. H - 4: The intrinsic region is able to sweep across a wide portion of the device in a low-doped LED, with the width increasing to the position depicted with the dotted lines when a strong reverse bias is applied (left), but able to move only 1 nm in an "as-designed" VCSEL (right).

(e.g., [9]). The geometric considerations are shown in Fig. H - 4. If the doping profiles are exactly as specified in the design (with no doping in the region between the mirrors), the intrinsic region will widen only 1 nm as the reverse bias is increased to -10V, and only a tiny

volume will be swept by modulating the applied reverse bias.

H.2.2 I-V characterization

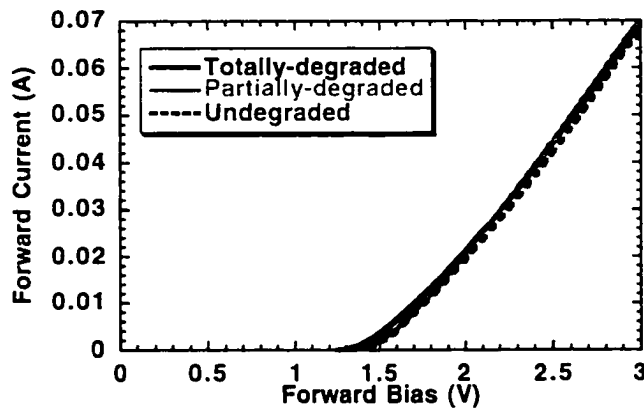


Fig. H - 5: Forward-bias I-V curve show a slight decrease in the turn-on voltage for rapidly degraded devices.

I-V characterization is a simple and common method of characterizing laser diodes before and after degradation to look at how they have changed [8, 10, 11]. Measurement is extremely accurate with the right equipment (> 5 decimal places), and measurements can be taken

across more than 10 orders of magnitude. A number of parts of the I-V curve can be characterized separately, giving a great deal of information about what's going on inside the device.

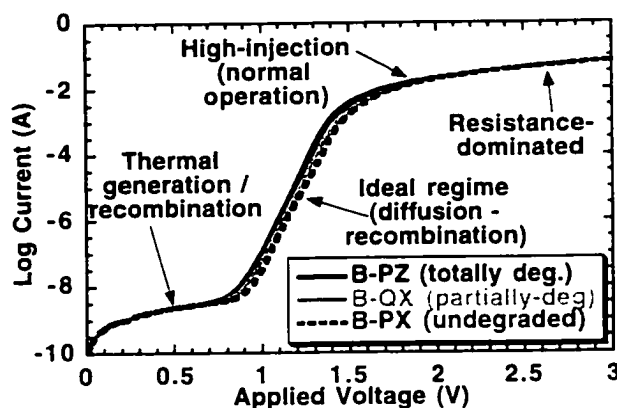


Fig. H - 6: Forward-biased I-V curve (log scale) shows increased current for a given voltage (or a reduction in voltage for a given current).

present in this region. Between 0.9–1.5V, ideal recombination / diffusion (with $n = 1$) takes place in the ideal diode. For our lasers, the ideality factor “ n ” was approximately 1.6–1.8. Above that, high-level injection increases n to 2, and finally, series resistance limits any further attempt of the curve to follow the exponential relationship [10, 12].

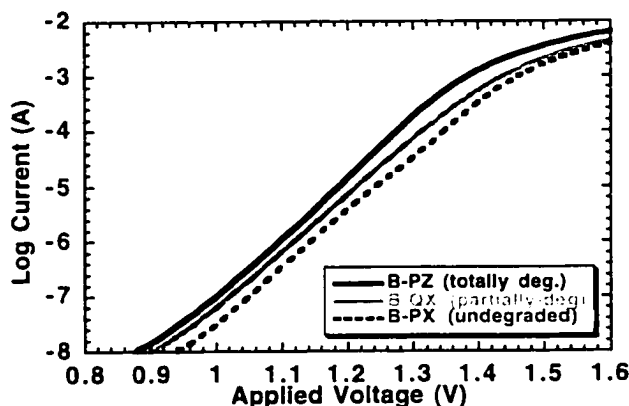


Fig. H - 7: Closeup of “ideal” portion of I-V curve below lasing threshold. Current is increased by a factor of 4, or voltage reduced by ~ 0.08 V, after degradation.

The linear and logarithmic forward-biased I-V curve are shown in Fig. H - 5 and Fig. H - 6, respectively. For normal GaAs diodes, the recombination of thermally generated current is important below ~ 0.9 V for most lasers, and follows the form $I = \exp(qV/nkT)$, with the ideality factor $n \approx 2$. However, on our VCSELs, it appears that a nearly constant 200–230 M Ω resistance is

Note that the curves change little after degradation, except in the ideal diffusion-recombination regime, which is expanded in Fig. H - 7. A number of explanations are possible for the lower voltage (for a fixed current) or the higher current (for a fixed voltage) observed in the degraded VCSELs. One possible explanation would be increased

recombination at non-radiative centers around the device edges. We also expect reduced contact resistance, and reduced lateral resistance under the proton implanted regions due to the aging process.

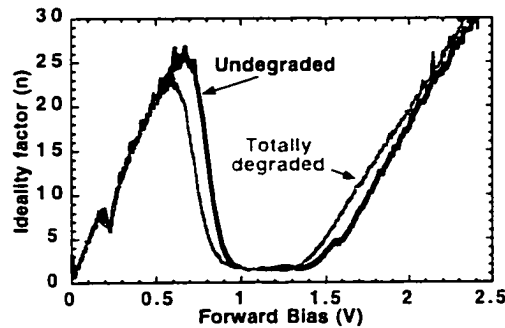


Fig. H - 8: Ideality factor for a VCSEL before and after degradation.

Another method of analysis and comparison is the use of the ideality factor “n” defined above. We derive the ideality factor from our data using the definition $n = (kT/q) / \{d(\ln I)/dV\}$. The result is shown in Fig. H - 8. We are not able to draw useful information from this, as were Magistrali et al., since resistance dominates the VCSEL curve across almost the entire operating range, due to

the much smaller contact area present in VCSELs than in an ordinary stripe laser. (Soderstrom et al. cite the series resistance of a VCSEL as being $30\ \Omega$, while it is only $4\ \Omega$ for a CD laser [13].). The “ideality factor” is not meaningful except in the narrow “ideal range” $V < 0.9$ or > 1.6 V, due to the domination of resistive effects. However, the leftward shift as well as the increase in differential resistance after aging are clearly visible.

In reverse bias, from 0 to -7 V the thermo-tunnel current dominates [10]. At

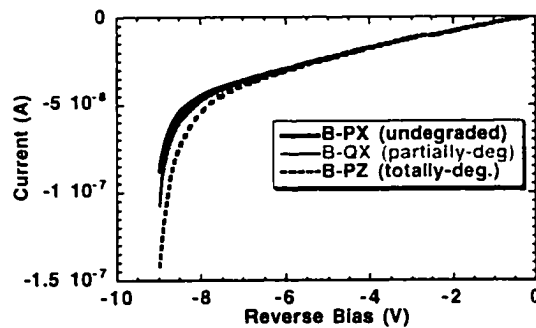


Fig. H - 9: Reverse-bias I-V curve shows reduced breakdown voltage (and a softer “knee”) for rapidly degraded devices.

reverse biases larger than -7 V, avalanche breakdown is evident, and occurs earlier in aged VCSELs. The reverse bias characteristics are seen in Fig. H - 9. It is not clear what changes have taken place to lower the breakdown voltage, but the reduction in breakdown may be a good marker for how far the degradation process has progressed.

References for Appendix H:

- [1] Y. M. Cheng, R. W. Herrick, A. C. Yen, P. M. Petroff, M. K. Hibbs-Brenner, and R. A. Morgan, "Defect-related degradation in vertical-cavity surface-emitting lasers," *To be published*, 1997.
- [2] L. Raddatz, I. H. White, H. D. Summers, K. H. Hahn, M. R. Tan, and S. Y. Wang, "Measurement of guiding effects in vertical-cavity surface-emitting lasers," *IEEE Photonics Technology Letters*, vol. 8, pp. 743-5, 1996.
- [3] J. Ko, M. J. Mondry, D. B. Young, S. Y. Hu, L. A. Coldren, and A. C. Gossard, "Threshold reduction by rapid thermal annealing in MBE-grown AlInGaAs multiquantum well lasers on GaAs," *Electronics Letters*, vol. 32, pp. 351-352, 1996.
- [4] C.-C. Wu, K. Tai, K.-F. Huang, and C.-Y. Chang, "Reliability of proton implanted vertical cavity surface emitting lasers," *International Journal of High Speed Electronics and Systems*, vol. 5, pp. 731-64, 1994.
- [5] E. S. Yang, "Formation of interface states and defects in GaAs-Al_xGa_{1-x}As DH lasers under room-temperature cw operation," *Journal of Applied Physics*, vol. 45, pp. 3801-3805, 1974.
- [6] M. M. Sobolev, A. V. Gittsovich, M. I. Papentsev, I. V. Kochnev, and B. S. Yavich, "Degradation mechanism of GaAs/AlGaAs quantum well laser," *Fizika i Tekhnika Poluprovodnikov*, vol. 26, pp. 1760-7, 1992.
- [7] M. M. Sobolev, A. V. Aittsovich, S. G. Konnikov, I. V. Kochnev, and B. S. Yavich, "Deep level defects detection in degrading GaAs/AlGaAs quantum well laser," *Material Science Forum*, vol. 143-147, pp. 1547-1552, 1994.
- [8] I. Rechenberg, G. Beister, F. Bugge, G. Erbert, S. Gramlich, A. Klein, J. Maege, M. Pilatzek, U. Richter, S. S. Ruvimov, H. Treptow, and M. Weyers, "Potential sources of degradation in InGaAs/GaAs laser diodes," *Mater. Sci. Eng. B, Solid-State*, vol. B28, pp. 310-13, 1994.
- [9] K. Kondo, O. Ueda, S. Isozumi, S. Yamakoshi, K. Akita, and T. Kotani, "Positive feedback model of defect formation in gradually degraded GaAlAs light emitting devices," *IEEE Transactions on Electron Devices*, vol. ED-30, pp. 321-326, 1983.
- [10] T. V. Torchinskaya, A. A. Shmatov, and M. K. Sheinkman, "Recombination-enhanced transformation of deep centers in red light-emitting AlGaAs diodes," *Physica Status Solidi (A)*, vol. 110, pp. 213-220, 1988.
- [11] F. Magistrali, E. Mariani, G. Salmini, and M. Vanzi, "Failure analysis of 980 nm high power lasers," *Proc. of the 20th Intl. Symp. Testing and Failure Analysis*, vol. ISTFA-20, pp. 335-340, 1994.
- [12] R. F. Pierret, "Section 6.2: Deviations from the ideal," in *Semiconductor Device Fundamentals*. Reading, MA: Addison-Wesley, 1996, pp. 260-281.
- [13] R. Soderstrom, K. Jackson, and D. Kuchta, "New 850 nm VCSELs and CD-type lasers provide interoperable low cost data links," presented at IEEE Lasers and Electro-Optics Society 1995 Annual Meeting., San Francisco, CA, USA, 1995.